

DOCTOR OF PHILOSOPHY

Simulation and Analysis of Gas Freeing of Oil Tanks

Chow, Kevin

Award date:
2010

Awarding institution:
Coventry University

[Link to publication](#)

General rights

Copyright and moral rights for the publications made accessible in the public portal are retained by the authors and/or other copyright owners and it is a condition of accessing publications that users recognise and abide by the legal requirements associated with these rights.

- Users may download and print one copy of this thesis for personal non-commercial research or study
- This thesis cannot be reproduced or quoted extensively from without first obtaining permission from the copyright holder(s)
- You may not further distribute the material or use it for any profit-making activity or commercial gain
- You may freely distribute the URL identifying the publication in the public portal

Take down policy

If you believe that this document breaches copyright please contact us providing details, and we will remove access to the work immediately and investigate your claim.

Simulation and Analysis of Gas Freeing of Oil Tanks

Kevin Chow

**A thesis submitted in partial fulfilment
of the University's requirements
for the Degree of Doctor of Philosophy**

February 2009

Coventry University

Acknowledgements

First and foremost, I would like to thank my family and friends for their support through this extended period of my life. A big thanks to my supervisor, Professor Holdø, for providing wisdom and guidance and opportunity, as well as the current and previous members of what is now EETARG at Coventry University for their input, support, and occasional humorous diversion in the face of computational difficulties.

I would also like to thank the members of staff at the University of Hertfordshire and also Høgskolen i Narvik/Narvik University College for accommodating me during the different phases of my work.

Abstract

This thesis presents an in-depth study of the gas freeing of marine crude oil tanks using numerical simulation, beginning with a general summary of the problem, followed by an outline of the objectives of this work and the main difficulties involved.

To outline essential background, a review of numerical methods, fluid flow, and related physical mechanisms has been undertaken, in addition to related ventilation fields, jet and jet impingement, and tanker-borne ventilation, in order to determine the state of the art and draw useful parallels between different ventilative fields, as well as identifying potential areas for model validation.

A room-ventilation test case was studied in order to demonstrate the numerical method. It was found that assuming adiabatic walls and ignoring radiation resulted in highly idealised temperature predictions, and that radiation played a large part in enhancing vertical temperature prediction by redistributing thermal energy.

For the gas-freeing analysis, the geometric models and solution procedures are introduced before simulation results presented and validated with analytical jet models and impingement penetration parameters. Analysis showed that the internal temperature of the tank was approximately homogeneous, allowing the tank to be considered isothermal. 2D simulations showed that after an initial period of time, the *relative* concentration distribution reaches steady state with decreasing average concentration as gas-freeing continues.

Discussion of the results followed, examining aspects surrounding heat transfer and the choice of turbulence model, analysing the differences in the results between the first and second-moment closure schemes and justification of assuming isothermal conditions. The variation in concentration was examined, and an analytical expression was derived which approximates the reduction in average gas concentration decay due to gas-freeing.

It has been shown that double-hulled construction renders the internal temperature variation to around 10% of the temperature difference between the sea and deck. During the gas-freeing process proper, it was shown that after any stratified layer has been eroded and a stable flow field established, the relative concentration distribution remains constant. Gas freeing times were shown to be heavily dependent on the volume flux (and thus air change rate), and mathematical relations derived in order to provide approximately predict the time to gas free a crude oil tank (COT) given particular initial conditions.

List of Nomenclature

Lower Case Latin

a	Coefficient of absorption
c	Speed of light in a vacuum
d	Diameter
e	Internal energy
f	Characteristic frequency
g	Gravitic acceleration
g'	Relative gravity
h	Height; Hub diameter (of fan); Convective heat transfer coefficient
h_0	Total height of chamber
k	Thermal conductivity; Turbulence Kinetic Energy (TKE)
l	Characteristic length scale; Slab thickness
l_m	Length scale of mixing
m_0	Initial species concentration
$m(t)$	Variation of species concentration over time
n_x	Normal wall distance along x
p	Pressure
q	Heat flux
$r_{0.5}$	Radius from jet centre at half-velocity
s	Spatial co-ordinate
\hat{s}	Direction unit vector
S_{ij}	Fluctuating strain rate
t	Time
t_{ir}	Initial region time
Δt	Time step
u	Velocity
$\langle u_i \rangle$	Spatially-filtered velocity
u_x	Friction velocity
u^+	Velocity normalised by friction velocity
$\overline{u_i}$	Mean fluctuating velocity (RMS)
$u(x)$	Velocity at position (x)

x	Co-ordinate (streamwise)
x_0	Virtual origin of jet
Δx	Distance/Cell characteristic length
y^+	Normalised wall distance

Upper Case Latin

A^*	Effective opening area
A_j	Jet vent area
B	Velocity decay
B_s	Buoyancy flux
C	Courant Number
C_R	Rotta's constant
C_s	Smagorinsky constant
C_μ	Coefficient of turbulent viscosity
$C(t)$	Variation of concentration over time
D	Coefficient of diffusion
E	Entrainment rate
F	Source term
G_k	Production of TKE
G_b	Buoyancy contribution to turbulence
H_i	Height of stratified layer
I	Radiation intensity
J	Diffusion flux
L	Characteristic length scale; local visual jet diameter
P_d	Normalised penetration depth
Q	Volumetric flow rate
S	Jet spreading rate
S_ε	Turbulence Dissipation rate source term
S_{ij}	Mean strain rate
T	Temperature
U	Mean supply velocity; Total heat transfer coefficient
V	Volume
ΔZ	Penetration depth

Greek and other symbols

ℓ	Integral length scale
β	Coefficient of thermal expansion; Total coefficient of absorption
δ	Viscous length scale; Neutral layer height; Stratified layer thickness
δ_{mix}	Length scale of mixed fluid at stratified interface
δ_{ij}	Kronecker delta
ε	Emissivity; Turbulence dissipation rate
ε_{ijk}	Dissipation rate tensor
η	Kolmogorov length scale; coefficient of mixing efficiency
κ	von Karman's constant
Γ	Coefficient of diffusion
λ	Taylor length scale; Air changes per hour
λ_B	Batchelor length scale
μ	Dynamic viscosity
μ_t	Turbulent viscosity
ν	Kinematic viscosity
ξ	Ratio of radial distance to jet radius
ρ	Density
σ	Stefan-Boltzmann constant; Turbulent Prandtl number
σ_s	Radiation scattering coefficient
σ_k	Turbulent Prandtl number for TKE
σ_ε	Turbulent Prandtl number for turbulence dissipation rate
τ	Shear stress; Kolmogorov time scale
τ_w	Shear stress at the wall
τ_{ij}	Reynolds shear stress
υ	Kolmogorov velocity scale
ϕ	Fluid property; Scattering phase function
ψ	Stream function
ω_k	Angular velocity
Ω	Solid angle
$\overline{\Omega_{ij}}$	Mean rate of rotation
Ω_{ij}	Rotation rate

Subscripts

i, j, k	Unit vectors (Einstein summation)
t	Turbulent
∞	Ambient
η	Spectral

Acronyms

ACH	Air Changes per Hour
API	American Petroleum Institute; density measure
CDS	Central Differencing Scheme
CFD	Computational Fluid Dynamics
CFL	Courant-Friedrichs-Levy (criterion)
COT	Crude Oil Tank
DNS	Direct Numerical Simulation
DO	Discrete Ordinates
dwt	Dead-Weight Tonnes
FPSO	Floating Production, Storage and Offloading
IMO	International Marine Organisation
ISGOTT	International Safety Guide for Oil Tankers and Terminals
LES	Large-Eddy Simulation
LFL	Lower Flammability Limit
LIF	Laser Induced Fluorescence
LRR-IP	Launder, Recce and Rodi, Isotropization of Production
MARPOL	International Convention for the Prevention of Pollution from Ships (MARine POLLution)
MILES	Monotonically Integrated LES
MUSCL	Monotone Upstream-centred Scheme for Conservation Laws
MWR	Method of Weighted Residuals
PISO	Pressure Implicit with Splitting of Operators
QUICK	Quadratic Upstream Interpolation for Convective Kinematics
RANS	Reynolds-Averaged Navier-Stokes
RJH	Rotary Jet Head
RMS	Root Mean Square
RNG	Re-Normalised Group
RSM	Reynolds Stress Model
RTE	Radiative Transfer Equation
SGS	Sub-grid Scale
SIMPLE	Semi-Implicit Method for Pressure Linked Equations
SKE	Standard K-Epsilon (turbulence model)
SOLAS	Safety of Life at Sea
TKE	Turbulent Kinetic Energy

TVD	Total Variation Diminishing
UFL	Upper Flammability Limit
ULCC	Ultra Large Crude Carrier
URANS	Unsteady Reynolds-Averaged Navier Stokes
VLCC	Very Large Crude Carrier
VOC	Volatile Organic Compound

Table of Figures

Figure 2.1- Plot of eddy wavenumber against spectral energy density based on the Kolmogorov energy spectrum.....	16
Figure 2.2 - Graphical representation of the resolved scales, modelled scales and interaction of the cutoff filter-width (dashed line).....	21
Figure 2.3 - Plot of near-wall region and correlation of commonly prescribed log-law	26
Figure 2.4 - Solar irradiation spectrum with various wavelengths of interest (Modest 2003:6).....	30
Figure 2.5 - Neutral Layer plots; enclosed room remote to surroundings (left); room open to external ambient conditions (right).....	33
Figure 2.6 - Air flow inside a typical room ventilated using displacement ventilation	34
Figure 2.7 - Schematic of characteristic regions (above) in a typical jet with relative velocity reference plot (below).....	44
Figure 2.8 - Plot of non-dimensionalised velocity trend with respect to downstream distance	45
Figure 2.9 - Comparison of Reynolds normal and cross stresses through the radius of a jet (Pope 2000:106).....	47
Figure 2.10 - Modes of surface deformation with increasing jet momentum	50
Figure 2.11 - Depiction of the different regimes, adapted from Cotel & Breidenthal (1997).....	51
Figure 2.12 - Results of Shy (1995) and Lin & Linden (2005), in combination with different correlations of results.....	54
Figure 2.13 - Shear-induced recirculation flow patterns driven by a jet supply in an obstructed enclosure.....	56
Figure 2.14 - Size comparison between typical COT (30m high), a typical human (1.8m high) and a typical double-decker bus (~4m).....	58
Figure 2.15 - View of the oil tanker AbQaiq. (Picture Credit - Photographer's Mate 1st Class Kevin H. Tierney, United States Navy).....	59
Figure 2.16 - Comparison of single-hull (left) and double-hull (right) internal structural details ...	59
Figure 4.1 - Schematic of environmental chamber domain and sizing (dimensions in metres).....	75
Figure 4.2 - Side view of smallest 36,000-cell mesh	77
Figure 4.3 - Isometric view of discretisation of medium-sized 173,600-cell mesh	78
Figure 4.4 - Side view of medium-sized 173,600-cell mesh.....	78
Figure 4.5 - Side view of the most dense 384,000-cell mesh.....	78
Figure 4.6 - Comparison of three different mesh densities using Loop 1 boundary conditions (Realizable K-E, 23°C wall temperature) without radiative transfer. Effect of lower density mesh is to reduce the temperature gradient over the stratified layer.....	79

Figure 4.7 - Comparison of three different mesh densities using Loop 1 boundary conditions (Realizable K-E, 23°C wall temperature) with radiative transfer. Reduced gradient effects previously seen across stratified layer no longer present. However, the thermal boundary layer at the floor and ceiling is slightly affected.....	80
Figure 4.8 - y^+ contours for 36,000-cell mesh. Most of the wall exhibits $y^+ < 50$	81
Figure 4.9 - Comparison of different engineering assumptions (adiabatic walls and neglecting radiative transfer) relative to the experimental results of Iial-Awad (2006).....	82
Figure 4.10 - Temperature contour plots of adiabatic wall conditions.....	83
Figure 4.11 - Temperature contour plot of conducting and radiating walls with air participation in thermal radiation.....	84
Figure 4.12 - Comparison of predicted vertical temperature profiles using different K-E turbulence models.....	84
Figure 4.13 - Contour plot of turbulence intensity for Loop 3 boundary conditions (Realizable K-E, 27°C wall temperature).....	85
Figure 4.14 - Contour plot of turbulence intensity for Loop 5 boundary conditions (RNG K-E, 27°C). Note higher scale limits.....	85
Figure 4.15 - Contour plot of turbulence intensity for Standard K-E (Loop 7). Scale is much higher than previous models.....	86
Figure 4.16 - Turbulence intensity field with adjusted scale - note the reduction of turbulence intensity around stratified layer.....	86
Figure 4.17 - Comparison of vertical temperature profile given different air absorptivities.....	87
Figure 4.18 - Comparison of different boundary conditions and experimental results.....	89
Figure 5.1 - 3D Model of crude oil tank showing internal structure; dimensions in metres.....	95
Figure 5.2 - Schematic of upper web frame dimensions (metres).....	96
Figure 5.3 - Schematic of lower half-width web frame dimensions (metres).....	96
Figure 5.4 - Schematic showing geometric location of venting positions (dimensions in metres)..	97
Figure 5.5 - Coordinate system and directional locations in crude oil tank.....	97
Figure 5.6 - Plan view of transition from regular hexahedral mesh (regular node spacing on the periphery) to prismatic cells in the outlet region (centre of figure) using a Delauney-generated mesh.....	98
Figure 5.7 - Plan view of transition from hexahedral elements to prismatic elements via a “butterfly” mesh around the supply vent - fine mesh (Mesh C).....	98
Figure 5.8 - Mesh distribution at floor of tank; Course Mesh A (Top); Medium density Mesh B (Middle); Dense Mesh C (Bottom).....	100
Figure 5.9 - Isometric view of COT wall mesh (Mesh A). Port, inboard (left on figure) and Starboard, outboard (right, angled floor).....	100
Figure 5.10 - Result of axisymmetric representation of COT.....	101

Figure 5.11 - Computational mesh of axis-symmetric domain; jet entry and direction is bounded by lower x-axis; thicker line above centre defines outlet vent.....	102
Figure 5.12 - Computational mesh involving 15m duct along rotational axis at bottom of figure, resulting in slight difference to mesh.....	102
Figure 5.13 - Local detail view of duct transition mesh; Inlet is the detail on the left.....	103
Figure 5.14 - Example of a portable gas-freeing fan with casing cut away	104
Figure 5.15 - Diagrammatic comparison of velocity profiles	104
Figure 5.16 - Comparison of Turbulent and Fan inlet velocity profiles.....	105
Figure 5.17 - Cutaway of typical structure cross-section, and approximation of structural section with respect to calculating heat transfer through section.....	107
Figure 5.18 - Nondimensionalised centreline velocity decay	112
Figure 5.19 - Axial velocity profiles at different downstream locations.....	113
Figure 5.20 - Contour plots of velocity of planar slices through the jet inlet centreline; considerable off-axis jet bending is evident; Red represents 50m/s	114
Figure 5.21 - Plot of Reynolds Stress of three meshes and three downstream points against correlation from Agrawal & Prasad (2003).....	114
Figure 5.22 - Images of y^+ in the internal impingement region (left) and external regions subject to jet impingement and recirculation (right) with coarse Mesh A	115
Figure 5.23 - Images of y^+ in the internal impingement region (left) and external regions subject to jet impingement and recirculation (right) with Mesh B.....	115
Figure 5.24 - Images of y^+ in the internal impingement region (left) and external regions subject to jet impingement and recirculation (right) with fine Mesh C	116
Figure 5.25 - Jet centreline velocity decay.....	117
Figure 5.26 - Non-dimensional axial velocity profile in the radial direction.....	117
Figure 5.27 - Graph of Reynolds-stress prediction using different turbulence models	118
Figure 5.28 - Temperature profiles averaged between spaces defined in Figure 5.29 to show differences in ventilated and un-ventilated upper-zone spaces.....	119
Figure 5.29 - Diagram of ventilated and un-vented upper frame-spaces	120
Figure 5.30 - Comparison of average temperatures in non-vented frame spaces.....	120
Figure 5.31 - Comparison of different thermal simulation cases	121
Figure 5.32 - Comparison of centreline velocity decays resulting from different inlet velocity profiles (Equation (2.77))	123
Figure 5.33 - Comparison of turbulent viscosity between different inlet conditions.....	124
Figure 5.34 - Comparison of downstream axial velocity profiles resulting from different jet inlet profiles.....	125
Figure 5.35 - Comparison of Reynolds stresses in the self-similar region from different jet inlet profiles.....	125

Figure 5.36 - Distribution of C_4H_{10} on plane through jet centreline	127
Figure 5.37 - Distribution of O_2 concentration on plane through jet.....	128
Figure 5.38 - Filled contour plots of velocity magnitude (top) and butane concentration (bottom) of slice through tank at 0.5m from floor	129
Figure 5.39 - General description of flow-field and dominant vortices; vector plot uses same colour scale	131
Figure 5.40 - Plot of layer heights versus time during gas free operations with different initial conditions.....	132
Figure 5.41 - Comparison of ventilation rates of different web spaces.....	134
Figure 5.42 - Comparison of normalised penetration depths against Richardson number to Shy (1995) and Lin & Linden (2005)	135
Figure 5.43 - Impingement zone C_4H_{10} concentration contour plots; a) 50m/s Jet from deck; b) 32.5 m/s ducted jet; c) 75m/s jet from Deck.....	136
Figure 5.44 - Contour plots of C_4H_{10} concentration in simulation 3F at different times during gas-freeing; a) 20.6s; b) 773s; c) 0.5 hrs; d) 0.93 hrs; e) 1.95 hrs; f) 3.47 hrs	137
Figure 5.45 - Contour plots of C_4H_{10} mass fraction in Simulation 3I; contour range has been manually adjusted and does not represent concentration maxima in tank; a) 0.41 hrs; b) 1.79 hrs; c) 3.18 hrs	137
Figure 5.46 - Histogram plots of C_4H_{10} concentration at two different times from simulation 3F; note similarity of distribution with decreasing concentration.....	138
Figure 5.47 - Histograms plots of C_4H_{10} concentration at two different times from simulation 3H - fully mixed initial state; again, concentration distribution is similar.....	139
Figure 5.48 - Histograms of C_4H_{10} mass fraction from simulation 3I (blocked); after removal of layer, distribution over time also becomes similar	140
Figure 5.49 - Time-history contour plots of O_2 mass fractions; a) 440s; b) 0.41 hrs; c) 1.52 hrs..	141
Figure 5.50 - Rate of change of global area-averaged oxygen concentration per air change	141
Figure 5.51 - Plots of minimum O_2 concentration during gas-freeing operation	142
Figure 5.52 - Decay of field-average CO_2 mass fraction during gas-freeing operation.....	142
Figure 5.53 - Plot of field-maximum concentration of CO_2 during gas-freeing operation	143
Figure 6.1 - Comparison of layer erosion rates between different turbulence models and buoyancy effects.....	146
Figure 6.2 - Comparison of gas freeing ventilation curves for K-Epsilon and Reynolds stress models, with and without buoyancy extensions	147
Figure 6.3 - Comparison of K (Top) and Epsilon (Bottom) in K-E and RSM models	148
Figure 6.4 - Comparison of K Production between K-Epsilon and Reynolds Stress models	150
Figure 6.5 - Comparison of effect of poor species convergence on rates of ventilation	152
Figure 6.6 - Overlay of various gas freeing plots of mass sum of butane in tank versus time.....	154

Figure 6.7 - Schematic of gas-freeing progression and separation of regions	155
Figure 6.8 - C ₄ H ₁₀ concentration contour plots showing movement of re-stratified butane at the top of the tank during gas-freeing. Left: 0.78 hrs; Centre: 1.34 hrs; Right: 1.62 hrs.....	156
Figure 6.9 - Comparative plots of butane remaining in tank between 3B (50m/s) and 3C (32.54m/s, 15m ducting) and 3D (75m/s), showing differences in initial region and time to layer erosion	156
Figure 6.10 - Comparison of Initial Region in stratified and fully mixed simulations	157
Figure 6.11 - Comparison of stream functions; Phase 3C (Left) with 15m duct and 7,110m ³ /hr flow rate; Phase 3D (Right) with 21,440 m ³ /hr flow rate; Note different contour ranges	158
Figure 6.12 - Comparison of stream functions; Phase 3D (Left) with 21,440 m ³ /hr; Phase 3B (Right) with 14,290 m ³ /hr flow rate.....	158
Figure 6.13 - Contour plots of stream-function for Simulation 3I. Left: Max = 21.7kg/s;	159
Figure 6.14 - Contour plot of density showing different rate of layer-erosion caused by obstruction	160
Figure 6.15 - Comparison of ventilation rates in each floor web-space compared to overall rate.	160
Figure 6.16 - Simulation 3I effective viscosity contour plots in obstructed geometry; Left: 0.41 hrs; Right: 3.18 hrs	161
Figure 6.17 - Normalised exponential decay curves of butane gas.....	163
Figure 6.18 - Graph of non-dimensionalised ventilation progression simulations against exponential decay curve	164
Figure 6.19 - Vector plots of slices through 3-dimensional domain showing principle air movements; Fore-aft planes (top left); Inboard-outboard plane through the jet axis (bottom right).....	166
Figure 6.20 - Surface velocity vectors showing direction and magnitude of flows near the wall .	167
Figure 6.21 - Butane mass fraction on a vertical normal plane 0.1m above the floor; note the higher concentration in the outboard corner, top right.....	168
Figure 6.22 - Comparison of analytical model to numerical results; $\eta=1$ in all four cases	170
Figure 6.23 - Comparison of analytical to numerical simulations; $\eta = 2/3$ for simulation 3B(RSM), and 0.6 for simulation 3I.....	171

Table of Tables

Table 2.1 - Values of Constants in the K-Epsilon model (Launder & Spalding 1974).....	23
Table 2.2 - New constants in RNG Model	24
Table 2.3 - List of terms in the Reynolds Stress Model	27
Table 4.1 - List of constant boundary conditions	76
Table 4.2 - Boundary conditions used in simulations	77
Table 4.3 - Temperature gradients for mesh densities, wall conduction (no radiation) case	80
Table 4.4 - List of Richardson numbers	82
Table 5.1 - Common material properties used	103
Table 5.2 - Calculation of area-weighted mean conductivity of double hull	107
Table 5.3 - Temperature boundary conditions of different walls	109
Table 5.4 - Composition of inert gas	110
Table 5.5 - Properties of volatile hydrocarbon chains @ 1 atm	110
Table 5.6 - Composition of gas mixture inside tank, by volume	111
Table 5.7 - Comparison of relative gravities and Richardson numbers for different deck temperatures in quasi-linear zone based on $u = 5\text{m/s}$	122
Table 5.8 - List of Simulations	131
Table 5.9 - Simulated maximum penetration depths	135
Table 6.1 - List of simulations, simulated time, final time-step and number of iterations	151
Table 6.2 - Comparison of predicted and actual initial region times	162
Table 6.3 - Example calculations of gas-freeing time based on perfect, ideal mixing with no initial region	169
Table 6.4 - Gas freeing times adjusted for 2/3 efficiency	172

Table of Contents

Acknowledgements	I
List of Nomenclature	III
Acronyms	VII
Table of Figures	IX
Table of Tables	XIV
1.0 Introduction	1
1.1 Aims and Objectives	2
1.2 Research Challenges	2
1.3 Scope of work	3
2.0 Theoretical Background and Literature Review	5
2.1 Chapter Overview	7
2.2 Mathematical Background and Numerical Methods	7
2.2.1 Navier Stokes Equations	7
2.2.2 Scaling Parameters	9
2.2.3 Numerical Considerations	11
2.2.4 Meshing and Filtering	13
2.2.5 Scales of Motion	14
2.2.6 Errors.....	18
2.2.7 Turbulence Modelling.....	19
2.2.8 Radiation Modelling.....	28
2.3 General Ventilation	32
2.3.1 Natural and Displacement Ventilation	32
2.3.2 Effect of Thermal Radiation on Ventilation.....	37
2.3.3 Mixing and Mixing Ventilation	38
2.4 Jet Flows	43
2.4.1 Round and Plane Jets	44
2.5 Impinging Flows and Stratification	49
2.5.1 Impinging Flows	49
2.5.2 Effects of Stratification	51
2.5.3 Stratification Breaking	53
2.5.4 Far-Field and Obstruction Effects	55
2.6 Tanker Ventilation	57

2.6.1	Introduction.....	57
2.6.2	Tanker Geometry	57
2.6.3	Current Methods	60
2.6.4	Existing Legislation and its Implications.....	61
2.6.5	Physics of Tank Ventilation.....	62
3.0	Model Design Methodology	67
3.1	Chapter Overview	68
3.2	Discretisation Scheme	68
3.3	Numerical Models	69
3.3.1	Turbulence Modelling.....	69
3.3.2	Radiation Model.....	70
3.4	Meshing.....	71
3.5	Boundary Conditions.....	72
3.5.1	Radiative Boundary Conditions.....	72
3.6	Solution methodology and Convergence.....	73
4.0	Validation of Numerical Method with Room Ventilation Study.....	74
4.1	Introduction.....	75
4.1.1	The Chamber.....	75
4.2	Model Design and Boundary Conditions	76
4.3	Results	79
4.3.1	Mesh Sensitivity.....	79
4.3.2	Comparison of Engineering Assumptions.....	81
4.3.3	Effect of Turbulence Models	84
4.3.4	Effect of Medium Absorptivity.....	87
4.3.5	Disparity between Simulated and Experimental Results	88
4.4	Summary and Conclusions.....	89
5.0	Crude Oil Tank Ventilation.....	92
5.1	Chapter Overview	93
5.2	Introduction.....	93
5.3	Model Geometry.....	94
5.3.1	Computational Mesh - 3D Domain.....	95
5.3.2	Geometry and Computational Mesh - 2D Axisymmetric Simulation.....	100
5.4	Boundary Conditions.....	103
5.4.1	Material Properties.....	103
5.4.2	Inlet Profile	103

5.4.3	Heat Transfer.....	106
5.4.4	Calculation of Heat Transfer Coefficients	107
5.4.5	Radiated Heat Transfer	108
5.4.6	Initial Temperatures	109
5.4.7	Air Composition and VOC Concentrations	109
5.5	Results 1 - Examination of Modelling and Boundary Conditions	112
5.5.1	Mesh Sensitivity.....	112
5.5.2	Turbulence Model.....	116
5.5.3	Thermal Analysis of Double-Hulled Tankers	118
5.5.4	Inlet Conditions.....	122
5.6	Results 2 - Analysis of Gas Freeing.....	127
5.6.1	Preliminary Examination of Gas-Freeing	127
5.6.2	Examination of Modelling Assumptions	129
5.6.3	General Gas Freeing Characteristics	130
5.6.4	Removal of Stratified Layer.....	132
5.6.5	Gas Distribution During Gas Freeing	136
6.0	Discussion	144
6.1	Chapter Overview	145
6.2	Discussion on Aspects of the Numerical Models	145
6.2.1	Effect of Dissipation-Equation Buoyancy Extensions	145
6.2.2	Turbulence Modelling.....	149
6.2.3	Convergence.....	150
6.2.4	Thermal Effects.....	152
6.2.5	Impingement Zone Behaviour.....	153
6.3	Examination of Gas Freeing.....	154
6.3.1	Prediction of Gas Freeing Operations	154
6.3.2	The Initial Region	155
6.3.3	Initial Region Dynamics	157
6.3.4	Determination of Initial Region Time.....	161
6.3.5	Exponential Decay Region.....	163
6.3.6	Discussion of 3-Dimensional Effects.....	165
6.3.7	Determination of Total Gas Freeing Times.....	168
6.3.8	Applicability of Regulations	171
7.0	Conclusions.....	173
7.1	Recommendations for Further Research.....	175
	References.....	176
	Appendices	188

1.0 Introduction

Oil tankers are responsible for the vast majority of oil movement worldwide, moving crude oil from the point of extraction to the refineries. Due to the large sizes of both the ship and the tanks in which the crude oil is carried, ventilation is a difficult task. When maintenance is required, all of the oil tanks on board the ship must be ventilated, and this cleaning takes place in a number of stages. After offloading, the inert tank may undergo a crude oil wash in order to remove wax deposits on the superstructure. After this is complete, inert gas fans are restarted, and the tank atmosphere is recycled (maintaining a low oxygen content) until the volatile organic compound (VOC) concentration is below 2% in a process called *purging*. After this is complete, deck-mounted fans are used to flush out (gas-free) the remaining VOC/inert gas mixture with fresh air to remove the remaining vapours from the tank. After this is complete, a number of additional processes may be performed inside the tank such as steam cleaning or mucking out the tank, as well as other maintenance operations, such as inspection, cold or hot work.

The field of study covered here examines the gas-freeing portion of this overall cleaning process. Although the term ‘gas-freeing’ has historically taken on a number of meanings, the gas-freeing process studied here is the operation whereby deck fans are used to remove both the inert gas mixture and remaining VOC vapours by continual supply of fresh air and exhaustion of the VOC/inert gas mixture.

Although the process of gas freeing is operationally simple, there are a large number of unknown factors surrounding it, and predicting the fluid interactions can be extremely complex due to the number of VOC gas species that evaporate from crude oil. Extant legislation defines general concentration levels required for different gas-free conditions (such as in International Safety Guide for Oil Tankers and Terminals (ISGOTT, 1996)) but does not define an air change requirement, even though air change requirements exist for the ventilation of many other parts of the ship. Therefore, the question of “how long must gas-freeing be performed?” remains open.

1.1 Aims and Objectives

The fundamental aims of the work carried out in this thesis are to expand the knowledge surrounding the gas freeing process, and more generally, the ventilation of very large enclosed spaces containing heavy vapours, by using validated numerical simulation to examine the evolution of such flow-fields during the process.

The aims and objectives of this work are as follows:

- To increase the understanding of the fluid flow and heavy gas interaction involved in gas-freeing operations;
- To study conjugate heat transfer inside a crude oil tank on a structurally modern oil tanker with a view to determining the strength of thermal effects;
- To examine the flow-field when gas-freeing in a series of ‘worst-case’ scenarios whereby all of the contents of the heavy VOC vapours are stratified at the base of the tank at the beginning of the gas-freeing operation;
- To gain a greater understanding of the evolution of the gas concentrations during the gas freeing process by running the aforementioned models to simulate several hours of time of the gas freeing process, i.e. from start to end;
- To use the above information to derive analytical correlations which can be used to predict the approximate gas freeing time given certain initial conditions.

1.2 Research Challenges

To study ventilation in such large scales coupled with multiple physical effects such as conjugate heat transfer and multiple gas species is not a straightforward problem, and there are a number of difficulties that arise as a result.

The most important difficulty is that of the method of analysis – in an ideal situation, a full scale experimental configuration would be adopted on a modern vessel using representative tracer gases coupled with multiple monitoring systems to both determine concentration in time and allow visualisation of the flow field, such as particle image velocimetry methods. However, this is extremely cost prohibitive due to not only the cost of charter, but also the cost of procurement and

configuration of the instrumentation. Safety is also a factor due to the sheer size and possibility of gas evolution from tank.

Smaller scale experimental methods are possible, but preclude an in-depth thermal analysis due to the difficulties in simulating radiative heat transfer. Additionally, in modelling the problem as a whole, reconciling all pertinent scaling parameters becomes incredibly difficult to the point where such experiments can only model isolated phenomena in a piece-wise fashion, instead of in unison.

As such, the use of numerical methods provides an alternative route to obtaining the required results.

The use of numerical methods brings its own unique challenges. A generic geometric model must be derived in order to determine the geometric and scale of the problem. In order to make the problem well-posed, initial conditions both inside and at the boundaries of the tank must be defined. The physical models being solved must be able to predict the fluid flow and energy transfer with an acceptable degree of accuracy, yet at the same time this required accuracy must be balanced against available computational resources. Underpinning both of these issues, in addition to the overall numerical methodology is that of validation – whilst numerical methods can be powerful tools, the results must be comparable to valid experimental results, both in order to determine accuracy, and to confirm the ability of the numerical model to properly predict the required physical mechanisms.

This validation requirement is a particular challenge as marine gas-freeing is a very rarely-studied topic, making direct validation of results virtually impossible. Thus, in order to demonstrate the validity of the results, a number of ‘partial’ comparisons have been made to demonstrate the ability to predict conjugate heat transfer (important in the analysis of the effects of heat transfer in gas freeing), convective jet flows (important in the creation and distribution of momentum and turbulence into the flow field) and impingement upon stratified interfaces (important in the prediction of such behaviour). By performing validation by parts, the numerical model can be fractionally validated in order to demonstrate the fidelity of the model as a whole, and also this method increases the available “pool” of experimental data against which comparisons can be made.

1.3 Scope of work

The earlier sections of the introduction highlight the field of study, aims and objectives, as well as providing a general overview of the challenges involved in this body of work.

Chapter 2 is comprised of the literature review. This begins by providing detail into the numerical and analytical models which form the basis of the numerical methodology used. This is followed by an examination of previous and related literature:

- General ventilation research and methods of ventilation; high momentum jet flows and analytical jet models;
- Impinging and stratified flows, including a general outline of both and correlations of stratification breaking;
- Tanker ventilation, which describes previous research into this specific application of ventilation, relevant physical mechanisms, as well as surrounding regulatory framework.

Chapter 3 describes the general rationale for the numerical approach used in the following chapters. Chapter 4 reports on a small-scale room ventilation case study which serves to validate the general numerical method and the accuracy of the heat transfer models, as well as commenting on the effects of different heat transfer modes and comparisons with experimental results.

Chapter 5 forms the beginning of the main study of marine gas-freeing. Firstly, the numerical methodologies and boundary conditions are described, and then the results of the three-dimensional, steady-state analysis are presented. This is followed by the presentation of the transient, 2-dimensional simulations. Jet dynamics and stratified layer behaviour are validated in this chapter.

Chapter 6 presents a discussion of the results, beginning with numerical aspects of the simulations, and then a critical examination of the gas freeing procedure and the derivation of an analytical model to predict gas-freeing times. Finally, Chapter 7 presents the conclusions of this study and proposes possible directions for further work.

2.0 Theoretical Background and Literature Review

2.1	Chapter Overview	7
2.2	Mathematical Background and Numerical Methods.....	7
2.2.1	Navier Stokes Equations	7
	Conservation of Mass	7
	Conservation of Momentum.....	7
	Conservation of Energy	8
2.2.2	Scaling Parameters	9
2.2.3	Numerical Considerations	11
	Differencing schemes	11
	Pressure Coupling and Cell Arrangements.....	12
	Unsteady Flows	13
2.2.4	Meshing and Filtering	13
	Temporal Discretisation	14
2.2.5	Scales of Motion	14
2.2.6	Errors.....	18
2.2.7	Turbulence Modelling.....	19
	Direct Numerical Simulation.....	20
	Large Eddy Simulation.....	20
	LES SGS Modelling.....	21
	K-Epsilon Models.....	22
	Buoyancy Effects in the Dissipation Equation	26
	Wall Functions.....	26
	Reynolds Stress Models.....	27
2.2.8	Radiation Modelling.....	28
	Radiative Transfer Equation.....	29
	Participating Media	30
	Solution Methods.....	31
2.3	General Ventilation.....	32
2.3.1	Natural and Displacement Ventilation	32
	The Neutral Layer.....	32
2.3.2	Effect of Thermal Radiation on Ventilation.....	37
2.3.3	Mixing and Mixing Ventilation	38
	Mixing Ventilation	40
	Jet Mixing.....	42
2.4	Jet Flows.....	43
2.4.1	Round and Plane Jets	44
	Self Similarity.....	45
	Numerical Studies	48
2.5	Impinging Flows and Stratification	49
2.5.1	Impinging Flows	49
2.5.2	Effects of Stratification	51
	Interfacial Layer	51
	Turbulence Decay.....	53

2.5.3	Stratification Breaking	53
2.5.4	Far-Field and Obstruction Effects	55
2.6	Tanker Ventilation	57
2.6.1	Introduction	57
2.6.2	Tanker Geometry	57
2.6.3	Current Methods	60
2.6.4	Existing Legislation and its Implications	61
2.6.5	Physics of Tank Ventilation	62
	Ventilating a Single Fluid	62
	Ventilation Involving Multiple Fluids	63

2.1 Chapter Overview

This chapter contains the literature review, and is divided into several subsections. Firstly, the physical mechanics that govern fluid flow, as well as the mathematical basis for simulation are introduced, in addition to ancillary numerical models involved in such simulations. Aspects of ventilation are examined; different types of ventilation and the design methodologies surrounding them; the effect of temperature variation and radiation in buoyancy-driven ventilation, and an examination of mixing parameters determined by jet mixing studies.

The next two sections examine simple classes of flows in order to define the pertinent physical mechanisms involved, and then describe correlations and mathematical models which can be used to describe them for the purposes of validation.

Finally, an introduction and review of existing work and legislation is present in the context of gas freeing.

2.2 Mathematical Background and Numerical Methods

2.2.1 Navier Stokes Equations

The dynamics of fluid flow were established independently by Claude-Louis Navier and George Stokes in the 19th century, establishing a relation between the actions of convective terms against viscous and pressure forces in a fluid. These principles are encapsulated within three governing equations which describe the conservation of mass, momentum and energy.

Conservation of Mass

$$\frac{\partial \rho}{\partial t} + \frac{\partial(\rho u_i)}{\partial x_i} = 0 \quad (2.1)$$

The conservation of mass ensures that given a closed volume, mass is constant regardless of the processes acting within, i.e. mass is neither created nor destroyed, only transferred, and is conserved.

Conservation of Momentum

$$\frac{\partial \rho u_i}{\partial t} + u_j \frac{\partial(\rho u_i)}{\partial x_j} = -\frac{\partial p}{\partial x_i} + \frac{\partial}{\partial x_j} \left(\nu \left(\frac{\partial u_i}{\partial x_j} + \frac{\partial u_j}{\partial x_i} \right) \right) + \rho g + F \quad (2.2)$$

The conservation of momentum in the Navier-Stokes equations account for the behaviour of a Newtonian fluid. Here, temporal and second-order convective terms are balanced by changes in local pressure and viscous effects. Other formulations of the momentum equation include

surface forces, i.e. pressure and viscous terms only. Here, body forces due to buoyancy ρg are included, and additional body forces (e.g. Coriolis effects, electromagnetic fields) would affect momentum conservation through source term F .

The buoyancy term can be approximated by the Boussinesq approximation, removing the need for the solution of density in the buoyancy term by treating density as a function of temperature:

$$g(\rho - \rho_0) = -\rho_0 g \beta (T - T_\infty) \quad (2.3)$$

The Boussinesq model works best in natural convection, where the density differences are small. The model is invalid when density differences are large and of the order of the fluid density:

$$\beta(T - T_\infty) \ll 1 \quad (2.4)$$

Conservation of Energy

$$\frac{\partial(\rho e_i)}{\partial t} + \frac{\partial(\rho u_j e_i)}{\partial x_j} = \frac{\partial}{\partial x_j} \left(k \frac{\partial T}{\partial x_j} \right) \quad (2.5)$$

The conservation of energy encapsulates the principles of the first law of thermodynamics applied to a control volume. Any temporal change in energy and work done is reflected by heat flux through the volume boundaries, represented by Fourier's law of conduction.

In the numerical solver used (Fluent Inc. 2005), the integral form of the conservation equations are solved, ensuring that mass is conserved. The equations can be solved in two different ways – explicit ('segregated') or implicit ('coupled'). The explicit segregated solver first solves the velocity field, which then uses a pressure coupling method to deduce the pressure field from the velocity field; pressure and velocity data are co-located at cell centres.

The implicit ('coupled') formulation solves the conservation equations simultaneously in a matrix. This has some speed benefits, but is numerically stiffer for low Mach or incompressible flows, and has a higher demand for volatile memory storage. Numerical stiffness is reduced by pre-conditioning (Weiss & Smith 1995) which scales the acoustic wave speed to the same order as the local velocity. As the implicit formulation is discretised in time, it mimics the time-marching methodology to solve steady state problems; by increasing the Courant number, it is possible to further accelerate the convergence of the simulation as long as the Courant number is within stable bounds. Excessive Courant numbers can cause the propagation of errors through the flow-field, resulting in divergence.

Analytical solutions of the fundamental equations can be used to derive scaling parameters to characterise similar flows.

2.2.2 Scaling Parameters

Scaling parameters can be used to characterise the flow in order for an experimental model to be used, or as a metric with which to gauge the dynamics of the flow.

One of the most important of these parameters is the Reynolds number:

$$Re = \frac{\rho ul}{\mu} \quad (2.6)$$

The Reynolds number is a ratio of inertial to viscous forces; as a secondary metric, it can also be used to determine how turbulent a flow may be expected to be. At low Reynolds numbers <10,000, the flow is likely to be laminar (in the case of pipe flow, $Re < 2000$) whereby the flow is regular and displays low diffusivities. Above this limit, the fluid transitions to turbulent flow, whereby its movement is pseudo-random and has diffusivities several orders of magnitude higher than laminar flows.

The Froude number is a ratio of inertial to gravitational (buoyant) forces:

$$Fr = \frac{u^2}{gl} \quad (2.7)$$

Most ventilative effects happen at low Froude numbers, as high inertial forces tend to turbulence, usually to the detriment of the stratified layer which is essential in some ventilative methods.

Using the Boussinesq approximation, a densimetric, or modified Froude number can be found, whereby:

$$Fr = \frac{u}{\sqrt{g'l}} \quad (2.8)$$

And:

$$g' = \frac{g(T_2 - T_1)}{T_\infty} \quad (2.9)$$

In essence, this is the inverse of the Richardson number.

The Richardson number is a measure of potential to kinetic energy, or the ratio of buoyant to inertial forces (i.e. the inverse of the modified Froude number). There are a number of different forms that the Richardson number can take, one of the more common ones being:

$$Ri = \frac{g'h}{u^2} \quad (2.10)$$

The Richardson number is commonly used as a measure of the stability of stratified fluids in many fields, from meteorological analysis through to ventilation. Stratified layers with Richardson numbers as low as $\frac{1}{4}$ have been shown to be stable under certain circumstances (Miles 1961). Another form of the Richardson number is evaluated based on local gradients:

$$Ri_g = \frac{-g \frac{\delta\rho}{\delta h}}{\rho \left(\frac{\delta u}{\delta h} \right)^2} \quad (2.11)$$

Here, unstable stratifications (e.g. top-heavy) flows are characterised by negative Ri_g values, and $Ri_g = 0$ represents a neutral state of buoyancy. This is sometimes rearranged in the following form:

$$Ri_g = \frac{N^2}{\left(\frac{\delta u}{\delta z} \right)^2} \quad (2.12)$$

Where N is the *Brunt-Väisälä* frequency, which represents the buoyancy frequency of a fluid parcel which has been displaced from a position of neutral-buoyancy, oscillating above and below this layer due to its initial displacement:

$$N = \sqrt{\frac{g}{\rho} \cdot \frac{d\rho}{dh}} \quad (2.13)$$

Using the Boussinesq approximation, the Richardson number can also be expressed in terms of temperature for thermally-driven flows:

$$Ri_g = \frac{-g\beta \frac{\delta T}{\delta h}}{\rho \left(\frac{\delta u}{\delta h} \right)^2} \quad (2.14)$$

Where β is the coefficient of volumetric thermal expansion.

The Planck number is a ratio of heat transfer from conduction as compared to that from radiation:

$$Pl = \frac{k}{4T^3 \varepsilon \sigma} \quad (2.15)$$

Here, k is the thermal conductivity through air, ε is the emissivity of the radiating wall surface and σ is the Stefan-Boltzmann constant, $5.67 \times 10^{-8} \text{ W.m}^2.\text{K}^{-4}$. For conditions when $Pl < 1$, the effect of radiation is increasingly dominant; when $Pl \ll 1$, then the contribution of conductive heat transfer is negligible compared to the contribution from radiation.

On the topic of diffusion, the Schmidt number is a ratio of momentum and mass diffusivities, similar to the Prandtl number in heat transfer:

$$Sc = \mu / \rho D \quad (2.16)$$

Schmidt numbers of gases are generally in the order of unity, but in turbulent flows, turbulent Schmidt numbers (where $\mu_{eff} = \mu + \mu_t$) can become very large.

2.2.3 Numerical Considerations

Computational Fluid Dynamics (CFD) is the primary numerical method used to solve the governing equations. In order to solve the continuous partial differential equations, the solution domain is typically discretised into a number of discrete volumes, and the governing equations expressed as a series of linear equations, depending on what differencing scheme is used to propagate the solution through the domain.

A number of different approaches for the solution of partial differential equations exist – finite difference, finite volume and finite element.

Traditionally, finite volume and finite difference methods are used in CFD. Previously, finite differences were used due to their ease of programming and relative simplicity. As more computational power was afforded, finite volume methods were used as this method allowed the solution of arbitrary meshes, whereas finite differences were restricted to structured grids. Finite element methods exist, but are less common as they require a different formulation for each application - a general arrangement is not possible for all cases. The solution method of finite volumes is far more flexible in terms of application, the main disadvantage being a reduction in accuracy for a given amount of computational power due to the interpolations used in the method.

The majority of numerical solvers use a combination of weighted residuals (MWR) allied to a multi-grid method (AEA Technology 2000) which accelerates convergence on larger grids. In summary, the method of weighted residuals iteratively solves by applying a correction based on the previous iteration:

$$\phi_{i+1} = \phi_i + A(\phi_c) \quad (2.17)$$

Where A is an under-relaxation factor - a factor of 1 means that the full correction is added to the existing value; if the corrections are large with respect to the existing value, applying under-relaxation factors <1 can help to reduce oscillatory behaviour, stabilising a divergent solution. By using a multi-grid method, which creates additional coarser meshes from the baseline mesh, errors of different wavelengths (which would normally be of too-long a wavelength to be easily reduced by applying the MWR alone) can be reduced, increasing convergence rates and convergence behaviour.

Differencing schemes

In the finite volume method, the simulated domain is discretised into a number of finite volumes, inside which the fluid properties are calculated at the cell centres. In order to propagate the boundary conditions through the flow field, differencing schemes are used which convey the

fluid properties in a physically correct manner across the cell faces. A large number of differencing schemes exist, varying from the simple upwinding schemes through to second order Monotonically Upstream-centred Scheme for Conservation Laws, (MUSCL) (van Leer, 1978), and flux-splitting, total variation diminishing (TVD) schemes.

Upwinding is the simplest and most inexpensive method, as it simply infers the properties of the upwind cell upon the downwind cell. Upwinding is diffusive when the flow orientation isn't along one of the local axes of the mesh, leading to *smearing* of results due to the averaging of adjacent cells only (see Section 2.2.6). A side effect of this numerical diffusion is *increased* numerical stability through the reduction of gradients. Second-order upwinding reduces the diffusion at the expense of a more complicated scheme.

The central difference scheme (CDS) is essentially a weighted average of the values at the cell centres, and at first appearance should yield higher accuracy than the simple upwinding model. Unfortunately, CDS does not differentiate between diffusion-dominated and convection-dominated effects, which can be represented by the Peclet number:

$$Pe = \rho u L / \Gamma, \quad \text{where } \Gamma \text{ is the coefficient of diffusion;} \quad (2.18)$$

At higher Peclet numbers, CDS schemes fail to function, leading to “wiggles” in the flow and divergence. Because LES and DNS simulations require far finer grids, the effective Peclet number is much lower, allowing the use of central difference-type schemes; however, for RANS simulations, which use coarser grids, CDS are not recommended.

The QUICK scheme of Leonard (1978) uses a quadratic interpolation so that sharper gradients are maintained, based on a weighted average of second order interpolations across adjacent cells and cell faces.

Pressure Coupling and Cell Arrangements

Calculation of pressure was historically a point of contention in CFD with incompressible flows, whilst pressure gradients have an effect on the momentum equations, there is no independent equation for the calculation of pressure. Calculating the pressure gradient directly from the same mesh used to calculate the velocity led to ‘chequer-boarding’ of the pressure field, encouraging the use of staggered grid arrangements as a solution. More modern use of non-orthogonal geometries and filtering techniques has brought co-located grids back to common use.

The main pressure coupling method is the Semi-Implicit Method of Pressure-Linked Equations, or SIMPLE (Patankar, 1980), which starts with an assumed pressure field and updates this field based on pressure corrections calculated from the momentum equations. A number of modifications of the original SIMPLE algorithm exist (e.g. SIMPLER, SIMPLEC, SIMPLEST, PISO) (Patankar, 1980; Fluent Inc., 2005; Vandoormaal, 1984), which modify the way that pressure or velocity corrections are treated in the algorithm.

Unsteady Flows

By expressing the equations as functions of time, they can be integrated over a finite time step in order to calculate transient effects on the flow field. Unsteady flows have an additional constraint whereby the time-step size Δt should be defined by a Courant number C of 1:

$$C = u \cdot \Delta t / \Delta x \quad (2.19)$$

Explicit solvers have strict stability requirements with regards to the Courant number, whereas implicit methods are much more tolerant to large time steps, as fluxes and sources are solved simultaneously from the unknown variables, rather than being calculated stepwise from known values (Anderson, 1995). This allows time-marching techniques with implicit solvers to be more expedient by using a larger Δt , so long as storage overheads can be realised. With more intensive methods like LES, the possibility of using large time-steps is negated because of the need to capture high wave-number flow features.

2.2.4 Meshing and Filtering

As the mesh controls the numerical solution of the equations, the actual distribution of the mesh can be extremely important, affecting the run-time behaviour and final outcome of the simulation, so demonstration of mesh insensitivity is important. However, there is no de-facto regimen that defines exactly what this distribution must be for every application. A number of criteria do exist, depending on the methodology - for example, LES must have a dense enough mesh such that the y^+ values at the walls is of the order of unity, defined by:

$$y^+ = u_\tau y / \nu \quad (2.20)$$

Which is defined by viscous scales at the wall, where:

$$u_\tau \equiv \sqrt{\frac{\tau_w}{\rho}} \quad \text{and} \quad \delta_\nu = \nu \sqrt{\frac{\rho}{\tau_w}} = \frac{\nu}{u_\tau} \quad (2.21)$$

Because the viscous boundary layer at the wall comprises of several layers, very different fluid behaviour occurs and the flow is highly anisotropic. This results in regions of high and low velocities. In Large Eddy Simulations (LES), these “streaks” must be resolved for the flow to be correctly predicted in the near field. The prescription of filter length scale in this situation is awkward, and typically $\sqrt[3]{\Delta x \cdot \Delta y \cdot \Delta z}$ is used. However, when using a block structured grid, this imposes an unacceptably fine mesh on the remaining flow-field (Piomelli, 1999). Unstructured and tetrahedral meshes can alleviate the problem, but may also introduce others.

For Reynolds Averaged Navier-Stokes (RANS) methods, a separate wall law (See Section 2.2.7) is employed to resolve the effects of the flow in the near-wall region. Because of this, the mesh need only resolve around $y^+ = 30-300$, at which point the wall-law equations take over in the calculation of flow. In terms of meshing elsewhere in the flow field, there are no strict resolution

requirements, other than maintaining mesh volumes with low skew and aspect ratio; many studies over the past decades have used varying degrees of mesh density, from fairly coarse meshes to quite dense ones, with fair to good accuracy, with the turbulence model showing a high degree of adaptability to varying meshes (Lauder, 1972). Conversely, DNS methods must resolve the mesh down to the Kolmogorov scale (Kolmogorov, 1941) in order to capture the smallest scales upon which the upper scales and the energy cascade depend upon. Additional chemical reactions can also impose other length scales which require resolution.

Temporal Discretisation

LES and DNS also have the added dimension of time which must be solved for. DNS, as well as being spatially discretised to account for the Kolmogorov scale, must also be solved in time steps small enough to resolve the Kolmogorov time scale:

$$\tau \equiv \left(\frac{\nu}{\varepsilon} \right)^{1/2} \quad (2.22)$$

As LES has a much coarser mesh with respect to DNS simulations, a time-step resulting from a Courant number of unity is not as small. Therefore, while the criteria is similar, the resulting time-scales that need to be simulated are orders of magnitude higher. It is possible to use a larger time-step than that defined by the CFL criterion, but then the possibility exists that certain temporal fluid motions are not being accounted for, as well as the potential for instability.

Stability is the only major criterion for RANS simulations, as their averaged nature reduces the strict coupling between solution time-step size and a particular eddy time scale. Therefore, it is common to expedite RANS simulations by using a larger time-step, though this is dependent on the solver type. Linear stability theory determined that explicit solvers are conditionally stable, dependant on the CFL criterion (Anderson 1995). The implicit solver used is unconditionally stable (Fluent Inc 2005), and therefore it is possible to use Courant numbers of tens to hundreds in extreme cases to accelerate the convergence of a simulation, though this must be tempered against the non-linear behaviour of the fundamental equations in conjunction with numerical effects, which usually limit the Courant number <50.

If chemical reactions are involved, additional time and length scales may need to be defined based on the reaction times and scales of the chemistry which affect the flow (Dimotakis 2005). It is also possible that these chemical reactions can lead to extremely high gradients, for example in temperature; this must also be compensated for by the mesh, time step and discretisation scheme.

2.2.5 Scales of Motion

Turbulent fluid flow is characterised by pseudo-random movements at many different length and time scales. The largest, or integral scales, are influenced by the largest geometric

factors, such as the physical bounds of the domain, whilst the very small, or Kolmogorov scales are defined by the diffusive action of molecular viscosity.

Since the Kolmogorov scales are directly related to the (viscous) properties of the fluid medium, they can be defined based on two variables; ε , the rate of dissipation and ν , the fluid viscosity:

$$\eta \equiv (\nu^3 / \varepsilon)^{1/4} \quad (2.23)$$

$$\tau \equiv (\nu / \varepsilon)^{1/2} \quad (2.24)$$

$$\nu \equiv (\nu \varepsilon)^{1/4} \quad (2.25)$$

The dimensions of the Kolmogorov scale are such that a Kolmogorov-derived Reynolds number is equal to unity:

$$\frac{\eta \nu}{\nu} = 1 \quad (2.26)$$

On the opposite side of the turbulence spectrum is the integral scale; as already noted, the integral scale is defined by domain-sized effects, such as geometry. Statistically, the integral scale can be determined by integrating the lateral correlation coefficients of turbulent velocity components.

At low Reynolds numbers, the difference between the integral and Kolmogorov scales is relatively small, but still a few orders of magnitude. As the Reynolds number increases, the difference between the scales grows. Relations between the scales can be derived from them to show their dependence on the Reynolds number:

$$\eta / \ell \sim (\nu \ell / \nu)^{-3/4} = \text{Re}^{-3/4} \quad (2.27)$$

$$\tau \nu / \ell = (\nu \ell / \nu)^{-1/2} = \text{Re}^{-1/2} \quad (2.28)$$

$$\nu / \nu \sim (\nu \ell / \nu)^{-1/4} = \text{Re}^{-1/4} \quad (2.29)$$

Given these scale relations, it can be expected that statistical independence and local isotropy will be more pronounced at higher Reynolds numbers. Indeed, if analysed from a spectral point of view, the disparity between the integral and Kolmogorov scales can be clearly seen:

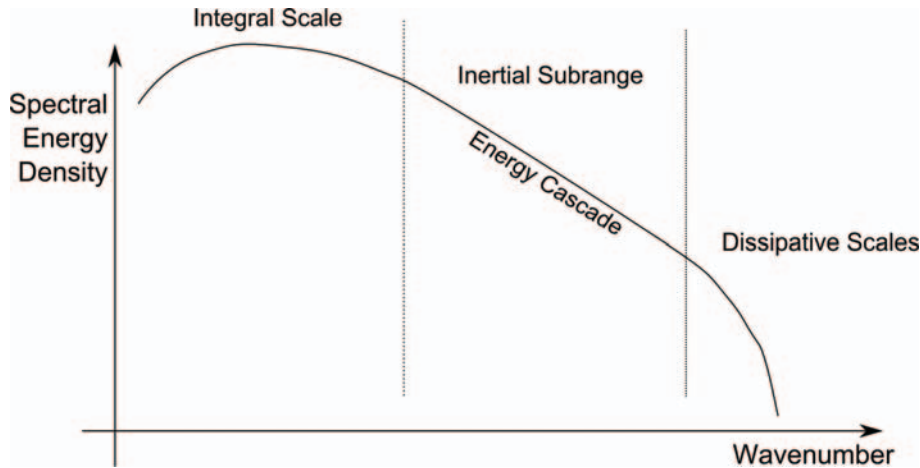


Figure 2.1- Plot of eddy wavenumber against spectral energy density based on the Kolmogorov energy spectrum

Figure 2.1 shows the distribution of turbulent energy at a high Reynolds number with respect to the frequency of motion in which the energy resides. The large integral scales represent turbulent scales associated with the production of turbulence, which are then taken out of the system in the dissipative scales by viscous action.

At high Reynolds numbers, a scale exists between the integral and the Kolmogorov scales known as the *inertial sub-range*. In the inertial-sub-range, turbulent energy is neither created nor destroyed, instead being *transferred* from larger scales to smaller ones by vortex stretching (Tennekes 1974); this process is referred to as the *energy cascade*.

Whereas flow at integral scales exhibits a high degree of anisotropy (i.e. the inequality of turbulent stresses), flow at smaller scales can exhibit “local isotropy”, where local refers to the small scales of the flow. Due to the short timescales at these wavenumbers, the small eddies respond very quickly to changes in the mean flow, leading them to be in approximate equilibrium with the local conditions of the mean flow. This gives rise to these small scales being called the *equilibrium range*. This isotropic behaviour in the small scales is the reasoning behind a number of turbulence models, for example subgrid-scale modelling in LES.

In steady homogenous shear flow where all averaged quantities are constant and the strain rate tensor is also constant, the production of turbulent kinetic energy through Reynolds stresses is equal to the rate of dissipation through viscous action; employing scale relations, the turbulent energy budget equation reduces to:

$$-\overline{u'_i u'_j} S_{ij} = 2\nu \overline{s_{ij} s_{ij}} \quad (2.30)$$

Where $\overline{u'_i u'_j}$ is the mean turbulence kinetic energy (TKE), and $\overline{s_{ij} s_{ij}}$ is the fluctuating strain rate. It has been shown (Tennekes 1974) that since the (integral) Reynolds number is large, the mean rate of strain S_{ij} is very large in comparison with the fluctuating strain rate:

$$\overline{s_{ij}s_{ij}} \gg S_{ij}S_{ij} \quad (2.31)$$

Therefore, any length scales involved with the fluctuating strain rate s_{ij} must be much smaller than the integral length scale if production and dissipation of turbulence energy is to be maintained. As small scales tend to be isotropic, this allows the derivation of another length scale:

$$\varepsilon = 2\nu\overline{s_{ij}s_{ij}} = 15\nu\overline{(\partial u_1 / \partial x_1)^2} = 15\nu u^2 / \lambda \quad (2.32)$$

The new length scale, λ , is the *Taylor microscale*, which can be experimentally measured due to its association with the curvature of spatial velocity autocorrelations, $\overline{(\partial u_1 / \partial x_1)^2}$. Using the simplified turbulent energy budget given above in Equation (2.30), the relation of λ to l can be given as follows:

$$\frac{\lambda}{l} = \left(\frac{15}{A}\right)^{1/2} \text{Re}_l^{-1/2} \quad (2.33)$$

Although the Taylor microscale is always much smaller than the integral scale, it does not represent dissipative scales as its derivation includes a velocity scale unassociated with dissipative eddies. However, as it is fairly easy to measure it experimentally, it is often referred to as the Reynolds number of turbulence, Re_λ :

$$\text{Re}_\lambda = \frac{u'\lambda}{\nu} = \left(\frac{20}{3}\text{Re}_l\right)^{1/2} \quad (2.34)$$

Although its definition makes it somewhat unclear as to which physical eddy sizes it relates to, Corrsin (1959) interpreted it as a ratio of the large eddy time scale ℓ/u to the time scales of strain rate fluctuations, λ/u .

Other important scales even smaller than the Kolmogorov scale exist. A smaller dissipative scale known as the Batchelor scale represents a scale where concentration gradients are smeared by molecular diffusion:

$$\lambda_B = \eta \cdot \text{Sc}^{-1/2} \quad (2.35)$$

In gas mixing, diffusive and viscous scales are similar as their Schmidt numbers are of the order of unity. In liquids and particulate clouds however, Schmidt numbers are several orders of magnitude higher, leading to much smaller Batchelor scales than even the Kolmogorov scale (Dimotakis 2005). As diffusive mixing is important in some flows such as the prediction of particulate-laden clouds, the Batchelor scale must also be considered, presenting an additional burden for DNS simulations.

2.2.6 Errors

Errors in simulations generally take place in three main forms:

- Geometry and boundary conditions, modelling
- Truncation/discretisation, numerical dissipation, “iteration” errors
- Errors in the software

The first group comprises of errors due to the inaccuracy of the models themselves, which can also include assumptions of neglectability of certain physical phenomena, such as adiabacity, or the use of the Boussinesq approximation to model buoyancy. Accuracy of the physical model is also a factor; for example, using a regular cuboid shape to model a room which has rounded corners and edges can have an effect on the results, for example with separation regions at the corners; prescribing a momentum inlet as a constant velocity source with uniform turbulence length scale and intensity will also introduce an error, as will the use of the K-Epsilon model itself, as fluid flow in reality is not steady state, nor uniform, and turbulence is not isotropic as the K-Epsilon model assumes. A DNS simulation of simple fluid flow is in theory the most accurate simulation, but then problems arise with boundary conditions and numerical issues – DNS requires much more information at boundary conditions to justify using such a detailed method both in space and time.

Truncation or discretisation errors are part of a numerical error that is a result of not using the full expansion of an infinite series, and best explained by examining a Taylor series of a simple forward differencing equation:

$$\phi_{i+1} = \phi_i + \left(\frac{\partial \phi}{\partial x}\right)_i \Delta x + \left(\frac{\partial^2 \phi}{\partial \phi^2}\right)_i \frac{\Delta x^2}{2} + \left(\frac{\partial^3 \phi}{\partial \phi^3}\right)_i \frac{\Delta x^3}{6} + \left(\frac{\partial^4 \phi}{\partial \phi^4}\right)_i \frac{\Delta x^4}{10} + etc \quad (2.36)$$

An exact calculation of ϕ will be found if a) the Taylor series is extended infinitely, or b) $\Delta x \rightarrow 0$. However, both of these criteria are impossible to achieve due to computational and spatial discretisation limitations. Therefore, depending on the order of a system, certain parts will be truncated. For example, in a second order system, the following is true:

$$\phi_{i+1} = \phi_i + \left(\frac{\partial \phi}{\partial x}\right)_i \Delta x + \left(\frac{\partial^2 \phi}{\partial \phi^2}\right)_i \frac{\Delta x^2}{2} \quad (2.37)$$

The higher order terms are ignored for expediency.

Essentially, the discretisation equation is only an *approximation* of the exact result. Including higher order terms can increase the accuracy, but this then has repercussions in terms of computing time and storage overheads.

Artificial (numerical) diffusion is also a process that can heavily influence results in simulations. Patankar (1980) showed that on a hexahedral mesh that uses upwinding schemes for

flow advection, fluid that moves across the grid 45 degrees to their principle axes will encounter a “smearing” effect due to the orthogonality of the upwinding scheme, leading to inaccurate results. Although in some instances of numerical simulation, this numerical smearing can increase the stability by reducing large gradients, it is generally an undesired side-effect of using a low order scheme. Modern high-resolution schemes are far more adept at reducing numerical diffusion; in fact, the use of particular flux limiters such as the “Superbee” (Roe 1986) can be overly “compressive”, in that they actually *reduce* the natural diffusion of the flow.

Iteration errors stem from the iterative nature of the solution of the Navier Stokes equations, as opposed to direct solution methods. Iterative processes are usually convergent on a set criterion, at which point the simulation is assumed to be complete. The difficulty here is twofold -

- the use of appropriate convergence criterion is important in order to determine the correct time in which a simulation is complete;
- that the iterative method still only represents an approximated prediction, and that an error will exist between the exact and the iterative solution;
- iterative errors increase with the number of cells (Ferziger & Peric, 2002).

The most common method of determining iteration error is through the sum of residuals, which are typically resolved to 1×10^{-3} . However, if steady state solutions are attempted, especially for strongly unsteady or periodic flows, convergence may not occur.

The final category of error involves errors with the solver itself, for example coding errors that are unresolved, or unusual solver behaviour that does not become noticeable straight away. This category is far more applicable to academic solvers, or solvers that are not maintained with respect to QC/QA systems and are untested or un-validated. Because this level of error resides with the actual code base rather than aspects over which the user has active control (unless the solver is user-coded), it is one of the most difficult problems to solve. However, as the work covered in this thesis uses a commercial code (Fluent Inc., 2005) that has been extensively used across many engineering fields, it is expected that errors of this kind are minimised.

2.2.7 Turbulence Modelling

Turbulence modelling is an integral component in industrial simulations. When Reynolds numbers of a flow increase past a certain transitional range, for example over 10,000 for unbounded flows, the flow becomes turbulent, characterised by greatly increased mixing with differing viscous effects. A distinguishing characteristic is the existence of different fluid packets of varying scales, from small to large eddies. The solution method for turbulent flows has historically been strongly coupled to the available computational power, as well as Boussinesq’s analogy of comparing turbulent shear stress with an artificial, or turbulent viscosity (Boussinesq 1877):

$$\tau_{ij} \equiv \overline{\rho u'v'} = \mu_t \frac{\partial u}{\partial y} \quad (2.38)$$

In the early years of CFD simulation, there was only sufficient computational power for the implementation of simple models, such as Prandtl's mixing-length models:

$$\mu_t = \rho l_m^2 \left| \frac{\partial u}{\partial y} \right| \quad (2.39)$$

Early models suffered from a lack of generality; for example, l_m in the mixing-length model is a set constant, and thus changing, or multiple length scales cannot be accounted for in that model. Increases in computational power afforded more sophisticated models to be implemented which increased the range of soluble problems. Modern computing facilities are available which have sufficient power to numerically simulate particular flows without any modelling at all, but only within low Reynolds numbers, using a method called Direct Numerical Simulation.

Direct Numerical Simulation

In numerical simulations, turbulence can be numerically resolved by the Navier Stokes equations as long as the smaller dissipative eddies are correctly represented at mesh level, which must be of sufficient resolution to capture these scales, usually of the Kolmogorov scales. This method is referred to as direct numerical simulation (DNS), and represents one of the most complex and computationally restrictive simulations, but yields the most information, both in terms of visualisation and in terms of data quantity. However, the variation in size between the smaller and the larger eddies varies greatly, through many orders of magnitude depending on the Reynolds number; as seen in Equation (2.27), the relative ratio of ℓ/η changes as per $Re^{3/4}$, so for three dimensional flow, the variation increases as per $Re^{9/4}$. By observation, it can be seen that engineering flows of interest, which traditionally have Reynolds numbers of 1×10^6 and above, will require impossibly fine meshes for DNS simulation. It is more common, as well as more computationally feasible, for flows of $Re < 1000$ to be studied. Although not as useful for engineering, such flows are still academically important, as the extra information yielded by DNS simulations can be used to further the fundamental physics behind fluid flow and turbulence transition. For flow at higher Reynolds numbers, a hybrid method called Large Eddy Simulation is used.

Large Eddy Simulation

The underlying assumption of LES relies on the knowledge that the dissipative scales are more isotropic in nature, and thus can be represented by a simple turbulence model, known as a subgrid-scale (SGS) model, which originated from the work of Smagorinsky (1963). By allowing the dissipative (Kolmogorov) length scales to be resolved by a turbulence model, the required mesh

resolution relative to DNS is greatly reduced. The larger scales, which are usually highly anisotropic and very much dependent on the flow being solved, are resolved by a sufficiently fine mesh, similar to DNS (Figure 2.2).

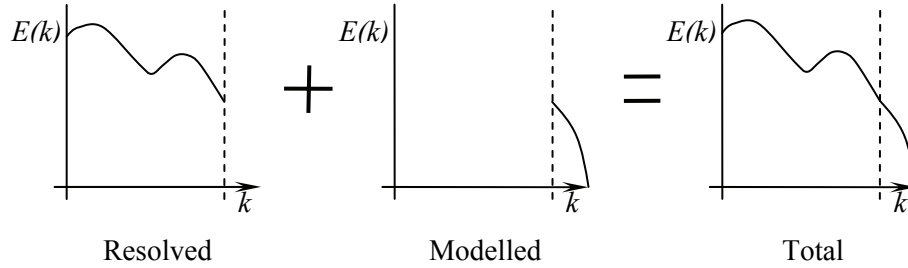


Figure 2.2 - Graphical representation of the resolved scales, modelled scales and interaction of the cutoff filter-width (dashed line)

This separation between resolved and modelled scales requires definition, and also a means to enforce this demarcation. To this end, *spatial averaging* is performed on the Navier-Stokes equations in order to pass only the small scales (high wavenumber) turbulent structures to the SGS model, similar to Reynolds decomposition:

$$\frac{\partial \langle \rho u_i \rangle}{\partial t} + \frac{\partial}{\partial t} (\langle \rho u_i u_j \rangle) = - \frac{\partial \langle p \rangle}{\partial x_i} + \frac{\partial}{\partial x_j} \left(\nu \left(\frac{\partial \langle u_i \rangle}{\partial x_j} + \frac{\partial \langle u_j \rangle}{\partial x_i} \right) \right) + \frac{\partial \tau_{ij}}{\partial x_j} \quad (2.40)$$

Spatial averaging requires the definition of a *filter*, which determines the cutoff length-scale of which eddies are resolved and which are passed on to modelled with the SGS model. The main difficulty in LES is that due to the definition of, and assumptions used in the creation of the SGS model, the cutoff length scale should be in the dissipative region. However, it is difficult to know in any great detail *a priori* what this length scale is throughout the flow-field without access to experimental or DNS results, resulting in the SGS model having to compensate for the disparity between ideal and simulated conditions.

LES SGS Modelling

The SGS model imparts effects through the Reynolds Stress tensor:

$$\tau_{ij} = \langle u_i u_j \rangle - \langle u_i \rangle \langle u_j \rangle \quad (2.41)$$

The second order term $\langle u_i u_j \rangle$ cannot be solved numerically, as it is a product of resolved and sub-grid velocities:

$$\langle u_i u_j \rangle = \langle \langle u_i \rangle \langle u_j \rangle \rangle + \langle \langle u_i \rangle u'_j \rangle + \langle u'_i \langle u_j \rangle \rangle + \langle u'_i u'_j \rangle \quad (2.42)$$

The first term on the right hand side is known as the *Leonard stress*, and comprises most of the energy transfer from large to small eddies; this term is directly solvable by the filtered

velocities. The two middle terms are known as the *cross-stresses*, and represents interactions between the resolved filtered scale eddies and the sub-grid scale eddies. This and the final term, known as the *Reynolds stress*, are known as “backscatter” terms, in that their dominant energy transfer direction is from the small to the large eddies.

A number of SGS models exist, the most common being the Smagorinsky model (Smagorinsky 1963), which is used to calculate the Reynolds stress tensor:

$$\langle u_i u_j \rangle = \rho \cdot \ell^2 \cdot \sqrt{2S_{ij}S_{ij}} \quad (2.43)$$

$$\text{Where } \ell = \min(\kappa d, C_s V^{1/3}) \quad (2.44)$$

Other models exist which improve on the physicality of the model (for instance, allowing C_s to vary so as to model backscatter) such as the models by Germano *et al.* (1991) model, and then modified by Lilly (1991), which are usually termed as “dynamic Smagorinsky” models in the literature, due to the variation of C_s . Although in theory, it is possible for C_s to become locally negative (i.e. energy moves from the small eddies to the larger eddies - backscatter), it is common to limit the minima to zero so as to prevent instability.

Not all authors use SGS models to dissipate the flow - Drikakis (2003) used a high-resolution numerical method (MILES, Sagaut (1998)) in order to control the dissipation without the use of an explicit turbulence model, on the basis that SGS actions on resolved scales are strictly dissipative. This method is also referred to as an implementation of Implicit LES (ILES, Sagaut (1998)).

K-Epsilon Models

Before the advent of powerful computers with which DNS and LES were possible, the most common turbulence model were in the class of two-equation models, in particular the K-Epsilon model of Launder and Spalding (1974). Like most algebraic models, the K-Epsilon model uses the Reynolds Averaged Navier Stokes equations:

$$\frac{\partial(\rho \bar{u}_i)}{\partial t} + \bar{u}_j \frac{\partial(\rho \bar{u}_i)}{\partial x_j} = -\frac{\partial \bar{p}}{\partial x_i} + \frac{\partial}{\partial x_j} \left(\nu \left(\frac{\partial \bar{u}_i}{\partial x_j} + \frac{\partial \bar{u}_j}{\partial x_i} \right) \right) - \frac{\partial}{\partial x_j} (\rho \overline{u'_i u'_j}) \quad (2.45)$$

In order to close the RANS formulation, in particular the Reynolds stress tensor, an appropriate formulation is required. The K-Epsilon model uses Boussinesq’s effective viscosity hypothesis (Boussinesq 1877, Launder & Spalding 1972) whereby the Reynolds stress is a product of the velocity gradient multiplied by a turbulent viscosity:

$$\tau_{ij} \equiv \overline{\rho u'_i u'_j} = \mu_t \frac{\partial u_i}{\partial x_j} \quad (2.46)$$

The turbulent viscosity is defined as such:

$$\mu_t = C_\mu \rho \cdot k^2 / \varepsilon \quad (2.47)$$

This indicates that the turbulent viscosity is a product of two variables (k , the turbulent kinetic energy, and ε , the rate of turbulence dissipation), the coefficient of turbulent viscosity, C_μ , and the local fluid density. To reduce the computational requirements, the derivation of the model assumes that the turbulent eddies are isotropic in nature, i.e. $\overline{u'} = \overline{v'} = \overline{w'}$. The transport of both turbulent kinetic energy and the dissipation allows the length scale to vary with the conditions of the flow:

$$\ell = \frac{k^{3/2}}{\varepsilon} \quad (2.48)$$

The definition of the k transport equation is based on work done by Hanjalic (1970):

$$\frac{Dk}{Dt} = \frac{1}{\rho} \frac{\partial}{\partial x_k} \left[\frac{\mu_t}{\sigma_k} \frac{\partial k}{\partial x_k} \right] + \frac{\mu_t}{\rho} \left(\frac{\partial u_i}{\partial x_k} + \frac{\partial u_j}{\partial x_i} \right) \frac{\partial u_i}{\partial x_k} - \varepsilon \quad (2.49)$$

The transport equation for ε is of a similar form, but introduces a number of constants which control the behaviour of the equation:

$$\frac{D\varepsilon}{Dt} = \frac{1}{\rho} \frac{\partial}{\partial x_k} \left[\frac{\mu_t}{\sigma_\varepsilon} \frac{\partial \varepsilon}{\partial x_k} \right] + \frac{C_1 \mu_t}{\rho k} \varepsilon \left(\frac{\partial u_i}{\partial x_k} + \frac{\partial u_j}{\partial x_i} \right) \frac{\partial u_i}{\partial x_k} - C_2 \frac{\varepsilon^2}{k} \quad (2.50)$$

Although a number of relations have also been used to define these constants, a series of values based upon the examination of free turbulence were suggested:

Table 2.1 - Values of Constants in the K-Epsilon model (Launder & Spalding 1974)

C_μ	C_1	C_2	σ_k	σ_ε
0.09	1.44	1.92	1.0	1.3

Due to the model's versatility over one-equation mixing-length models, and computational stability and expedience compared to the Reynolds Stress models (wherein six Reynolds stress equations are solved) it has seen widespread use in a wide number of flows, such as aerodynamic flows, chemical mixing, impinging and ventilative situations.

Yakhot and Orszag used renormalization group theory to re-define turbulent effects along the same lines as the K-Epsilon model (Yakhot & Orszag 1986a, Yakhot & Orszag 1986b, Lam 1992). The instantaneous Navier-Stokes equations are perturbed by a random force; this starting point allows the RNG method to proceed with the following logic: Turbulent energy is dissipated due to viscous forces at a given wavenumber and by filtering these smaller eddies out, the Navier-Stokes equations would still be approximately correct. If this filter is moved too far past the dissipation scales into the inertial subrange, the original Navier-Stokes equations cease to be correct. However, by recursively filtering the solution, the cutoff can be located to a more optimal

position whilst the effects of the energy transfer and dissipation are modelled by the μ_t equation, which is derived using an ε -expansion procedure.

This variation of the 2-equation model takes into account system rotation and high strain through changes in the dissipation equation and effective viscosity equation:

$$\frac{\partial}{\partial t}(\rho\varepsilon) + \frac{\partial}{\partial x_i}(\rho\varepsilon u_i) = \frac{\partial}{\partial x_i} \left(\alpha_\varepsilon \mu_t \frac{\partial \varepsilon}{\partial x_j} \right) + C_{1\varepsilon} \frac{\varepsilon}{k} (G_k + C_{3\varepsilon} G_b) - C_{2\varepsilon}^* \rho \frac{\varepsilon^2}{k} - R_\varepsilon \quad (2.51)$$

Where $C_{2\varepsilon}^*$ is:

$$C_{2\varepsilon}^* = C_{2\varepsilon} + \frac{C_\mu \eta^3 (1 - \eta / \eta_0)}{1 + \beta \eta^3} \text{ and } \eta = Sk / \varepsilon \quad (2.52)$$

To calculate the effective viscosity, a differential equation is derived from RNG techniques:

$$d \left(\frac{\rho^2 k}{\sqrt{\varepsilon \mu}} \right) = 1.72 \frac{\hat{\nu}}{\sqrt{(\hat{\nu}^3 - 1 + C_\nu)}} d\hat{\nu} \quad (2.53)$$

Where

$$\hat{\nu} = \mu_{eff} / \mu \text{ and } C_\nu \approx 100 \quad (2.54)$$

The RNG dissipation equation uses two new constants which are required for closure of the method. In the high Reynolds-number limit:

Table 2.2 - New constants in RNG Model

$C_{1\varepsilon}$	$C_{2\varepsilon}$	α_k	α_ε
1.42	1.68	1.393	1.393

The inverse Prandtl numbers α_k and α_ε are both 1.393 and the definition of eddy viscosity the same as in the standard K-E model in the limit of high Re, but in the low-Reynolds regime, they are derived from the following:

$$\left| \frac{\alpha - 1.3929}{\alpha_0 - 1.3929} \right|^{0.6321} \left| \frac{\alpha + 2.3929}{\alpha_0 + 2.3929} \right|^{0.3679} = \frac{\nu}{\nu_t} \quad (2.55)$$

α and α_0 are coefficients in the RNG analysis (see Yakhot & Orszag 1986b)). Finally, the last source term from Equation (2.51), R_ε , modifies the dissipation based on the *magnitude* of the strain rates, so that the model can account for rapid distortions in the flow field:

$$R_\varepsilon = \frac{\eta(1-\eta/\eta_0)}{1+\beta\eta^3} \frac{\varepsilon^2}{k} \quad \text{and} \quad \eta = Sk/\varepsilon \quad (2.56)$$

Another version of the K-Epsilon model was formulated by Shih *et al.* (1994), referred to as “Realizable” K-Epsilon. This version uses a different formulation of the dissipation equation:

$$\frac{\partial}{\partial t}(\rho\varepsilon) + \frac{\partial}{\partial x_i}(\rho\varepsilon u_i) = \frac{\partial}{\partial x_i} \left(\left[\mu + \frac{\mu_t}{\sigma_\varepsilon} \right] \frac{\partial \varepsilon}{\partial x_j} \right) + \rho C_1 S_\varepsilon - \rho C_2 \frac{\varepsilon^2}{k} \frac{1}{\sqrt{\nu\varepsilon}} + C_{1\varepsilon} \frac{\varepsilon}{k} C_{3\varepsilon} G_b \quad (2.57)$$

Compared to the standard K-Epsilon dissipation equation, the Reynolds stresses involved in turbulence production, $\overline{u'_i u'_j}$ do not appear with the C_1 term - instead, the strain rate is used in the equation for C_1 , which is no longer a constant:

$$C_1 = \max \left(0.43, \frac{\eta}{5+\eta} \right) \quad (2.58)$$

Where:

$$\eta = \frac{Sk}{\varepsilon}, \quad \text{and} \quad S = \sqrt{2S_{ij}S_{ij}} \quad (2.59)$$

As well as the modification of the “production” term in the equation, which is based on the concept of spectral energy transfer, the new model is more appropriate for the modelling of vortex stretching (Shih, *et al.* 1994). For closure, a dynamic variation of the eddy viscosity hypothesis is also used whereby C_μ is variable:

$$C_\mu = \frac{1}{A_0 + A_s U \frac{k}{\varepsilon}} \quad (2.60)$$

Where

$$U = \sqrt{S_{ij}S_{ij} + \tilde{\Omega}_{ij}\tilde{\Omega}_{ij}}; \quad \tilde{\Omega}_{ij} = \Omega_{ij} - 2\varepsilon_{ijk}\omega_k \quad \text{and} \quad \Omega_{ik} = \bar{\Omega}_{ij} - \varepsilon_{ijk}\omega_k \quad (2.61)$$

This accounts for the effect of mean rotation on turbulent stresses, which ensures the positivity of the dissipation equation without violating the Schwarz inequality in the case of large strains.

A result of this new formulation is that the ‘round jet anomaly’, whereby the spreading rates of round jets are over-predicted (but not in planar jets or wakes) that was evident in the standard and RNG models (Papageorgakis & Assanis 1994, Bardina *et al.* 1997) has been solved; other situations also see an increase in predictive accuracy over the standard model (Shih *et al.* 1994). Also, unlike the RNG model, no new model constants are required to close the solution. In terms of computational requirements, the Realizable model requires more than the standard K-Epsilon model of Launder of Spalding (1974), but is less intensive than the RNG model of Yakhot and Orszag (1986a).

Buoyancy Effects in the Dissipation Equation

Buoyancy effects are accommodated in the K-Epsilon models through a function involving the density gradient and ratio of turbulent viscosity and turbulent Prandtl number. Turbulent generation/suppression through this buoyancy source is enabled by default in the K-equation, but due to modelling uncertainties, its addition in the dissipation equation is optional. The strength of buoyant generation/suppression on the Epsilon equation can be optionally modelled through the $C_{3\varepsilon}$ parameter:

$$C_{3\varepsilon} = \tanh\left|\frac{v}{u}\right| \quad (2.62)$$

Where v and u are perpendicular components of velocity, and the u velocity is aligned with the gravity vector. Essentially, when the dominant flow vector is aligned with the gravity vector, the $C_{3\varepsilon}$ parameter is non-zero and adds the buoyancy contribution to the Epsilon equation.

Wall Functions

The presence of walls has a profound effect on the near-wall flow field, creating a great deal of shear. As the wall is approached, the local flow can be characterised by three distinct regimes - the viscous sublayer, the buffer layer, and the Log layer, shown in Figure 2.3.

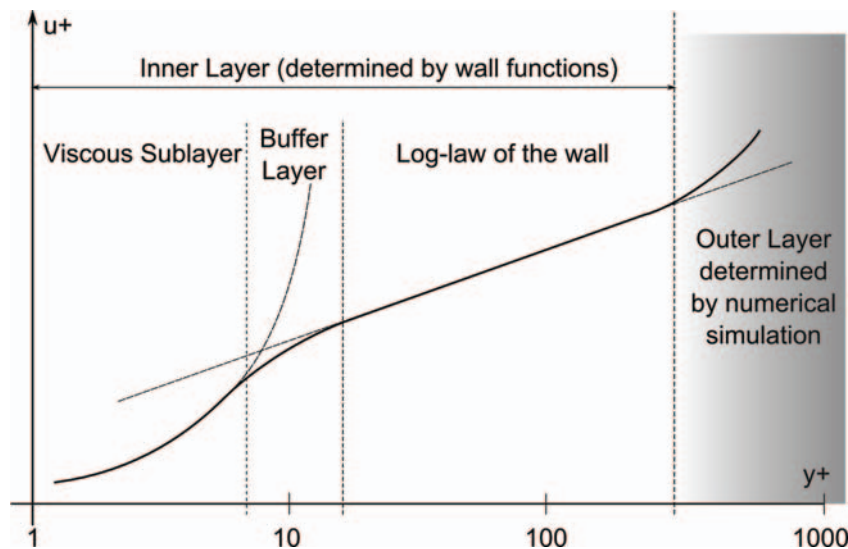


Figure 2.3 - Plot of near-wall region and correlation of commonly prescribed log-law

The viscous sublayer closest to the wall, bound by $y^+ < 5$, is where the fluid attains a semi-laminarised state, marked by slender structures referred to as “streaks” (Davidson (2004) describes these coherent structures in detail). Moving further away, the buffer layer marks a flow transition at $5 < y^+ < 40$ where the flow changes from a pseudo-laminar flow to one that behaves accordingly to

the log law. Inside the corresponding Log layer, the flow behaves according to the following logarithmic law:

$$\frac{U}{\sqrt{\tau/\rho}} = \frac{1}{\kappa} \ln \left(\frac{Ax_2(\tau/\rho)^{1/2}}{\nu} \right) \quad (2.63)$$

Or more commonly:

$$u^+ = \frac{1}{\kappa} \ln y^+ + B \quad (2.64)$$

Where B is a positive coefficient that is Reynolds-number dependent, and is around 5.2.

The behaviour of the flow is accurately described by this equation between $30 < y^+ < 300$ (See Figure 2.3), which gives rise to the meshing requirement given earlier in Section 2.2.4.

Reynolds Stress Models

The Reynolds Stress Models (RSM) are the most complex Reynolds-Averaged models of turbulence, whereby transport equations (derived from the RANS) for each of the Reynolds stresses are solved; in essence, the effective viscosity hypothesis is *not* required to convey the effects of turbulence, as the Reynolds stresses are directly calculated.

As a result of its basis, the derivation of the Reynolds transport equations brings about a number of new terms, but in general the equations are of the form:

$$\frac{\partial}{\partial t} \overline{\rho u_i u_j} = -C_{ij} - P_{ij} - G_{ij} + \phi_{ij} - TD_{ij} - PD_{ij} - VD_{ij} - \varepsilon_{ij} + S_{ij} \quad (2.65)$$

Where the individual terms are listed in Table 2.3 below:

Table 2.3 - List of terms in the Reynolds Stress Model

C_{ij}	Exact	Convective Transport
P_{ij}	Exact	Turbulent Production
G_{ij}	Modelled	Buoyant Production
ϕ_{ij}	Modelled	Pressure Strain
TD_{ij}	Modelled	Turbulent Diffusion
PD_{ij}	Neglected*	Pressure Diffusion
VD_{ij}	Exact	Viscous Diffusion
ε_{ij}	Modelled	Rate of Dissipation
S_{ij}	Modelled	Additional Source terms

* Pressure diffusion is neglected through the use of the generalised gradient diffusion hypothesis of Daly & Harlow (1970)

A consequence of the model is that not all of the new terms are fully closed, and require a degree of approximation. Of the most important of these, and with the RSM class of models in general, is the way in which ϕ_{ij} is modelled. Generally, the pressure-strain term is itself a combination of three related functions:

$$\phi_{ij} = (\phi_{ij})_i + (\phi_{ij})_r + (\phi_{ij})_w \quad (2.66)$$

The first two terms are contributions due different rates of strain; $(\phi_{ij})_i$ is the *slow rate-of-strain* mode whereby the mean velocity gradients are zero ($Sk/\varepsilon = 0$), and was proposed by Rotta (Rotta 1951, in Pope 2000) to account for a (linear) return to isotropy of turbulence when subject to low pressure strain rates. $(\phi_{ij})_r$ is the *rapid pressure strain* term proposed by Naot, Shavit & Wolfshtein (1970), determined by rapid distortion theory in the limit when mean velocity gradients are large (i.e. $Sk/\varepsilon \rightarrow \infty$) to account for the isotropisation of production. The final term, $(\phi_{ij})_w$, is termed the *wall reflection* term, and considers the blocking effect of wall on turbulence.

The combination of the first two terms forms the basis of the ‘‘LRR-IP’’ model by Launder, Reece and Rodi (1975):

$$\phi_{ij} = -C_R \frac{\varepsilon}{k} (\overline{u'_i u'_j} - \frac{3}{2} k \delta_{ij}) - C_2 [(P_{ij} + C_{ij} + G_{ij} + F_{ij}) - \frac{3}{2} \delta_{ij} \frac{1}{2} (P_{kk} + C_{kk} + G_{kk})] \quad (2.67)$$

Where the production terms are as listed in Table 2.3 above, and Rotta’s constant, C_R , and the second model constant C_2 are 1.8 and 0.6 respectively.

The wall reflection term is also subject to both slow and rapid pressure distortions, and generally takes the form:

$$(\phi_{ij})_w = C \frac{\varepsilon}{k} (\overline{u'_k u'_m n_k n_m} \delta_{ij} - \frac{3}{2} \overline{u'_i u'_k n_j n_k} - \frac{3}{2} \overline{u'_j u'_k n_i n_k}) \frac{\ell}{y} \quad (2.68)$$

Where C is a model constant, and ℓ/y is a ratio of turbulence length scale ($\ell = k^{3/2}/\varepsilon$) to distance from the wall. This wall term acts to reduce the stresses $\overline{v^2}$ and \overline{uv} and augment $\overline{u^2}$ and $\overline{w^2}$ when in proximity to a wall.

2.2.8 Radiation Modelling

Radiation modelling is the last of the three methods of heat transfer. However, unlike conduction or convection, radiation does not require a medium through which to propagate, but instead travels much more directly. Because electro-magnetic energy travels irrespective of a fluid, it requires a separate and unique method of solution as it is not accounted for in the conservation equations.

In older simulations and analytical studies of heat transfer in low-temperature conditions, such as with classic building ventilation cases, it was common to assume that radiative transfer was negligible in the face of conventional heat transfer methods, i.e. conduction and convection. Part of the reasoning for this is due to radiative heat fluxes depending on the *fourth* power of temperature differences:

$$q \propto T_1^4 - T_2^4 \quad (2.69)$$

The conservation of energy in fluids is linear in temperature and involves four dimensions in space and time. Radiative transfer has seven variables and occurs over much larger scales, and because it involves the electromagnetic radiation, rather than molecular excitation, its effects do not decrease as the Knudsen number approaches unity.

Radiative Transfer Equation

The radiative transfer equation (RTE) defines the energy balance of radiated energy travelling in the direction \hat{s} within fine beams of area dA from point s to $s + ds$:

$$\frac{1}{c} \frac{\partial I_\eta}{\partial t} + \frac{\partial I_\eta}{\partial s} = a_\eta I_{b\eta} - a_\eta I_\eta - \sigma_{s\eta} I_\eta + \frac{\sigma_{s\eta}}{4\pi} \int_{4\pi} I_\eta(\hat{s}_i) \Phi_\eta(\hat{s}_i, \hat{s}) d\Omega_i \quad (2.70)$$

Because the scales involved in the speed of light are orders of magnitude outside of most terrestrial applications, the first term is usually neglected (Modest 2003). Also, the transient term is neglected as the irradiation dealt with in this work is of a constant nature, and is assumed not to vary greatly over the duration of the radiative transfer. These assumptions allow the RTE to be shortened to a more common form:

$$\frac{\partial I_\eta}{\partial s} = a_\eta I_{b\eta} - \beta_\eta I_\eta + \frac{\sigma_{s\eta}}{4\pi} \int_{4\pi} I_\eta(\hat{s}_i) \Phi_\eta(\hat{s}_i, \hat{s}) d\Omega_i \quad (2.71)$$

Because radiation is transferred by a much more direct manner, it makes simulation somewhat difficult because of existing finite difference/volume methods of calculating fluid flow. Also, as radiation is the transfer of electromagnetic quanta, it subject to many more effects:

- Scattering by small particulates
- Specular and partially-specular reflection
- Hemispherical directionality of materials
- Absorption and emission through participating media and semi-transparent solids
- Multiple wavelength bands

Radiated energy from the sun covers a large number of wavelengths, but can be analogised with a spectral blackbody emission spectrum centred at 5777K and normalised to 1367W/m² (Figure 2.4). The most important wavelengths involved in radiative heat transfer are those of the

infra-red band, of 1nm to 100nm. Inside this relatively narrow band occurs most of the heat transfer between surfaces and participating media.

Figure 2.4 - Solar irradiation spectrum with various wavelengths of interest (Modest 2003:6)

Participating Media

Gases are weak participants in radiative heat transfer, and their participation rests upon the contributions of a small number of gases. Air is composed of a large number of components which play a part in various physical mechanisms, but in radiative heat transfer, two specific components - carbon dioxide and water vapour - are contributory to radiative heat transfer.

Gas energy transfer occurs when the concerned molecules are struck with EM radiation at their resonant frequency, causing a change in their electron energy levels. When the electron then drops to its equilibrium energy level, it releases its excess energy, which is then possibly absorbed by a neighbour molecule. In this respect, gas is fully participating, i.e. it not only absorbs, but it also emits infra-red radiation.

Literature on the individual emissivities of water vapour and carbon dioxide separately are fairly thorough at higher temperatures (Hottel & Sarofim 1967). However, in air, water vapour and carbon dioxide co-exist and have a primary resonance band overlap at 2.7 μ m. Due to this overlap, simple summation of emissivities is not accurate as the actual emissivity is slightly less lower. Methods for calculating emissivities for both carbon dioxide and water vapour have been formulated by Tien (1968), but a more recent method by Leckner (1972), which uses a series of correlation coefficients to derive the combined emissivity, has been found to be more accurate (Modest 2003).

In reality, while experimental and theoretical methods are able to produce predict radiative properties of gases inside a large range of temperatures, it is understood that such a complex

phenomena is difficult to predict with great accuracy (Modest 2003). In numerical simulations, this is also compounded by the requirement to specify accurate gas compositions. Given the strength of water vapour in radiation and its variability in the air, accurate recording of boundary conditions must be made in order to ensure the accuracy of predictive methods.

Solution Methods

There are many methods of solving the RTE. General solutions like the P-1 and Rosseland approximations expand the radiation intensity I into an orthogonal series of *spherical harmonics*, but only function accurately when the optical thickness $\alpha\ell$ is large, or more accurately, radiated intensities are isotropic (Modest 2003). Other models, such as surface-to-surface models calculate the geometrical view-factors to determine the emissivities, which are then used to calculate radiative transfer, but models of this kind are only able to model surface radiation, neglecting participating media, such as air. Finally, one of the more complex models, the discrete ordinates (DO) model, solves the RTE for a finite number of solid angles based on the existing finite volume mesh (Raithby 1999). However, this has an increasingly high computational overhead depending on the resolution of the angular discretisation, and the number of radiation bands.

2.3 General Ventilation

A large amount of literature exists surrounding both numerical and experimental studies on ventilation and buoyant flows. A good introductory review of natural ventilation is given by Linden (1999) which covers both displacement and mixing ventilation at low Froude numbers.

In general, there are two main ventilation types:

Displacement ventilation occurs at relatively low Reynolds and Froude numbers, and relies on pressure differences between the fluid and the ambient surroundings to drive the flow, usually as a result of fluid buoyancy. This buoyant difference is the crux of the displacement ventilation method, and can itself be driven by large temperature differences. The buoyant fluid rises, entraining and transporting contaminant or used air, which is exhausted at ceiling level. Fresh, colder air is supplied at a lower level to continue the process.

Mixing ventilation relies on the application of a high momentum source to disturb the fluid and contaminants, creating turbulence and mixing the fluids together. The internal pressure increase allows the mixture to be exhausted through an outlet. Mixing ventilation, and mixing in general tend to be used in different situations than displacement ventilation due to the higher momentum fluxes involved.

2.3.1 Natural and Displacement Ventilation

Natural ventilation is the ventilation of an area which is driven solely by pressure differences in the fluid(s) under study. This pressure difference is usually the result of buoyancy differences in the air, which can be increased by using stack or chimney effects, or reinforced as a result of external factors, such as wind. Because they both operate in similar flow regimes, natural ventilation and displacement ventilation can be used to compliment each other.

The Neutral Layer

One of the main factors that describe the design of the ventilation system is the *neutral layer* (or *neutral level*), which is the vertical height at which there is a balance between internal and external effects. Depending on whether an enclosure is open to the external atmosphere or not, a number of definitions (See Figure 2.5) of the neutral layer are used by different authors.

In naturally-ventilated enclosures, i.e. one that is open to the external atmosphere, the neutral level is determined by the external ambient surroundings, whose vertical hydrostatic pressure dp/dh is linear. The vertical pressure inside the enclosure to be ventilated will, at some height, coincide with the linear hydrostatic pressure of the ambient surroundings – this is the neutral level (Linden 1999).

In enclosed environments, the external environment has less influence upon the room being studied, so a different method is used to determine the neutral level. Stymne *et al.* (1991) and Xing

& Awbi (2002) express the neutral layer as being the height where the internal temperature profile coincides with the mean wall temperature, which is also equal to the mean contaminant concentration in the recirculation zone. They also state that theoretically, the neutral layer is located where an airflow balance exists, i.e. the buoyant flow rate is equal to the supply flow rate, which is also stated by Auban *et al.* (2001), who examined thermal plumes in stratified environments using an ethanol solution.

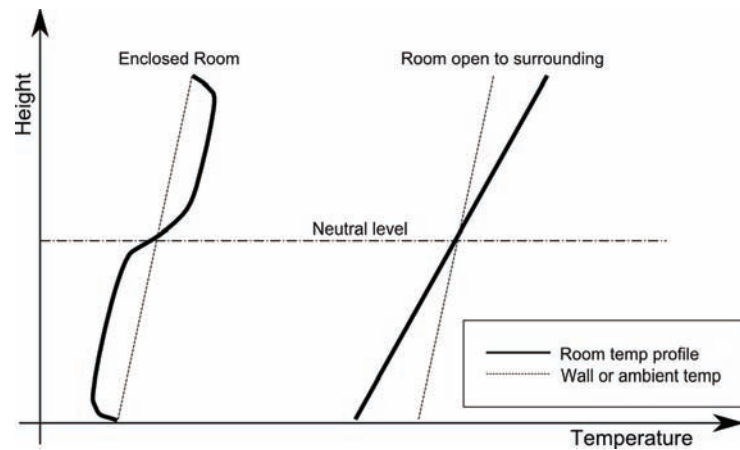


Figure 2.5 - Neutral Layer plots; enclosed room remote to surroundings (left); room open to external ambient conditions (right)

In examining full-scale experiments of room ventilation, Iial-Awad (2006) defined the neutral layer as a saddle point in the temperature profile:

$$\left(\frac{d^2T}{dz^2} \right)_{z=h+\frac{\delta}{2}} = 0 \quad (2.72)$$

Fluid above and below the neutral layer will flow in or out of the system depending on the pressure difference between the two. This is an important characteristic of the ventilation system, especially for the ventilation of smoke and fires, as the neutral level determines the locations of the supply and exhaust vents, and the demarcation between them.

Mundt *et al.* (1994) examined previous literature, finding a correlation between the nondimensional air temperature with respect to the ventilation flow rate, concluding that the temperature gradient formed inside the room is not dependant on the location of the heat sources themselves. A series of empirical models were used to predict convective flows based on equations for heat-emitting point sources without temperature gradients, and axisymmetric turbulent plumes. The prediction based on turbulent plumes was found to be better; Xing & Awbi (2002) also used this model to aid in the prediction of the neutral level height in conjunction with models by Stymne *et al.* (1991) with fair results, noting that if the room's thermal load grew above 45 W/m², the neutral layer rose in a non-linear fashion for a given linear variation in ventilation rate because the

increased thermal load caused both warming of the upper and lower zones, reducing the temperature gradient. Their predictions for the neutral layer height were also slightly higher than most of the measured experiments, which was attributed to unsteady variation of ambient weather conditions and the fountain effect that an upward plume would create when impinging on the ceiling, when it's free-rising height was larger than the height of the ceiling. This caused down-drafts around the plume that would cause the neutral layer to be subject to a negatively buoyant flow.

The occurrence of the neutral layer forms the basis of the displacement ventilation concept, allowing contaminants to be removed from the inhabited region due to buoyancy arising from a temperature gradient which, in small spaces, is only weakly dependent on the location of the heat sources which give rise to the gradient (Mundt 1995). While the vertical contaminant concentration profile may stratify about the neutral layer, the temperature profile may not stratify with a distinct interface and remain essentially linear, depending on a combination of geometry, ventilation rates, thermal loading and fluid properties.

Most models of small room-sized displacement ventilation assume heat emission to be point sources, which then creates a self-similar plume of buoyant air; a number of authors use a model attributed to (Morton 1956, in Mundt 1995) to calculate it's effects and momentum transfer. Air in the lower zone is entrained by the plume, which then allows it to rise either into the upper zone, or a stratified layer if one exists.

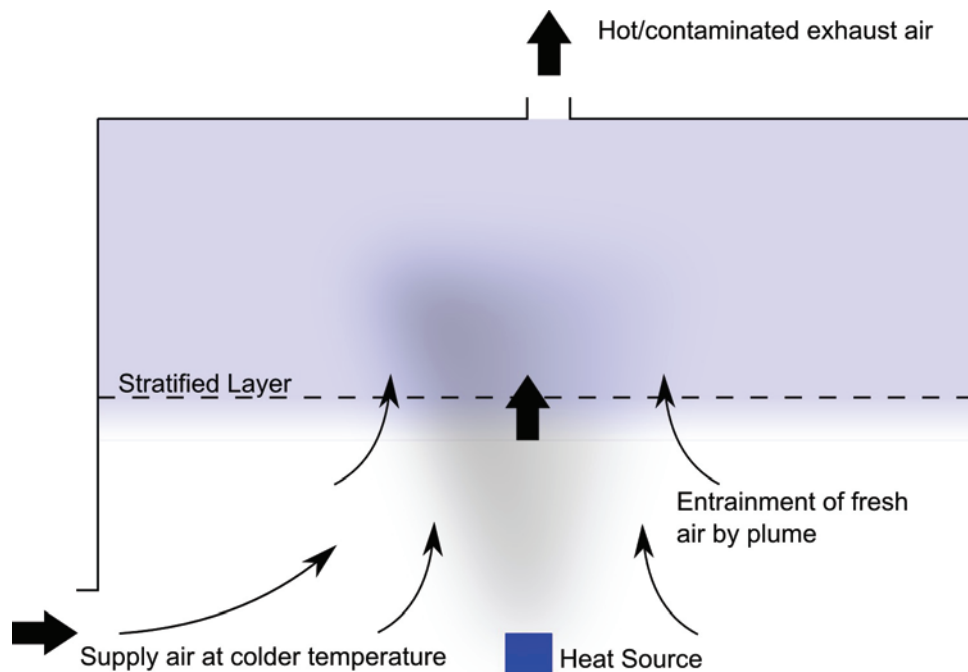


Figure 2.6 - Air flow inside a typical room ventilated using displacement ventilation

If a stratified layer exists, then vertical transport may be inhibited depending on the local Richardson number (Equation (2.10)). If the Richardson number is low enough, the layer may not

be at the point of laminarisation, and vertical transport within the layer may exist via Bénard cells. If the layer is made less stable still, it will be subject to increasing instability through shear-induced structures, such as Holmboe or Kelvin-Helmholtz instabilities.

As it is not desirable to have large air velocities in inhabited areas due to occupant discomfort, natural or displacement ventilation methods are preferred in these locations. Holford & Hunt (2003) analytically and experimentally studied the displacement ventilation of atriums of given conditions. In particular, they found that the addition of an atrium increases the buoyant flux by increasing the stack pressure which drives it, reducing the ambient temperature of an adjoining storey. However, it also reduces the effective opening area that ventilates the storey, potentially reducing the overall efficiency.

The analytical model was experimentally verified using a salt-water bath technique, which was in approximate agreement with the model. Hunt *et al.* (Hunt *et al.* 2001, Hunt & Linden 1999) uses this technique widely, although it is known that the saline fluid used has diffusivities three orders of magnitude less than that of air, leading to sharper density gradients. Radiative heat transfer that takes place under normal situations is not accounted for using this method (Howell & Potts 2002) which, especially on more humid days, can affect the internal distribution of temperature. However, in the limit whereby radiative and diffusivity conditions are either small or of no consequence, salt-bath techniques provide useful and very clear results due to the difference in diffusivities. Auban (2001) performed experiments using ethanol as a solute coupled with laser-induced fluorescence (PLIF) techniques to examine the effects of a buoyant plume in a confined environment, confirming that remote from the plume (>0.6 plume diameters) the stratification interface layer height was proportional to a combination of buoyant fluxes and ventilation flow rates: (Auban 2001)

$$h \propto B_s^{-1/5} Q^{-3/5} \quad (2.73)$$

Skistad (1998) and Calay *et al.* (2000) proposed an interesting method of selective ventilation using displacement ventilation methods. Inside large factory buildings, a number of different tasks occur concurrently, and each has its own ventilative requirements. Because of this, and utilising thermal stratification, the stratified layer was partitioned using temporary vertical walls which were suspended 3-4m above ground (to allow unhindered access at ground level) without a full connection to the ceiling; in essence, the hanging walls contained the stratified layer only. This division of stratification allowed the contaminants to be restricted to their own partitioned airspace both horizontally and vertically without physically impeding the work below, and allowing the design of specific ventilation systems to deal with those contaminants alone. They noted that the gradient of the vertical temperature profile affected the resistance of the layer to disturbance, and demonstrated that selective withdrawal methods can work for gradients as low as 0.125°C/m.

A large number of numerical simulations for predicting displacement ventilation flows exist for a large number of configurations due to the flexibility of simulative methods for modelling a wide variety of flows; however, numerical modelling also adds a number of complications due to turbulence prediction and accuracy of boundary conditions.

Earlier work by Chen (1995) examined a number of different K-Epsilon-type turbulence models as applied to natural, forced and mixed convection as well as impinging jets in 2 dimensions, and found that while the mean velocity predictions were generally satisfactory, the isotropic nature of the K-Epsilon models made simulation of anisotropic conditions inaccurate, such as Reynolds stresses and secondary flow features. Kuznik et al. (2006) used a number of different K-Epsilon and K-Omega models on an unstructured mesh with second-order upwinding schemes to model wall-jet ventilation, and while his results in the near-field of the jet were good, all of his models performed less well downstream and were less accurate in resolving the cross-section profiles of the jet.

Jiang & Chen (2003) compared buoyancy-driven flows with large side-openings using experimental methods and two CFD models, one using RANS turbulence modelling (specifically, the standard K-Epsilon model of Launder & Spalding 1974) and another using LES-based methods involving the standard and dynamic Smagorinsky models. The prediction of temperature profiles by both RANS and LES models were of similar quality with the models following roughly similar trends. On the other hand, the predicted velocity profiles (both RMS and mean) had a greater degree of variance, both in comparison to each other and with respect to the experimental results. This difference resulted in the RANS model over-predicting the air exchange rate (ACH) by around 20%, whereas the LES model was within the scope of measured values. Further work conducted by Jiang & Chen (2001) examined natural ventilation in buildings using the same numerical methods, and concluded that due to the averaging procedure in RANS calculations, the simultaneous exchange of air into and out of the room is cancelled out, resulting in under or over-predictions of air change rates, though this requires further study.

In the examination of room ventilation with thermal stratification, Jouvray *et al.* (2006) compared a number of eddy-viscosity and Reynolds-stress models in a series of comparative simulations, examining velocity and temperature profiles, finding little difference in accuracy between the K-Epsilon models, though they performed better in comparison to the K-L models. Similar to Jiang & Chen (2001), Jouvray *et al.* (2006) found that RANS models performed less well in the determination of velocities, with LES providing closer agreement to experimental results; however, the difference was of the order of 10%, and in many cases the second-order K-Epsilon model had a predictive accuracy similar to that of LES. A final conclusion made was that many performance aspects of the models were highly case-dependant, so it is difficult to compare models without considering more general cases.

Ji *et al.* (2007) examined an atrium scenario previously covered analytically by Holford & Hunt (2003) using numerical simulation coupled with a 2-equation RNG turbulence model. Their predictions agreed favourably with the experimental model, except in the case of an unventilated atrium, where the CFD model tended towards a fully mixed condition in comparison to the experiment which exhibited a stratified layer separating the atrium into two zones. The authors posited three possibilities for this discrepancy - the high diffusivity of heat in air (compared to the diffusivity of brine in water as used in the experiment), over-prediction of turbulent viscosity leading toward increased mixing at the layer, and thirdly, because the simulation was run in steady state, it may be possible that in the limit of time, the experimental result could also have tended toward a fully mixed result; this latter case was investigated with a transient simulation, and a stratified layer was found to exist, but the layer descended over the course of time. One aspect that is not modelled by either experimental method or simulation by Ji *et al.* (2007) is that of radiation, which would increase the tendency towards a fully mixed state - the heat energy warmer upper zone would be radiated down to warm the lower zone, and the reduced temperature gradient across the stratified layer would further weaken it, reducing the Richardson number.

2.3.2 Effect of Thermal Radiation on Ventilation

In the past, radiative contributions to heat transfer have usually been neglected or roughly accounted for empirically due to the complexity of radiative transfer prediction, unless radiation formed a large and visible part of the system under examination, such as in solar heating or thermal regulation in rarefied atmospheres. However, in more recent times with higher availability of computational power and more complex numerical methods to solve general cases of the radiative transfer equation, these effects are being included in more analytical and numerical simulations in order to account for all forms of heat transfer.

Early work examining the effects of thermal radiation on ventilation were performed by Li *et al.* (1993), who studied a 41.58m³ room with a floor-level supply and an exhaust located high on wall. A heat source was located in the middle of the room, causing a convective plume. The interior walls were initially lined with aluminium sheet resulting in low emissivities, and then compared to black walls which absorbed more radiated energy. They found that the radiation from the upper zone warmed up the lower air zone and the lower wall by around two degrees; this also reduced the temperature gradient across the stratified layer. Conversely, the ceiling was *colder* than the upper zone air temperature, and the floor was *warmer* than the lower zone air temperature due to radiative transfer between them, coinciding with the results of Mundt (1995). As expected, this result was magnified when the black, higher emissivity walls were used.

Glicksman & Chen (1998) carried out a numerical analysis and found that although the highest radiant energy flux occurs next to the radiating wall, the absorptivity is dependant on the

path length, so the absorption peak would be some way away from the wall. They also noted that although radiation is a second-order effect in the thermal boundary layer, radiated energy in a large enclosure with a large amount of surface area can be equivalent to, or exceed that by natural convection. From simulated work, Kondo *et al.* (2000) also came to the same conclusion in the case of large enclosures; all authors also understood that water vapour plays a large part in the absorption/emission process of air.

Kondo *et al.* (2000), and in other literature (Siegel & Howell 2002, Modest 2003, Bejan & Kraus 2003) show that air has two main participating components – carbon dioxide and water vapour. Carbon dioxide is a strong absorber, but due to its low concentration in air (~0.035%), it has less effect; it also shares absorption bands with water vapour, and as such the absorption of the two together is not as simple as the summation of the effects of both. As such, Kondo *et al.* (2000) and Howell & Potts (2002) assumed that water vapour was the only participant.

Investigations by Howell & Potts (2002) into the behaviour and properties of the salt bath experimental methodology used by Linden and others (Linden 1990, Linden 1999, Hunt *et al.* 2001) found that radiative effects are not accounted for using this method. It is also noted that the diffusivities of air and the salt-baths are vastly different, so that whilst the experimental methods used by Linden *et al.* are able to simulate convective buoyancy effects, the different diffusivities lead to overly-sharp gradients, and that radiative effects are unable to be simulated.

Recent work by Bournet *et al.* (2007) computationally examined the ventilation of a multi-span greenhouse in two-dimensions using a 2-band radiation model to account for the radiative surface-to-surface interactions, differentiating between the radiative behaviour of glass and other surfaces. The banding was split between 0-3 μm and 3-100 μm ; for glass, the former was largely transmissive, while the longer wavelengths were strongly absorbed. Simulated temperatures relative to experimentally measured values was fairly close, usually to less than a degree in temperature, which validated the capability of the simulation method.

2.3.3 Mixing and Mixing Ventilation

Mixing ventilation uses a wholly different strategy to displacement ventilation. Where the latter uses fluid buoyancy and stratification to control the ventilation, mixing ventilation uses a more active method whereby momentum sources are used to *break up* any stratification and entrain both contaminated and uncontaminated air, mixing them both up and exhausting them. Obviously, air at high velocity is not conducive to high comfort levels, so mixing ventilation is seldom used in areas of high human occupation. However, in other circumstances, mixing ventilation may be the only possible method due to a combination of size, mixture of contaminants (which may be toxic) and geometry; as displacement ventilation relies on buoyancy, it has fixed time and velocity scales which may not be adequate to solve the ventilation problem, either due to time constraints, or other reasons, for example if dense gases need to be removed. In such cases, mixing ventilation is used.

Although mixing ventilation has a lower mixing efficiency than buoyant flow (Linden 1999) which requires the forced flow rate to be several times higher than that of the buoyant flow in order to achieve the same level of mixing, jet mixing, using fans or otherwise, are usually simple to implement. Hunt & Linden (1999) formulated an equation to calculate a critical Froude number based on the room geometry only, whereby the flow transitions from displacement ventilation to mixing ventilation. At this critical Froude number, the maximum ventilation rate by displacement ventilation also occurs:

$$Fr_{crit}(0) = \sqrt{\left(\frac{a_w^{3/4}}{A^* H^{1/2} \alpha} \left(H - \frac{h_L}{2}\right)\right)^2} - 1 \quad (2.74)$$

Here, a_w is the area of opening on the windward side of the building and H is the difference in height of the leeward (h_L) and windward openings. Although this can be used as a guideline to determine the upper limits of displacement ventilation, it can also be used as a marker for the lower limit of mixing ventilation.

Mixing takes place at distinct scales of motion (Dimotakis 2000). The largest stage is dubbed the *entrainment* stage, where the fluid engulfs large pockets of the other species into the turbulent flow region; the *stirring* scales, where the creation of large interfacial surfaces occurs to accommodate the final stage, *molecular mixing*. These scales of mixing (termed *initial*, *intermediate* and *final* stages by Eckhart (Eckhart 1948, in Dimotakis 2005) also correspond to the flow of turbulent energy from large scale production to viscous dissipation in the energy cascade (See Figure 2.2). Based on a series of turbulent mixing data, Dimotakis, and acknowledged by Shy (1995), proposed that an enhanced turbulent-mixing state occurs above a Reynolds number $Re > 10^4$, or Taylor-Reynolds number of $Re_t > 100$, though he added that whilst the mixing transition occurs over a relatively narrow range of Reynolds numbers (compared to turbulent flow transition), the Reynolds number(s) in question depend upon the flow, and perhaps on the definition of the Reynolds number itself, being the least well-defined for a turbulent jet.

Jets are usually used as a driver for mixing ventilation because they are mechanically simple to implement. Dynamically, they rely on turbulent kinetic energy to entrain and mix the fluid parcels, creating a velocity field with as little “dead zone” (regions of stagnancy) as possible. Compared to buoyancy-driven ventilation methods, turbulent mixing is not as efficient by way of only 20% of the turbulent kinetic energy being used for the mixing (Linden 1999). As a result, higher flow-rates must be used in order to achieve the same level of mixing energy used in the ventilation process as buoyancy-driven ventilation. However, unlike buoyancy-driven ventilation, they can be used with negatively-buoyant contaminants when the choice of in- and outlet placement is restricted - to remove a non-buoyant gas, a buoyancy-driven flow would require an outlet be placed at the lowest level.

Mixing Ventilation

While the higher flow rate, and thus higher velocities required aren't desirable from a comfort point of view, industrial and chemical applications have no such restriction, and the ability to create high momentum jets with relative ease makes turbulent mixing quite attractive. This differing methodology gives rise to a new set of metrics.

$$\text{ACH} = Q / V \quad (2.75)$$

Air changes per hour (or ACH) is defined as the ratio between the incoming air supply volume flow-rate (in m³/h) to the total room volume, and in certain applications (for example on ocean-going vessels) is used as a defining criteria to ensure that a space is well ventilated to avoid hazards, such as explosive mixtures of gases.

Residence time is defined as the time it takes for the average fluid parcel to be entrained or mixed, and exhausted; mathematically this is equivalent to the reciprocal of the ACH. However, this definition is in the average, and does not account for extremes, such as inlet-outlet "short circuiting" (whereby a jet inlet intended to mix the surroundings is drawn to a low-pressure outlet), or stagnant fluid zones where fluid may exist for long periods before being refreshed due to low circulation.

Mixing or blending time is often used as a criterion in chemical engineering, and differs from ACH in that it is a measured quantity as opposed to a specification based on few boundary conditions. Experimentally measurable using concentration or conductivity tests, mixing time presents the time taken for the mixture to reach a particular level of homogenisation, usually 95%. Numerical simulations have the added benefit that the entire flow field is known, so simulation of a passive scalar or injection of discrete particles can be further used to enhance knowledge of the system.

Although not as common as displacement ventilation in offices and occupied spaces, mixing ventilation is more commonly employed in industrial buildings, and also places where VOC or air contamination by toxic fumes is a factor. Fires and road tunnels are also applications of jet mixing-ventilation.

Brown & Dabberdt (2003) performed CFD studies of forced ventilation of a covered roadway section using the RNG K-Epsilon turbulence model, concluding that their simulations gave good qualitative agreement, and that the major pertinent flow features were well represented. This is an important reality that should not be ignored when conducting numerical simulations involving Reynolds-averaged simulations - the effect of smaller-scale fluid actions are represented by turbulent viscosity, leaving only the much larger scales to be represented by the flow field. Also, compared to work involving natural and displacement ventilation presented in Section 2.3.1, the higher-Reynolds flows in mixing ventilation yield better velocity predictions.

Lee & Awbi (2004a and 2004b) conducted ventilation effectiveness studies involving jet mixing from a ceiling-mounted orifice, and the effects of partitions on the flow-field. Experiments were then compared to numerical simulations, which correlated well with the experimental results. Their CFD study was able to simulate the experiment with good trend prediction, although the bounds are offset somewhat from the experimental results. When the partition was added, they found that the variation of the gap size altered the recirculation around the partition; too large a gap would cause a more backflow due to momentum transfer balances into the partitioned zone, which affected the ventilation efficiency.

2-dimensional numerical VOC emission and ventilation studies have been conducted by Kim *et al.* (2002) for emissions in a small scale painting operation, whereby a toluene vapour source is located on a table. A ceiling-mounted jet some distance away from the table supplies fresh air, causing two primary recirculation vortices; one small rotational system above the table, and a larger one between the jet and the table. They found that the interaction of these two systems results in the entrainment of toluene vapours, and that the rotation is such that the vapours are entrained vertically upwards. By locating the outlet inside the smaller vortex above the table where VOC concentration is higher, the flow of toluene vapour to the rest of the room is reduced. By placing the exhaust in the contaminated zone, the contaminants can be “short-circuited” out of the system without having to first pass into the cleaner zone; this separation of zones by fluid movement is similar to displacement ventilation, where zonal separation is maintained by fluid buoyancy. The interaction of the two rotating systems causes a central vertical motion at the interface of the two vortices; the location of an exhaust vent roughly in line with this system results in marginally more efficient ventilation and reduced residence times (Kim *et al.* 2002). Of course, this effect is entirely dependant on the flow-field, which can be very easily disturbed. Lee & Awbi (2004) found out that by adding a small gap under the partition, flow from the jet impingement zone helped to create recirculation in the contaminated zone, but when the gap under the partition was increased in size, recirculation was destroyed again, reducing the ventilation efficiency.

Gilham *et al.* (2000) examined dense gas release inside a chamber using numerical methods compared to experimental work by (Bettis & Allen 1997, in Gilham *et al.* 2000) of an accidental release of a dense gas inside a chlorination room. A relatively coarse mesh of 55,000 cells was used to determine concentration and temperature time histories of injected Freon-22 (R-22). Qualitative comparisons varied, for example the trend of the temperature prediction at a particular location was accurate, but the predicted absolute values were around 3-5 degrees lower than the experimental. The accuracy of the concentration time histories also varied, being more accurately predicted for the jet injection of Freon, than in the case where Freon was released in an evaporating pool, where the concentration only loosely followed the experimental results. The lower accuracy of some of the results was examined, and the main sources of error were judged to be the high y^+ values (which ranged from 105 to 500), resulting in poor near-wall turbulence

prediction that could contribute to artificially increased mixing. In the evaporating pool simulation, the flow was heavily reliant on buoyancy effects driven by temperature and density variations in the flow field. Neglecting the thermal inertia of the machinery in the room, and not accounting for the heat capacities of the walls may have contributed to prediction inaccuracies.

Jet Mixing

In chemical industries, the primary focus has been towards using jets to mix chemical components. Two major variables are of interest in chemical jet mixing - mixing time (also referred to as blending, or homogenisation time), and entrainment rates. The jet length or throw is sometimes used as a parameter in order to define empirical formulae to predict blending times based on certain boundary conditions.

Early work on mixing tetra-ethyl lead and various motor oils was performed by Fossett & Prosser (1948) who performed a large number of experiments in different sized mixing vessels from 75 to 15,000m³. Early soda-mixing tests in a 1.67m³ tank saw a number of effects with some tests at low-Reynolds numbers failing to mix at all; instead, the fluids stratified into a more dense layer below the water, prompting an investigation of buoyant effects. They found that by elevating the jet nozzles and thus projecting the fluid in an arc, it was possible to distribute the soda across the tank more uniformly. A series of experiments ascertained that if an insufficient combination of elevation and jet velocity were used, the jet did not penetrate the upper layer stratification, leading to poor mixing. From these tests, they formulated a critical Froude number:

$$Fr_c = \frac{U^2 \sin^2 \theta}{Ng \left(\frac{\rho_2 - \rho_1}{\rho_2} \right)} \quad (2.76)$$

Where U is the jet velocity, θ is the jet angle and N is the internal nozzle diameter. Compared to Equation (2.74), this critical Froude number is based solely on jet dynamics, and in Figure 4 of Fossett & Prosser (1948), when plotted against excess head h (determined by $h = v^2/2g$, which is used as a pressure metric in some engineering fields), they found that the increase of excess head had a linear relationship with regards to the increase of Froude number, but when the excess head was around 80-120, an increase in h did not correspond to an increase the Froude number.

Blending or mixing time is a frequently studied parameter, resulting in a number of formulations (for example, Patwardhan 2002) which are usually functions of the jet characteristics (velocity or jet length), and also occasionally include variables related to tank geometry. In many studies, the jet flow rate and the geometry are such that air-change rates are quite high, so that the study becomes one of optimising the flow field and reducing dead zones (Jayanti 2001) or increasing entrainment or shear (Zughbi 2004). The results are usually fairly good correlations for

that particular geometrical configuration, but these correlations are not general enough to be used elsewhere, except as a founding basis for a new equation. One aspect that is noticeable is the dependence on Reynolds number, whereby blending time is inversely proportional to the Reynolds number.

This is perhaps not surprising since, especially in smaller, structurally simple tanks where the geometry and local velocity field is such that stagnant zones are small, the momentum of the jet is able to induce a large amount of shear, entrainment and mixing of the contents; variation of the Reynolds number controls the rate of this shear, which then affects the time taken to mix. If the flow field is such that there are stagnant regions of fluid, then the direct correlation will be skewed due to these regions being poorly ventilated, and any increase in Re (and thus jet momentum) may not change the local flow field enough to increase the level of mixing in this region. Grenville & Tilton (1996) analysed earlier data from a number of sources (Fossett & Prosser 1948) (Fox & Gex 1956) but instead of forming a mixing time based on jet data, they proposed that, based on work by Corrsin (Corrsin 1964, in Grenville & Tilton 1996), the mixing should be determined based on turbulent dissipation. However, because the turbulent dissipation close to the jet and at a point remote from the jet differs by so much, the mixing time will be dependent on a region far from the jet due to the lower dissipation.

Other authors have examined other methods to increase the efficiency of jet mixing. Using a single fixed jet gives rise to a specific average flow-field, but problems arise if this flow-field is not optimum (for example stagnation due to blockages). One method is to use spatially periodic injection of fluids, as studied by Ranade (1996); by alternating the supply jet location, a number of different flow fields are created. Interestingly, they found that depending on how they alternated the jets, the mixing time may not necessarily be reduced. They did, however, find that alternating between jets flowing in different directions enhanced the dispersion of the tracer fluid as compared to using a single steady jet supply, due to the increase in shear.

Nordkvist et al. (2003) examined a different method of varying jets using a rotary jet head (RJH) mixer, functionally similar to the rotary head machines used onboard oil tankers during a crude oil wash. In practice, fluid is supplied to the RJH, which is then expelled out of the multiple nozzles at high pressures, and applying it to biochemical mixing processes, they found that compared to the more traditional means of mechanical stirring, the RJH delivers comparable performance for similar power requirements, but mixing times can be reduced by using higher flow rates through larger-diameter nozzles, or by using multiple rotary machines.

2.4 Jet Flows

A jet is characterised as a stream of fluid with a high momentum, as opposed to a plume whose movement is primarily due to buoyant forces. Jets are one of the most common phenomena found, and are seen in many applications. Jet mixing, for example, is used in many chemical

industries due to the high mixing rates generated by turbulent mixing, and simple mechanical implementation. In mixing ventilation, jets are also used when human comfort is not a primary factor, for instance in marine gas freeing and manufacturing centres (Baker *et al.* 2002).

A fluid jet has three distinct regions, characterised by the nondimensional downstream distance relative to the jet diameter. The potential core, which occurs just downstream of the nozzle ($0 < x/d < 10$), has a high centreline velocity with little decay from the velocity at the nozzle. In many cases, a *vena contracta*, or slight local acceleration, is present half way in the potential core due to streamline curvature from the sudden expansion of the nozzle orifice into the surroundings. The potential core ends when the laminar shear layers that form at the periphery of the jet have grown to the point where they meet in the centreline of the jet. The second region is known as the characteristic decay ($10 < x/d < \approx 40$), where the jet expands at constant rate of spread. The velocity decays significantly at the initial transition but decreasing further downstream, assuming an inverse logarithmic profile, or when plotted non-dimensionally, a line with a constant slope.

The final region is the axisymmetric decay region ($x/d > 40$). In this region, the jet continues to decay until there is not enough momentum to overcome viscous dissipation forces. For round jets, it is likely that the velocity profiles are already self-similar and the turbulent statistics likewise. In a plane jet, the centreline mean velocity becomes increasingly self-similar and axisymmetric in profile, which in the limit become axisymmetric.

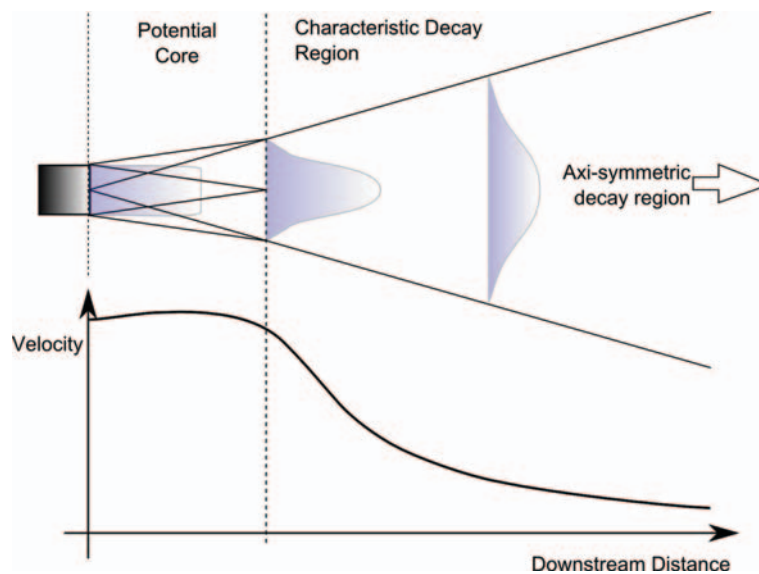


Figure 2.7 - Schematic of characteristic regions (above) in a typical jet with relative velocity reference plot (below)

2.4.1 Round and Plane Jets

Round jets and plane jets are two main types of jet defined by the orifice they are projected from; round jets are from circular orifices, whereas planar jets tend to be from rectangular orifices

of increasingly high aspect ratio. Jets are driven by a pressure drop through an orifice (List, 1982). The macro-dynamics of round jets in particular are quite well understood, and a number of monographs concerning their mathematical description are available (for example, Abramovich 1963, Gurevich 1965, List 1982, Agrawal & Prasad 2003).

Self Similarity

In general, the mean velocity field of a round jet can be described by the nozzle diameter, the downstream distance and the jet's velocity - as long as the jet is fully turbulent (i.e. has a high-enough Reynolds number), the Reynolds-dependence vanishes (Pope 2000) and the jet characteristics are functions of distances and velocity only. The axial variation of centreline velocity with downstream distance is defined by:

$$\frac{U}{u(x)} = \frac{(x - x_0)/d}{B} \quad (2.77)$$

Where d is the nozzle diameter, B is an empirical constant (which for round jets ≈ 6), and x_0 is the *virtual origin*, where the velocity plot intercepts the x-axis:

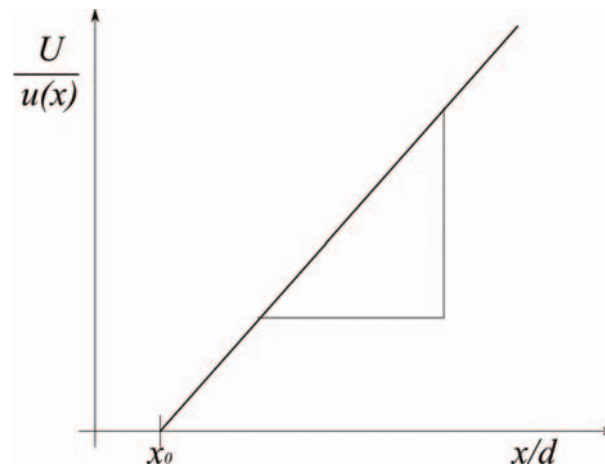


Figure 2.8 - Plot of non-dimensionalised velocity trend with respect to downstream distance

The linear behaviour only exists downstream of the nozzle, as in the near-field region close to the orifice the jet has yet to become self-similar. For a plane jet, self-similarity is asymptotic only after a certain number of diameters downstream; work by Gutmark (1976) showed that a planar jet became self-similar not only in mean velocity but in turbulence characteristics also, at around $x/d > 40$. Quinn (1992) performed experimental work looking at a number of jet aspect ratios allowing a comparative study of plane jets of increasingly high aspect ratio and round jets, whereby it was shown that the transition to self-similarity increases as per the aspect ratio; perfectly round jets develop self-similarity earlier on, whilst higher aspect-ratio jets develop further downstream.

Self-similarity in jets also applies to other aspects of the jet as well - spreading, entrainment and Reynolds stresses. Hinze (1975) recognised that velocity and turbulent statistics may not necessarily become self-similar simultaneously, and although mean velocity in an axisymmetric jet may become self-similar as soon as $x/d > 10$, turbulent stresses take longer.

Non-dimensional plots of mean axial velocity in the radial direction inside the self-similar region all converge on a same, almost Gaussian curve, indicating that the jet spread is linear. This gives rise to the following spreading rate equation:

$$S = \frac{dr_{0.5}(x)}{dx} \quad (2.78)$$

The spreading rate, S , has been experimentally determined to be around 0.1 by a number of authors (Pope 2000).

Jets of intermediate nozzle shape also display degrees of self-similarity; Singh *et al.* (2003) examined the behaviour of heavily confined round jets of aspect ratios up to 2 and of different nozzle shapes, finding that the planar jet and the circular jet represent maxima and minima cases, with the other (square, elliptical and triangular) jets falling somewhere between the two, both in terms of lateral velocity profiles (jet spread) and in terms of centreline velocity decay.

Because all of the physical conditions of the flow become predictable in the self-similar region, a number of methods exist which allow the modelling of this kind of flow. Pope (2000) outlines one method which involves an asymptotic analysis, resulting in a boundary-layer equations which then need closure, usually by the assumption of a constant turbulent viscosity. Agrawal & Prasad (2003) follow a different route, using integral methods to form another model for the flow, allowing the computation of lateral velocity for a free jet, plume or wake.

The lateral velocity will, due to conservation of mass, become negative near the periphery of the jet, indicating the entrainment of surrounding air. Agrawal & Prasad (2003) used the following expression of lateral velocity in the self-similar region:

$$\frac{V(\xi)}{U} = \frac{S}{2\xi} \left(-1 + \exp(-\xi^2) + 2\xi^2 \exp(-\xi^2) \right) \quad (2.79)$$

Where $\xi = r/b$, the non-dimensionalised radial distance from the jet core, and S is the jet spreading rate, as defined above.

The turbulent anisotropy of jets is well known (Pope 2000, Davidson 2004), whereby the axial normal stress $\overline{u'^2}$ is almost twice as much as the lateral and vertical normal stresses, $\overline{v'^2}$ and $\overline{w'^2}$. The cross-stress, $\overline{u'v'}$, on the other hand, has a much lower magnitude in comparison; this is seen graphically in Figure 2.9.

Figure 2.9 - Comparison of Reynolds normal and cross stresses through the radius of a jet (Pope 2000:106)

This poses an interesting issue, for in numerical simulations of turbulence, the assumption of the Boussinesq eddy-viscosity assumption (used in many two-equation turbulence models) assumes the isotropy of turbulence. In practice, numerical results from this so-called “mixing-length” assumption are still fairly accurate, and is covered by Pope (2000) and Davidson (2004). The main failure of such eddy viscosity models is the over-prediction of velocity in the jet periphery, though this been eliminated in modern K-Epsilon models; see Section 2.2.7.

Free, turbulent round jets, being axisymmetric, evolve in a uniform way; their initial formation sees the creation of laminar shear layers. These shear layers quickly become unstable, forming ring-vortices which then pair off and break up (Popiel & Trass 1991, List 1993). These initial vortices have been found to be coherent, described by a Strouhal number, $St = fd / U$, in the range of 0.3-0.5 (Popiel & Boguslawski 1979, List 1993). Downstream of this initial region of large coherent structures, instability and possible interaction of helical modes leads to breakdown into smaller-scale turbulence.

Due to the strong dependence of jets on their initial shear layers, they are quite unstable and very dependent on their surroundings. This instability has been examined and utilised in some practical scenarios. Lawson & Davidson (2000) studied this oscillatory phenomenon using both experimental and 2D numerical simulations. Their studies found that the liquid jet oscillation was dependent on its confinement as well as the jet orifice itself. The jet oscillation was initiated through small natural perturbations in cross-flow near the orifice; the jet asymmetry set up recirculation cells inside the chamber, which perpetuated the oscillation. By artificially perturbing the initial region of the jet, using a physical or fluidic excitation device, it is possible to control the oscillations (for example, Travincek *et al.* 2002).

As seen already by Dimotakis (2000) and Shy (1995) and touched upon in Section 2.3.3, turbulent jets undergo a form of transition between $Re > 10^3$ and $Re > 10^4$ whereby at lower Re the turbulent vortices occur in large-scale coherent structures; above this transition, turbulence occurs on large and small scales, making the periphery interface of the jet far more intricate.

Numerical Studies

Turbulent free jets represent one of the major cases of shear flows (the other two being boundary layers and wakes) which are commonly simulated through numerical methods. As such, there is a large amount of literature on such, which also include validations of different turbulence models.

In the past, computational simulations of round jets were met with some difficulty due to the round jet anomaly whereby the spreading rates of round jets were over-predicted. However, with the development of more sophisticated turbulence models (Section 2.2.7) and higher computational power, modelling jet physics is possible to a higher degree of accuracy, and with the capability to perform simulations with much less modelling (e.g. LES, DNS), greater *information* about the jet is possible. Because shear flows are quite well understood already, simulations of jets are usually in combination with a number of other flows of interest; for example, impinging flows (Jiang *et al.* 2002, , Tsubokura *et al.* 2003, Popiel & Trass 1991, Beaubert & Viazzo 2003, Popiel & Boguslawski 1979), oscillatory studies (Travincek *et al.* 2002, Lawson & Davidson 2000), jet-driven mixing (Shah & Furbo 2003, Zughbi & Rakib 2004, Lee & Awbi 2004a, Patwardhan 2002), or, as with earlier papers, flow validation (Craft *et al.* 1993, Shih *et al.* 1994).

2.5 Impinging Flows and Stratification

Impinging flows are those which examine a plume or jet directed at a surface or another fluid e.g. air in water, or buoyant contaminants impinging on a thermally stratified layer, such as natural ventilation methods studied earlier in Section 2.3.1. Given the importance of stratification, both thermal and densimetric, to ventilation, it is important to understand the physics involved in stratified and impinging flows in order to maximise the efficiency of their ventilation. In particular, the breaking of stratified layers is of interest due to the flow features expected from the analysis in Section 2.3.3.

2.5.1 Impinging Flows

Impinging flows are commonly used in industrial applications because of the high heat and mass conductivity in the stagnation region (Tsubokura *et al.* 2003). From a scientific position, this is interesting from multiple points of view; researchers have studied the effects of impinging heat and mass transfer with a view to forming empirical relations correlating, for example, the Nusselt and Reynolds numbers due to the impingement (for example, Eren *et al.* 2006). Other researchers are interested in the fluid structures of the impingement region and the way the jet interacts with it.

Compared to the earlier review of jets, where a large amount of research was directed towards the self-similarity in the downstream regions, impinging heat transfer is concerned with the initial region of the jet. Most impinging flows involve a short distance between the jet orifice and the impingement plate, so the dynamics of the near-field region of the jet become important.

Impinging flows have been well studied using numerical methods (Nguyen & Evans 2006) partly because of academic interest, but also due to the wealth of flow structures that are present in fluid impingement from round and plane jets, which has led to a number of highly detailed LES and DNS simulations, for example Chung *et al.* (2002), Tsubokura *et al.* (2003) and Jiang *et al.* (2006). Although validation against experimental results are needed to lend a firm basis to the results, numerical methods allow researchers to perform “thought experiments”; Jiang *et al.* (2006) examined the effect of small inlet perturbations on the projected flow and impingement region on a low-Reynolds ($Re = 1000$) jet into still surroundings using DNS, using the excitation to prompt the creation of shear-layer coherent structures.

Chung *et al.* (2002) numerically examined the change in mass and heat transfer as well as performing visualisation of the ring vortices which emanate from the jet orifice. The impingement heat transfer was very unsteady and oscillatory in time, and at the stagnation point the peak heat transfer differed from the time-mean value by 20%, due to the primary vortices periodically emanating from the jet nozzle down into the impingement region, causing a complex flow structure there. The creation of these “primary vortices” at the orifice were captured by Popiel & Trass

(1991), who performed experiments of smoke-wire visualisation of free and impinging jets at low nozzle-to-plate ratios.

If the fluid jet impinges on another fluid, the properties of that fluid come into play. Because the fluid is no longer impinging on a rigid surface, the surface being impinged upon will deform depending on the jet. If the jet supply has enough momentum and/or the density gradient across the interface is low enough, the jet will penetrate into the other fluid; Figure 2.10 illustrates the different impingement regimes.

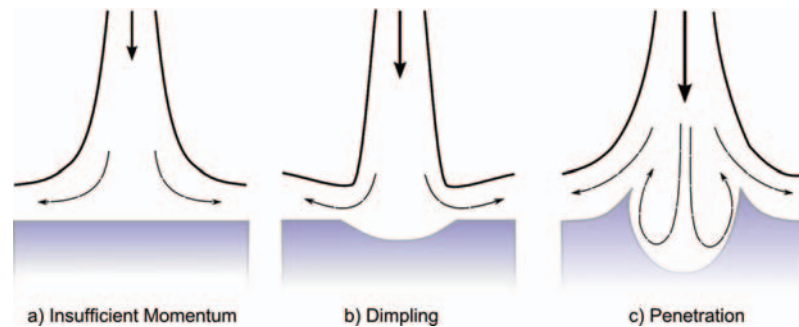


Figure 2.10 - Modes of surface deformation with increasing jet momentum

From Figure 2.10, a) depicts a scenario whereby the supply of fluid (which can be, for example a buoyant or negatively buoyant plume) entrains the surrounding medium of denser fluid, but lacks sufficient momentum to reach the interface; instead, it rises as the buoyancy of the jet overcomes its momentum, pushing back up through the denser medium, entraining more fluid and creating a density stratification. Due to the excess inertia of the plume, it will initially rise, then sink back to equilibrium at a neutral height, analogous to the first front in Baines & Turner (1969) and also Cardoso & Woods (1993).

If the momentum of the jet is such that the jet core can impinge upon the layer but not break it, it will ‘dimple’ the layer, as in Figure 2.10, b), before intruding sideways. Although this mode does not directly penetrate the layer, if the local Richardson number $Ri < 1$, the resulting shear flow may give rise to destabilising turbulent modes such as Kelvin-Helmholtz instabilities, resulting in the eventual destruction of the layer. If $Ri > 1$, for example due to turbulence decay from buoyancy, the shear flow may laminarise without destabilising the layer. Although described by Turner (1979), Sherman (1978) presents some interesting conclusions about Kelvin-Helmholtz instabilities, whereby they require a sharp interface to initiate, and that they are self-limiting whereby an interface that has been thickened by Kelvin-Helmholtz-driven mixing will decay unless the shear increases, or the layer becomes sharp again.

Finally, if the supply has sufficient momentum ($Ri \ll 1$), the jet will be able to pass through the stratified layer and proceed into the other fluid. Depending on the conditions of the jet, it is possible for the jet to *detrain* (Cotel 1995, and Cotel & Breidenthal 1997), whereby fluid is

expelled from a turbulent flow like a jet or a plume, when passing through a stratified interface. Cotel & Breidenthal (1997) experimentally determined a series of detrainment regimes, demarcated by a mixture Richardson-number:

$$Ri_{mix} = g \frac{\rho_{mix} - \rho_2}{\rho_2} \cdot \frac{\delta_{mix}}{(U/2)^2} \quad (2.80)$$

When the mixed Richardson number $Ri_{mix} \ll 1$, no detrainment occurs; At intermediate values of Ri_{mix} , *delayed detrainment* occurs, whereby penetration occurs and detrainment occurs somewhere downstream of the fluid interface. Depending on the H_i / d ratio, *prompt detrainment* may also occur, whereby the jet penetrates, but at the same time fluid at the periphery of the jet is left at the interface. Finally, at $Ri_{mix} \approx 1$, the jet may penetrate but maintains insufficient momentum, becoming a fountain. These regimes are illustrated below in Figure 2.11.

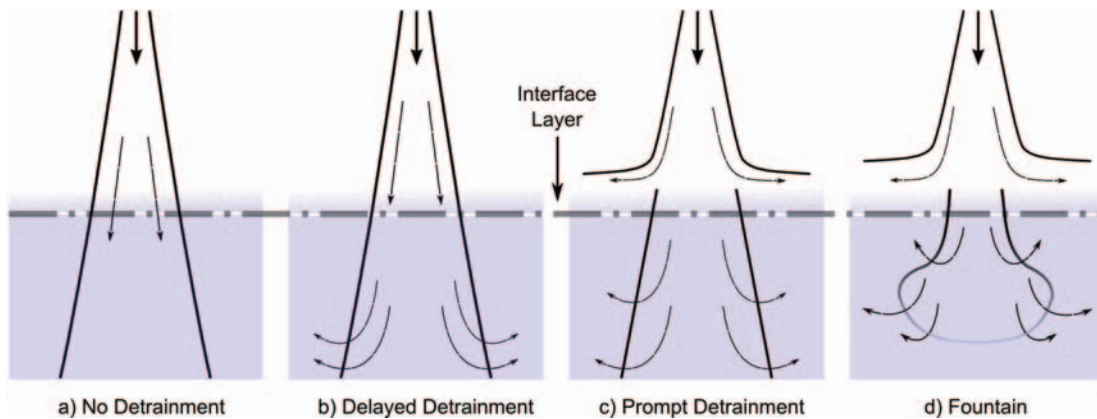


Figure 2.11 - Depiction of the different regimes, adapted from Cotel & Breidenthal (1997)

2.5.2 Effects of Stratification

As already presented in Section 2.3.1 concerning ventilation, stratification can occur when a density gradient exists in an environment where buoyant forces are dominant over inertial forces, characterised by a Richardson number of unity or greater. Work done by Miles (1961) solved the inviscid, incompressible equations describing small perturbations of periodic shear flow, and found that for fluids of those conditions, Richardson numbers as low as 0.25 would result in stable layers. However, as noted by Fernando (1991), in practical situations this stable Richardson number can vary depending on the “boundedness” of the flow.

Interfacial Layer

The most visible and straight-forward scenario of stratification is that of an air-water interface (or equally, any gas-liquid interface); both are fluids, however they have densities of

vastly different magnitudes. When a jet of air is projected at the interface, the air does not travel very far into that interface, resulting in a “dimpling” deformation (Figure 2.10b). As the momentum of the jet supply is increased, the flow of air will become sufficient to penetrate the stratified interface. However, because of the large disparity between densities, the buoyant force of the liquid will not allow the jet of air to enter very far into the liquid before it is turned back on itself (similar to the fountain, Figure 2.11d). As already recorded above, the ratio of jet inertia to the buoyancy strength of the interface is quantified in the Richardson number. Some authors (Iial-Awad 2006, Abib & Jaluria 1995), also specify a *degree of stratification*, although this formulation varies from author to author; for example, from Iial-Awad (2006):

$$DS = \frac{\left(\frac{dT}{dz}\right)_{layer}}{\left(\frac{dT}{dz}\right)_{domain}} = \frac{\left(\frac{d\rho}{dz}\right)_{layer}}{\left(\frac{d\rho}{dz}\right)_{domain}} \quad (2.81)$$

As a ratio of temperature or density gradients across the layer and the domain, the degree of stratification is an expression of the buoyant strength of a layer.

As well as the change in density across a layer, the stratified layer thickness is also a defining characteristic of the strength of a layer. In a completely still, adiabatic and laminar environment, the molecular diffusivity is the physical mechanism for which a layer of two fluid species will be created (Landau & Lifshitz 1987); in non-adiabatic room ventilation scenarios where thermal buoyancy (as opposed to densimetric differences) drives the flow, *thermal* diffusivity is important. As mentioned previously, in salt bath experiments (Linden *et al.* 1990, Hunt *et al.* 2001, Holford & Hunt 2003) the diffusivity of salt in water, being as low as it is, gives rise to very sharp gradients (as well as having the side effect of making flow visualisation very clear). However, this artificially increases the degree of stratification in comparison to a full-scale experiment or simulation.

In practice, fluids are never completely still or adiabatic, and rarely entirely laminar, so the stratified layer will be subject to some degree of shear-induced mixing driven by ambient flow, which makes the determination of stratified layer thickness difficult as it would vary in practice, depending on the surrounding conditions.

In the absence of shear, interfacial mixing is dependent on turbulence generated elsewhere and reaches the surface through turbulent diffusion (Fernando 1991). This kind of shear-free turbulence can also be produced by oscillating grid experiments, for example by Fernando & Long (1985) who studied linearly-stratified fluids; among their findings was that the thickness of a shear-free layer grows proportionally with depth independent of Ri .

More conventional shear-driven turbulence at the interface gives rise to instabilities, such as the Kelvin-Helmholtz instabilities described earlier. At large Ri , however, KH-type instabilities do not occur, and instead internal waves become the prime mechanisms, but only if there is enough energy for them to ‘break’ will there be a large production of turbulence (Smyth & Moum 2001: 2947-2955).

Turbulence Decay

The ability of stratified layers to decay turbulence is well known, and covered in a number of articles, for example Riley & Lelong (2000) and Davidson (2004). Essentially, the stratified layer inhibits the development of vertical length scales, whilst encouraging the growth horizontally across the layer. This results in anisotropic “pancaking” of turbulent eddies, which resemble round, thin disc-like shapes. If a Local Froude number is defined as:

$$Fr_L = \frac{\overline{u'}}{N \cdot l} \quad (2.82)$$

Where $\overline{u'}$ is an RMS turbulence velocity signal, l is a length scale of energy-containing eddies and N is the buoyancy frequency (or Brunt Vaisala frequency) defined as:

$$N = -\sqrt{\frac{g}{\rho} \cdot \frac{d\rho}{dh}} \quad (2.83)$$

Then at Local Froude numbers $Fr_L < 1$, the disc-shape eddies arrange themselves into partially decoupled layers which are able to slide over one another, creating large amounts of shear which promote inter-layer mixing between them, driven by horizontal vorticity which acts to dissipate most of the turbulent energy. Therefore, in strong (stable) stratification, vertical motions are inhibited whilst horizontal motions are enhanced, which also becomes a primary driver in viscous dissipation. Fernando (1991) displayed that such flattening of eddies may be more evident only above $Ri > 15$.

2.5.3 Stratification Breaking

Of importance in this study is the ability of a particular jet to be able to penetrate a given stratified layer separating two (or more) fluids of unequal densities. As already seen, this is largely dependent on the Richardson number, which depends on the interface and the incoming jet. From Cotel (1995) and Cotel & Breidenthal (1997), it can also be seen that the (nondimensionalised) interface distance, H_i / d can also be a factor.

Shy (1995), using LIF methods applied to a series of vertical jets over ranges of $3380 > Re < 23400$, showed that the penetration depth in a two-layer stratification over a range of Ri from 0.2 to 5, were inversely proportional to the initial Ri . Modelling the jet as a series of large scale vortices and accounting for the baroclinic vorticity generation, Shy formulated that the penetration depth was:

$$P_d = \frac{\Delta Z}{L} = C_3 Ri^{-1}, \text{ where } C_3 = 0.72 \quad (2.84)$$

Shy (1995) found that after penetrating the interface, shear at the periphery of the jet creates a semi-mixed layer inside the denser fluid; inside this layer, the jet can detrain, whereby the

relatively-buoyant fluid parcels in the jet have insufficient vertical momentum to continue descending, and so swell outward, away from the jet and then ascend back to a point of neutral buoyancy. This detrainment may also create Kelvin-Helmholtz instabilities which helps to entrain fluid first, into the detrainment region of the jet and then into the original jet core. Shy (1995) identified the mixing transition explained above by Dimotakis (2000) in stratified interfaces, which is driven by the appearance of smaller-scale eddies. Interestingly, the experimental results which led to the formulation of Equation (2.84) show no apparent dependence on Reynolds number, whereas the jet mixing has been shown to have a distinct change at around $Re = 10^4$; Cotel *et al.* (1997) proposed that this transition occurs at around $Ri = Re^{0.25}$.

In comparison to the experiments by Shy (1995), Lin & Linden (2005), whilst studying the entrainment due to a turbulent fountain at $Ri \approx 1$ found that their results for penetration distance coincide, but do not necessarily agree with, the results of Shy (1995); because Lin & Linden studied a fairly narrow range of Richardson numbers, the majority of their results coincided with $P_d = 1$ which was reached by Shy (1995). However, the *trend* of their results suggest a shallower correlation with Richardson number, on the order of $Ri^{-1/4}$. This is speculative however, as there is insufficient range of Richardson numbers to contradict Shy’s formulation (as noted by Lin & Linden 2005) - their results could also be interpreted as a limiting ‘plateau’ whereby $Ri < 1$ follows a more linear relationship with regards to local impingement diameter and penetrative depth in the range examined. Generally, the results incorporate a general entrainment law:

$$E \propto Ri^n \tag{2.85}$$

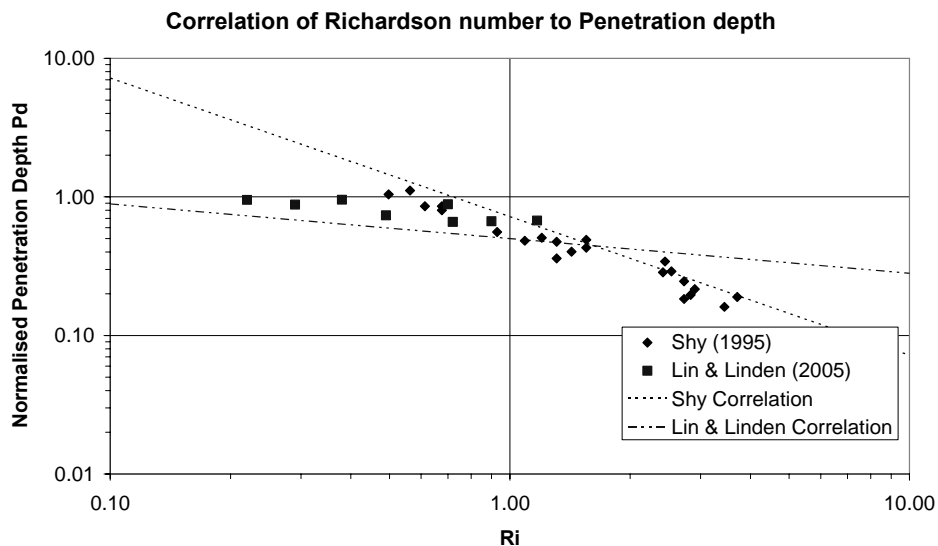


Figure 2.12 - Results of Shy (1995) and Lin & Linden (2005), in combination with different correlations of results

lial-Awad (2006) formulated a different method derived from an energy balance of a jet against the buoyancy potential of the stratified layer, using this perspective to express the critical velocity required to puncture a stratified layer:

$$\Delta\rho gh \cdot (A^* \cdot \sqrt{g' \cdot h}) = \frac{1}{2} \rho u^2 \cdot (u \cdot A_j) \quad (2.86)$$

Here, the effects of the stratified layer are separated to the left side of the equation, and the effects due to the incoming supply jet on the right. The hydrostatic pressure and buoyancy flux of the stratified fluid is balanced by the dynamic pressure and flow rate of the jet. When compared against his results, the critical velocity and critical momentum based on Equation (2.86) had a fair agreement with some of his results, but suffered from a degree of scatter, and his work did not show any particular Reynolds-number dependence. Indeed, based on the results from Shy (1995) and Lin & Linden (2005), the only dependence is on the Richardson number, and even the turbulent mixing transition that occurs around $Re = 10,000$ (Dimotakis 2000) does not factor into the model.

2.5.4 Far-Field and Obstruction Effects

In most experiments, the impingement zone is of prime importance, so the flow field further away is usually not recorded, or only given an approximate analysis. However, when a flow is bounded whilst still having a very large lateral extent, far-field effects which are very far from the jet impingement zone ($> 50x/d$) are still important if homogenisation of the entire contents is the ultimate aim.

In this far-field region, the direct effect of jet impingement may not necessarily affect the flow by a large amount, especially if the impingement zone is blocked by geometry. However, the entrainment of ambient fluid into the jet will give rise to large regions of turbulent, recirculating fluid, which will also shear and mix with surrounding fluid zones as well as interacting with the geometry. This gives rise to a complex flow field, for example Figure 2.13.

In Figure 2.13, the base of the enclosure is divided by a tall partition, so that the stratified region below is divided. The jet impinges and punches through the stratified layer, spreading out radially upon the floor of the enclosure. This will create a large amount of shear and turbulence in the stagnation region as well as between the jet fluid and the lower zone fluid, possibly leading to rapid destruction and entrainment of the stratified layer at Point A.



Figure 2.13 - Shear-induced recirculation flow patterns driven by a jet supply in an obstructed enclosure

At Point B, in the far field which is remote from the jet and separated by the vertical obstruction, shear and entrainment driven directly from the jet momentum is blocked by the obstruction. Because of this, mixing of the stratified layer in Point B is determined by the recirculation of the upper zone fluid instead of through direct impingement of the jet. The upper zone circulation then causes shear on the stratified interface, causing mixing through instabilities covered earlier in Section 2.5.2. Because this then comes down to instability driven by shear (which would also be the case if Point B was some large distance from the jet impingement zone), the analytically derived Miles-Howard theorem (1961) concerning the stability of parallel shear flows when $Ri > 0.25$ serves as a useful demarcation. The effects of far-field mixing therefore assume the physics of shear-driven mixing of fluids, the mechanisms of which have been discussed earlier throughout Section 2.5.1.

2.6 Tanker Ventilation

2.6.1 Introduction

Ventilation, in application to crude oil tankers, is a common issue in that there are many areas of the ship that require ventilation for the continued operation of the ship and safety of its crew; for example, accommodation areas, boiler and engine rooms. The scope of this thesis examines the ventilation of one of the largest enclosures for which ventilation is, at some stage, required - the crude oil tank (COT).

Due to the volatile nature of the cargo carried, and given the elapsed time during a typical journey from the oil rig or FPSO (Floating Production, Storage and Offloading) ship to the oil terminal, an amount of the crude will evaporate. If inspection of the structure inside the tank is required, the removal of these vapours becomes of paramount importance to ensure the safety of the crew and the ship. What makes this particularly difficult is the fact that, depending on the oil carried, crude oil consists of a large number of fractions which, over the course of transport, evaporate into a multitude of different gases with their own properties, many of which are heavier than air; on the other hand, other crudes ('light' crudes) may evaporate into lighter-than-air fractions. In a practical scenario, by the end of the transport voyage, a crude oil tank would be filled with a combination of light and heavy components which would need to be inerted and removed prior to a tank inspection. Once ventilation of one tank is completed, the next tank would probably then be ventilated - depending on the size and design of the tanker, anywhere from 10 to 30 COTs can exist on a typical VLCC.

2.6.2 Tanker Geometry

Typical oil tankers vary greatly in terms of size and gross tonnage. In the 1950s, average oil tanker sizes were below 100,000 dwt; a large proportion of civil petroleum tankers were T2-type tankers originally built during the course of World War II. These cargo vessels were of 24,000 dwt with depths of around 9 metres. Over the following forty years, tanker sizes increased greatly, culminating in the 564,000 dwt *Seawise Giant* (ex- *Jahre Viking*, classified as a "ULCC") (Intertanko 2001:6), containing some 46 COTs of up to almost 30m deep, and the French *Batillus*-class ships at 555,000dwt. Although these outsized vessels represent the extreme end of the tonnage range, the large majority of modern crude carriers, by tonnage, are of the VLCC¹ range of

¹ The actual demarcation between the different ship classes varies across different sources; INTERTANKO define VLCCs as being above 200,000 dwt, whereas other sources range from 170,000 to 250,000. Part of this variation may be due to the association of VLCC with the Malaccamax nomenclature, which defines the maximum vessel size which can navigate the Strait of Malacca.

160,000 to 320,000 dwt (LRS 2003). Large numbers of smaller tankers exist, for example in the Aframax and Suezmax sizes (80,000 to 160,000 dwt)

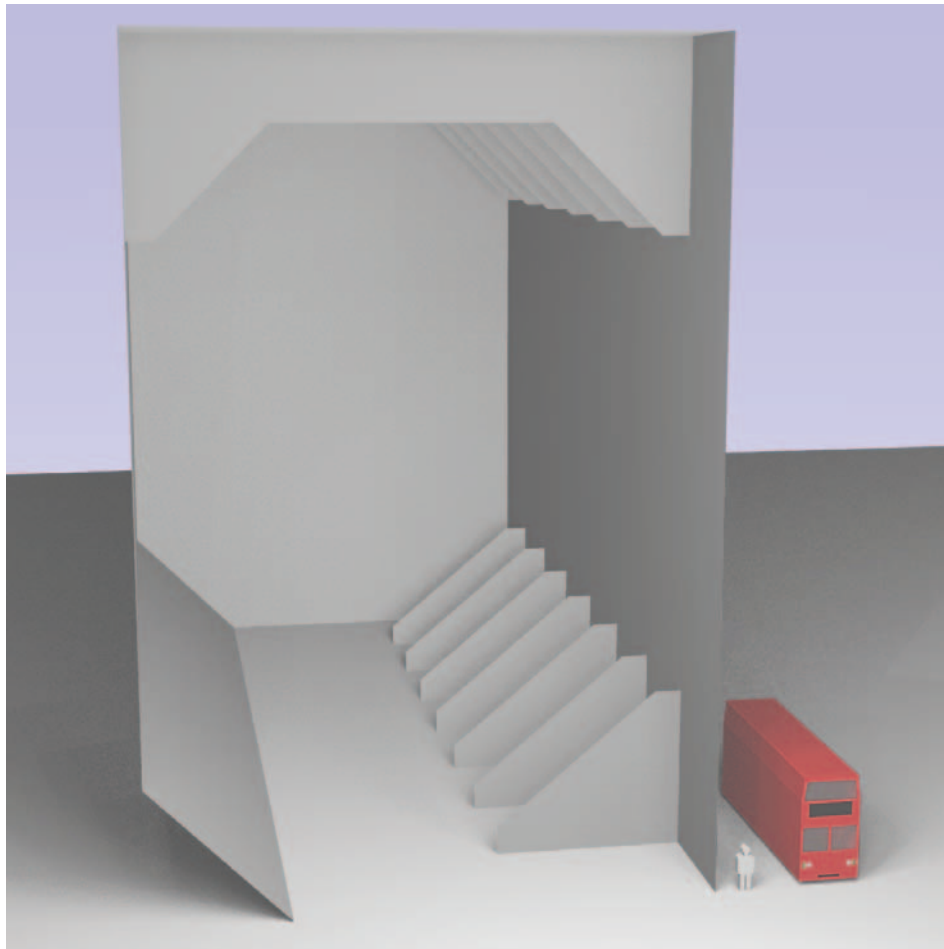


Figure 2.14 - Size comparison between typical COT (30m high), a typical human (1.8m high) and a typical double-decker bus (~4m)

Up until the 1980's, almost all newly-built oil tankers were *single-hulled*, whereby the structural walls of the COT were also the external hull of the ship itself, so only a single wall separated the oil from the water. New legislation ruled that by 2025, all crude oil tankers must be of *double hulled* construction (IMO 1998, IMO 2006), in response to a number of tanker casualties and subsequent oil spillages. The concept of a double hulled construction was that in the event of grounding or hull loss due to damage (for example in a collision), only the outer hull would sustain damage, leaving the cargo-carrying inner-hull intact, preventing oil spillage.

Figure 2.15 - View of the oil tanker AbQaiq. (Picture Credit - Photographer's Mate 1st Class Kevin H. Tierney, United States Navy)

This legislative change has a number of significant repercussions on the internal tank geometry. In the older single-hulled tankers, structural rigidity is maintained with a large amount of internal structure on the interior of the tank. Some of this structure included web frames up to 5m tall, pitched every 5m to 10m (typically) running along both the floor and the ceiling, and a series of longitudinal strengtheners running fore-aft.

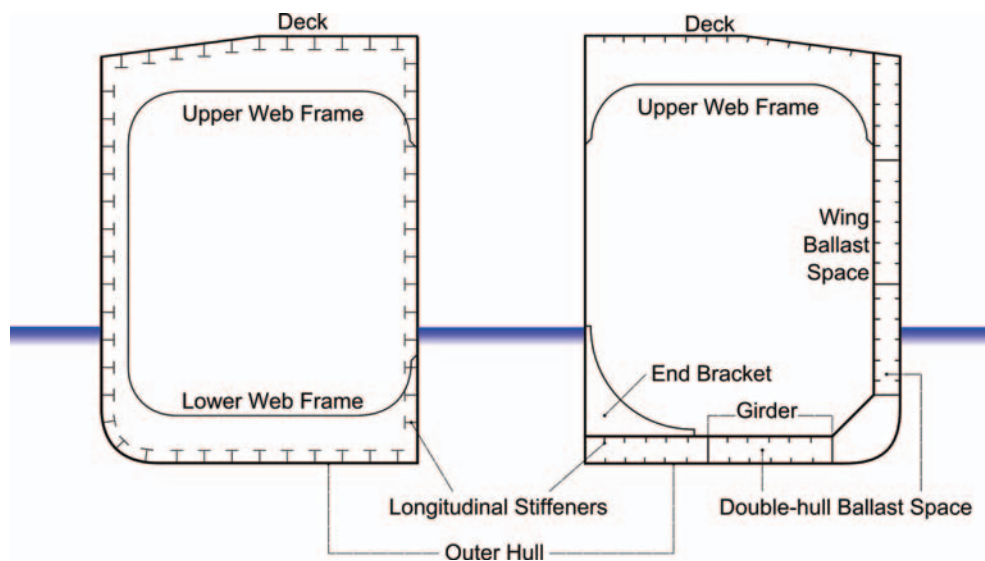


Figure 2.16 - Comparison of single-hull (left) and double-hull (right) internal structural details

The addition of space between the hulls on modern double-hulled tankers has allowed the movement of structure that was previously inside the tank to the void-space between the external wall and the inner wall. This results in a tank that is much “cleaner” – there is less wetted area inside the tank, and much less structure (Tanker Structure Co-operative Forum 1995) (TSCF). The void space also creates an insulation layer, similar to void cavities in buildings, leading to lower heat losses than with previous tanker designs. This retention of heat is referred to as a “Thermos bottle” effect in some literature (Intertanko 2002, OCIMF 1997), and to reflect the higher thermal

insulation, though it has far-reaching consequences concerning structural integrity, corrosion and fatigue.

2.6.3 Current Methods

The process of making a COT 'gas free' is part of a series of procedures which contribute to the overall ventilation of a tank, and is usually preceded by an inert gas cycle whereby the COT is filled with either an inert gas or flue gas from engine exhaust. This is done to remove the oxidising agent to prevent any possibility of an explosion. Sometimes, a crude-oil wash or water wash cycle is performed to remove solid emulsifications of crude oil that can build on the tank structure up over time. Before gas freeing begins, the COT is also *purged* - the inert gas generators are used to pump the COT continually with inert/flue gas, and the exhaust is measured until VOC concentrations are below 2% by volume. Therefore, the contents inside the tank prior to the gas-freeing operations consists of a mixture of volatile organic compounds (VOCs) and inert gases with a low (<8%) oxygen content. In an ideal case, this mixture would be uniform, but if a period of time has passed between the end of the inerting/tank washing cycle and the gas-freeing cycle, the contents may stratify. Depending on the orientation and location of the inert gas supply, a particular level of mixing may occur, and it is possible that during the purging stage, only the lighter oil fractions may be exhausted due to their buoyancy, leaving stratified layers of heavier compounds in the tank. It is from this state that gas-freeing begins.

The current gas freeing procedure consists of injecting air at from the atmosphere into the tank using a fixed or portable fan mounted at deck level, which is usually some 20-30m above the floor level of the tank. The high-velocity air jet created by the fan is designed to be projected far down to the base of the tank, where it will entrain any gas mixtures along the way and maintains enough momentum to break up any stratified layers that may occur inside. Vents opened at deck level allow the gas/air mixture to escape, though the number and distribution of opened vents depends upon the exit velocity reaching a certain velocity as per SOLAS (IMO 2004). This is so that exhausted vapours are projected far enough from the deck that they can disperse, and do not form explosive mixtures of gases near the ship.

Internal geometry of the tank can be complex, for example if there is protruding internal reinforcing structure; this was particularly the case for older, single-hulled tankers whose single hull required a large amount of internal framing to maintain structural rigidity against bending and buckling. In cases like this, frames 2m tall and higher dominate a large amount of the floor and ceiling areas; longitudinals (smaller structural members with a 'T' cross-section, similar to stringers found in aircraft fuselages) also ran along the tank for additional buckling resistance. Though necessary for hull strength, these features cause problems during the gas freeing operation as the internal frames restrict the spreading of the jet and partition the flow-field (Chow *et al.*

2005). As previously mentioned, some double-hulled tankers offload a large proportion of this internal structure to the void space between the two hulls, making jet ventilation easier.

The difficulties in gas freeing the entire volume using a fan in a fixed position throughout the process is known intuitively, so a number of methods are used in practice should VOC vapours be located in an area far from the proximity of the jet impingement zone. For situations such as this, flexible ducting can be attached to the fan and lowered into the deck so that the air jet can be directed at different locations inside the tank to provide a more localised momentum source. The ducting itself is usually constructed from a tough, coarse-fibre fabric with internal reinforcing rings, and is designed to be collapsible for easy storage. Because of this construction, the interior diameter is somewhat less than the standard supply diameter, and its flexible nature results in an interior profile that is undulating, not smooth. Some ducting designs are based on a series of interlocking rings, in which case the ducting does not form a solid duct, so it is possible for air to escape through gaps between interlocking rings if the pressure is high enough. Generally, ducting creates an additional problem, as the large majority of deck fans are of the axial type which are unable to deliver a large pressure head. The pressure drop through the ducting can greatly reduce the throughput of the fan, requiring the fans to be run for longer to deliver the same air volume that an unimpeded fan would be able to deliver.

2.6.4 Existing Legislation and its Implications

The quality that a tank has to be ventilated to depends on the work that will be done after ventilation is complete. The International Safety Guide to Tankers and Terminals (OCIMF, *et al.* 1996) defines a number of conditions:

- Gas freeing for the reception of cargo should be ventilated until testing confirms that the hydrocarbon gas concentration throughout the tank does not exceed 40% of the lower flammability limit (LFL).
- Gas freeing for entry into the tank and cold work without breathing apparatus requires hydrocarbon content to be less than 1% of the LFL and additional tests to monitor oxygen content and other toxic gases are to be conducted as appropriate.

Of interest is the lack of an air change condition. Almost all enclosed areas onboard a ship are given an air change, or air change per hour condition with regards to ventilation, however this is not so in crude oil tanks, and even a guideline minimum number of air changes is not given.

Another consideration is with regards to air sampling within the tank. A marine chemist is required to experimentally monitor the air inside the tank before it can be certified gas free (IMO 2004, OCIMF *et al.* 1996, Savage 1976). However, despite the best efforts of the crew, it is possible for localised pockets of gas to exist within the tank which elude detection as thorough methods of visualising the conditions inside the entire tank at this time are impossible. Given the nature of the

operation, it is in every ship operator's interest to maintain the highest level of safety during the gas freeing operation. However, if a crew is pressured by tight deadlines, it is possible for a tank to remain unsafe despite the efforts of the marine chemist; incidents such as with the Han Seng (Devanney 2006) and the Bow Mariner (USCG 2005) are a constant reminder that unsafe operations can result in fatalities.

2.6.5 Physics of Tank Ventilation

The same physical mechanisms governing fluid flow and energy also govern tank ventilation, in increasing degrees of complexity and significance depending on the number assumptions made, for example neglecting radiant effects, heat transfer, etc. The recent change in construction philosophy (IMO 2006) which dictated that modern tanker constructions must be of double hull, instead of single hull, changes the significance that particular physical effects have on the contents of the tank. The increased insulation has been reported to result in temperature differentials of 15°C between the inside of the tank and the sea (OCIMF 1997). These higher temperatures differentials may promote stratification, especially if there is a corresponding increase in the vertical temperature gradient in the COT itself.

Ventilating a Single Fluid

If a typical closed crude oil tank is assumed to be filled with air, then the evolution of the initial flow-field would be determined by thermal conditions. In hot conditions, the deck would act as a heat source (due to solar absorption), which would then be transferred to the contents of the tank. In adiabatic conditions, the tank may, in the limit of time, become homogenised with respect to temperature. In reality, heat loss through the sides of the tank will reinforce stratification, since air at the bottom of the tank will tend towards the temperature of the sea, and the air near the deck will rise to the temperature of the deck itself. However, radiative effects act to homogenise the temperature field by transferral of thermal energy from the warmer zones to the colder ones.

When a jet is supplied to the tank, the air inside will be mixed by shear, subject to the same principles as examined in Section 2.3.3, only on a much larger scale. In the upper regions of the tank, the outer shear layers of the jet will entrain air, and also give rise to recirculation elsewhere in the tank. The impingement region will create a large amount of turbulence and mixing, and the supplied fluid will then intrude sideways along the floor of the tank. If there is a strong buoyancy difference between the supplied air and the stagnant air at the base of the tank, the sideways intrusion of air will be subject to these buoyancy forces. Because the supplied air is likely to be colder, it will initially be a negatively buoyant jet. However, if it entrains enough ambient (warm) air as it is projected downwards, and/or the lower zone of the tank is relatively colder, the air that impinges on the floor of the tank may in fact be relatively buoyant, and may be subject to a

“fountain” effect (Figure 2.11) depending on the buoyancy difference. Since the only density difference will be driven by thermal effects, it is likely to be on the order of 0.1 kg/m^3 .

Like any other ventilation case, the geometry is very important to the evolution of the flow field during the gas-freeing process, particularly with respect to blockage, and propagation of shear flows and turbulence to the far field. Typically of modern double-hulled tankers, though the floor of the tank does contain a number of frames, they are only partial length, so that the entire floor of the tank is accessible. The ceiling of the tank, however, is usually dominated by full-length frames as the deck is not double hulled, and so requires more structure to increase buckling resistance (TSCF 1995). This divides the ceiling section into a series of cavities through which flow cannot easily propagate longitudinally, making ventilation of these areas difficult if the deck temperature is high (resulting in these regions containing buoyant air).

Ventilation Involving Multiple Fluids

For a tanker that has been offloaded, the remaining fluid inside the COT is a complicated mix of many different gas species. The air will have been inerted, so the composition (and properties) of the air will be vastly different; regulations stipulate that the oxygen content must be below 8% (IMO 1990) and usually this is replaced with either nitrogen (N_2) or carbon-dioxide, which is a strong absorber of thermal radiation (Modest 2003). The composition of the VOC gas inside the tank is subject to a large number of possibilities, simply because each of the hundreds of different types of crude oil, which may be heavy or light (regarding density and viscosity), sweet or sour (regarding sulphur levels), or have different evaporative properties. Heavy crudes consist of longer-chain hydrocarbons, and usually have higher densities (lower API) and are more viscous. Because of this, they generally are not volatile to the extent that lighter crudes are, though it is possible that they may emit small amounts of heavier VOCs. Crude oil assays performed by petroleum industries to ascertain the properties of the crude do show how much of the crude evaporates, but not the composition of the vapours. As well as this, the purging operation that occurs before the gas freeing begins removes a large amount of VOC vapour (until VOCs comprise 2% of the exhaust by volume IMO (2004)), but the composition that remains inside the tank is unknown - it is also possible that the purging operation only removes the lighter vapours, whilst the heavier ones descend to the bottom of the tank and form a stratified layer - this is dependent on the IGS system fitted, its location and orientation, and also the *method* in which it is used; inert gas purging can be used in a number of dilution (mixing) and/or displacement modes, depending on their layout on the ship.

When a high-velocity jet is supplied, the resulting flow field depends largely on the contents of the tank, published data of which are difficult to find, especially after the conclusion of the purging procedure. If, after the purging operation, the fluid inside is homogeneously mixed, (i.e. assuming that the inert gas fans are capable of total homogenisation) then it is likely that gas

freeing will continue to maintain fluid homogeneity and concentration levels in the exhaust would vary logarithmically with respect to ventilation time, as gas-freeing fans are usually capable of similar flow rates. However, it is also possible that upon completion of the purging operation, the tank still contains oil vapour - the operation is assumed complete when the exhaust gas contains less than 2% of VOC by volume. If the lighter vapours are entrained and exhausted whilst the heavier fractions stratify, the behaviour from the point of view of the *exhaust*-gas monitor would be indicative of a purged atmosphere, but the heavier gases will still reside inside the tank, which will cause a problem if the gas-freeing fan cannot deliver sufficient momentum to entrain these fluids.

The primary method of gas freeing is through dilution, or mixing ventilation. As reviewed previously in Section 2.3.3, mixing requires fluid to be entrained through interfacial surfaces, where increasingly small scale dynamics mix the fluid(s) at molecular levels. By creating large amounts of shear flow, the fluid can be mixed faster. If a stratified fluid rests at the base of the tank, and the supplied jet does not have enough momentum to break through the layer, it will impinge upon it and spread out sideways (See Figure 2.10, and Section 2.5). Although the resulting shear flow will be able to erode and slowly mix the stratified layer, the heavier entrained fluid may lack sufficient vertical momentum to be able to be exhausted. In this case, the jet air supply will thicken the stratified layer, and rely on other shear-driven recirculation flows above the layer to provide additional momentum and entrainment to exhaust the VOC gases.

If the jet *does* have sufficient momentum to penetrate the layer and impinge on the surface of the tank, the intense generation of shear and supply of fresh air *inside* the VOC layer will create larger interfacial regions through which fluid can be entrained. Additionally, because the entrained fluid would still likely have a lower density than the stratified layer, it would gain vertical momentum from the buoyancy difference, making exhaustion easier.

Existing research into gas-freeing is quite limited and little modern literature exists on the subject. Savage (1976) presented an overview of the process of gas freeing and tank cleaning, although the procedures have changed since then with the mandatory introduction of inert gas generators. Probably the most representative study (albeit concerning ballast space J-tanks) is one performed by the American Bureau of Shipping (2004), whereby the results from a single transient simulation is presented, concerning sequential inerting, and then re-oxygenating of the ballast space. The volume examined was 14,000m³, and heavily obstructed by structure to the extent that the ballast space was effectively partitioned into a large number of smaller spaces ventilated by a number of smaller openings. The process is shown diagrammatically, and the entire tank shown to have been fully inerted and then subsequently re-oxygenated with only two air changes, despite the high level of structural obstruction.

Qualitative numerical studies were undertaken by Chow et al. (2005), examining the flow-field generated inside a number of different geometries with varying levels of structural obstacles.

Those examined included a small product tanker with corrugated walls (as opposed to structural frames) and a larger tank of single-hulled design, which exhibited large zones of stagnant air due to structural blocking. A comparison was also performed by adding web frames at floor level to a tank which previously had none; it was found that the floor frames significantly impeded the extent of radial spread of air in the impingement zone.

The thermal conditions inside a modern double-hulled cargo tank are well known qualitatively from anecdotal evidence from ship operators, but more quantitative information is seldom available. The most thorough investigation was performed by Saunders (1965), who experimentally examined the heat losses on a single-hulled wing tank on a pair of tankers around 20,000 dwt in order to determine the amount of heating a cargo would require. Although the instantaneous average heat transfer coefficients across any surface varied greatly depending on inclement weather and sea states, the most severe (i.e. highest loss) conditions were given as $8.5\text{W/m}^2\text{K}$ from the deck and bottom, and $18.7\text{W/m}^2\text{K}$ from the tank sides. Double-hulled tankers have an additional void space which greatly insulates the cargo tank, and introducing complexity into the mechanisms of heat loss - temperature gradients between the outer and inner hull may drive convective currents inside the ballast tank, but the convection occurs inside confined spaces dictated by the arrangement of structure. As reported earlier, evidence from tanker operators suggest that during ballast voyages, internal temperatures can be as much as 15 degrees higher than the external sea temperature. It is possible for gradients to be even higher - as this was *during* a voyage, there would have been some additional convective transfer from the ship's motion.

The levels of gas concentration inside the cargo hold depend greatly on the type of crude, the temperature and pressure in which they are kept. Higher temperatures and lower pressures allow crudes to undergo more evaporation than would otherwise be the case in ambient conditions. Work performed by Logan & Drinkwater (1961) presented some of the earliest studies into tank gas composition and gas freeing methods in the late 50s when tonnages were still low, and before inert gas generators were widespread. Concentrations of gases in ullage spaces were found to be saturated with hydrocarbons to the extent that the mixture was many times higher than the upper flammability limits (LFL), so the air-gas mixture was far too rich for ignition to occur. Although it is difficult to compare amounts because of the different procedures now in place, the most common liberated gases were propane and butane; some lighter crudes (Kuwait blends) also had large amounts of ethane, whereas slightly heavier crudes (Arabian blend) had a higher concentration of pentanes.

A number of studies have examined the evaporative behaviour of crudes, for example, Fingas (Fingas 1994, Fingas 1997), found that oil evaporation isn't strictly boundary-layer regulated (evaporation rate dependence on level of saturation of the boundary layer) and that the

rate of evaporation for oils is logarithmic in time (compared to water, which is linear). Husain *et al.* (2003) examined crude oil gas emission under negative pressures with a view to forming a technique to limit hydrocarbon emissions of crudes in-transit, and presented gas emissions of different density crudes by component. Finally, Oldervik *et al.* (2000) presented gas compositions during tanker loading operations as part of the VOCON (VOC Emission Control Systems for Shuttle Tankers and Floating Storage Systems) project.

Although the emission from oil after a journey will vary, the majority of evaporated components are of smaller hydrocarbon chains due to their lower boiling temperatures; principally, Heptane (C₇) and smaller hydrocarbons are the most common. Partly because of this, crude oil assays performed by the petroleum industry to determine chemical composition are of limited value since hydrocarbon chains are listed in ranges (due in part to the sheer number of chains, which number in the hundreds).

3.0 Model Design Methodology

3.1	Chapter Overview	68
3.2	Discretisation Scheme	68
3.3	Numerical Models	69
	3.3.1 Turbulence Modelling.....	69
	3.3.2 Radiation Model.....	70
3.4	Meshing	71
3.5	Boundary Conditions	72
	3.5.1 Radiative Boundary Conditions.....	72
3.6	Solution methodology and Convergence	73

3.1 Chapter Overview

As this work uses predictive numerical simulation in order to obtain results, the numerical methods used and the models involved are of paramount importance to obtaining a valid solution.

This chapter describes the common modelling configurations used in the simulations described later in the thesis, providing justification for the choice of discretisation scheme, turbulence and radiation model selection. Applicable boundary conditions, meshing requirements and convergence criteria are also examined.

3.2 Discretisation Scheme

As covered in Section 2.2.3, a number of discretisation schemes are available - first and second order upwinding, a power-law scheme, QUICK (Leonard *et al.* 1978) and MUSCL (van Leer 1978) schemes.

First order upwinding schemes tend to be extremely stable in low Mach systems and this presents convergence advantages in marginally stable solutions. Due in part to the numerical diffusion that occurs when flow is not orthogonal to the flow lines (Patankar 1980), accuracy is traded for stability. Upwinding can, however, be used as a stepping stone towards a final solution if instabilities occur early in the simulation, whereby its numerical stability is used to create a better initial flow field before higher order methods are used to raise the level of accuracy. The power-law scheme results in less numerical diffusion, but is still only first order accurate.

The MUSCL scheme of van Leer (1978) and the QUICK scheme of Leonard *et al.* (1978), have been used for mass momentum and energy equations. The MUSCL scheme is based on a combination of central and second-order differencing, whilst QUICK is based on weighted averages of second order upwind or central differencing. However, unlike the MUSCL scheme, the QUICK scheme implementation is unable to function at the interfaces of unstructured grids, in which case it defaults to second-order upwinding.

The MUSCL scheme is used for the majority of simulations where there are large gradients, or when the gradients present are important (e.g. densimetric stratification) because the higher-order scheme ‘sharpens’ such gradients. While the QUICK scheme is only second order accurate, it requires less CPU power, and so can be used as a ‘precursor’ scheme to allow faster initial convergence (in the same way as using first-order upwinding to ‘prime’ the flow-field).

3.3 Numerical Models

3.3.1 Turbulence Modelling

A number of turbulence modelling methods were used in early test case work, including LES, in order to examine their predictive accuracy and to form methodological procedures for their implementation. LES is particularly attractive, due to its more realistic representation of larger length-scale flow characteristics and turbulent eddies by direct numerical representation. However, due to the sheer physical domain size and range of anticipated Reynolds numbers in the gas-freeing scenario (ranging from 1×10^7 at the nozzle exit down to below 10,000 in some areas remote from the jet), the LES method would require excessive amounts of computational storage, power and runtime; turbulence, and thus LES are inherently time-dependant. For this reason, models of the K-Epsilon type were used. Due to the number of K-Epsilon variations that exist, further explanation of the models under consideration is given.

Although the baseline K-Epsilon model of Launder and Spalding (termed the Standard K-Epsilon model, or SKE) has been modified over the years (extensions to the near-wall region and to compressible flows, for example), a number of well-known problems still exist;

- The usage of effective viscosity μ_t (a scalar) to impart the effects of Reynolds stresses $\overline{u_i' u_j'}$ (a tensor) limits the model to linear stress-strain relationships (poor prediction in non-equilibrium, separated or strongly-buoyant flows).
- The prediction of turbulence production can be vastly over-estimated in stagnation regions; explanations have been given by a number of authors - anomalous normal stress differences predicted by the eddy viscosity equation (Laurence 2002); abnormal growth of the turbulent time scale k / ε (Durbin 1995).
- There is an insensitivity to anisotropy and disorientation of normal strains from Reynolds stresses - in turbulent shear flow, normal strain rates are zero, but Reynolds-stresses are unequal (Pope 2000) - this leads to an inability to predict stress-driven secondary flows. Again, this is a result of the linear stress-strain relationship brought about by the eddy-viscosity model.

The RNG model of Yakhot and Orszag (Yakhot & Orszag 1986b) introduced a mathematically rigorous alternative derivation of the mean flow equations, resulting in different coefficients. The commonly used form implemented in most CFD software involves major changes to the dissipation Equation (2.51) in Section 2.2.7. The natural extension to low-Reynolds numbers has provided a useful tool for industrial simulations without requiring additional wall damping

terms as the low-Reynolds RNG model implementation can be used right to the near-wall region without requiring a separate wall law.

However, literature (Laurence 2002, Pope 2000, Haroutunian 1995) has shown that the *ad-hoc* R_ε term (Equation (2.56)), which was not part of the original RNG derivation of Yakhot & Orszag (1986b), is the primary driver that affects the predictions (Haroutunian 1995); Unfortunately, because of the dependence on strain rate *magnitude*, it does not differentiate between flow expansion and contraction (or acceleration and deceleration) (Hanjalic 2004), such that some flow simulations can be aided by the extra term, whilst others can be hindered. Flows subject to expansion benefit from the increased dissipation, whilst in an equivalent compressive flow, the R_ε term would bring the same result - the correction always acts to decrease k (Hanjalic 2004).

The final model examined is a more recent model by Shih *et al.* (1994), which derives the ε transport equation based on the mean-squared fluctuating vorticities. Unlike the SKE or RNG models, the production of TKE is not involved in the dissipation equation.

The main difference involved with the Realizable K-E model is a modified eddy-viscosity equation, which has been reformulated to account for a number of known shortcomings with the original K-Epsilon viscosity model:

- C_μ naturally varies depending on the flow; for example in boundary layer flow, C_μ takes the standard value of 0.09, whilst in homogeneous shear flow, is closer to 0.05;
- In regions of large mean strain rate (e.g. $Sk/\varepsilon > 3.7$), it is possible for realizability constraints to be violated, and may also violate the Schwarz inequality;
- The plane jet/round jet anomaly.

In academic flows such as round and planar jets and shear flows, the model has been shown to behave more correctly than the standard K-Epsilon model, as well as accounting for compressive/expansive shear, which the RNG model fails to account for (Shih 1994, Haroutunian 1995).

All models will be compared in a typical room ventilation case (Section 4.0) in order to determine which model is likely to perform better.

3.3.2 Radiation Model

The discrete ordinates method with extensions to unstructured grids by Raithby (1999) has been used in this work to account for thermal radiation. The DO method is capable of modelling all optical thicknesses, whereas limited solutions such as the Rosseland and P-1 models are only useful in optical thicknesses above 3, as their low-order approximations are only accurate in media with near-isotropic radiative intensity.

Although it is possible to use direct surface-to-surface radiation transfer models to calculate radiant exchange, this becomes increasingly complicated with geometry, and also cannot take into account absorption and emission by the medium which, in large spaces or spaces containing highly absorbent gases, may not be appropriate. Although this represents a smaller assumption in room ventilation, it is not appropriate when simulating much larger enclosures.

Unlike other models, the DO method can account for non-grey radiation across a number of different wavelength bands, and can account for multiple participating media with different properties, making it particularly useful in the tanker ventilation study. The implementation used is also far more amenable to parallel processing than other models, even though the model itself is more complex. It is also subject to some shortcomings that are reminiscent of low-order issues with finite volume methods; the DO method is subject to *false scattering*, where in low spatial discretisation resolution, a collimated beam will gradually lose quality, i.e. its fineness will reduce and its projected area will increase as it travels, leading to the irradiation of collateral media and geometry. Another issue concerns the case of low angular discretisation, and can be summarised as thus: if a group of beams are projected far away from a source of high emissive power, they will spread out to such an extent that geometry straddling the beams that would normally be irradiated falls *between* the beams - this is referred to as the *ray effect*, and can be reduced by increasing angular discretisation (Modest 2003).

3.4 Meshing

Due to the selection of K-Epsilon models, the level of spatial discretisation required is not coupled to any specific eddy size, so in terms of the macro-scale flow-field, appropriate levels of meshing are to be determined through the use of mesh sensitivity testing. For flows sensitive to boundary-layer effects, use of the log-law for wall regions dictates that y^+ values be kept in the range of $30 < y^+ < 300$.

Although the lack of eddy size coupling (compared to LES or DNS) suggests that the K-Epsilon model is able to compute turbulence effects irrespective of mesh size, another issue must also be accounted for by the mesh - that of numerical behaviour. Although a particular mesh density may be capable of resolving turbulence behaviour, numerical artefacts can be introduced if the mesh is of poor quality.

As such, sensitivity testing is required in order to examine the combination of turbulence model, mesh density and thus resolved scales, and their effects on numerical prediction and numerical stability. Although the turbulence model can work for a wide range of mesh densities, the results may not necessarily vary consistently with the mesh; for example, it is possible to have four different mesh densities whereby a single particular mesh configuration yields results that are significantly different to the others; usually, this is the result of the mesh only *partially* resolving an eddy scale that is *not* resolved in a lower-density mesh (and correctly accounted for by the

turbulence model) but *fully resolved* in the next higher-density mesh. As this interaction between the resolved scales and their numerical effects and the effects of the predicted flow field on y^+ values are difficult to determine *a priori*, mesh testing is required.

3.5 Boundary Conditions

As with any numerical solution, the results are dependent on the initial conditions, and thus it is important that boundary conditions are as accurate as possible, and are prescribed in an accurate way.

Boundary conditions can be defined using two main ways - as constants (Dirichlet-type), or as gradients (Neumann-type). The majority of boundaries are defined by constant conditions - inlet velocities, temperatures and turbulence conditions, and most instances, this supplies enough boundary information for a correct flow prediction. However, when considering temperature boundary conditions, it is important that the correct wall temperature is defined. If the external wall temperature of an enclosure is prescribed to a flow simulation inside, the inner wall temperature will differ depending on the wall conductivity and the internal flow conditions. If the conductivity is not given, or the wall has a strongly anisotropic conductivity when only a constant conductivity given, the resulting flow prediction may be badly affected, especially if thermal effects are dominant.

3.5.1 Radiative Boundary Conditions

Due to the complexity of radiative emission (directionality, frequency dependence, influence of surface conditions, and in the case of participating media, the influence of gas composition), exact realistic quantities for material absorption and emission that are directly appropriate to the current situation are non-existent, and the approximate nature of radiation from participating media is acknowledged (Modest 2003). It is far more common for researchers to assume an approximate whole-field value for the absorptivity/emissivity if only a single participating fluid is present, e.g. Howell & Potts (2002) (0.1m^{-1}), Kondo *et al.* (2000) (0.1-0.27 depending on case).

For surface materials, a number monographs (Hottel & Sarofim 1967, Bejan & Kraus 2003, Modest 2003), contain tables for total emissivities and have been used based on the nearest appropriate material type. Due to the dependence of radiative transfer on surface roughness (especially in metallic absorbers/emitters), emissivities should also be considered approximate in lieu of measured quantities.

3.6 Solution methodology and Convergence

In general, the solution methodology varies depending on the behaviour of the mesh and physics being studied. Common to all simulations are mild initial relaxation as the initial flow-field develops, after which relaxation is reduced to allow faster convergence.

Two solution methods have been used - an implicit time-marching method, and an explicit 'segregated' solver. The exact solver used depends on the physics the simulation encounters. For example, in (natural) ventilation cases when fluid buoyancy dominates convective forces (i.e. at high Richardson numbers), the strong coupling of body forces leads to faster solution through the use of implicit, time-marching solution methods (Ferziger & Peric 2002). In this case, heavier under-relaxation is applied by reducing the time-step Courant number. During the simulation, the Courant number begins at a low value around unity, and then subsequently increased as the simulation progresses in order to accelerate convergence. With the segregated solver, mild to heavy under-relaxation is used in the beginning (depending on initial stability) and then increased as the simulation progresses.

The convergence metrics for a 'normal' simulation with strong convection terms are not applicable to simulations involving large Richardson numbers. The most usual method of measuring convergence is through the reduction of scaled variable residuals. However, in ventilation, thermal effects (and their propagation) are based on the energy equation, and have long propagation times due to low conductivities and/or diffusivities. Therefore, whilst the convective variables will converge to 1×10^{-3} and energy to 1×10^{-6} , it is common for the temperature and density fields to still be in an unsteady state. Because almost all cases are expected to involve some form of temperature or densimetric calculation, temperature (or density) results are monitored at particular heights in the flowfield, and a converged simulation is judged to occur when the temperature varies less than 0.5K/500 iterations.

4.0 Validation of Numerical Method with Room Ventilation Study

4.1	Introduction	75
4.1.1	The Chamber	75
4.2	Model Design and Boundary Conditions	76
4.3	Results	79
4.3.1	Mesh Sensitivity	79
4.3.2	Comparison of Engineering Assumptions	81
4.3.3	Effect of Turbulence Models	84
4.3.4	Effect of Medium Absorptivity	87
4.3.5	Disparity between Simulated and Experimental Results	88
4.4	Summary and Conclusions	89

4.1 Introduction

This chapter examines a room-ventilation case study which is used to test the numerical and modelling methodology proposed in the previous chapter. The effects of different heat transfer idealisations on the resulting predicted vertical temperature profile is examined, as well as the strength of thermal radiation in small enclosures and low temperature differences.

The original study was comprised of a series of experiments involving ventilation flows conducted by Iial-Awad (2006), who performed experiments concerning the thermal stratification of the chamber. In particular, he studied mechanisms influencing the interface height of the stratified layer given a specific momentum and thermal flux and exhaust vent height, and what parameters control the breaking of the stratified layer. The chamber was specifically configured to create a stable stratified layer using both a hot and a cold momentum source to reinforce buoyancy. Instantaneous temperatures were periodically measured after a set period of time elapsed (~2 hours) to allow a steady state to occur. Temperatures were measured in the centre of the room using a thermocouple stand with 18 probes, and smoke injection was occasionally used for visualisation of the extent of the thermal stratification.

4.1.1 The Chamber

The University of Hertfordshire's environmental chamber is a 7.5m x 5.6m x 3.0m thermally insulated room that allows accurate control and monitoring of internal thermal conditions. The chamber itself was constructed on an insulated floor laid with a 100mm layer of concrete, below which an additional 100mm of polystyrene foam was laid. The walls of the chamber were comprised of a 125mm thick polyurethane foam wall with a white polyester finish with a similar construction for the ceiling of the chamber.

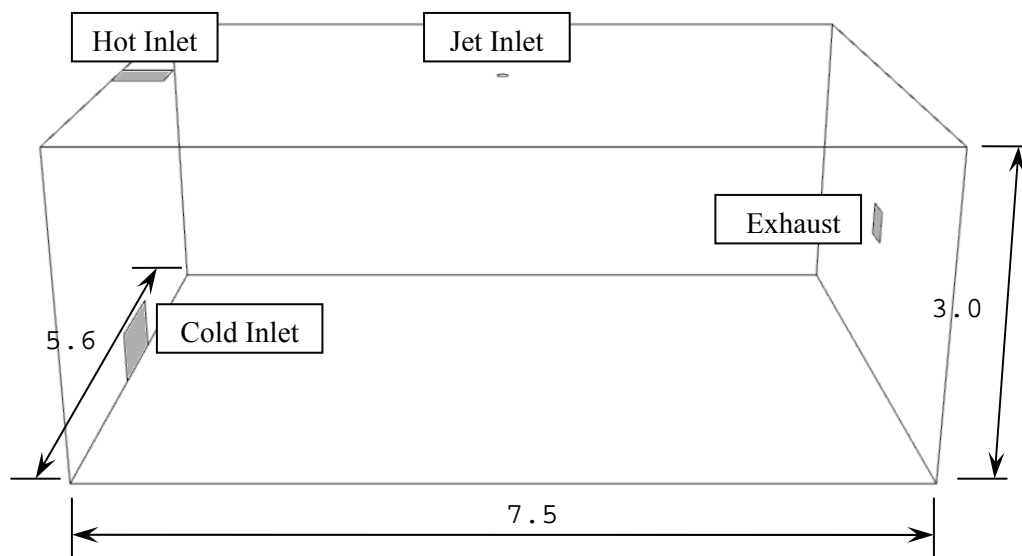


Figure 4.1 - Schematic of environmental chamber domain and sizing (dimensions in metres)

There were four momentum sources in the experimental configuration – a cold supply (1m x 0.5m vent area) at floor level on it's side; a hot supply (0.5m x 0.5m area) mounted at ceiling level blowing vertically downwards into the chamber; an exhaust vent (0.1m² area, square) mounted in the centre of the far wall, centred on a vertical position 1.5m from the floor, and a circular jet inlet into the chamber mounted centrally in the ceiling, blowing down, 0.11m diameter (Figure 4.1).

All of the air supply and exhaust vents were fitted with grilles in order to provide isotropic turbulent conditions, and are aligned along a central plane dividing the room in half.

4.2 Model Design and Boundary Conditions

The geometry of the room and the momentum source boundary conditions have been incorporated into a series of hexahedrally meshed domains. Momentum sources have been specified using velocity inlet conditions (see Table 4.1) and the outlet boundary has been modelled as a non-recirculating outflow boundary. Turbulence conditions were prescribed using intensity and length scale, assuming an intensity of 5% and a length scale of 2.5cm based on the metal grille meshing over the inlets.

Heat losses at the walls were calculated using data for thermal conductivities based on the construction materials from Bejan & Kraus (2003) and Lienhard & Lienhard (2006), resulting in a conductivity of 0.162W/m²-K, as compared to 0.186W/m² derived by Pikos (2006) who used standardised data from ASHRAE tables (ASHRAE 2001). Similarly, the floor was calculated to have a conductivity of 0.2 W/m².

Table 4.1 - List of constant boundary conditions

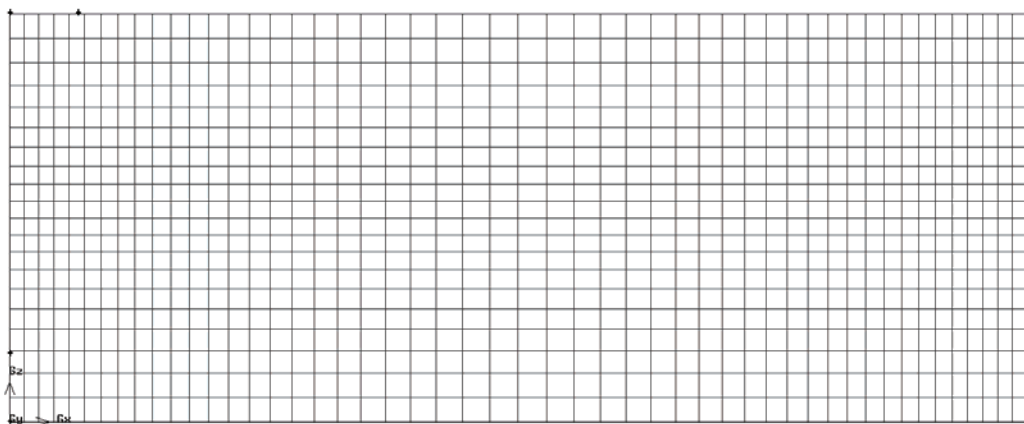
	Area (m ²)	Velocity (m/s)	Temperature (°C)
Cold Inlet	0.5	0.2	23
Hot Inlet	0.25	0.2	45
Exhaust	0.11	-	-

Velocities and temperatures for the momentum supplies were fixed throughout the range of simulations performed, leaving only the thermal and radiative boundary conditions variables. A wide range of different boundary conditions were used, as listed in Table 4.2.

Table 4.2 - Boundary conditions used in simulations

Loop #	Turbulence Model	Wall Temperature (°C)	Internal Emissivity	External Emissivity	Absorption Coefficient (m⁻¹)
1	Realizable	23	0.6	0.5	0.1
3	-	27	0.1	0.1	0.1
4	-	27	0.1	0.1	0.0
5	RNG	-	-	-	-
7	SKE	-	-	-	-
9	Realizable	27	0.6	0.5	0.05
12B	Realizable	Ceiling, 5 W/m ² Floor, 15 W/m ² Sides, 10 W/m ²	0.6	0.5	0.05
13	-	Ceiling, 2 W/m ² Floor, 10 W/m ² Sides, 5 W/m ²	-	-	-
14	-	Ceiling, 4 W/m ² Other Walls, 0 W/m ²	-	-	-
16	-	Ceiling, 5 W/m ² Other Walls, 6 W/m ²	-	-	-

In order to verify mesh independence from the turbulence model as well as ensuring that the mesh resolution at the wall was adequate for correct transferral of energy through the thermal boundary layers or on the accuracy of the radiation model, a number of meshes were created. The meshes were discretised into 36,000, 173,600, and 348,000 hexahedral cells, shown below.

**Figure 4.2 - Side view of smallest 36,000-cell mesh**

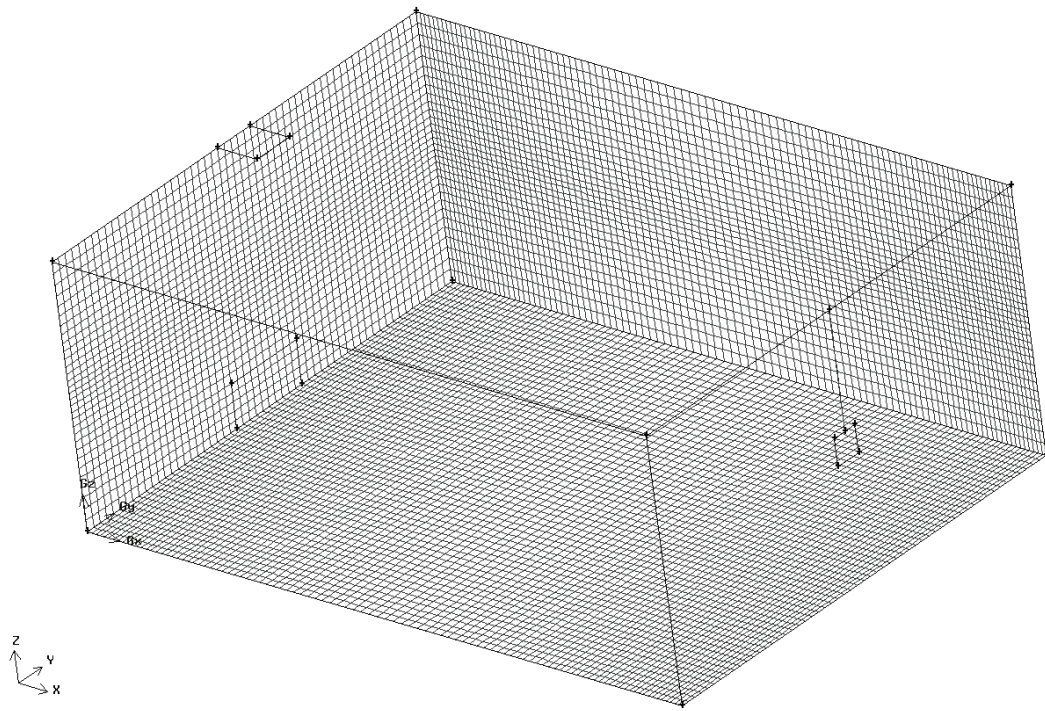


Figure 4.3 - Isometric view of discretisation of medium-sized 173,600-cell mesh

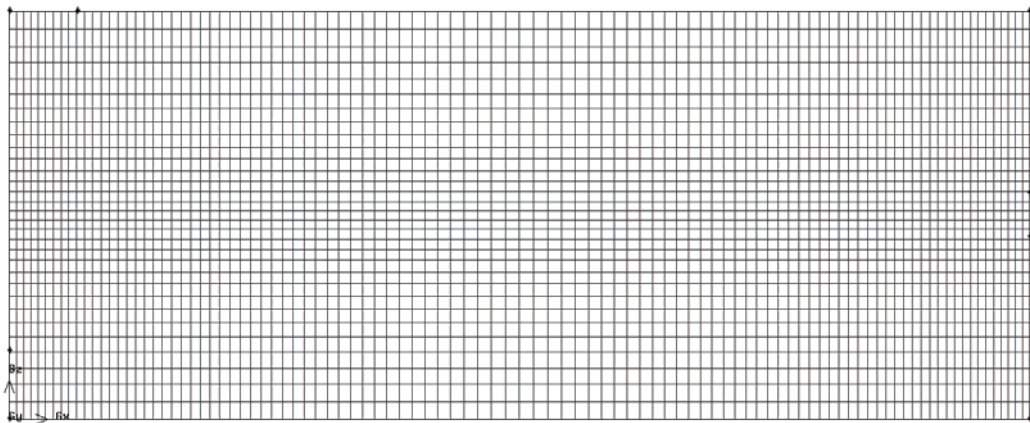


Figure 4.4 - Side view of medium-sized 173,600-cell mesh

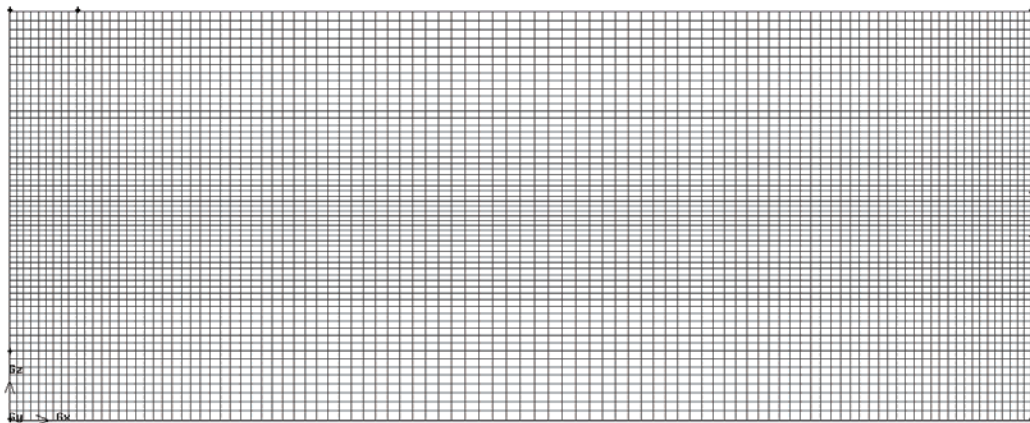


Figure 4.5 - Side view of the most dense 384,000-cell mesh

4.3 Results

4.3.1 Mesh Sensitivity

Three meshes were examined to investigate the influence of mesh density on predictive accuracy, using Loop 1 boundary conditions (all walls temperatures at 23°C, Realizable K-E model, with and without radiation with absorptivity = 0.1m^{-1}). The meshes were all hexahedral and used a similar layout of cells, with global mesh density being the only major change (see Figure 4.6 and Figure 4.7).

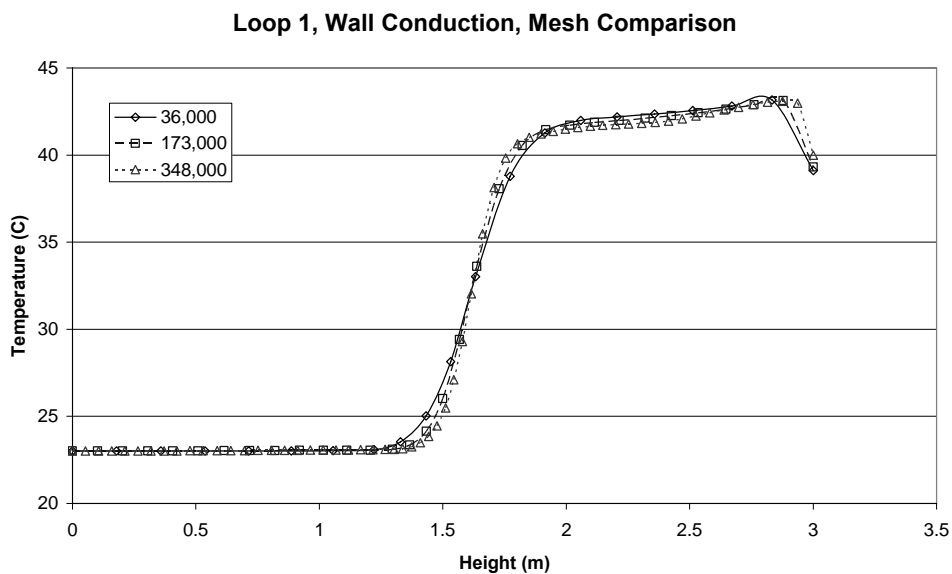


Figure 4.6 - Comparison of three different mesh densities using Loop 1 boundary conditions (Realizable K-E, 23°C wall temperature) without radiative transfer. Effect of lower density mesh is to reduce the temperature gradient over the stratified layer

As can be seen, the reduction of cells along the vertical plane causes no major differences in the determination of the temperature field with respect to the maximum and minimum boundaries or the main profile shape, but there are a number of interesting minor effects. In Figure 4.6, it can be seen that the reduction in vertical mesh density causes the temperature gradient across the stratified layer to become reduced in lower cell densities (Table 4.3). At the upper boundary close to the ceiling, the temperature gradient in the thermal boundary layer is reduced with the lower density mesh, causing a 1-degree difference between the least and most dense mesh. This is due to the lower resolution, whereby the cell node adjacent to the wall was actually outside the boundary layer.

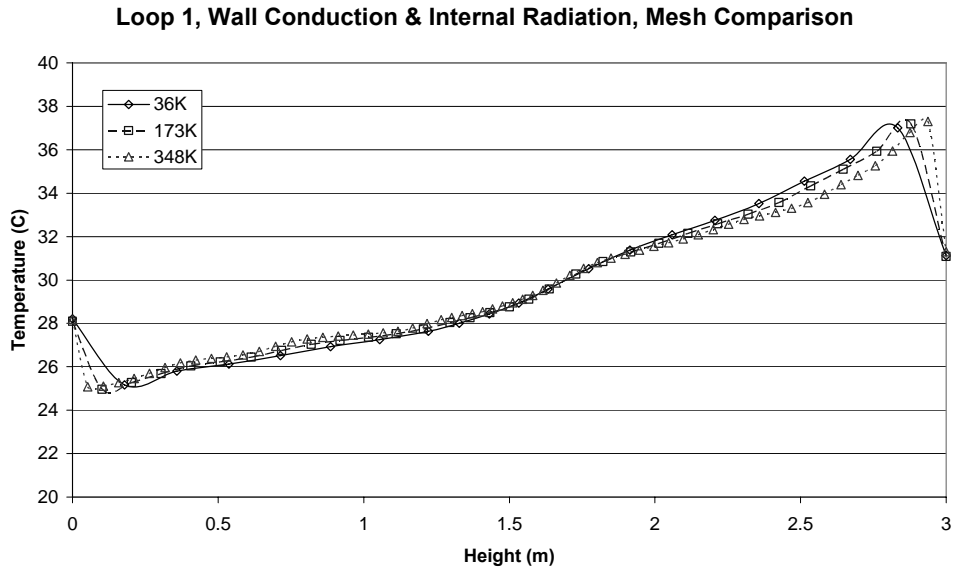


Figure 4.7 - Comparison of three different mesh densities using Loop 1 boundary conditions (Realizable K-E, 23°C wall temperature) with radiative transfer. Reduced gradient effects previously seen across stratified layer no longer present. However, the thermal boundary layer at the floor and ceiling is slightly affected

Table 4.3 - Temperature gradients for mesh densities, wall conduction (no radiation) case

Case	T_1	T_2	dh	dT/dh
Experimental (Iial-Awad 2006)	33.5	37.9	0.29	15.18
36,000 Cells	25.0	38.8	0.34	40.43
173,600 Cells	24.1	38.1	0.29	47.21
384,000 Cells	25.5	40.7	0.29	52.14

Sufficient resolution in the near-wall region is important to ensure that momentum and heat transfer in these regions are correctly accounted for. Transient simulations by Gilham *et al.* (2000, p41) found that using a mesh with insufficient wall resolution ($y^+ > 200$) contributed towards incorrect predictions of heat transfer. The smallest mesh examined in this case study (Figure 4.8) has a maximum y^+ of ~130 only at the exhaust vent due to localised flow acceleration; elsewhere the y^+ values are < 50 .

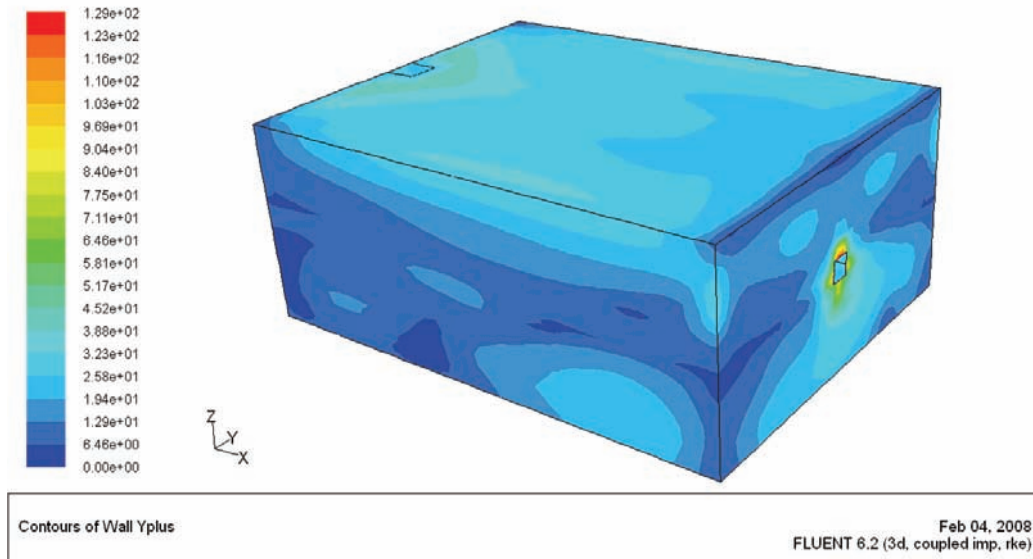


Figure 4.8 - y^+ contours for 36,000-cell mesh. Most of the wall exhibits $y^+ < 50$

Figure 4.7 involves the same geometric and momentum supply conditions, but modelling the radiative transfer between the walls and the air as a relatively strongly absorbing/emitting medium. Because the effect of radiative transfer is to reduce the temperature gradients by redistributing the thermal energy throughout the room, the differences across the region of the stratified layer between the high and low cell-count simulations are reduced; in fact, across the stratified layer, the predictions of the three meshes are virtually identical. The reduced cell mesh still has difficulty resolving the thermal boundary layers; in the lower zone, this has no major effect on the prediction (the thermal boundary layer is simply “thicker”), but on the upper zone, the increased size of the boundary layer causes the simulation to be slightly over-predictive. The upper bound maximum temperature is the same, but the increased thickness of the boundary layer has displaced this maxima to occur at a lower height, resulting in a steeper temperature gradient.

To summarise, the reduction of mesh cells has two major effects:

- Increase in thermal boundary layer due to insufficient resolution
- Reduction in temperature gradient in regions of sharp gradients

4.3.2 Comparison of Engineering Assumptions

A number of simulations have been run using a number of different boundary conditions in order to examine the simulative accuracy relative to the experimental work of Iial-Awad (2006), and also to examine the effects of boundary conditions, or the lack thereof, on the predictive accuracy of the simulations.

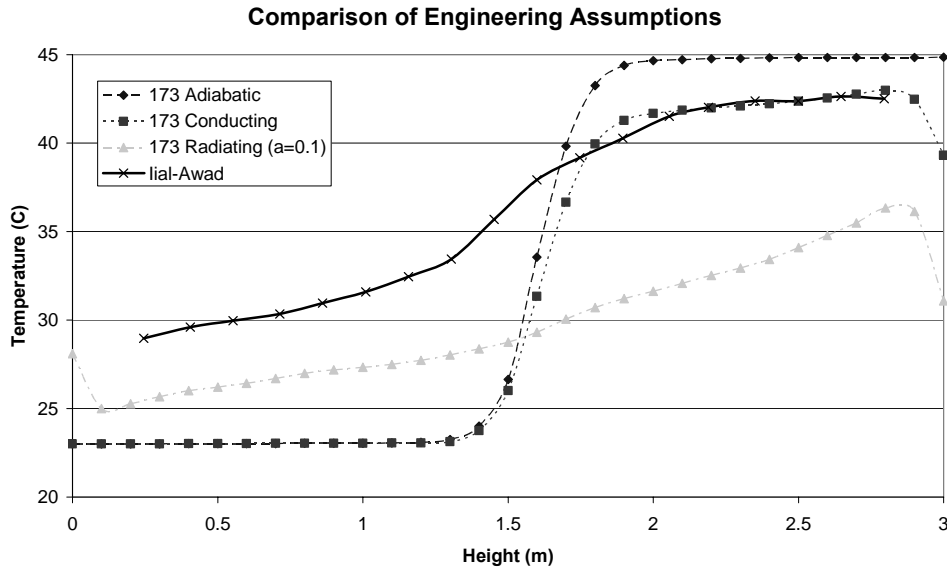


Figure 4.9 - Comparison of different engineering assumptions (adiabatic walls and neglecting radiative transfer) relative to the experimental results of Iial-Awad (2006)

Figure 4.9 shows a comparison of three different simulated scenarios against the original results of Iial-Awad (2006) - adiabatic and no radiation, non-adiabatic and no radiation, non-adiabatic and radiating. It can be seen that the assumptions of adiabatic heat transfer with no radiation leads to the prediction of an idealised temperature field with maxima and minima temperatures dictated by the cold and hot inlet temperatures, and the stratified layer located between. The temperature profile inside the hot and cold zones are uniform up until the steep temperature interface between them.

The non-adiabatic simulation with no radiation is similar to the adiabatic simulation below the stratified layer, in that the cold zone is of uniform temperature. However, the upper zone temperature is lower than the hot supply temperature by around 2-3 degrees, and displays a slight gradient towards the ceiling. The wall temperature is set equal to the cold supply temperature, and so the upper zone wall temperature falls away near to the wall.

Table 4.4 - List of Richardson numbers

Case	T_1	T_2	h	Ri
Experimental (Iial-Awad 2006)	33.5	37.9	0.29	1.09
Adiabatic, No Radiation	26.6	39.8	0.2	2.18
Conduction, No Radiation	26.0	36.7	0.2	1.76
Conduction, Radiation	28.8	30.7	0.3	0.48

The non-adiabatic, fully radiating simulation (third case) is markedly different to both previous simulations, whereby the demarcation between the two zones is far less clear due to the

temperature profile no longer exhibiting a distinct two-zone appearance. The lower zone temperature is no longer uniform or equal to the cold inlet temperature and has increased by an average of 4 degrees. Where previously a stratified layer occurred in the temperature profile, only a small “kink” remains, with a low Richardson number (See Table 4.4) in comparison to the previous cases and the experimental result. The temperature increases almost linearly towards the ceiling. This can be seen clearly by a comparison of Figure 4.10 and Figure 4.11 - the adiabatic simulation in Figure 4.10 shows a very strong temperature gradient between the two zones, which themselves are mostly isothermal. Figure 4.11 shows a much more gradual change in vertical temperature profile.

The internal ceiling wall temperature is colder than the air layer under it, and the floor is warmer than the air immediately above it, which was also found by Li *et al.* (1993, p37) in their examination of displacement ventilation. This is due to the redistribution of thermal energy by radiation - the hotter upper zone radiates energy away to the lower zone, causing an increase in wall temperature there, and if air participates in the radiation, the air is heated directly rather than through conduction/convection near the wall, which then also emits thermal energy to surrounding air molecules.

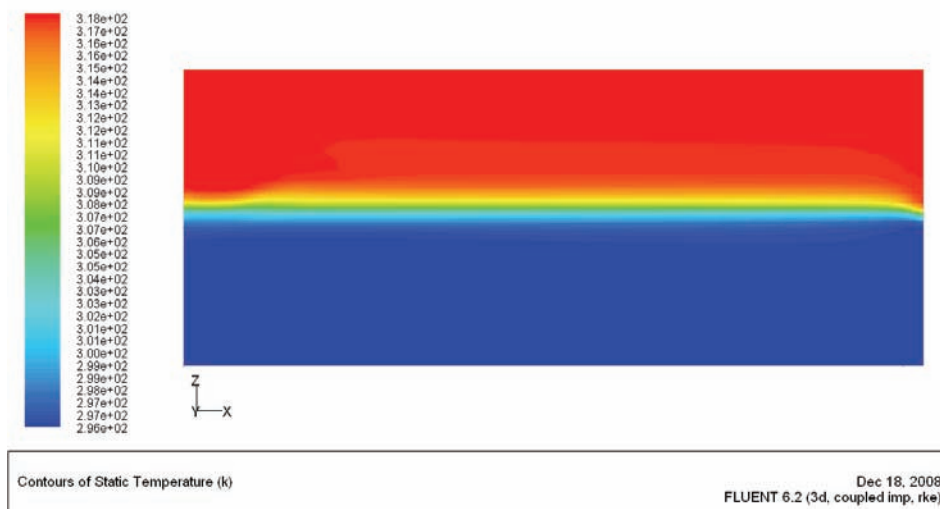


Figure 4.10 - Temperature contour plots of adiabatic wall conditions

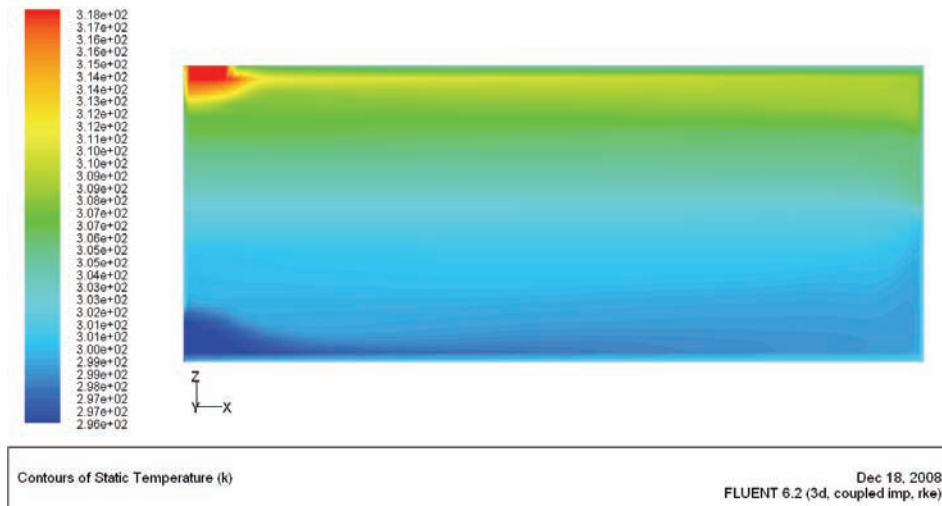


Figure 4.11 - Temperature contour plot of conducting and radiating walls with air participation in thermal radiation

4.3.3 Effect of Turbulence Models

Although the local flow is of a low-Reynolds number type, it is important that the turbulence model used is stable in this flow regime and not liable to produce spurious results in these off-design conditions, to ensure that the turbulence model can function in potentially low convective conditions in future cases. The effect of different 2-Equation turbulence models are shown in Figure 4.12 with Loop 3 boundary conditions (Realizable K-E, 27°C wall temperature). It can be seen that the effect of different 2-equation turbulence models is not significant in terms of effects upon the temperature profiles at the centre of the room.

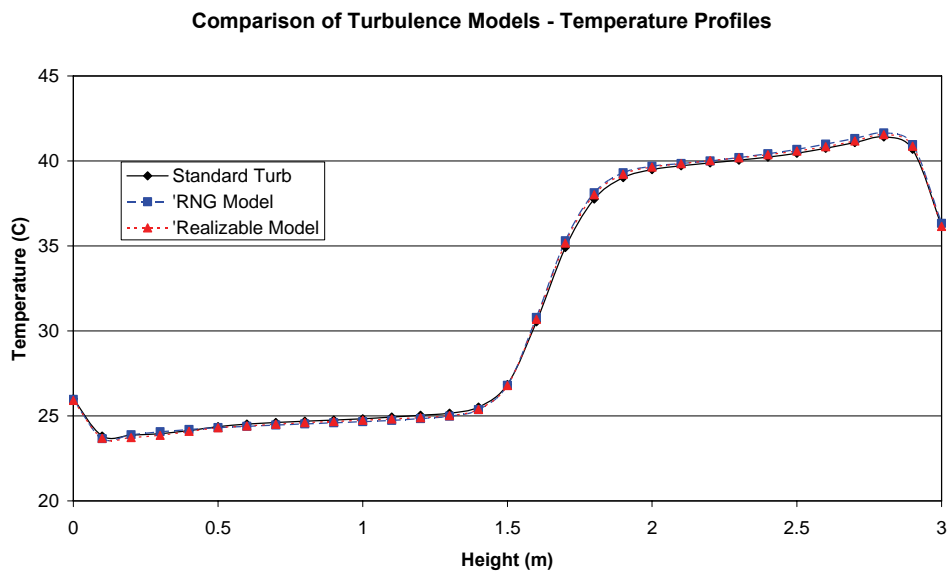


Figure 4.12 - Comparison of predicted vertical temperature profiles using different K-E turbulence models

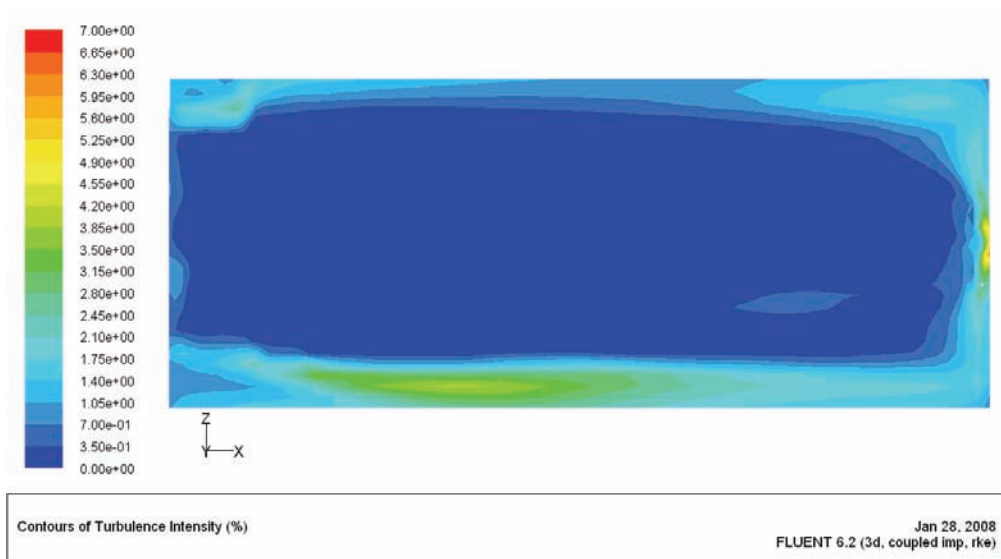
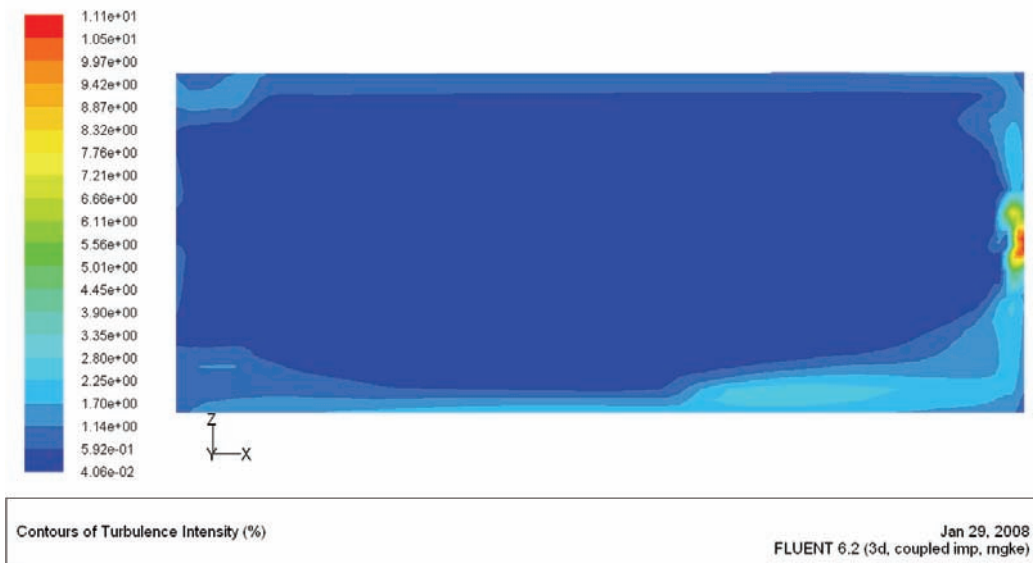


Figure 4.13 - Contour plot of turbulence intensity for Loop 3 boundary conditions (Realizable K-E, 27°C wall temperature)



**Figure 4.14 - Contour plot of turbulence intensity for Loop 5 boundary conditions (RNG K-E, 27°C).
Note higher scale limits**

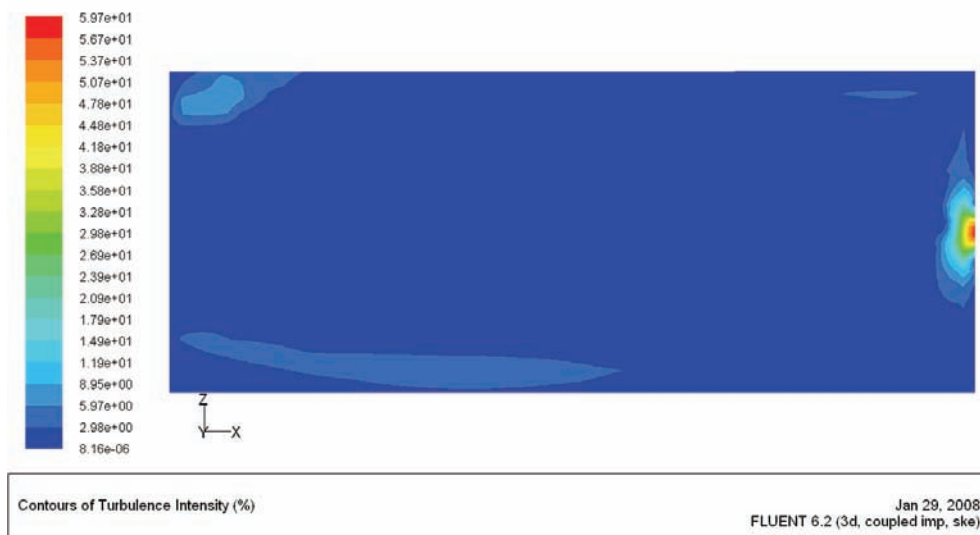


Figure 4.15 - Contour plot of turbulence intensity for Standard K-E (Loop 7). Scale is much higher than previous models

Because the velocities are so low, the magnitude of air turbulence is not high in this particular case, generally having intensities of around 10% at the exhaust, and around 5% near the floor and ceiling. Figure 4.13, Figure 4.14, and Figure 4.15 show the contour plots of the turbulence intensity across the centre of the room. The main effect of the turbulence is to energise the lower-zone boundary layer, causing an increase in transfer of thermal energy from the thermal boundary layer to the surrounding air, warming the lower zone. Between the upper and lower boundary layers, the turbulence intensity is further reduced. Figure 4.16 shows a range-limited contour plot of turbulence intensity so that the effect of turbulence decay in the region of the stratified layer can be seen with greater clarity.

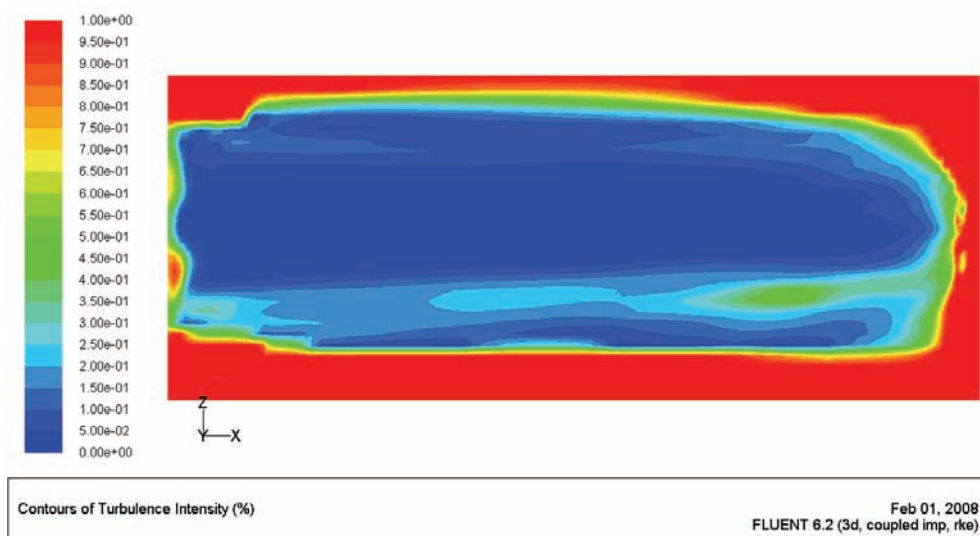


Figure 4.16 - Turbulence intensity field with adjusted scale - note the reduction of turbulence intensity around stratified layer

Examination of the turbulence intensity field shows that while the Realizable and RNG K-E models are able to simulate the low-Reynolds velocity field well with maximum turbulence around the exhaust, use of the Standard K-E model results in erroneous, very high turbulence intensity peaks (Figure 4.15).

Another effect that is more difficult to visualise is the convergence behaviour of the three models. The RNG and Realizable models converged without difficulties, but the SKE model required very heavy under-relaxation of both turbulence transport equations in order to converge, though even this still caused the prediction of erroneously high levels of turbulence. Even then, as seen in Figure 4.15, the scale of the turbulence intensity is still very much higher than the other two models; the SKE model peaks with 60%, whereas the RNG model and Realizable models predict 11% and 7% respectively.

Although the magnitude of turbulence does not have the same importance or effect in low-Reynolds calculations, it is important that the turbulence model selected is able to function in these conditions without instability, as the next study will encounter both low and high-Reynolds flows.

4.3.4 Effect of Medium Absorptivity

Changes to the absorptivity coefficient for the same boundary conditions (Loop 4 - no radiative participation from the air) are shown in Figure 4.17. As seen, the effect of increasing the absorptivity causes the increased re-distribution of upper zone temperature into the lower zone, causing a reduction in the stratification strength. At increasingly higher absorptivities, the temperature profile becomes almost linear, even across a relatively large temperature range as is simulated here.

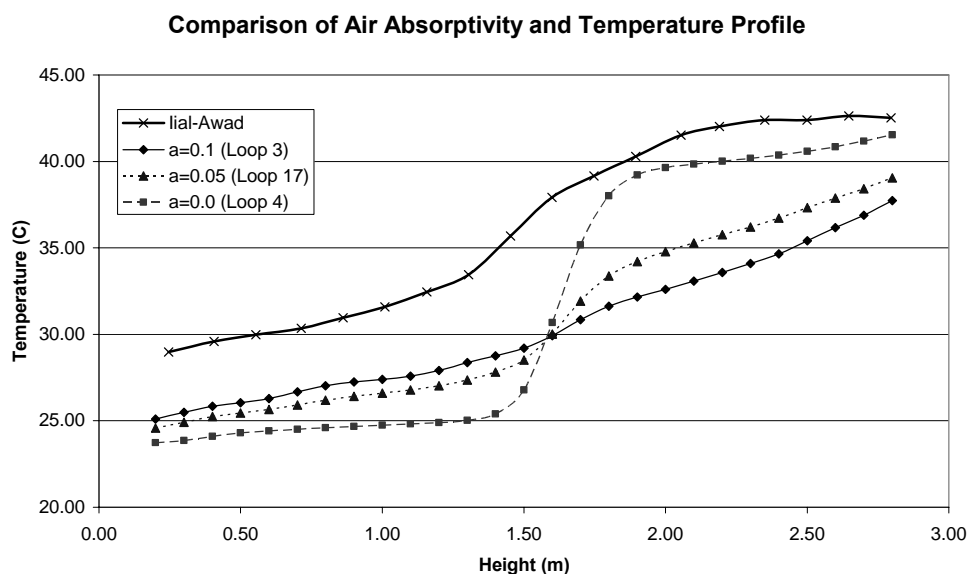


Figure 4.17 - Comparison of vertical temperature profile given different air absorptivities

In comparison to the previous examination of assumptions of adiabatic and non-adiabatic flow, it can be seen that internal radiative transfer is a strong contributor to the heating of the lower zone air. Heat conduction from the wall to the air relies on turbulence to increase the effective diffusivity of the air, so heat transfer through the lower zone is of a low order - in a completely laminar room, heat transfer would be limited to time and velocity scales defined by molecular diffusion. Radiation is a much more direct method that is not restricted to zones near the wall, and the results here display similar trends to those found by Kondo *et al.* (2000, p38), who examined room ventilation with different relative humidities.

From a reversed point of view, it can be seen that increased radiative participation of the internal medium through higher absorptivities controls the temperature gradient, and thus the stratified layer thickness. Therefore, in a more humid environment (in a warmer climate), or a carbon dioxide rich medium (for example in an enclosure filled with combusted exhaust gas to reduce oxygen content) the absorptivity of the gas would be increased, resulting in higher radiative transfer, which acts against the formation of a steep temperature gradient, and thus reduction in the Richardson number, leading to weaker stratification. It is worth noting that the results here seem to agree with the statement by Colomer *et al.* (2004) whereby in the optically thick limit (i.e. high absorptivity) the fluid behaves as if it has a higher thermal conductivity, as radiation would become a local phenomenon similar to conduction, resulting in a temperature profile that is more linear.

4.3.5 Disparity between Simulated and Experimental Results

From Figure 4.9, it is immediately visible that there is a “temperature deficit” between the simulated predictions and the experimental results, similar to the difficulties found by Gilham *et al.* (2000), whereby there was an inadequate retention, or more likely, supply of heat energy into the domain, so that predicted temperature profiles were below those exhibited by the experiments. Here, part of the difficulty was an incomplete description of the boundary conditions *external* to the simulated domain - external wall temperatures and convective conditions (thus affecting direct heat exchange through the walls), external radiation contributions (and thus external ambient air compositions, humidity), and also any solar load additions to the room.

Given the difficulty in reconstructing the surrounding boundary conditions, it was instead decided to follow a more systematic approach whereby instead of attempting to model heat transfer through the boundaries, direct heat fluxes were supplied instead.

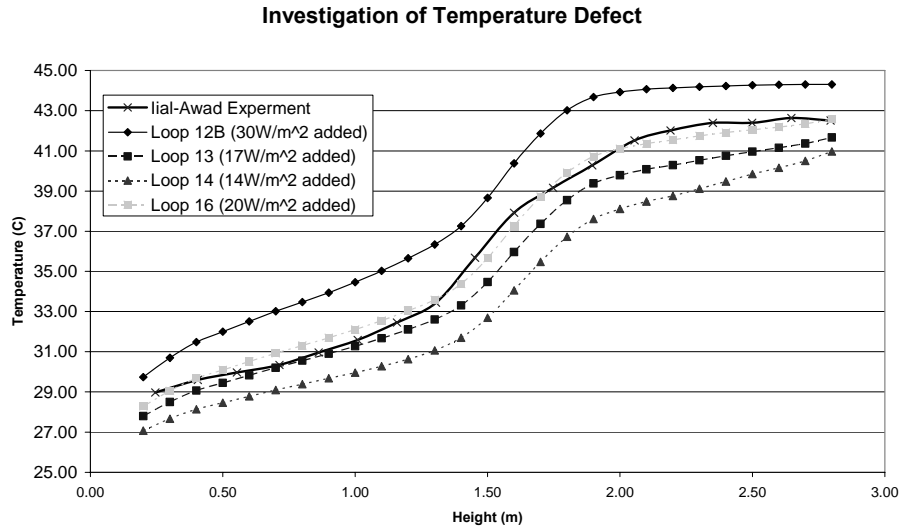


Figure 4.18 - Comparison of different boundary conditions and experimental results

As reported above, the air absorptivity can be used to control the temperature profile, whereby increased absorptivities reduced the amount of stratification due to increased thermal redistribution. As the results from the test where $\alpha = 0.05$ produced a similar profile to experimental results, this was used with the wall fluxes being the only required changes.

Figure 4.18 shows the results of the different iterations with respect to the original experimental results. It can be seen that Loop 16 simulations (Realizable, $5\text{W}/\text{m}^2$ input from Ceiling, $6\text{W}/\text{m}^2$ from other walls) show the closest agreement with the experiments, though this boundary condition set exhibits a surprising amount of thermal input into the system; the ceiling is subject to a $5\text{W}/\text{m}^2$ heat flux, and all other walls are subject to a $6\text{W}/\text{m}^2$ flux. It is unlikely that this additional thermal loading would be due to convection or conduction, as this would require the external walls to be significantly warmer than the inside air due to the high level of thermal insulation of the environmental chamber. Given the magnitude of the heat flux into the chamber, it is unlikely that heat would be generated by a single “point source” inside the chamber such as an occupant or energy-consuming devices; however, a combination of these in conjunction with thermal radiation as a means to add heat, which given that the majority of experimental work occurred during the summer season, is possible.

4.4 Summary and Conclusions

A series of numerical simulations based on the work of Iial-Awad (2006) have been performed using a finite volume solver coupled with turbulence and radiation heat transfer models in order to determine the accuracy of numerical simulations compared to experimental work. In order to determine the effect of different parameters, including mesh density, certain thermal

assumptions, turbulence and effects from radiative heat transfer, numerical simulations have been carried out and compared.

The work described here found that the variation of mesh density has a number of minor effects which, when coupled with additional numerical models, produce relatively little variation in thermal profile of around 1 degree in the upper zone (Figure 4.7), due to better resolution inside the thermal boundary layer in the denser-mesh simulations.

Turbulence model comparisons confirmed that the SKE model of Launder & Spalding (1974) is unsuited for this type of flow, producing spuriously high turbulence levels at the exhaust and hot inlet, as well as having poor convergence behaviour. The RNG (Yakhot & Orszag 1986b) and Realizable (Shih *et al.* 1994) models converge well with similar results.

Overall, the results have demonstrated that the assumptions of adiabatic heat transfer and negligible radiative heat transfer in room ventilation flows are **not** appropriate, as both assumptions have large effects upon the predicted temperature distribution in the room. Allowing non-adiabatic heat transfer affected the upper zone by reducing the upper temperature bound reached through heat transfer out of the system through the ceiling. Radiative heat transfer was also shown to have a large effect on the temperature profile when the participation of air in the radiation model was accounted for, even though the problem is optically thin. Essentially, radiation redistributed the thermal energy in the upper zone to increase the lower temperature colder zone, as found by other authors (Li *et al.* 1993, Glicksman & Chen 1998, Kondo *et al.* 2002, p37). The “linearising” of the temperature profile has an effect of reducing the Richardson number of the stratified layer, making it weaker, and is sensitive to the absorption coefficient, similar to that found by Howell & Potts (2002).

Finally, the simulation work presented here has shown that internal boundary conditions alone are not sufficient to describe the internal temperature field. External conditions have the capacity to greatly affect the flow field and temperature distribution, especially when inside a radiating background subject to potential solar loading. As buildings in general become much more thermally insulated, radiation heat transfer will become more important, requiring more detailed experimental measurements and studies.

In summary:

- This thermal simulation case is mesh insensitive as long as the thermal boundary layer is adequately resolved;
- The SKE turbulence model is not suitable for low-Reynolds flow, whereas the RNG and Realizable model are able to resolve the flow with similar results;
- The assumption of adiabatic and non-radiating enclosures in room ventilation simulation is not valid and has a large effect on the temperature profile;
- Surface to surface radiation allows warmer upper-zone walls to heat up lower-zone walls;

- Participation of air in radiative transfer, even when the optical thickness is low, has a large effect on the temperature profile and Richardson number;
- Boundary conditions internal to the room are no longer sufficient to completely describe the overall temperature field - external conditions such as radiative loading, materials and wall temperatures should be recorded;
- If sufficiently accurate boundary conditions are supplied, simulation of all three methods of heat transfer can result in an accurate prediction of not only the temperature bounds, but the internal temperature *distribution* inside a room.

5.0 Crude Oil Tank Ventilation

5.1	Chapter Overview	93
5.2	Introduction.....	93
5.3	Model Geometry.....	94
5.3.1	Computational Mesh - 3D Domain	95
5.3.2	Geometry and Computational Mesh - 2D Axisymmetric Simulation	100
5.4	Boundary Conditions.....	103
5.4.1	Material Properties	103
5.4.2	Inlet Profile	103
	Profiles for Turbulent Developed Pipe Flow	105
	Profiles for Flow from an Axial Fan.....	106
5.4.3	Heat Transfer.....	106
5.4.4	Calculation of Heat Transfer Coefficients	107
5.4.5	Radiated Heat Transfer	108
5.4.6	Initial Temperatures	109
5.4.7	Air Composition and VOC Concentrations	109
5.5	Results 1 - Examination of Modelling and Boundary Conditions	112
5.5.1	Mesh Sensitivity.....	112
	Comparison of Predicted Jet Dynamics.....	112
	Comparison of Wall y^+	115
5.5.2	Turbulence Model	116
5.5.3	Thermal Analysis of Double-Hulled Tankers	118
	Examination of Different Temperature Conditions	121
	Comparison to Densimetric Differences.....	121
5.5.4	Inlet Conditions.....	122
5.6	Results 2 - Analysis of Gas Freeing.....	127
5.6.1	Preliminary Examination of Gas-Freeing	127
5.6.2	Examination of Modelling Assumptions	129
	Assumption of adiabatic conditions and the absence of radiation	129
	Idealisation of VOC Vapours	130
5.6.3	General Gas Freeing Characteristics	130
5.6.4	Removal of Stratified Layer	132
	Effect of Jet Velocity.....	133
	Effect of Obstructions on Layer Erosion	133
	Stratified Layer Penetration.....	134
5.6.5	Gas Distribution During Gas Freeing	136
	Butane Distribution	136
	Oxygen and CO ₂ Distribution.....	140

5.1 Chapter Overview

This chapter forms part of the main thesis, and is essentially separated into three sections; the first three subsections 5.1 to 5.3 present the critical questions that lead onto the modelling approach and collation of applicable boundary conditions. Section 5.4 presents the results of the 3D simulations, which are used primarily for validation of the supplied jet and thermal analysis in order to determine the strength of thermal effects.

Section 5.5 presents the results of the gas-freeing analysis, from both initial 3D simulations as well as the in-depth 2D study. Validation is performed against existing impingement penetration studies. The change in concentration and distribution of an initially stratified butane layer is presented, and the changes in average and max/min carbon dioxide and oxygen concentrations presented, in the case of re-oxygenation of the atmosphere for habitability.

5.2 Introduction

After a number of journeys, the cargo tank inside a VLCC will become corroded by loading and unloading operations, thermal expansion, hydraulic forces and microbial corrosion acting on it through its lifetime. To monitor, inspect and perform any required repair work, the tank must be rendered safe by gas freeing after the cargo is removed. It is typical to purge and gas-free away from the terminal the tank to ready the tank for admission of new cargo, or more generally to remove the oil vapour at a location that does not pose a safety hazard (gas-freeing at the terminal usually forbidden unless specialist equipment exists to process the oil vapour).

Because earlier work (Logan & Drinkwater 1961, Saunders 1965) was conducted in the period before widespread adoption of double-hulled tankers, and specifically with Logan & Drinkwater (1961, p65), before inert gassing became a requirement, there is a great disparity in previous work and what occurs today. Although catastrophic explosions on board tankers are now very rare, there are still instances where people working inside tanks have been subjected to a toxic atmosphere due to incomplete gas freeing (Department for Transport 2005). Another matter that also causes growing concern is scrapping operations; with regulations stipulating that the retirement of single-hulled tankers are to be accelerated, a large number of tankers will be resigned to the scrapyards. A recent study (COWI A/S 2004) shows that the large majority of ship-scrapping operations take place in India, Bangladesh and Pakistan, with a smaller but increasing minority occurring in China. In these countries, especially Bangladesh and Pakistan, regulation is especially loose, for example the issuance of a gas-free certificate is not required prior to the beginning of work. Although altering national legislation is outside the scope of this work, the investigation of modern gas-freeing processes and internal tank flows very important to this industrial operation,

and the wellbeing of those involved. Given the acceleration concerning the scrapping of ships, it is possible that a number of ships may lie on a scrapping beach for extended periods of time until there are sufficient resources to proceed with dismantling. Depending on the length of this waiting period, remaining oil in the tank can evaporate into gas and stratify.

The settling of heavy oil vapour creates a difficult problem for gas-freeing operations, raising a number of questions:

- Can the gas-freeing fan deliver sufficient momentum to destroy the stratified layers?
- If not, how can the stratified layers be disrupted to encourage entrainment and exhaustion?
- If heavy vapours are disturbed, is there a sufficiently vigorous velocity field to ensure their removal, as opposed to their entrainment and transport to a stagnant part of the tank?
- Does the change in thermal conditions arising from double-hulled construction pose an additional problem?

5.3 Model Geometry

Although COT geometry varies from ship to ship, most ships share common geometric features:

- Upper full-length structural frames support the deck;
- Lower half-width frames support the inboard vertical wall;
- Typical COTs heights are 30m tall;
- Typical COT volumes are between 20,000 to 30,000 m³.

For this study, these features have been incorporated in a generic model based on typical double-hulled VLCC wing tanks. The generic tank modelled here has a total volume of 23,500m³ with overall dimensions as shown in Figure 5.1.

Because the time to gas-free lies in the order of hours, special attention must be given to the method of simulation. A number of simulation modes exist; a steady-state simulation can give indications on the final state of the tank (for example, areas of stagnant, unmixed gas), but cannot be used to determine intermediate states between the initial and final state, and information on elapsed time is lost. A transient simulation infers the most detail, but carries a great cost in terms of computational resources depending on the model. A fully three-dimensional model would have a higher fidelity, but will prove extremely taxing to simulate for such a long period of time; on the other hand, a two-dimensional simulation would only enable a very generic representation of the tank. Because of these conflicting requirements, two geometric models will be used to simulate aspects of the gas-freeing process - a larger, fully three-dimensional mesh, and a two-dimensional

mesh based on an idealisation of the 3D mesh will be used to model the gas-freeing process in its entirety.

5.3.1 Computational Mesh - 3D Domain

The tank features half-width floor frames and full length ceiling frames pitched at 5m. The outboard lower corner of the tank is angled. 4 air vents of 0.318m diameter are placed at regular intervals at the deck height (Figure 5.4).

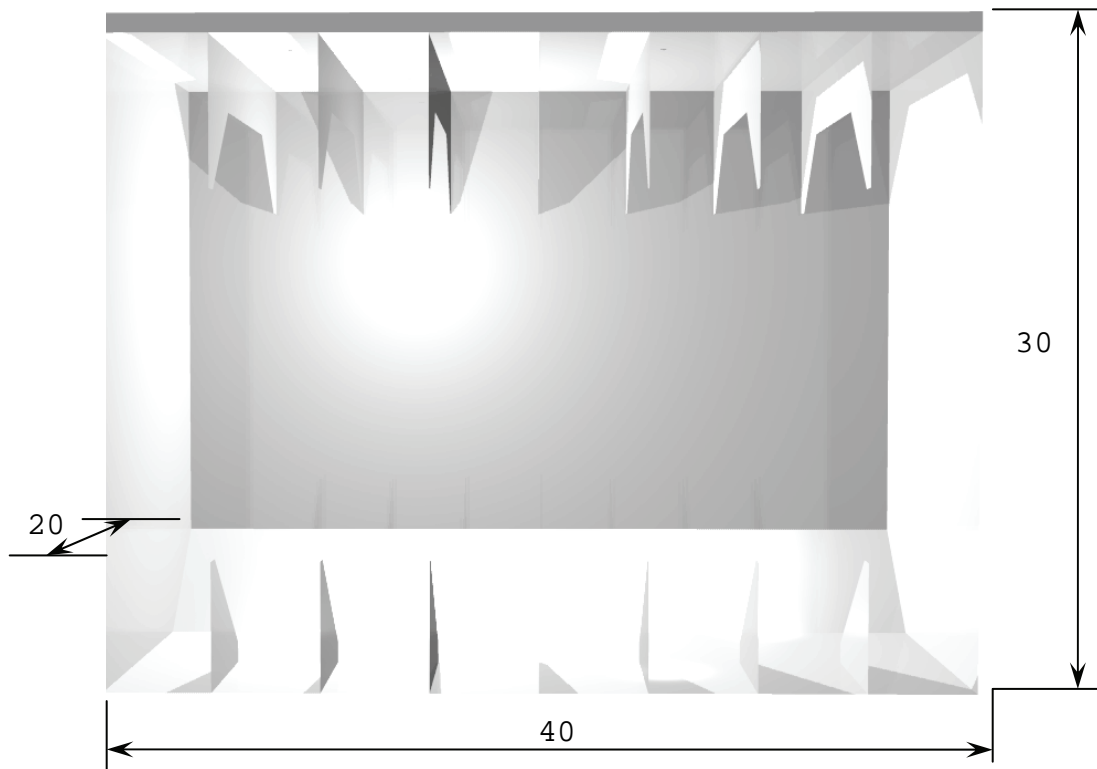


Figure 5.1 - 3D Model of crude oil tank showing internal structure; dimensions in metres

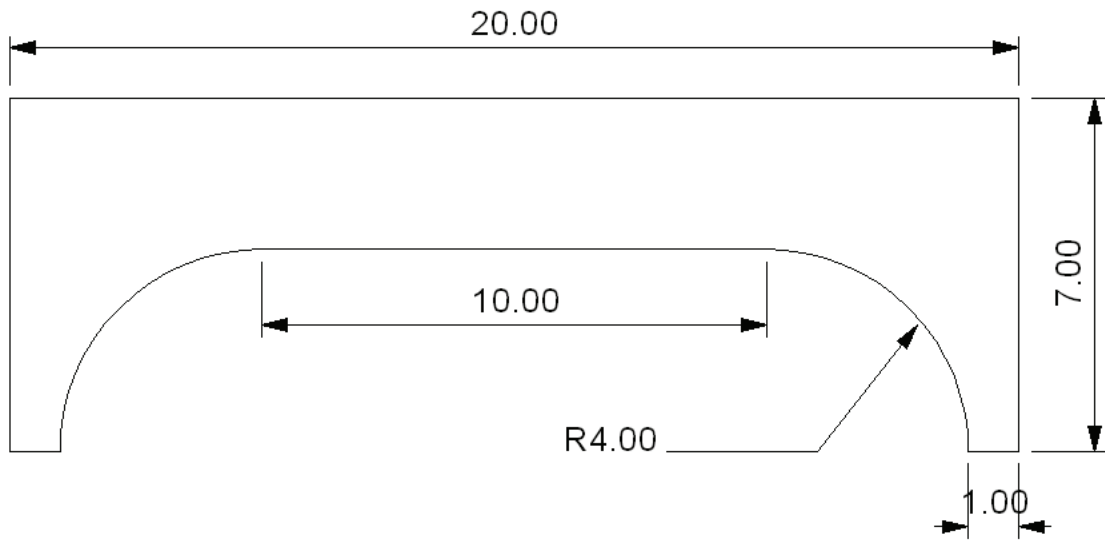


Figure 5.2 - Schematic of upper web frame dimensions (metres)

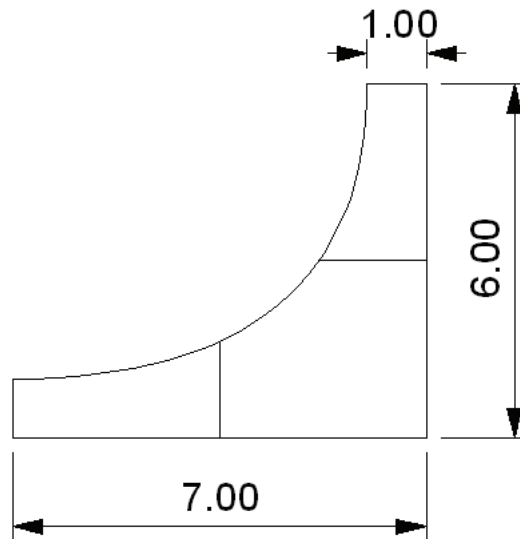


Figure 5.3 - Schematic of lower half-width web frame dimensions (metres)

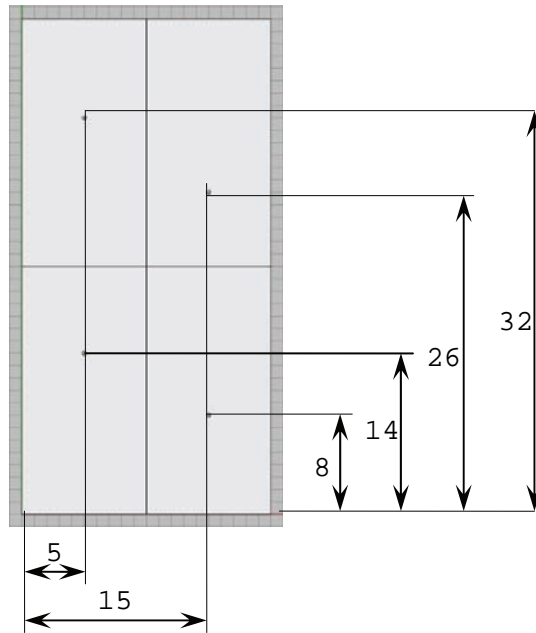


Figure 5.4 - Schematic showing geometric location of venting positions (dimensions in metres)

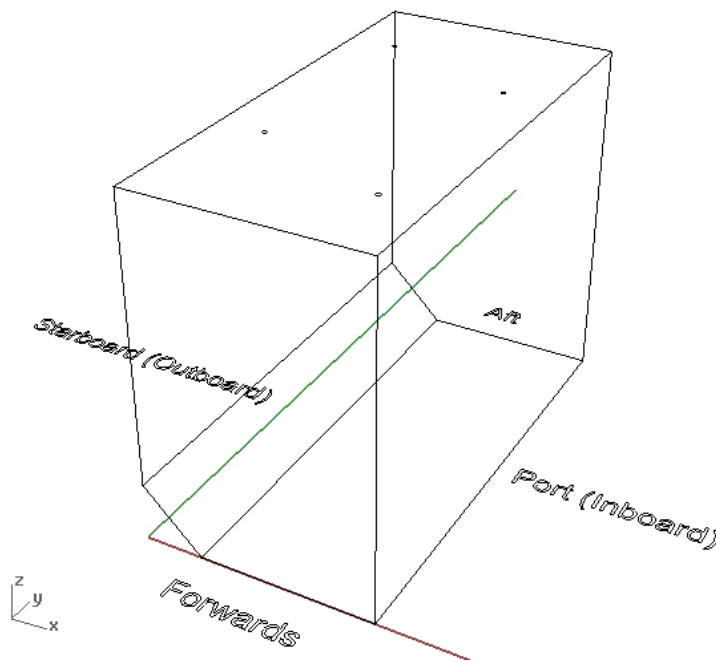


Figure 5.5 - Coordinate system and directional locations in crude oil tank

The majority of the tank geometry lies along orthogonal lines, lending itself to hexahedral cell mapping. However, the structural frames, inlet and exhaust vents, which contain elliptic curves, make conformal mapping of solely hexahedral elements impossible. To accommodate the differing geometry, the final meshes are a combination of orthogonally mapped hexahedral cells and tetrahedral cells. To maintain hexahedral meshing through the majority of the volume, only the area surrounding curved geometry is separated into a different mesh zone, wherein a tetrahedral

mesh is applied. Transition from a hexahedral mesh to a Delauney tetrahedral mesh requires a separate mesh zone, and also the appropriate grading of tetrahedral mesh cells to an appropriate scale at the geometric feature.

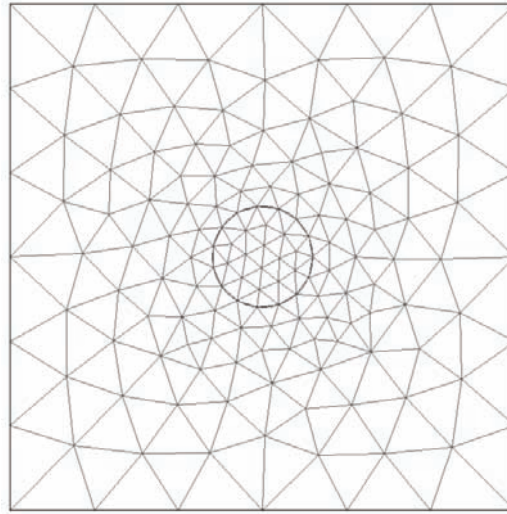


Figure 5.6 - Plan view of transition from regular hexahedral mesh (regular node spacing on the periphery) to prismatic cells in the outlet region (centre of figure) using a Delauney-generated mesh

Compared to the exhaust vents, where the velocity profile of the outgoing air is not as important, the jet inlet is meshed with a higher density because of the need to resolve an appropriate velocity profile at the inlet and capture its effects downstream. This area was meshed using prismatic elements extruded to the base of the tank, and an interface with the hexahedral surroundings was created using a “butterfly mesh”, whereby a central ‘core’ is surrounded by four mesh quadrants which allows the mesh to propagate gradually, rather than suddenly.

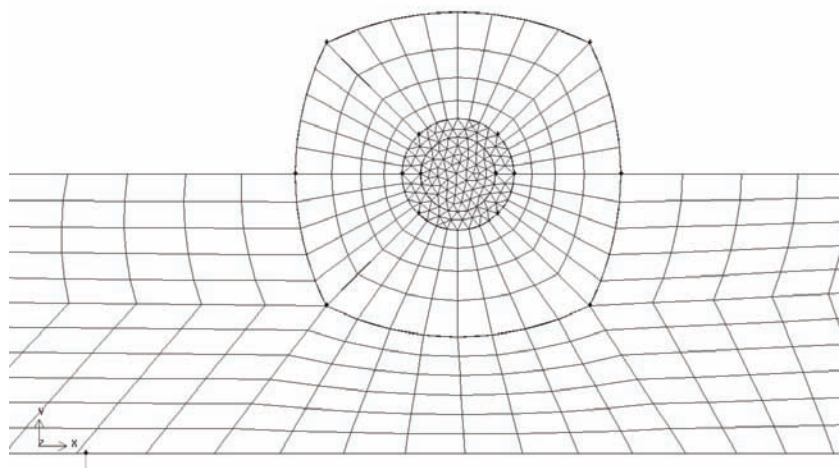
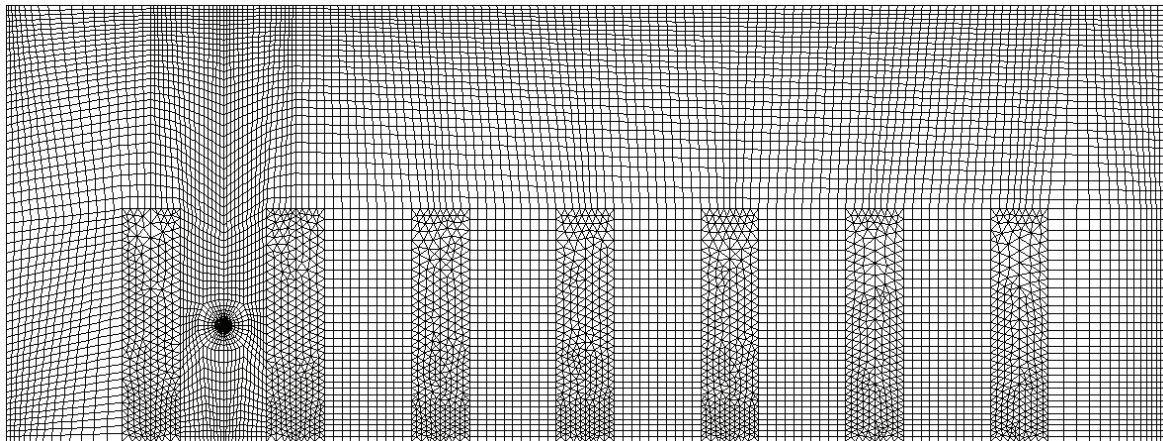
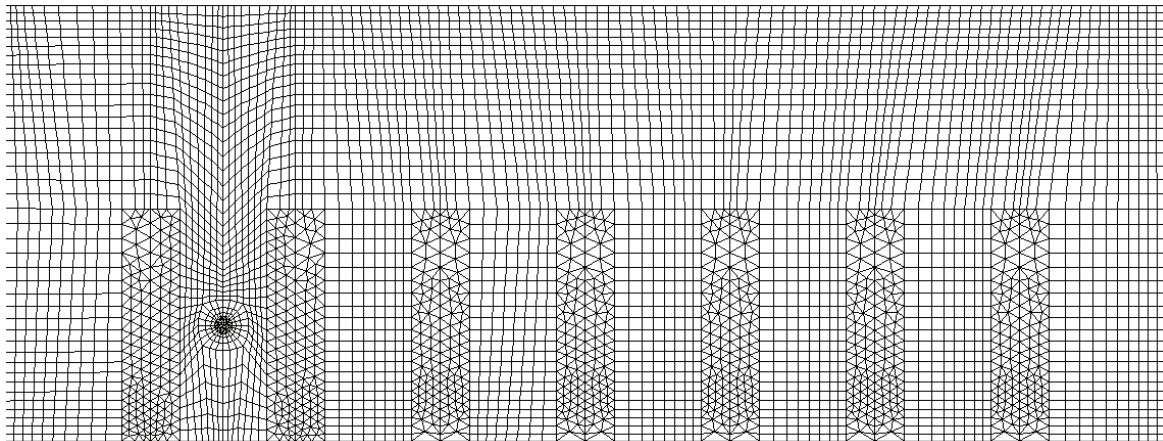


Figure 5.7 - Plan view of transition from hexahedral elements to prismatic elements via a “butterfly” mesh around the supply vent - fine mesh (Mesh C)

Although it is possible to mesh the entire volume using tetrahedral cells, the triangulation method used to propagate the Delauney mesh results in a totally unstructured mesh with no coherent orthogonality at all. For flows which exhibit no dominant streamline direction, this would not necessarily be an issue, however, the expected flow inside the crude oil tank would consist of a number of wall-bounded flows and jet flows, all of which lie along orthogonal directions. Meshing the entire volume in a totally unstructured grid will exacerbate issues such as numerical dissipation, convergence (due to skewed cells) and the prediction of gravity-dominant layers, which tend to lie along an orthogonal axis perpendicular to the vertical axis.



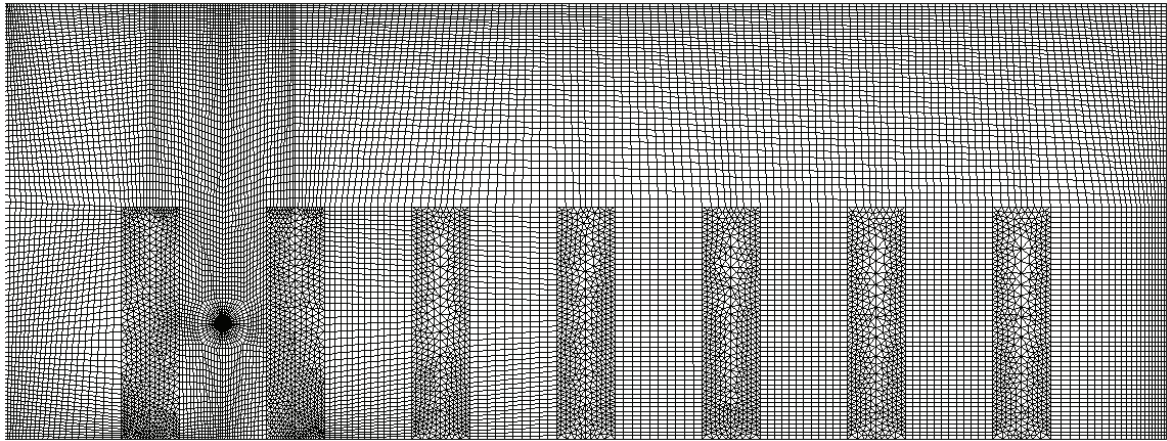


Figure 5.8 - Mesh distribution at floor of tank; Course Mesh A (Top); Medium density Mesh B (Middle); Dense Mesh C (Bottom)

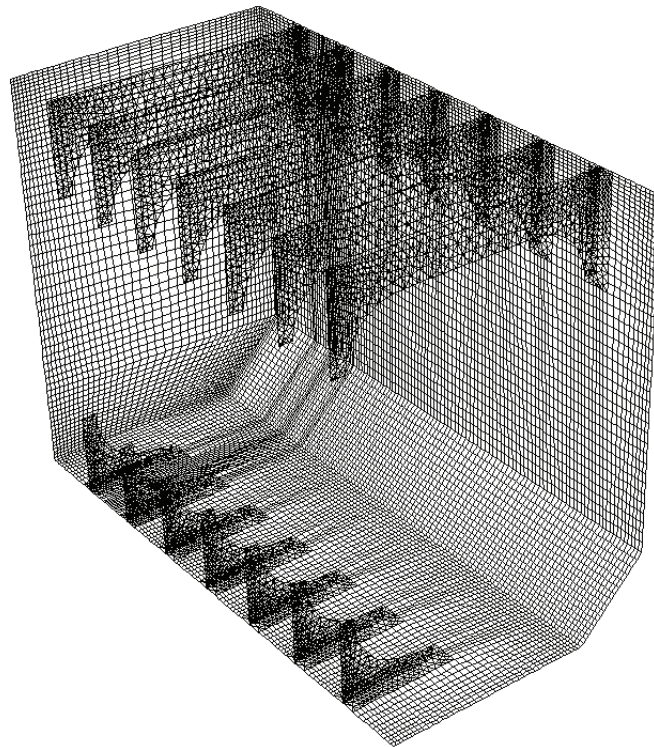


Figure 5.9 - Isometric view of COT wall mesh (Mesh A). Port, inboard (left on figure) and Starboard, outboard (right, angled floor)

5.3.2 Geometry and Computational Mesh - 2D Axisymmetric Simulation

As mentioned previously, a fully 3D URANS simulation requires far more computational resources than a two-dimensional simulation, and due to the size of the problem this can result in excessive run-times; clearly, a two-dimensional simulation can address this at the expense of idealised geometry.

Derivation of the two-dimensional mesh requires that the Reynolds number of the jet, Richardson number across the layer and ratio of volumes must be similar for the simulation to be physically equivalent:

$$\text{Re}_{2D} \approx \text{Re}_{3D}; \quad \text{Ri}_{2D} \approx \text{Ri}_{3D} \quad (5.1)$$

$$\left(\frac{A_{jet}}{A_{plan}} \right)_{2D} \approx \left(\frac{A_{jet}}{A_{plan}} \right)_{3D} \quad \text{and} \quad \left(\frac{Q_{jet}}{V_{COT}} \right)_{2D} \approx \left(\frac{Q_{jet}}{V_{COT}} \right)_{3D} \quad (5.2)$$

The obvious choice to preserve geometric equivalence with the 3D case is a derived planar 2D model. Although Reynolds and Richardson numbers are equivalent, a planar 2D configuration violates similarity of area and volume ratios, and the jet will behave as a plane jet, as opposed to a round one. Therefore, an axisymmetric 2D model must be used. Although an axisymmetric domain is a departure from the more typical cuboid shape of most COTs, it is a necessary one, and some salient features from a typical COT can still be implemented.

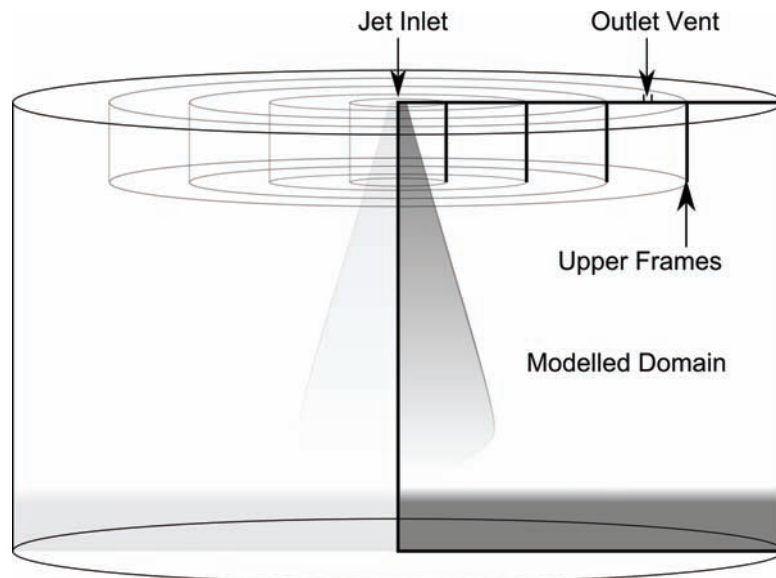


Figure 5.10 - Result of axisymmetric representation of COT

Due to the cylindrical co-ordinate system, geometric features such as the lower half-frames have been removed as they are not able to be represented in a 2D plane. As the upper frames are full span, they can be retained. The discretised mesh is derived from a slice through the densest 3D simulation mesh in terms of overall cell numbers across the plane. However, the axisymmetric nature allows the use of a fully structured, orthogonal mesh, reducing expected numerical diffusion (as most flow will lie along orthogonal axes) and reducing the creation of highly skewed cells that can occur in tetrahedral meshes.

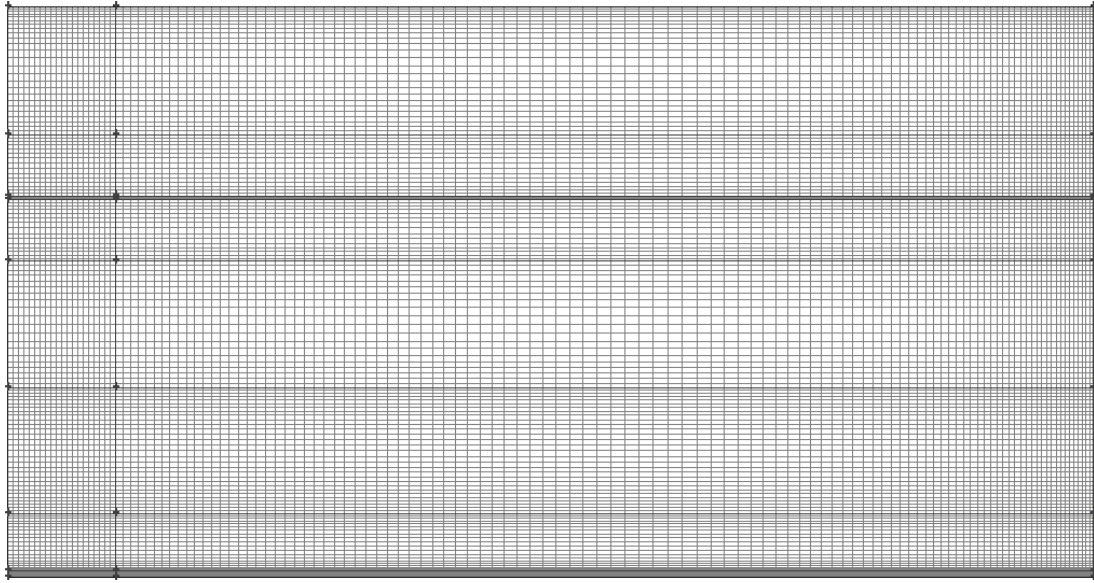


Figure 5.11 - Computational mesh of axis-symmetric domain; jet entry and direction is bounded by lower x-axis; thicker line above centre defines outlet vent

Some gas freeing operations also utilise a length of ducting in order to be able to direct the jet around the tank, and to enable the jet to be projected from a nozzle lower down in the tank, at the expense of volume flow rate due to the greatly increased pressure loss. To account for this possibility, a separate mesh has been derived from the previous mesh is shown in Figure 5.12 whereby a 15m duct extends from the fan exit. Taking into account duct construction (Section 2.6.3) it is assumed that the ducting causes the effective internal diameter to reduce to 0.278m after passing through a 0.5m nozzle from the fan exit.

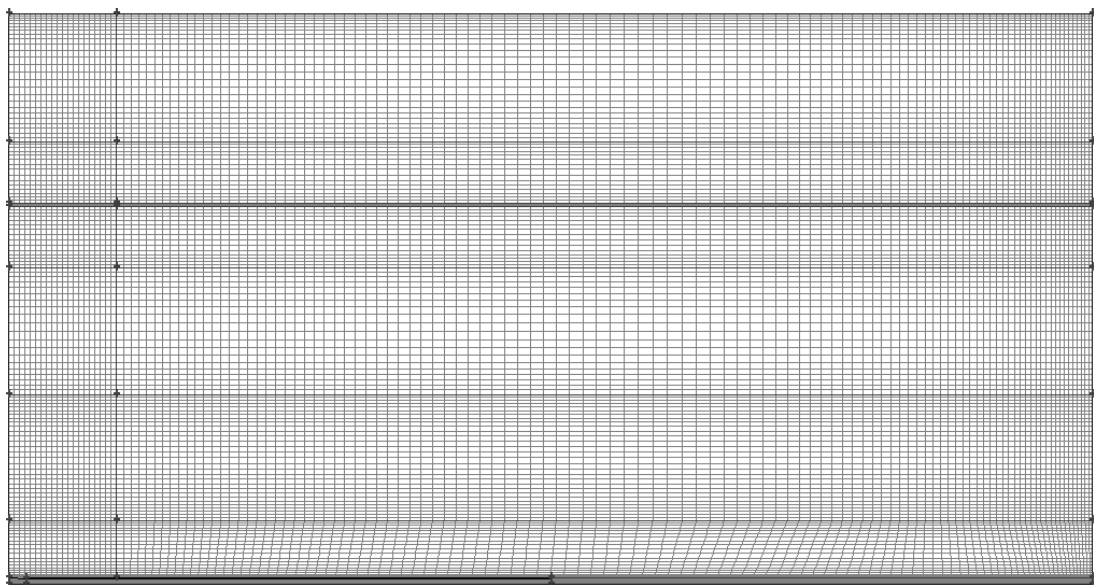


Figure 5.12 - Computational mesh involving 15m duct along rotational axis at bottom of figure, resulting in slight difference to mesh

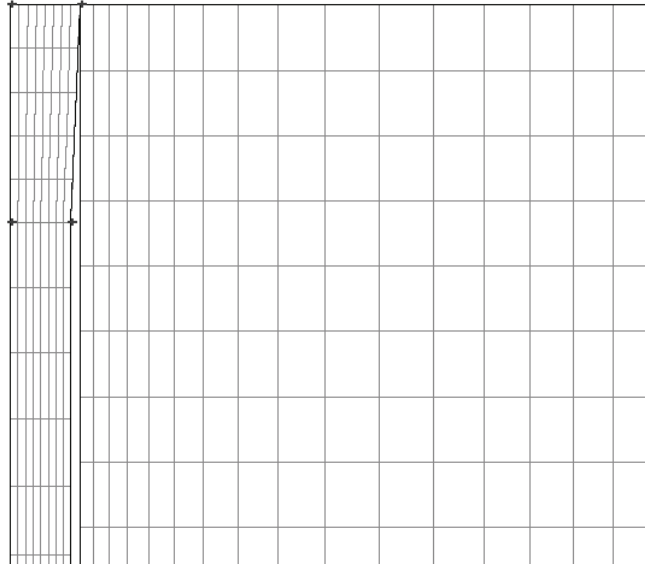


Figure 5.13 - Local detail view of duct transition mesh; Inlet is the detail on the left

5.4 Boundary Conditions

5.4.1 Material Properties

Material data is taken from Bejan & Kraus (2003) and Leinhard & Lienhard (2006). Approximate densities and isobaric heat capacities are given. It is assumed that the ship hull is constructed using low-carbon steel.

Table 5.1 - Common material properties used

	Air (15°C)	Hull Walls
Density (kg/m ³)	1.226	8000
C _p (J/Kg.K)	1006	500
Thermal Conductivity (W/m-K)	0.0252	55
Absorption Coefficient (m ⁻¹)	0.1	0.85

5.4.2 Inlet Profile

A typical gas-freeing fan is of an axial type, where air travels axially through the inlet to the outlet (in comparison to a centrifugal fan, where the air leaves perpendicular to the inlet axis). The exact configuration of the fan varies, but many of them - especially portable fans, where size and weight is of concern - consist of two stages; a single rotor stage, and a downstream stator stage. The rotor imparts a high axial and tangential velocity to the air, and the stator stage is responsible for transferring some of the remaining tangential velocity into static pressure and straightening the flow.

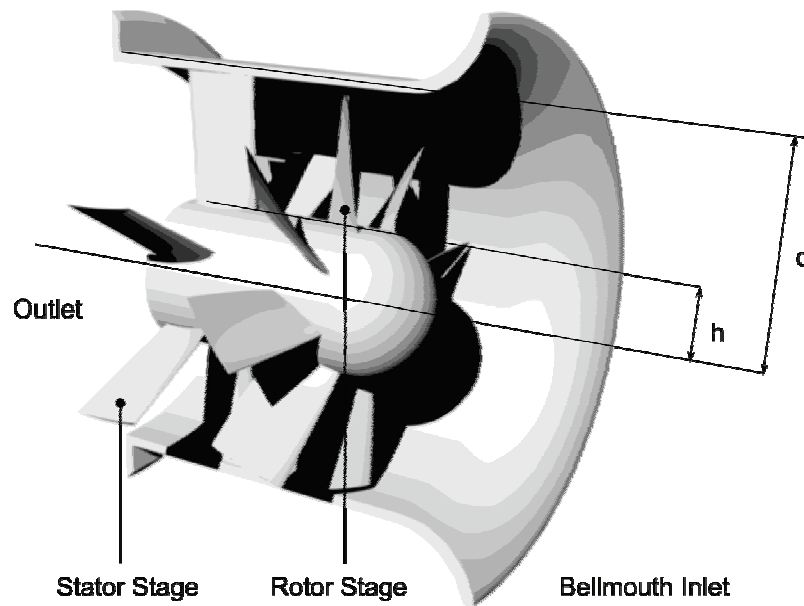


Figure 5.14 - Example of a portable gas-freeing fan with casing cut away

Typically, the rotor consists of more than four blades; higher pressure fans usually have a higher number of blades. Due to noise concerns, the stator consists of a different number of blades which does not share a common factor with the number of rotor blades so that they share different characteristic frequencies (Wallis 1983); the stator also acts as the support structure onto which the rotor and hydraulic/gas motor is mounted. Because this driving motor may be large, the hub/diameter ratio (h / d) may be fairly significant, leaving a large wake area directly downstream of the motor. Nevertheless, because the greatest tangential velocity will be at the tips, the velocity profile at the outlet is very different to developed flow in axisymmetric pipes (Figure 5.15 below).

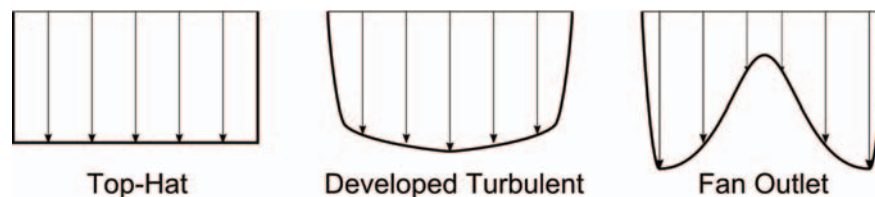


Figure 5.15 - Diagrammatic comparison of velocity profiles

The velocity profile downstream of the final (stator) stage and in the centre of the fan is typically characterised by a *low* axial velocity because of the low tangential velocities that are inferred so close to the hub of the fan, as well as the wake behind the motor. Conversely, the velocities near the tip have the potential to be at the highest because of the higher tangential velocity; a fan designed as such can very well have a linear velocity profile shortly downstream of the stator - the hub with the lowest velocity and the tip with the highest. If the fan is designed to operate in more adverse conditions (off-design behaviour) then the blade tips of the rotor and stator stages may have tapering chords and different pitch, limiting tip velocity, but generating a greater

pressure head; this leads to a velocity profile which instead of being linear, flattens out towards the hub. With these few considerations, it is easy to see that the velocity profile is subject to a number of variations depending on the requirements of the fan. The attachment of a section of straight, rigid ducting or a diffuser at the fan exhaust would, in the limit, allow the development of a standard turbulent velocity profile; however, this would reduce the total flow rate due to the increased pressure resistance through the duct.

As the prescription of different velocity profiles affects the jet and its behaviour downstream, it is important that effect of each is studied to determine the impact of assumptions of the profile used.

Profiles for Turbulent Developed Pipe Flow

The developed turbulent velocity-profile is based off of the following empirical formula:

$$\frac{u(x)}{U} = \left(\frac{y}{r}\right)^{\frac{1}{n}}, \text{ where } n = 3.45 \text{ Re}^{0.07} \tag{5.3}$$

Turbulence properties of the flow are also supplied based on Equations (2.46) to (2.48). The length scale is calculated from Nikuradse’s empirical equation for the radial distribution of length scale (Launder & Spalding 1972):

$$\frac{\ell_m}{r} = 0.14 - 0.08\left(1 - \frac{y}{r}\right)^2 - 0.06\left(1 - \frac{y}{r}\right)^4 \tag{5.4}$$

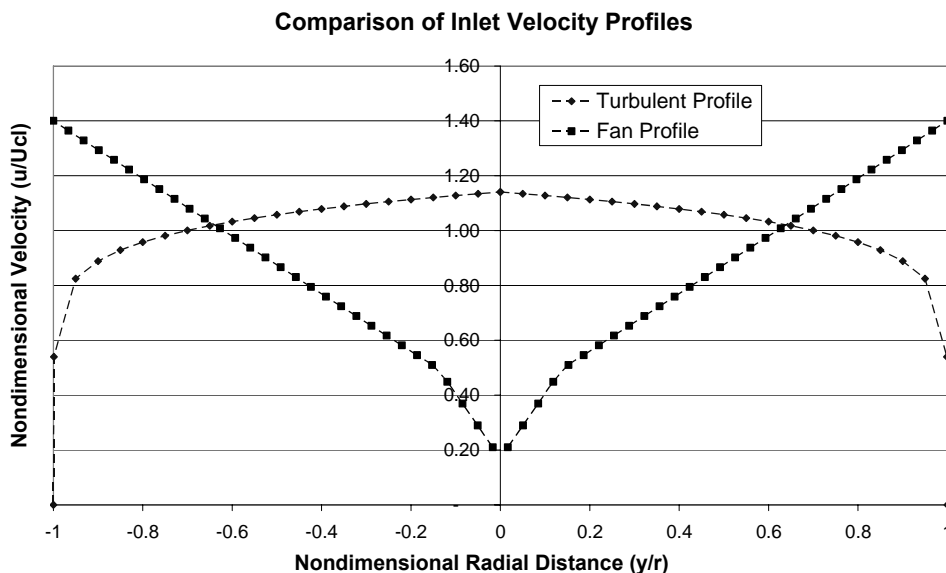


Figure 5.16 - Comparison of Turbulent and Fan inlet velocity profiles

Profiles for Flow from an Axial Fan

Because marine gas freeing fans of the axial type are primarily designed to deliver a high volumetric flow rate, the resulting profile has a very high velocity at the periphery, which decreases towards the centre of the radius due to the fan hub. Depending on the rotor/stator arrangement, the velocity profile can vary between fans. For this study, the downstream profile will be assumed to be a bi-linear profile from the hub to the tip, with the lowest axial velocities at the hub. As the physical size of most gas freeing fans are restricted to ensure portability, it is not possible to add stator stages to completely eliminate swirl, so tangential velocities must also be defined.

Velocity and turbulence quantities have been taken from an earlier study (Chow 2005) which examined the performance of a number of high-performance axial-type gas freeing fan configurations, from which velocity, TKE, and turbulence dissipation rate data are taken from the outlet face.

5.4.3 Heat Transfer

The shift from single-hulled to double-hulled tankers has been a point of interest as the effective rate of heat transfer has reduced due to what has been dubbed a “Thermos bottle effect”, leading to a number of problems such as corrosion (OCIMF 1997, Intertanko 2002). The addition of the second hull creates a three-layer system - the two hulls, and most importantly, the void space between them, similar in configuration to most building constructions. This creates far greater thermal insulation than would otherwise be the case with a single hull.

Work by Saunders (1965, p65) supplied initial values for heat transfer coefficients during a voyage, and showed that the sides of the tank are subject to over twice as much heat transfer than the deck and bottom, and that the walls to other tanks have the lowest heat transfer rate. However, the instrumented tankers were of *single-hulled* construction, so in practice the heat simply has to be transferred through a single layer of hull plating. For double-hulled tankers, the structural arrangement is different. Little published work on the heat transfer of double-hulled tankers exist, so the heat transfer must be calculated. An approximated but representative geometric form was adopted based on a cut-away 5m square section from which a bulk heat transfer coefficient is calculated.

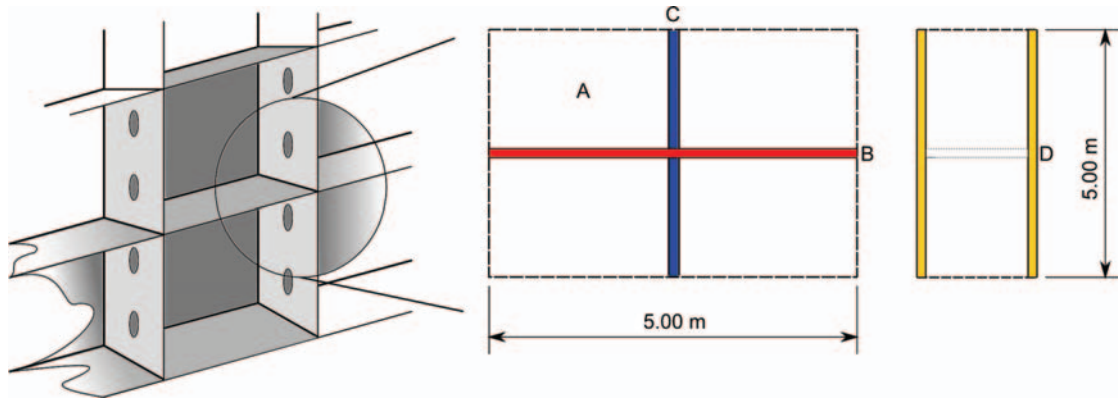


Figure 5.17 - Cutaway of typical structure cross-section, and approximation of structural section with respect to calculating heat transfer through section

5.4.4 Calculation of Heat Transfer Coefficients

In standard composite slab-wise heat conduction, the following equation is used to couple both effects into a combined expression for the heat conduction coefficient:

$$U = \frac{1}{\frac{1}{h} + \sum \frac{l_n}{k_n}} \tag{5.5}$$

Here, the geometry differs in two dimensions, so in order to calculate the slab-wise conduction through the double hull space, an area-weighted average conductivity of the central void space (represented by objects A, B and C from Figure 5.17 above) must first be calculated.

Table 5.2 - Calculation of area-weighted mean conductivity of double hull

Component (Figure 5.17)	Dimensions (m)	Area (# off) (m ²)	Component Conductivity (W/mK)	<i>k</i> * <i>A</i> (m ² -W/mK)
A - Air Void	2.487 x 2.487	6.186 (4)	0.025	0.154
B - Horiz Girder	0.0254 x 5	0.127 (1)	55	6.985
C - Vert. Girder	2.487 x 0.0254	0.0631 (2)	55	6.949
TOTAL		25		14.553
	Area-weighted average conductivity			0.582
				W/m-K

Using the values for the derived geometry from Table 5.2 above, and the material properties data from Table 5.1, the conductivity *k* for this centre section is found to be 0.582 W/m-K. If this average value is assumed to be uniform throughout the central void space, the total conductivity for the void space and the two hulls which enclose the centre section can be calculated

using Equation (5.5). The resulting initial slab conductivity of the hull using this method is found to be around 0.29W/m-K.

The calculation of turbulence convective heat transfer h can be calculated through the Reynolds, Nusselt and Prandtl numbers using the relation (Lienhard & Lienhard 2006):

$$Nu = 0.0370 \cdot Re_l^{0.8} \cdot Pr^{0.43} \quad (5.6)$$

$$h = \frac{Nu}{L} \cdot k \quad (5.7)$$

If it is assumed that the depth of the ship when empty is 3 metres, and that the density of water is 1000 kg/m³, then the resulting Reynolds number is $\sim 3 \times 10^6$. If it is further assumed that the Prandtl number of the water is uniform at 7, the resulting Nusselt number is around 13,000. The resulting external convective heat transfer coefficient is around 2,500 W/m²K. However, when this is combined with the existing conductivity of the wall, the resulting conductivity is virtually the same because the conduction of heat through the double hull and void space limits the total heat transfer rate through the tanker hull. Therefore, the double hull can be represented by a thermal conductivity of 0.29 W/m-K. The upper deck and web frames are *not* double-hulled members, and are represented by $k = 55$ W/m-K.

5.4.5 Radiated Heat Transfer

The calculation of thermal radiation here follows the methodologies outlined in Section 3.3.2 and Section 4.2; the main differences in this case are the wall conditions and the multiple species.

The primary construction material of tankers is mild steel. Polished metals generally have low absorptivities, whereas oxidised layers on the metal increase absorptivities (for example, heavy oxidation of aluminium has been measured to increase the total normal emissivity (and by Kirchoff's law, absorptivity) by a factor of ten (Siegel & Howell 2006). Oxidation on metal surfaces is common, although bare metal showing rust may occur, indicating corrosion and total erosion of any surface treatment used to inhibit oil accretion on the metal. It may be revealed after a complete tank wash, and also serves to show the variability of the metal surface, finish, and resulting radiative conditions in the tank.

Lastly, thin layers of (emulsified) oil residue may also occur. Oil and lacquer paints on metals greatly increase the total normal emittance as high as 0.9 for a thick coating (Modest 2003). Lubricating oil layers of increasing thickness have been shown to lead to a corresponding increase in emissivity (Hottel & Sarofim 1967). For example, in the same reference, a "thick oil layer" on nickel results in an emissivity of 0.82, compared to 0.045 for the polished metal alone.

The combination of oxidation, surface treatments and oil layers make it virtually impossible to analytically derive an absorption coefficient. However, given the reasoning outlined above and the increase in absorptivity in dielectrics (some electrical-grade oils are used for this purpose), it is assumed that all hull surfaces have an average absorptivity of 0.85.

5.4.6 Initial Temperatures

Depending on what destinations a tanker will visit, the climate it is subject to is likely to vary quite significantly; tankers visiting the North Sea oil fields may be subject to near-freezing conditions, whilst tankers plying Middle Eastern routes are likely to be subject to warm seas and very strong solar heat loads, possibly with deck temperatures around 65 degrees (Rauta 2004). Average sea and sea-level ambient temperatures can be found in Energy Institute (2004).

As mentioned in the literature, the change of modern ship designs has increased the level of insulation of the tank, which results in vastly different temperature conditions inside relative to retired single-hulled tankers. As seen in the room ventilation cases (Section 4.3) and other literature (Iial-Awad 2006, Pikos 2006, Mundt 1995, Section 2.4), the strength of a stratified layer is dependent on the layer Ri , and thus the temperature differential. Double-hulled construction reduces the temperature differential, and a review of thermal radiation effects have shown that radiative transfer acts to further homogenise the vertical temperature profile. Although a thorough comparison of the thermal scenarios in single- and double-hulled tankers is outside the scope of the work presented here, it is important that the modern double-hulled case is examined, especially with respect to the density gradients within the tank.

Table 5.3 - Temperature boundary conditions of different walls

Case	Fore/Aft Temp (°C)	Starboard Temp (°C)	Floor Temp (°C)	Deck Temp (°C)	Floor/Deck dT
Hot	30	20	25	50	25
Cold	15	10	5	30	25
Very Hot Deck	35	35	25	70	45

5.4.7 Air Composition and VOC Concentrations

When ready for gas freeing, crude oil tanks contain a mixture of two gas types - inert/flue gas, and hydrocarbons. The former are used to reduce the oxygen content below flammability limits and usually have a higher concentration of CO₂ or N₂, with O₂ levels around 2%. The composition of inert gas used is given in

Table 5.4 below.

Table 5.4 - Composition of inert gas

Name	Formula	% By Volume
Oxygen	O ₂	2
Nitrogen	N ₂	83
Carbon Dioxide	CO ₂	15

Crude oils contain a large range of different hydrocarbon chains. However, only the shorter hydrocarbon chains are found in VOC vapours, simply because they have lower boiling points (See Table 5.5). As light crudes contain more shorter-chain hydrocarbons, they are more volatile.

The most detailed investigation of gas concentrations inside the tank are those performed in support of the VOCON project (Oldervik *et al.* 2000), where methods of reducing evaporative losses during loading and offloading were examined. Of particular interest is the degree of detail of gas composition coming from the tanks by the simulation, whereby hydrocarbons up to C₆ (Hexane) are listed individually, and C₆+ chains are summed, allowing suitable initial conditions to be derived from the same conditions used in the gas extraction simulation.

Table 5.5 - Properties of volatile hydrocarbon chains @ 1 atm

Name	Formula	Norm. Boiling Point (°C)	Rel. Dens. (Air = 1)
Methane	CH ₄	-162	0.55
Ethane	C ₂ H ₆	-89	1.05
Propane	C ₃ H ₈	-42	1.6
Butane	C ₄ H ₁₀	-1	2
Pentane	C ₅ H ₁₂	36	2.5
Hexane	C ₆ H ₁₄	68	2.97
Heptane	C ₇ H ₁₆	102	3.5

Data from Oldervik *et al.* (2000) shows that initially, as much as 14% (by volume) of the gas inside the tank are hydrocarbons. From the data, the initial composition of the gas inside the tank are given below in Table 5.6:

Table 5.6 - Composition of gas mixture inside tank, by volume

Name	Formula	% by Volume
Methane	CH ₄	0.525
Ethane	C ₂ H ₆	2.100
Propane	C ₃ H ₈	5.250
ΣButane	C ₄ H ₁₀	3.815
ΣPentane	C ₅ H ₁₂	1.610
ΣHexane+	C ₆ H ₁₄ ⁺	0.700
Oxygen	O ₂	1.72
Carbon Dioxide	CO ₂	12.90
Nitrogen	N ₂	71.38

One difficulty with the VOCON data is that although the gas inside the tank has been inerted, it has not been purged, which would occur prior to gas freeing. The purging operation adds a large degree of uncertainty to the initial conditions inside the tank, but based on the details from Oldervik *et al.* (2000), it can be assumed that the lighter fractions of hydrocarbons are exhausted. However, the heavier fractions are more likely to still be present. Propane, butane (n- and iso-) and pentane make up the bulk of the heavier-than-air fractions. In the following simulations, butane is used as the sole representative gas in place of different combinations of propane, butane and pentane, as well as to reduce computational requirements.

5.5 Results 1 - Examination of Modelling and Boundary Conditions

5.5.1 Mesh Sensitivity

In order to ensure that results are independent of the mesh, three different meshes have been created to examine the influence of mesh distribution and density upon simulated results. In order to compare mesh sensitivities, the characteristics of the jet will be examined, primarily because of the wealth of analytical models, experimental data and general knowledge of this class of shear flow. Also, the jet is responsible for much of the turbulence generated in the system which is convected around the tank volume, so the accurate prediction of this is a necessity.

Wall y^+ values, which are a measure of perpendicular wall distance with respect to the local flow conditions, will also be examined in the three meshes.

Comparison of Predicted Jet Dynamics

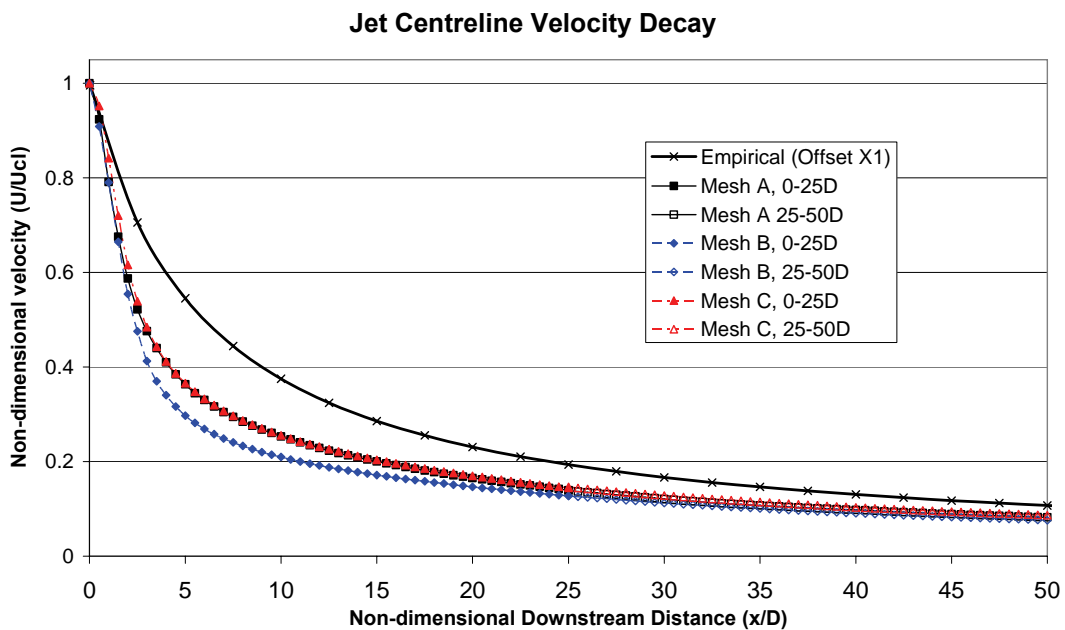


Figure 5.18 - Nondimensionalised centreline velocity decay

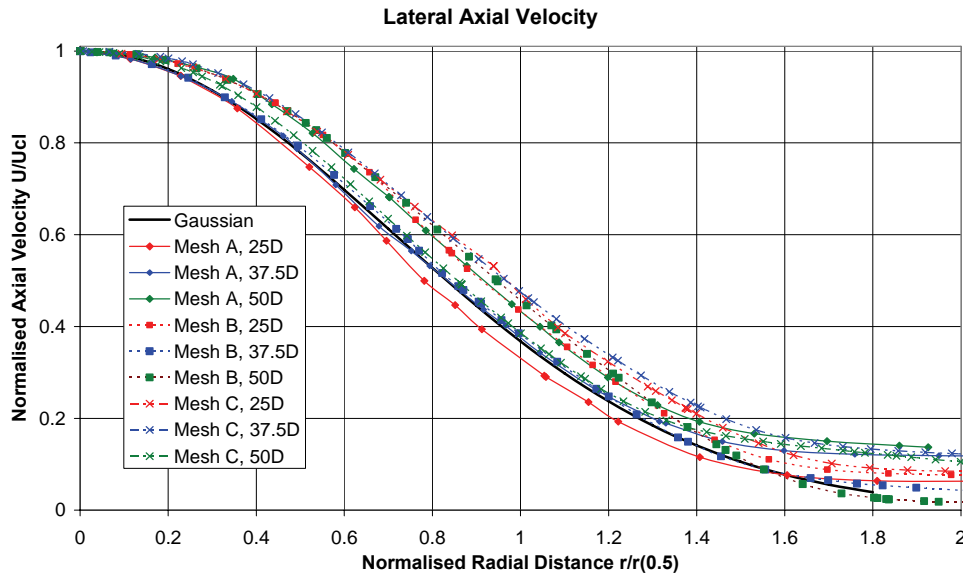


Figure 5.19 - Axial velocity profiles at different downstream locations

Initial, attention will be focused to meshes A to C. Compared to the common self-similar analytical solution (for example, Pope 2000, p45), there are a number of observations to be made:

- None of the predictions on any mesh match the established self-similar jet velocity-decay curve;
- In general, there is a 10% over-prediction of lateral axial velocity profile (jet spread) in most regions of the jet on most meshes;
- Mesh A and Mesh C show remarkably similar prediction of velocity decay given the 6-fold increase of mesh cells in Mesh C;
- Mesh B exhibits a higher dissipation of centreline velocity in the initial region of the jet.

The first point is an interesting one which warrants further attention, and comes as a result of a number of assumptions of the jet, the effects of the geometry, and also the jet model itself. All standard literature of analytical solutions of jet flows begin with the assumption that the jet is free and unbounded, being issued from a sharp-edged nozzle after some distance such that the jet supply has a conventional turbulent velocity profile. In these ideal situations, the jet assumes a self-similar profile as studied in Section 2.4. However, in the case examined here, none of these assumptions are applicable in their entirety - the issue of the velocity profile is quite important, but will be expanded in 5.5.4 and not covered here.

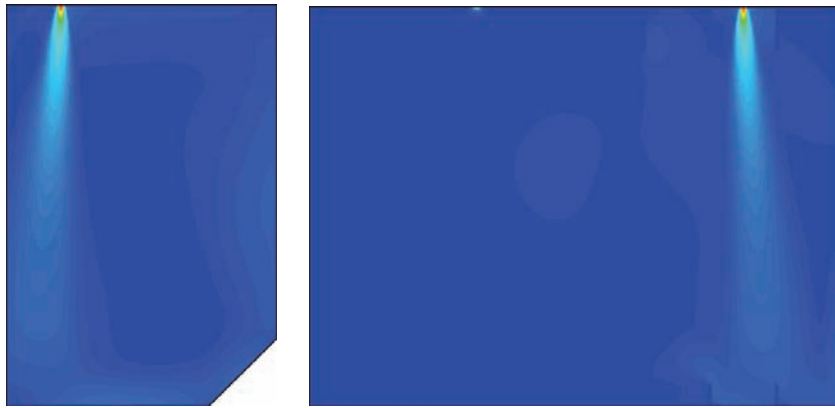


Figure 5.20 - Contour plots of velocity of planar slices through the jet inlet centreline; considerable off-axis jet bending is evident; Red represents 50m/s

This leaves the major assumption that the jet is free, and it is evident that it is not totally free - Figure 5.20 shows a slice through the centreline of the jet origin. From this, the influence of the wall on the jet can be seen. The jet is not a wall jet, but is under the influence of a nearby bound. This attracts the jet due to the Coanda effect, causing it to bend towards the wall. In combination with the inlet conditions, this leads to a profound initial region velocity decay.

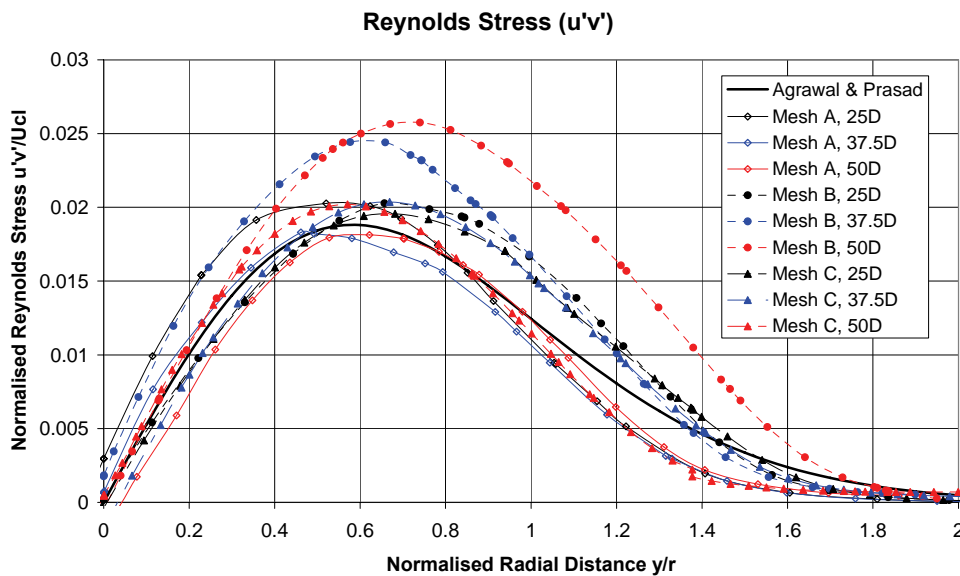


Figure 5.21 - Plot of Reynolds Stress of three meshes and three downstream points against correlation from Agrawal & Prasad (2003)

For ease of comparison, the $\overline{u'v'}$ Reynolds stress derived from the turbulence quantities and compared with analytical results from Agrawal & Prasad (2003), presented in Figure 5.21. The Reynolds stress has been calculated using the Boussinesq eddy-viscosity equation using Equation (2.38):

$$\overline{u'v'} = -\nu_t \left(\frac{\partial u_i}{\partial r} \right) \tag{5.8}$$

Again, the coarse and fine mesh are in good agreement, but the medium-density mesh predicts exaggerated values that are out of agreement compared to the other predictions and the analytical model from Agrawal & Prasad (2003).

Comparison of Wall y^+

The maximal wall y^+ is quite high on all simulations, due to the high flow velocity and resulting high shear stress. With reference to Figure 5.22 to Figure 5.24, it can be seen that several regions are subject to high y^+ values:

- The impingement zone;
- Two lower frames in the impingement zone;
- The angled floor and starboard lower wall;
- The forward wall closest to the jet;
- The port-side wall in the immediate vicinity of the jet.

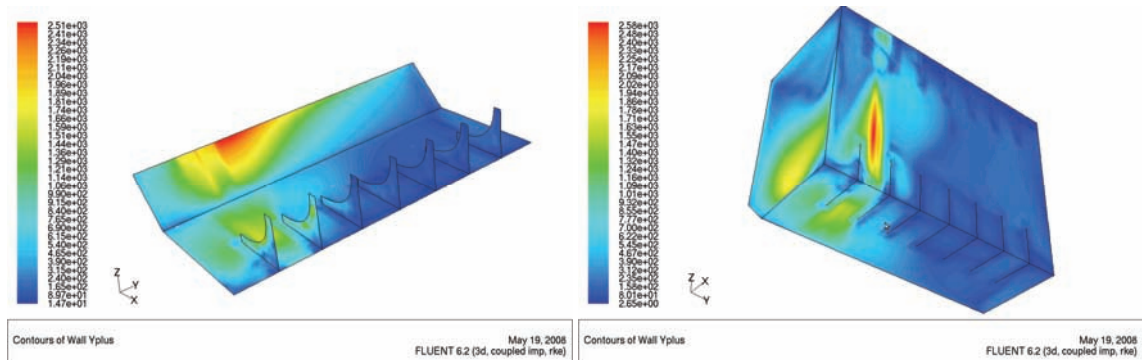


Figure 5.22 - Images of y^+ in the internal impingement region (left) and external regions subject to jet impingement and recirculation (right) with coarse Mesh A

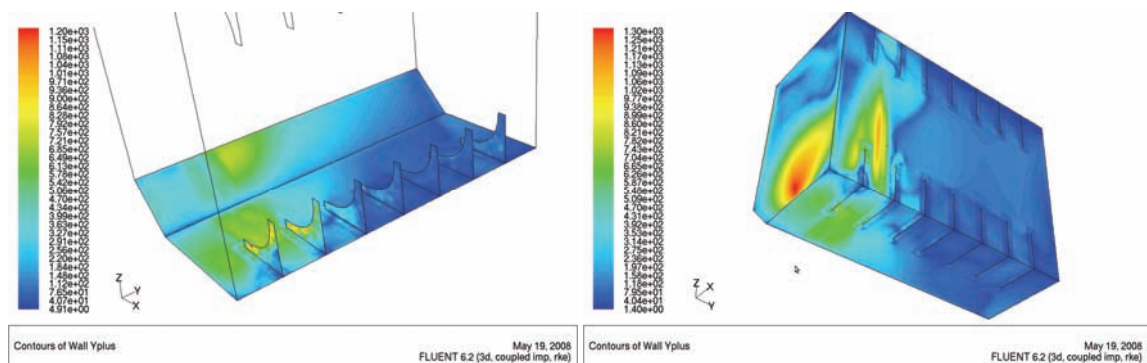


Figure 5.23 - Images of y^+ in the internal impingement region (left) and external regions subject to jet impingement and recirculation (right) with Mesh B

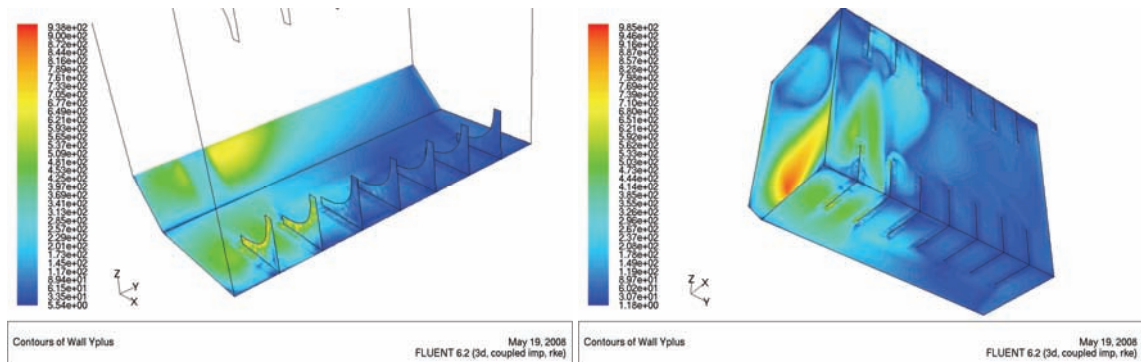


Figure 5.24 - Images of y^+ in the internal impingement region (left) and external regions subject to jet impingement and recirculation (right) with fine Mesh C

As can be seen, the maximum y^+ ranges from over 2000 in the expected areas in Mesh A, whereas the refined Mesh C has a maximum y^+ of just below 1000, which occurs on the leading edges of the lower web frame; the surrounding areas have on average a y^+ below 700. Clearly, the higher density mesh has the most favourable y^+ values.

Additionally, Mesh C also has a higher number of cells across the inlet face, allowing a more accurate definition of inlet velocity and turbulence profiles.

5.5.2 Turbulence Model

The earlier case study validated that the Realizable turbulence model of Shih *et al.* (1994, p25) is able to perform in the lower Reynolds-number regime. The gas-freeing scenario is a culmination of a number of different phenomena - low Reynolds-number flows which are potentially buoyancy driven, high-Reynolds-number jet/shear flows, all subject to multi-species mixing and thermal effects. This change in conditions require the turbulence model to be re-examined, so as to ensure that the model is suitable in all of these conditions.

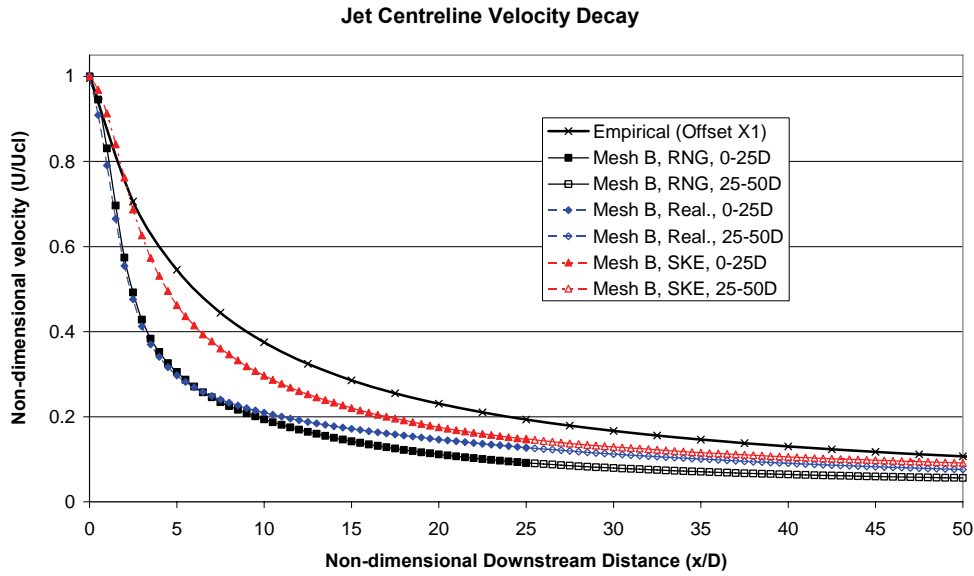


Figure 5.25 - Jet centreline velocity decay

As can be seen, there is considerable difference between the predictions of centreline velocity decay Figure 5.25 between the SKE model of Launder and Spalding (1974) and the RNG model from Yakhot and Orszag (1986b). The SKE model retains a fair amount of centreline velocity in comparison to both the RNG and Realizable models, which drop off velocity quite rapidly due to the high initial shear. Further downstream, the RNG model has a lower self-similar velocity trend compared to the SKE model; although the Realizable model had a similar initial trend to the RNG model, the self-similar region is predicted more similar to the SKE model.

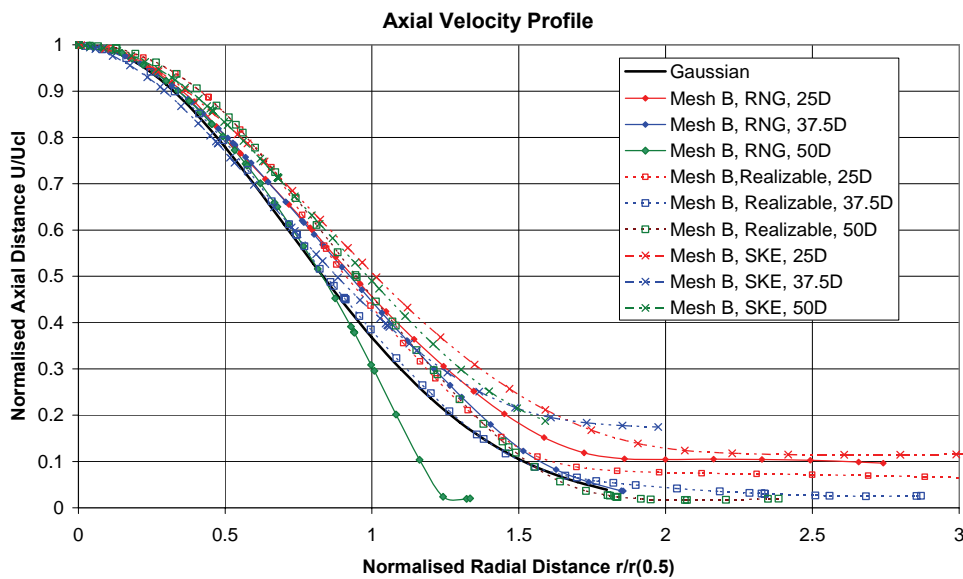


Figure 5.26 - Non-dimensional axial velocity profile in the radial direction

The axial velocity profiles show that compared to a free jet, there is a degree of scatter from all models. However, the greatest deviation occurs with the SKE model, which overestimates by around 10% above the Gaussian velocity profile of Agrawal & Prasad (2003, Equation (2.78)), and is also a verification of the effects of the round jet anomaly that is evident when using the SKE model. By comparison, both the RNG and Realizable models are in approximate agreement with slight over-predictions of around 5% throughout the radial direction.

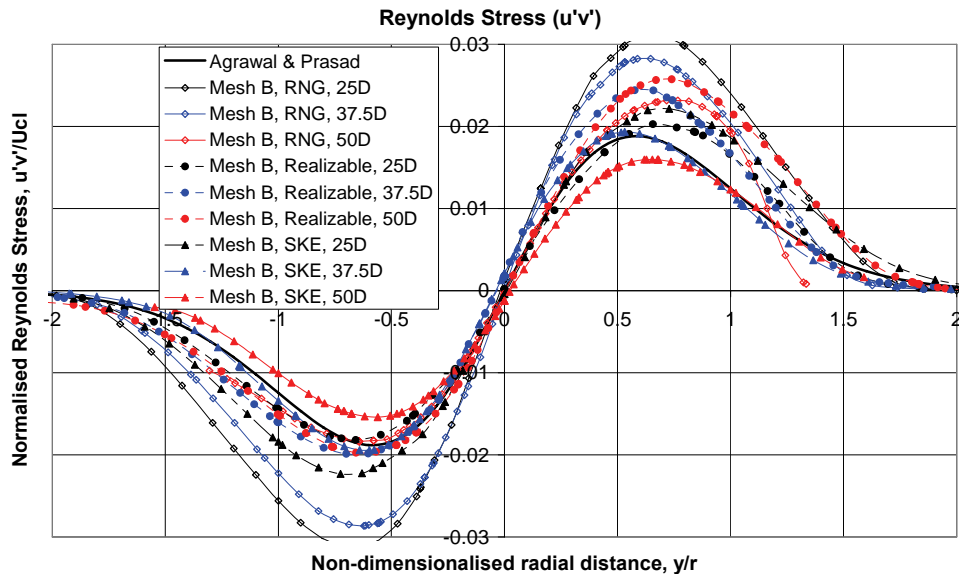


Figure 5.27 - Graph of Reynolds-stress prediction using different turbulence models

The Reynolds stresses in Figure 5.27 have been calculated using the Boussinesq eddy-viscosity, and show a large degree of scatter. Here, the SKE model and the Realizable model show the closest agreement with the profile from Agrawal & Prasad (2003), whereas the RNG model predicts peaks which are almost twice as high as the analytical profile.

Although all three models show agreement with results in different areas, the SKE model's known over-spread of radial velocity profile has been verified, and the RNG model has shown to over-predict turbulence properties in the radial direction. The Realizable turbulence model has, on average, been shown to be more consistently accurate over most of the criteria, and from a practical standpoint, has 'better behaved' convergence behaviour than both the RNG and SKE models. With this, and the results from the previous case study (where the SKE model was found to be the most deficient), the Realizable K-E model will be used for the rest of the results.

5.5.3 Thermal Analysis of Double-Hulled Tankers

In the normalised vertical temperature profile plots shown in Figure 5.28, it can be seen that there are three zones in the vertical profile:

- A lower zone from the floor to a height of 5 metres ($h/h_0 \approx 0.2$), where the temperature falls away towards the floor temperature;
- A central zone ($0.2 < h/h_0 < 0.75$), where the temperature gradient is roughly constant, or according to a slightly inverse power law;
- An upper zone ($h/h_0 > 0.75$) where the temperature profile increases markedly towards the deck.

The increased near-wall temperature in the lower zone shows the effect of radiative transfer as covered in Section 2.2.8, whereas towards the ceiling, different effects occur. The relatively sharp increase in temperature gradient near the ceiling coincides with the lower edge of the ceiling-mounted structural frames. These frames obstruct the longitudinal re-circulation of air, and as the air between the frames is not involved in the large scale recirculation of air deeper in the tank, it acts as an insulating layer which builds up heat from the deck immediately above, losing heat only by entrainment from larger-scale recirculation at the lower edge of the web frame. Where the upper web-space is connected to an exhaust vent, the steep linear temperature gradient is not evident, with the profile instead increasing more gradually until near the wall; this comparison can be seen in Figure 5.29 below, which also shows the demarcation between the different thermal zones.

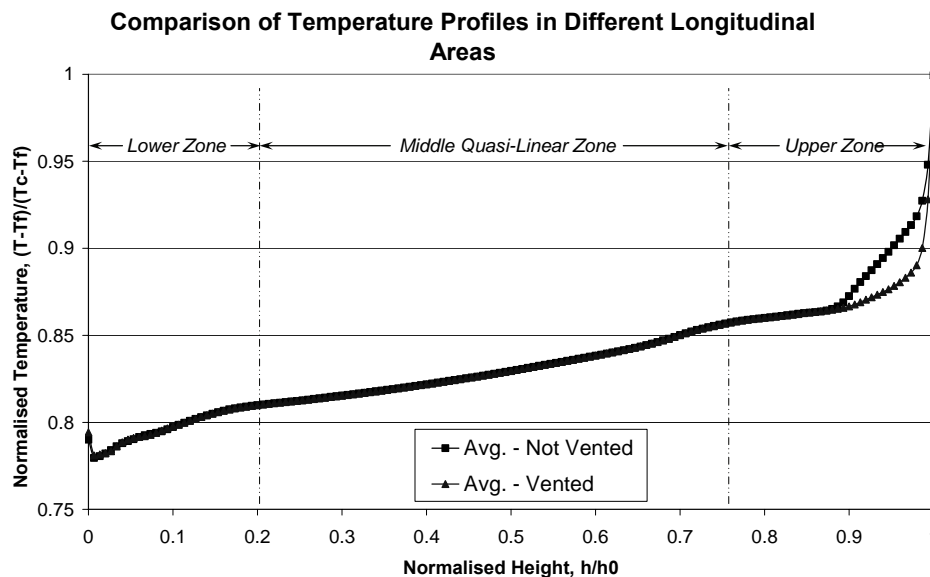


Figure 5.28 - Temperature profiles averaged between spaces defined in Figure 5.29 to show differences in ventilated and un-ventilated upper-zone spaces

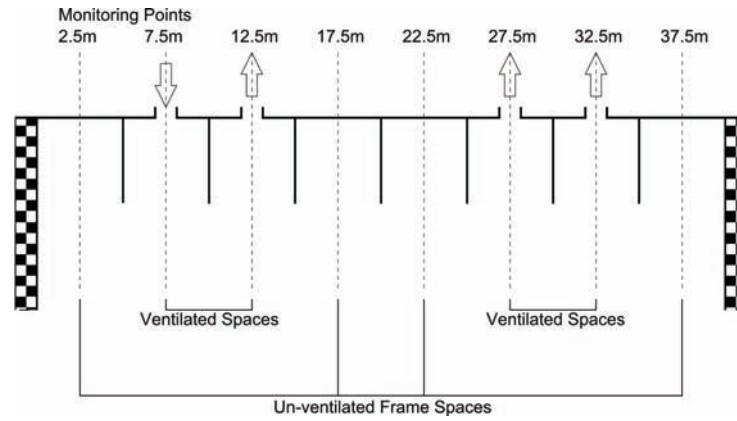


Figure 5.29 - Diagram of ventilated and un-vented upper frame-spaces

The high internal temperatures shown here agree with known observations (Rauta 2004) whereby the internal tank temperatures are far higher than the seawater temperature. The *minimum* tank temperatures at the floor are around 20 degrees higher than that of the defined sea-level temperature. Therefore, in double-hulled tankers, it can be seen that the deck temperature is dominant in defining the internal temperature conditions.

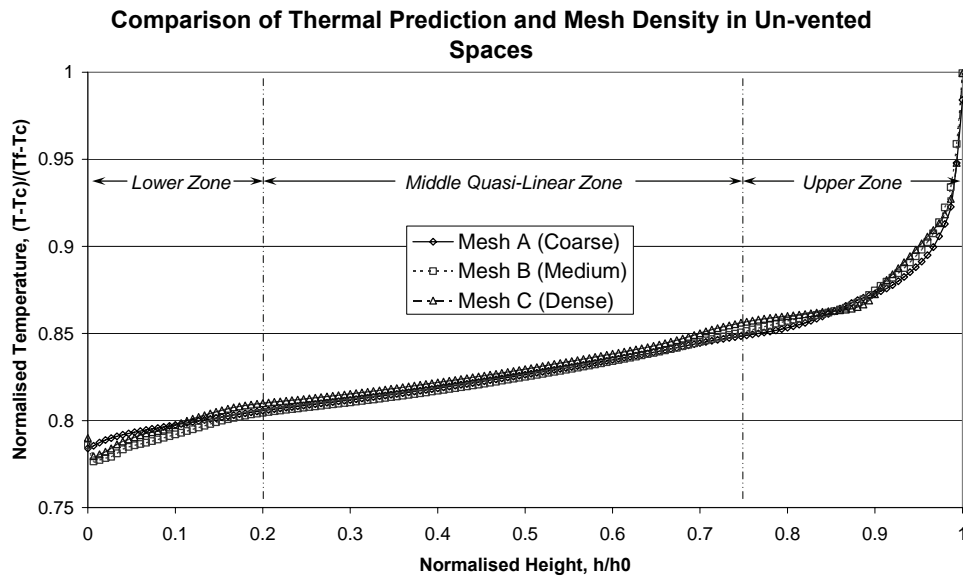


Figure 5.30 - Comparison of average temperatures in non-vented frame spaces

A comparison of temperatures in non-vented frame spaces (described in Figure 5.29) can be seen in Figure 5.30 above for the different meshes. The differences between the meshes are slight, with an absolute difference of around 0.25K near the ceiling at $h/h_0 = 0.95$. The two higher density meshes (B & C) also show greater agreement with each other compared to mesh A, indicating that the numerical predictions are converging at the higher mesh densities. Figure 5.30

shows that the thermal case is largely mesh insensitive, and so the mesh requirements are dictated mainly by the convective prediction and y^+ concerns.

Examination of Different Temperature Conditions

In order to find a thermal case most likely to result in a large temperature gradient (and thus more likely to result in thermal stratification), a group of simulations were performed for different thermal conditions, shown in Table 5.3.

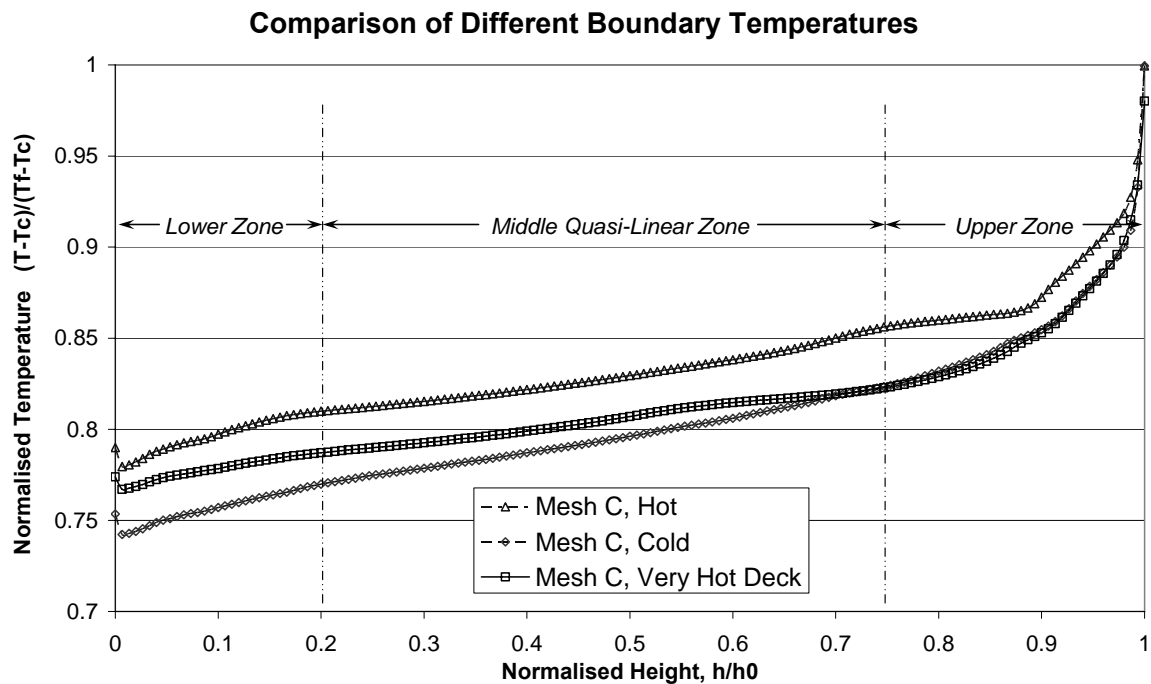


Figure 5.31 - Comparison of different thermal simulation cases

Figure 5.31 shows the non-dimensionalised results of the three different thermal cases in the non-vented frame areas, where it can be seen that despite the disparity between the deck and floor temperatures, the temperature across the majority of the profile remains between 0.75 and 0.85 of the total temperature differential between the ceiling and floor, reaffirming the dominance of the deck temperature; for all three cases, the absolute temperature difference across the quasi-linear zone is between 1 and 2 degrees.

Of interest is that although the temperature differentials are different, there is no major indication of a specific stratified layer, with the ‘Very Hot Deck’ case remaining approximately linear over the majority of the temperature profile.

Comparison to Densimetric Differences

The relatively minimal temperature gradients from the thermal analysis suggests that when compared to the densimetric situation with a layer of heavy vapour, the physical effect of the

temperature field may be negligible in comparison to the momentum of the jet as well as compared to the expected stratification strength of the VOC vapour.

To quantify the strength of the temperature field, the Richardson number defined in Equation (2.10) for temperature gradients is used to determine the Ri across the quasi-laminar zone defined above.

Table 5.7 - Comparison of relative gravities and Richardson numbers for different deck temperatures in quasi-linear zone based on $u = 5\text{m/s}$

Case	T_1	T_2	g'	Ri
Cold Deck	24.25	25.60	0.0447	0.0297
Hot Deck	45.25	46.42	0.0361	0.0240
Very Hot Deck	60.42	62.05	0.0479	0.0318

The resulting Ri is two orders of magnitude below unity, suggesting that the thermal field alone has a negligible effect, i.e. that the flow will be convection dominated.

In comparison, the (Boussinesq) reduced gravities of both cases are vastly different (butane has a reduced gravity of 10.2), and the stratified layer caused by the heavy Butane gas results in a much higher Richardson number, indicating a strong and stable layer is present, and implies possible ventilation difficulties. Because of the vast difference between the thermal and the densimetric strengths, it can be assumed that the thermal conditions inside the tank are unimportant during gas freeing.

5.5.4 Inlet Conditions

As seen in the mesh sensitivity (Section 5.5.1), the initial region of the jet is subject to a large velocity decay above that which is exhibited by a free jet. This is not necessarily a sign of simulation inaccuracy, but a sign of the inaccuracy of the *assumption* in the analytical model used as a basis for comparison. The underlying assumptions of the self-similar jet profile is that the velocity profile just upstream of the inlet is that of a developed turbulent velocity profile, and that the jet is unconfined. The developed turbulent velocity profile is central to most studies of free jet experiments, and affects the development of the initial jet region. The confinement of the jet front after emerging from the orifice also affects the development of the jet and turbulent predictions. Both of these assumptions are not applicable in the test case geometry examined here. However, that doesn't necessarily mean that comparisons to jet profiles are irrelevant, but instead introduces additional uncertainty. This can be mitigated by examining the prediction of different inlet velocity profiles (Figure 5.32).

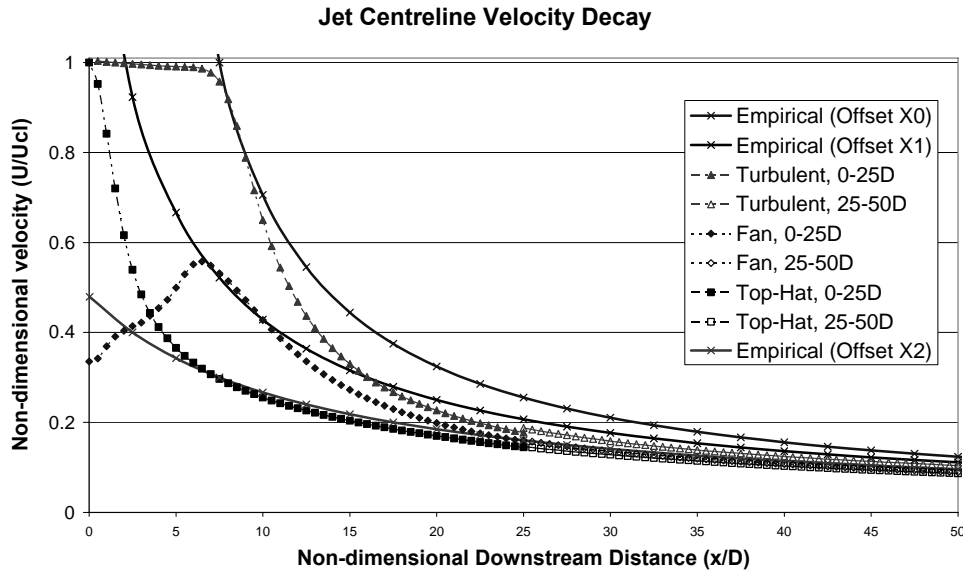
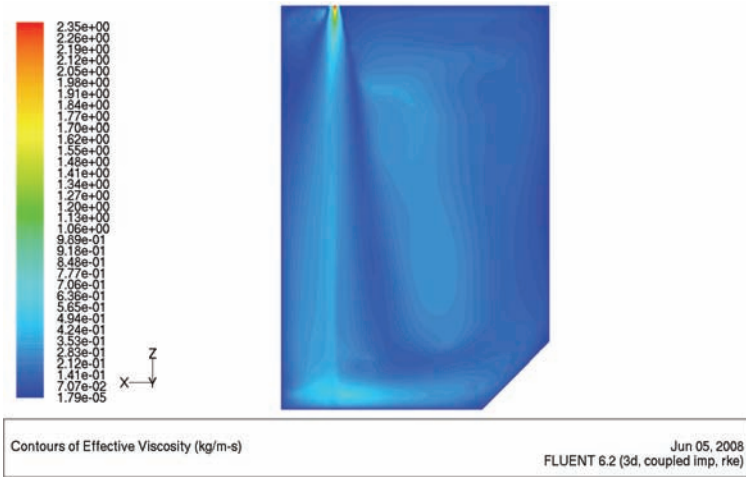


Figure 5.32 - Comparison of centreline velocity decays resulting from different inlet velocity profiles (Equation (2.77))

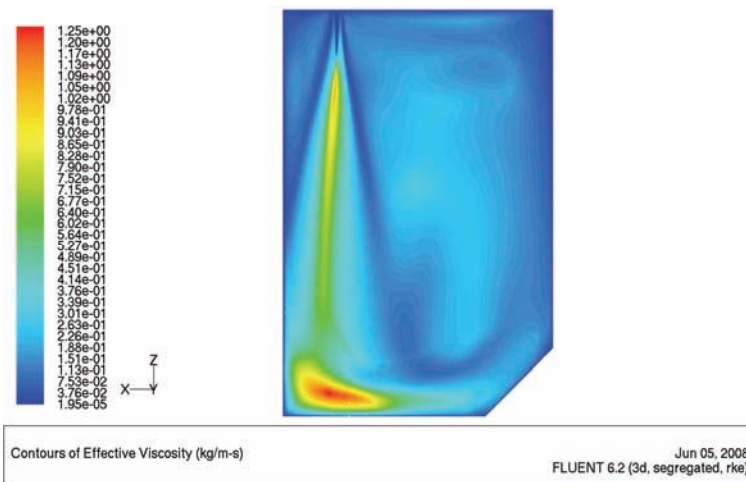
The centreline velocity decay shows the most difference between the simulations. The top-hat constant-velocity profile has an extremely short initial region in comparison to the turbulent-velocity profile. The fan velocity profile yields an unusual velocity decay curve in the initial region, due to the low centreline and high peripheral velocities, which converge some distance downstream (depending on the shear layer growth) at the end of what would be the potential core in a standard jet.

The lack of potential core region in the ‘Top-Hat’ profile is primarily due to a single cause, which is related to the profile of turbulent statistics across the inlet as opposed to the velocity profile. Although the constant velocity distribution across the inlet will produce higher shear at the periphery, the constant *turbulence* distribution results in a distorted development of the jet. Inside the pipe or channel before the formation of the jet, the distribution of turbulent viscosity and Reynolds stresses are at the lowest in the centre of flow, and highest near the walls, and as the flow is projected from the orifice, these conditions play a part in the evolution of the initial region of the jet, leading to the characteristic velocity decay curve. However, with the imposition of a constant turbulent condition, the initial region evolves differently. If the prescribed turbulent intensity is too high, the jet will exhibit high amounts of turbulent diffusion reducing the potential core length. If the turbulent intensity is too low, the jet will form an unduly long potential core.



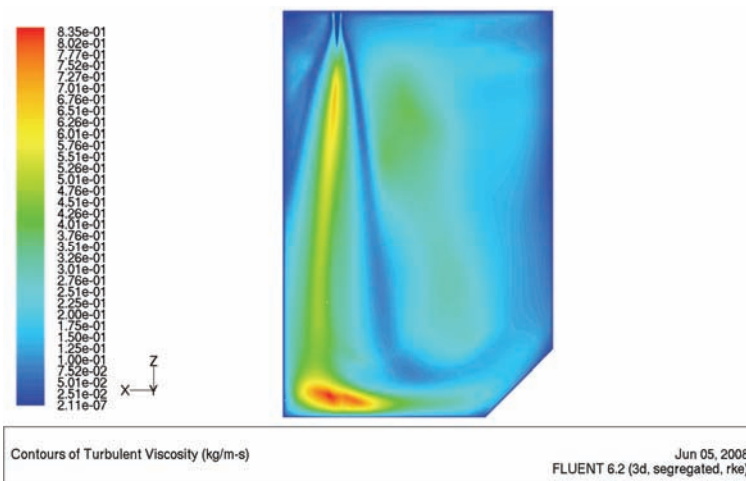
Top-Hat Inlet Profile

Constant turbulence definition at inlet creates high amount of turbulent viscosity, leading to early breakdown of centreline velocity, resulting in a short potential core.



Turbulent Inlet Profile

Here, the profile has low levels of turbulence in the centreline, making it possible to see the characteristic shear layers converge.



Fan Inlet Profile

The primary difference compared to the turbulent inlet profile is the velocity profile, whereby maximum velocity occurs away from jet centre. Shear layer development is similar to the turbulent condition.

Figure 5.33 - Comparison of turbulent viscosity between different inlet conditions

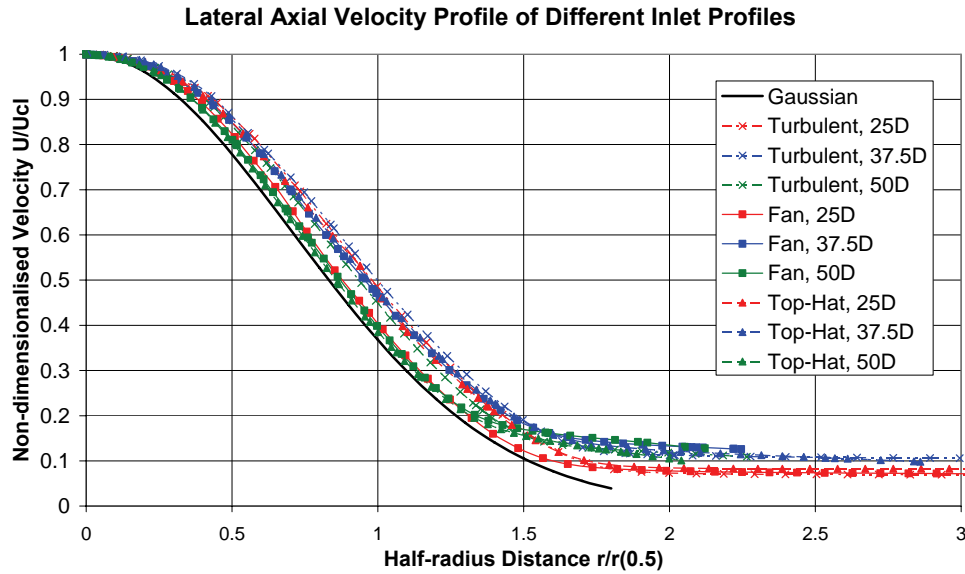


Figure 5.34 - Comparison of downstream axial velocity profiles resulting from different jet inlet profiles

The axial velocity profiles in the self-similar region are similar for most simulations, with slight over-prediction in comparison to the Gaussian profile of Agrawal & Prasad (2003). Of minor interest is the distribution of axial profile in the 37.5*d* location; most of the jet predictions in this region have a higher degree of over-prediction (10%, compared to <5% for the downstream locations). This may be partly due to geometric conditions - the jet is almost wall-bounded on one side, restricting the amount of spread along that direction, which encourages the jet to bulge out in other directions to conserve momentum.

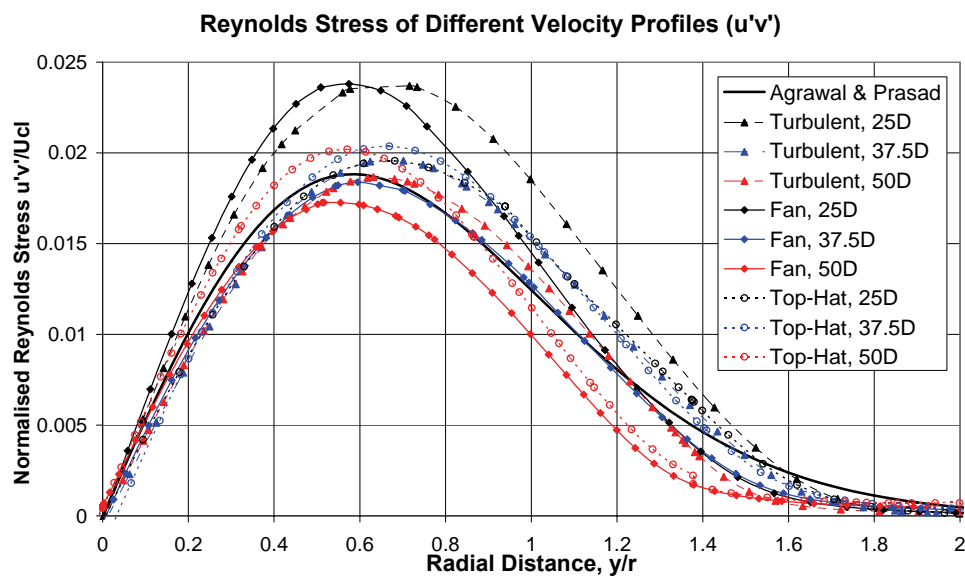


Figure 5.35 - Comparison of Reynolds stresses in the self-similar region from different jet inlet profiles

The Reynolds stress graphs are shown in Figure 5.35. The majority of plots are within the vicinity of the derivation from Agrawal & Prasad (2003). Both the turbulent and fan profiles show higher predictions of Reynolds stress in the $25d$ downstream location; however this is still before the zone of self-similarity, indicating that the jets are not yet self-similar. Further down-stream predictions ($37.5d$ and $50d$) are within 10% for the turbulent inlet profile case.

5.6 Results 2 - Analysis of Gas Freeing

Previous sections have covered the boundary conditions and the sensitivity of assumptions surrounding them (heat transfer and inlet profiles). The focus of study now moves onto the actual gas-freeing operation itself.

The progress of the gas-freeing operation depends on the “severity” of the initial state prior to beginning the gas-free operation. In an ideal case, the contents inside would be fully mixed, whereas the worst-case scenario would involve oil vapours forming a stable, stratified layer at the bottom of the tank. It is this worst-case scenario which will be examined here, under a series of different configurations.

5.6.1 Preliminary Examination of Gas-Freeing

In order to qualitatively examine the behaviour of gas-freeing processes inside the domain, initial quasi-steady-state simulations were conducted using the 3D domain. Although steady state simulations only infer flow details in the limit of $t \rightarrow \infty$, convergence of species in the flow-field during the progression of the simulation, as well as the decay of residuals, can be used to help determine aspects of the gas-freeing process. The initial state of the simulation is defined with a 14%/vol butane content stratified in the floor of the tank, and the surrounding air has the concentrations given in Table 5.4 previously.

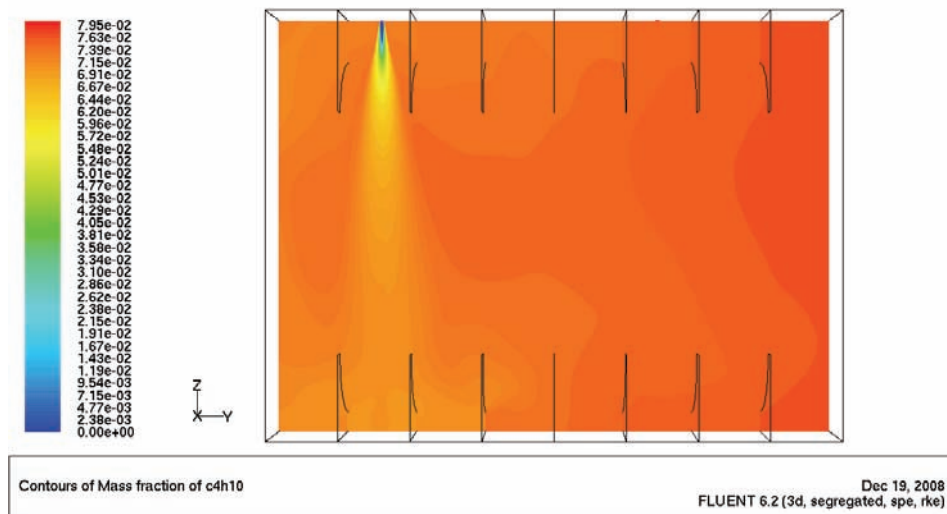


Figure 5.36 - Distribution of C_4H_{10} on plane through jet centreline

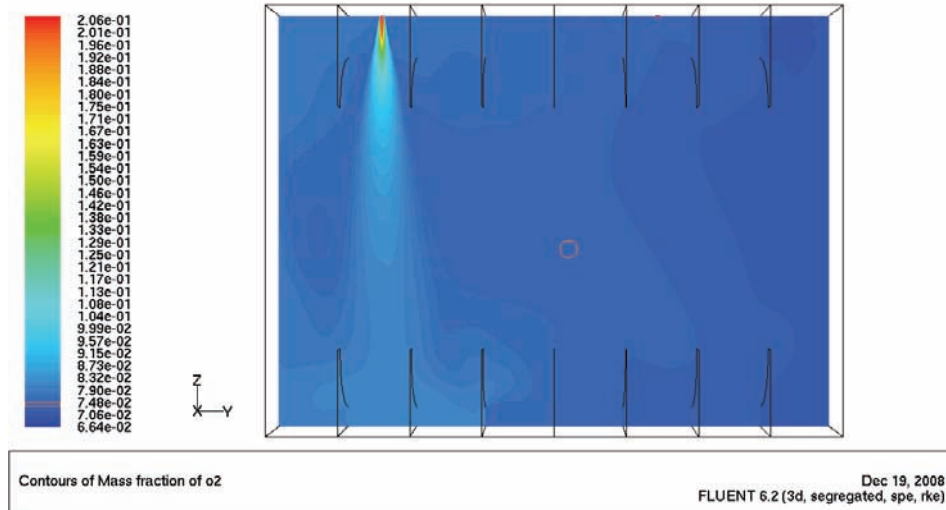


Figure 5.37 - Distribution of O₂ concentration on plane through jet

Distributions of C₄H₁₀ and O₂ from a point in the steady-state simulation are shown in Figure 5.36 and Figure 5.37 respectively; these are from a solution whereby the momentum residuals are in the order of 1×10^{-5} , with species residuals around 4×10^{-6} ; this corresponds to around 65,000 iterations from the initiation of the simulation. Even though the species residuals are relatively low, it can be seen that the concentration of butane is still relatively high, with a maximum of 7%. However, the initial stratified layer from which the simulation was started from has since been removed, and the remaining butane is distributed around the tank as would be expected from a mixing-type ventilation process. This suggests that the time taken for the removal of the stratified layer is less in comparison to the overall flushing time required to reduce gas concentrations inside the tank in this kind of geometry. The extent of the remaining butane coupled with the number of iterations passed suggests that the residence time of the VOCs in the tank is very high.

In general, the distribution of contaminants are related to the velocity field; low velocity areas are subject to poor recirculation, so concentrations are higher. This is reflected in the simulations; however, the actual range of predicted butane concentration is quite narrow, with maximum and minimum mass fractions of 0.0818 and 0.0705 respectively - there are no regions of significant butane concentration in areas of low velocity; distributions at floor level are compared to the local velocity magnitudes in Figure 5.38.

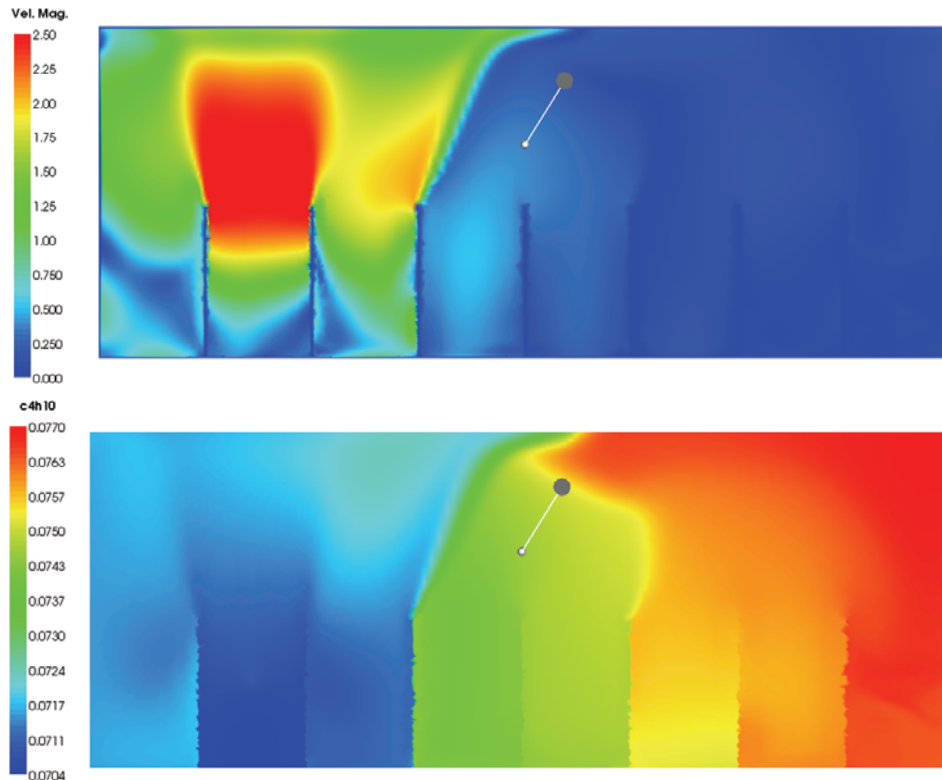


Figure 5.38 - Filled contour plots of velocity magnitude (top) and butane concentration (bottom) of slice through tank at 0.5m from floor

This initial simulation shows that it is possible to gas-free a tank using jet gas-freeing methods, but due to the low air change rate, the vapours are still resident for long periods of time as suggested by the steady state simulation. Unsteady simulations will provide a better representation of the gas-freeing process as well as helping to determine key points in the process, such as the removal of the stratified layer, and decay rates as time passes.

5.6.2 Examination of Modelling Assumptions

Due to the encountered high requirement of computational resources required for the previous 3-dimensional simulation (several weeks of computation for a single 3D steady-state run on an 8-core computer), simulating such a long process like gas-freeing is difficult. To circumvent this difficulty, the 2D mesh (Section 5.3.2) will be used. Also, the results from (Section 5.5) allow justification for a number of further assumptions to be made in order to reduce the resource overhead.

Assumption of adiabatic conditions and the absence of radiation

As seen in Section 4.0 and in Chow *et al.* (2005, Appendices), thermal boundary conditions are important when studying buoyancy-driven ventilation. However, as seen in Section 5.5.3, the effects of radiation and thermal effects in a modern, double hulled tanker result in a vertical temperature profile which has a limited degree of variation of around 3 degrees in the majority of

the tank (Figure 5.30 and Figure 5.31). Because of the limited thermal gradients and the fact that due to the gases involved, densimetric differences between the VOC vapours and flue gas are an order of magnitude larger than those brought about by thermal buoyancy, the tank can be assumed to be adiabatic, and radiation ignored.

Idealisation of VOC Vapours

As shown in Section 5.4.7, a number of VOCs can exist inside a tank depending on the grade of crude oil carried. Simulating many different types of vapour would require the conservation equations to be solved many times, so to reduce CPU overhead a single representative heavy gas is used. Although hexane (C_6H_{14}) is the heaviest gas, it is unlikely to evaporate from crudes in large quantities due to its high boiling point; instead, n-butane is a much more representative vapour, and will be used in the simulations here.

5.6.3 General Gas Freeing Characteristics

The overall process can be described in a series of distinct phases:

- Jet entry into tank (beginning of gas freeing)
- Jet impingement on layer
- Total erosion of stratified layer
- Vapour transport to exhaust vent
- ‘Gas-free’ reached

The first two phases occur rapidly, requiring the jet enter and reach the layer. Whilst these two phases occur within the first thirty seconds, the time taken to erode the stratified layer can be on the order of an hour depending on the amount of gas in the layer, and the shear rate (which is dependent on the impingement velocity); the time taken to reach gas free can take many more hours.

The developed flow-field inside the tank contains a number of characteristic features. Jet entrainment and sideways shear creates a large scale “primary vortex” which helps to transport and mix vapours in the far field, away from the jet. Secondary eddies form between the frame spaces, driven by entrainment from the primary vortex. Figure 5.39 below shows field plots of the flow-field, highlighting these characteristics.

Table 5.8 - List of Simulations

Phase Name	Flow Rate (m ³ /hr)	Mean Jet Velocity (m/s)	Notes
3B (NoFBE ^A)	14,290	50.0	14% Butane
3B (FBE ^B)	14,290	50.0	14% Butane
3B (FBE, RSM)	14,290	50.0	14% Butane; Reynolds Stress Model
3C (No FBE)	7,110	32.5	14% Butane; 15m Ducting @ 0.278m diameter
3C (FBE)	7,110	32.5	14% Butane; 15m Ducting @ 0.278m diameter
3D	21,440	75.0	14% Butane, higher flow rate
3F	14,290	50.0	4% Butane
3H	14,300	50.0	2% Butane; Initially fully mixed
3I	14,300	50.0	4% Butane; 2m tall structural frames at base of tank
3J	71,660	25.3	4% Butane 1m diameter jet entry; high flow rate

^A NoFBE - Epsilon-equation buoyancy extensions not used

^B FBE - Epsilon-equation buoyancy extensions enabled

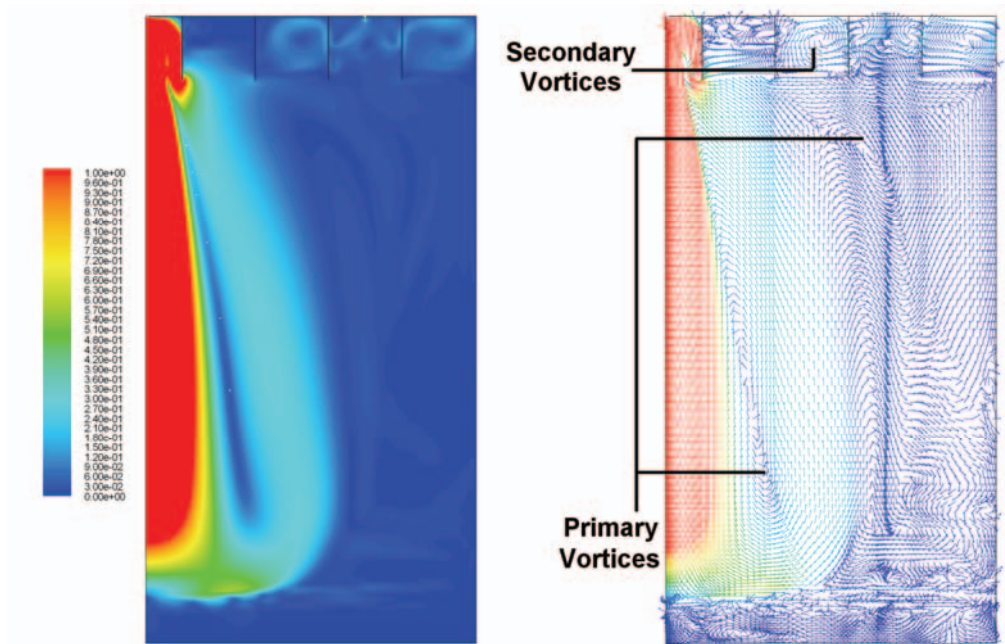


Figure 5.39 - General description of flow-field and dominant vortices; vector plot uses same colour scale

5.6.4 Removal of Stratified Layer

The process of stratified layer erosion is dominantly shear-driven. Due to low ratio of jet impingement area compared to layer surface area, there is sufficient volume of air in the tank to enable the formation of large scale eddies in the tank which are driven by entrainment of the jet and lateral shear by air that has impinged on the layer. The latter is an important shear mode, because on board oil tankers, the jet is typically mounted on the deck so that the distance to the stratified layer is great, and that any air jet will spread out and lose kinetic energy due to entrainment, which could affect layer erosion.

Simulations 3B to 3D are initiated with a 4.8m thick layer of butane at the base of the tank, which corresponds to around 14% of butane. Table 5.8 shows the specifications of each simulation; the jets in simulations 3B and 3D are supplied from the deck, whereas 3C is supplied into a duct 15m into the tank. Due to the large amount of butane, determination of the stratified layer heights can be determined by the maximum density gradient:

$$h = \text{MAX}\left(\frac{d\rho}{dz}\right) \quad (5.9)$$

Data from this analysis are subject to the limited discretisation by the meshing, which manifests as a slightly stepwise variation in the layer height.

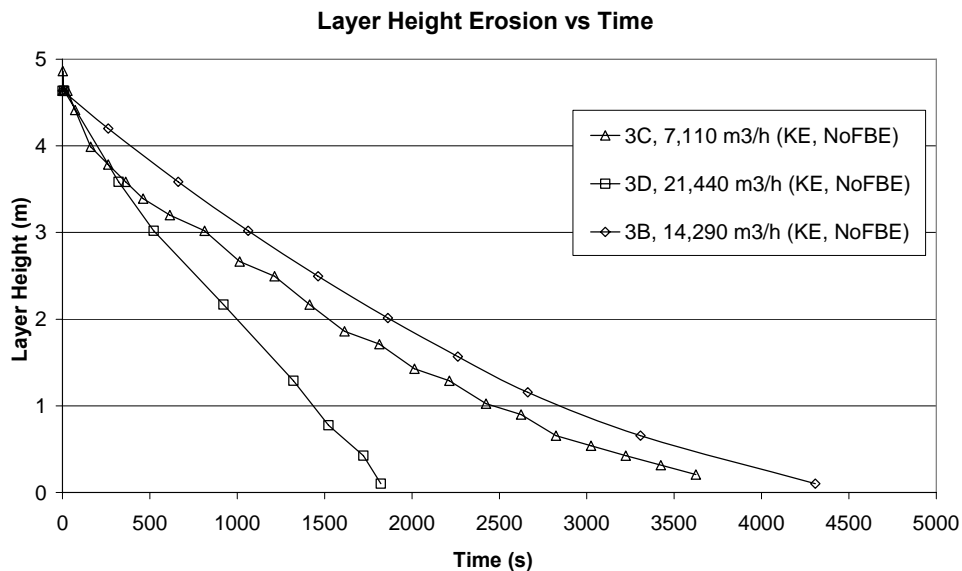


Figure 5.40 - Plot of layer heights versus time during gas free operations with different initial conditions

Figure 5.40 shows that the erosion of the layer is very slightly curved over most of the period, with erosion rates decreasing slightly towards the end of the process. By passing the jet through a 15m duct and directing a stronger jet at the layer, it can be ventilated marginally faster,

although this affects the effective flow rate due to pressure losses through the ducting. Using a higher volume flow rate fan, the layer erosion time can also be reduced substantially even though the jet supply is at deck level.

Effect of Jet Velocity

It is intuitively expected that a higher jet velocity will prove more able to remove any stratified layer due to higher momentum being brought into the impingement zone, and also a greater degree of entrainment to drive vortices that shear parts of the layer far from the impingement zone.

From Figure 5.40, it can be seen that with such large amounts of vapour, the time taken to totally erode the layer can be as long as a number of hours. Increasing the jet air velocity (simulation 3D) makes a very large difference with respect to the rate of layer erosion, halving the time to layer erosion.

It is known that tanker operators use ducting to disturb pockets of gas in confined geometry; this method of ducting has been extended to examine its ability to remove the layer, and is also shown in Figure 5.40 (simulation 3C). It can be seen that with ducting, a lower inlet-velocity air jet can reduce the time to erode the layer, but the reduced flow rate due to increased pressure loss limits the ability of the ducted jet to erode the layer faster. By comparison, this suggests that the volume flow rate is an important variable in layer erosion, but ducting the jet to increase local flow conditions near the layer can speed up layer erosion by a small amount.

Effect of Obstructions on Layer Erosion

Simulation 3I involves the addition of 2m high structural members along the base of the tank to serve as obstructive geometry in the stratified zone, with a 0.5m thick layer of stratified butane. As a result of the reduced amount of butane compared to previous runs, tracking layer height by the local maximal $d\rho/dz$ gives a poor representation due to the reduced layer thickness; also, the variation of shear through each of the web spaces varies, and due to the low entrainment at the far field, the layer height found by tracking the interface can actually increase when the layer concentration reduces due to shear, which lacks sufficient energy to transport contaminants out of the web-space due to lower rates of entrainment by the weaker secondary vortices, resulting in a thicker layer of diluted gas.

Instead, the ventilation of the stratified layer is determined by an integral of the butane mass inside the 2m tall web space, and is shown in Figure 5.41.

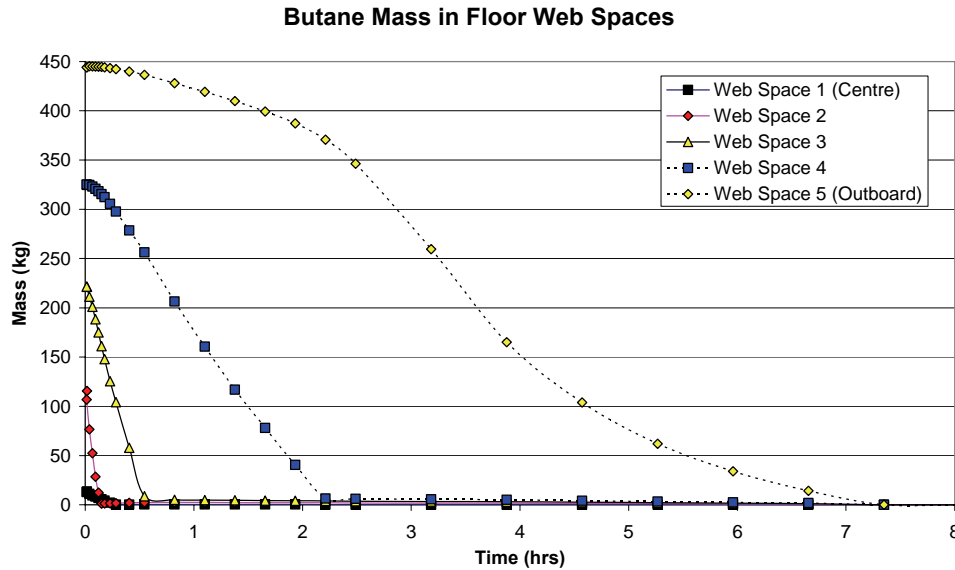


Figure 5.41 - Comparison of ventilation rates of different web spaces

Here, Web Space 1 is directly beneath the jet supply in the impingement zone; conversely, Web Space 5 is located adjacent to the outboard wall, farthest from the jet. It can be seen that areas close to the jet are ventilated relatively quickly, following an almost linear rate of ventilation. Further away, the rate of ventilation decreases dramatically, indicated by the slope of the plots in Figure 5.41. At the most remote region, the time taken to erode the layer takes around 7.5 hours, and the rate of erosion is non-linear. This confirms the necessity to adequately ventilate obstructed areas remote from the jet.

Stratified Layer Penetration

Figure 5.40 indicates that by ducting the jet, a higher degree of layer erosion can be obtained. Comparisons of the impingement zone show differences in the penetration depth depending on both the configuration and the turbulence modelling. The penetration depths and simulation configurations for simulations with high initial butane concentrations are listed in Table 5.9. The characteristic scales for the Richardson numbers are based on stratified layer thickness and velocity local jet velocities determined by a self-similar jet model given in Equation (2.77), similar to that used by Shy (1995, p45).

As covered in Section 2.4.1, the spreading rate B is typically around 6 for a free jet in the self similar region. The spreading rates for the simulations covered here varied between 3 and 5, due to a combination of confinement, downstream influences and non-similarity due to the short down-stream distance.

Table 5.9 - Simulated maximum penetration depths

Sim	Penetration Depth (m)	Predicted Jet Width	Flow Rate (m ³ /hr)	<i>Ri</i>	Spreading Rate, <i>B</i>	Notes
2A	0.94	12.28	14,676	19.55	3.8	Fully 3D, Buoyancy Extensions
2B	1.74	12.96	20,549	6.27	4.6	Fully 3D, Buoyancy Extensions
3B	1.25	8.39	14290	12.39	4.38	2D, Buoy. Ext., RSM
3B	0.6378	11.51	14290	12.42	5.13	2D, No Buoy. Ext., KE
3C	0.9206	7.97	7110	7.16	5.03	2D, No Buoy. Ext., KE
3D	0.8478	13.50	21440	14.85	3.43	2D, No Buoy. Ext., KE
3F	0.28	14.27	14290	19.12	5.21	2D, No Buoy. Ext., KE, Thin Layer

Comparison to the results of Shy (1995) and Lin & Linden (2005, p54) are shown in Figure 5.42. It can be seen that the numerical predictions are subject to much higher *Ri* than studied by both Shy and Lin & Linden. Although the results are scattered, there is a general trend similar to the $P = 0.72Ri^{-1}$ found by Shy (1995) as opposed to the flatter correlation proposed by Lin & Linden, although data points are required to examine this relationship fully.

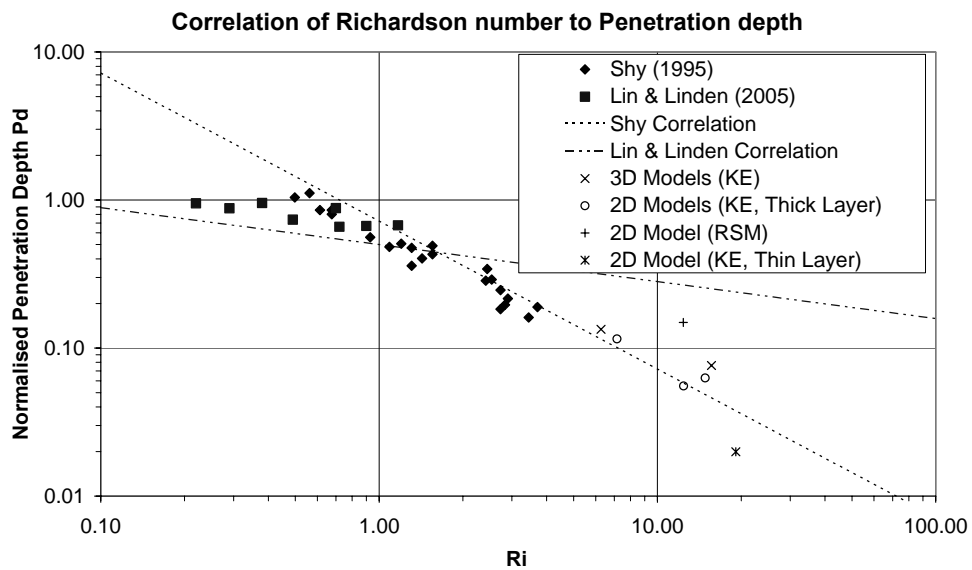


Figure 5.42 - Comparison of normalised penetration depths against Richardson number to Shy (1995) and Lin & Linden (2005)

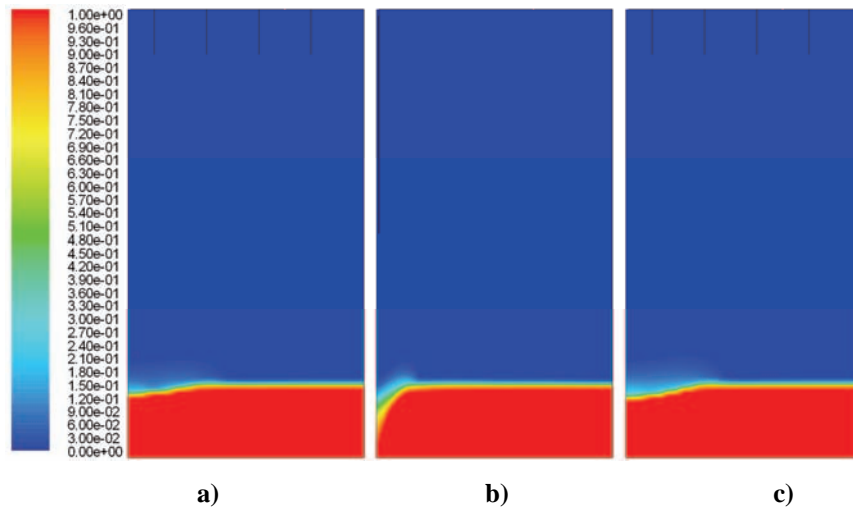


Figure 5.43 - Impingement zone C_4H_{10} concentration contour plots; a) 50m/s Jet from deck; b) 32.5 m/s ducted jet; c) 75m/s jet from Deck

The effect of the different jet conditions upon the impingement zone can be seen in Figure 5.43, which shows the dimpling effect of the jet leading edge on the stratified interface. The jets supplied from deck level both give a small amount of deflection on the layer, whereas the ducted jet supplies a higher momentum flux, punching through the layer and creating a depression inside the layer.

5.6.5 Gas Distribution During Gas Freeing

Although aspects of gas freeing, such as the overall behaviour and ventilation rate have been examined, the *distribution* of gas during the process itself must be investigated - are some critical areas of the tank subject to poor ventilation, and how is this affected by simple obstructions?

Butane Distribution

From simulation 3F Figure 5.44 shows a series of contour plots of the butane gas concentration for different periods during the gas-freeing process; Figure 5.46 shows the associated histograms for the same time steps. It can be seen that the upper web-spaces take longer to ventilate due to the obstruction of the structural frames, since entrainment is only provided through weaker secondary vortices, similar to the effect of structural blockage on layer erosion; however, once this space ventilates (after around 1.5 hours) the relative *distribution* of gas in the flow-field remains the same (Figure 5.46), with the average concentration of gas decreasing as the operation continues.

The effect of obstructions on the floor of the tank have already been shown from a general perspective, and it is known that the obstructions in the far field cause the region furthest from the

jet to decay slowly. In terms of gas distribution, the results of C_4H_{10} concentrations can be seen in Figure 5.45, with histogram plots in Figure 5.48.

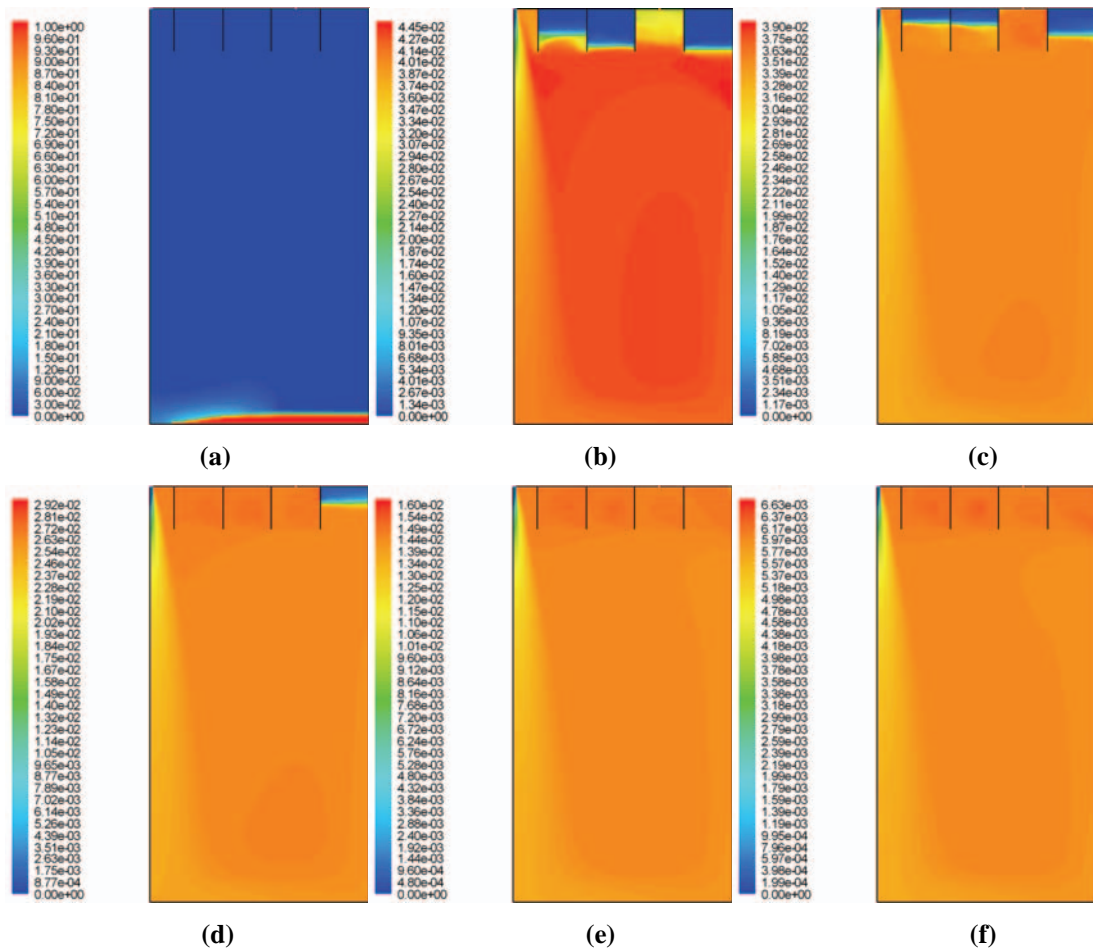


Figure 5.44 - Contour plots of C_4H_{10} concentration in simulation 3F at different times during gas-freeing; a) 20.6s; b) 773s; c) 0.5 hrs; d) 0.93 hrs; e) 1.95 hrs; f) 3.47 hrs

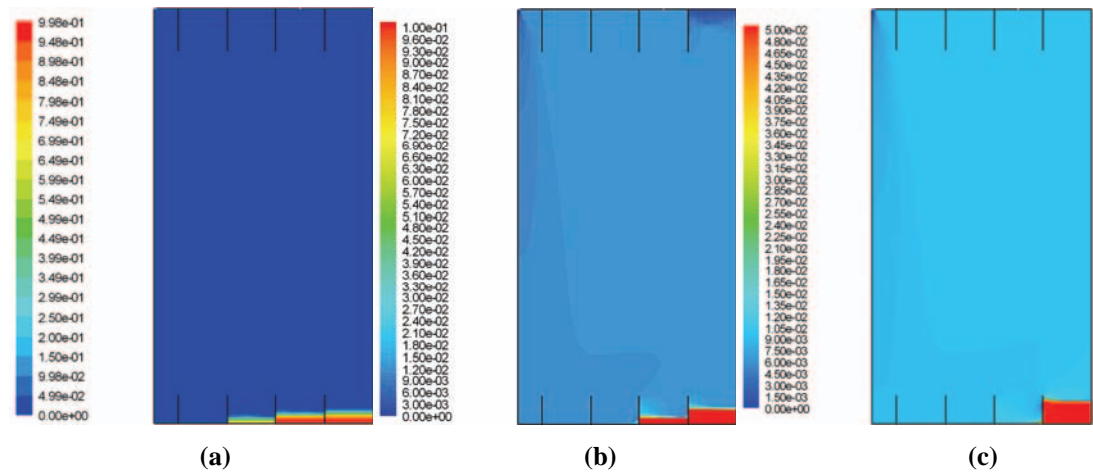


Figure 5.45 - Contour plots of C_4H_{10} mass fraction in Simulation 3I; contour range has been manually adjusted and does not represent concentration maxima in tank; a) 0.41 hrs; b) 1.79 hrs; c) 3.18 hrs

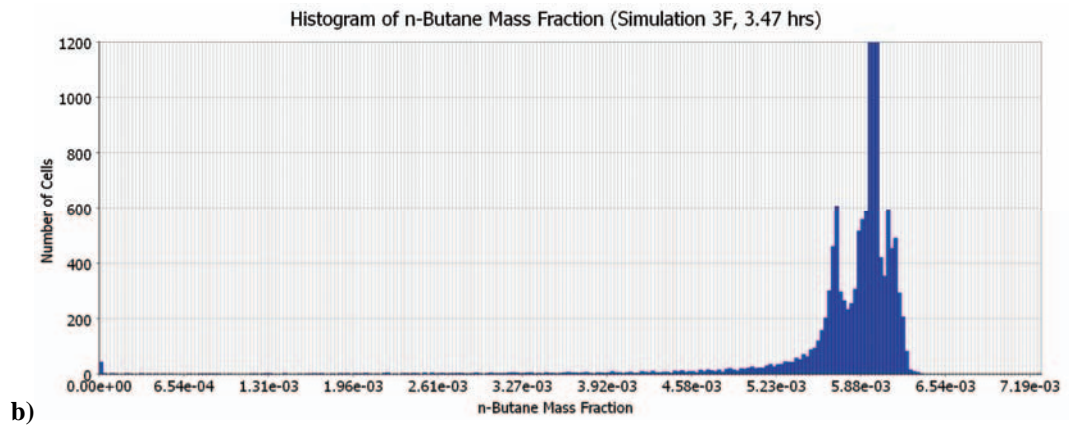
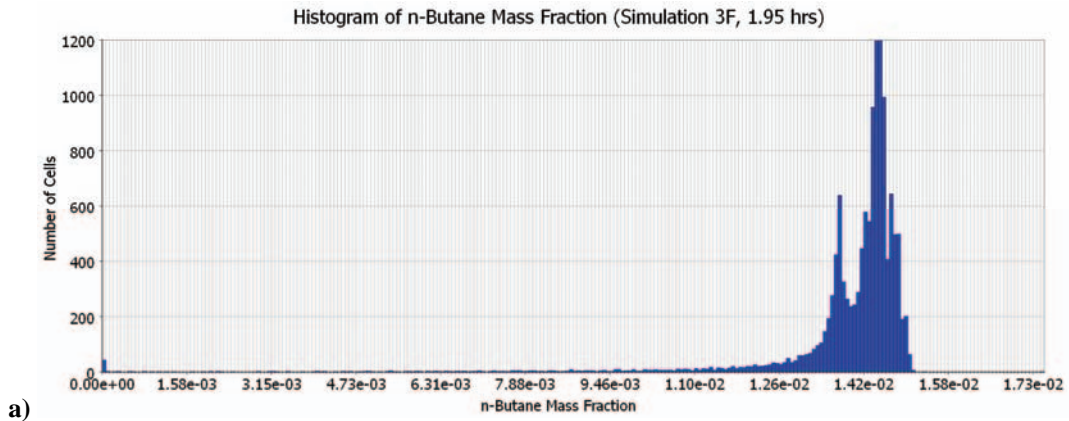
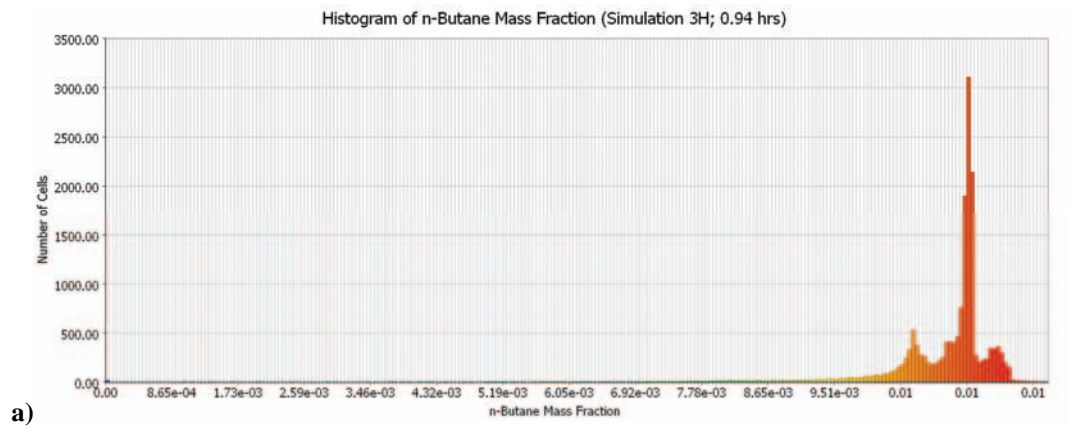
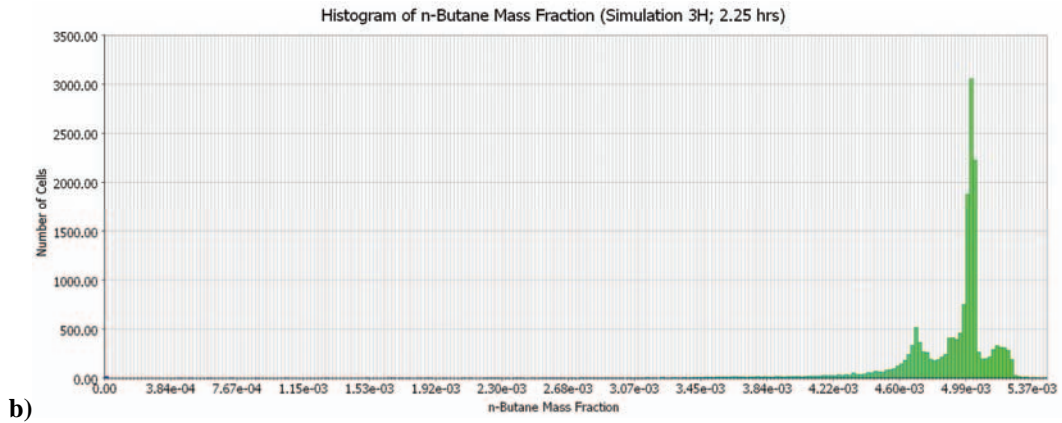


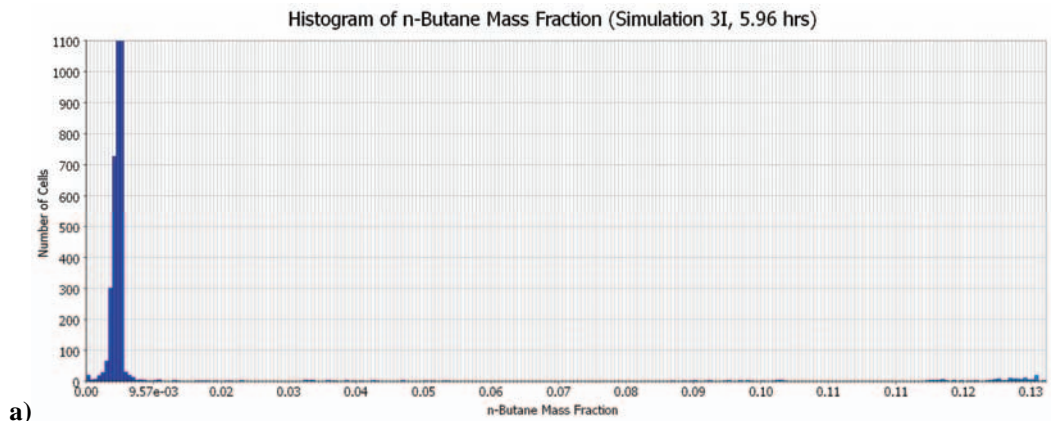
Figure 5.46 - Histogram plots of C_4H_{10} concentration at two different times from simulation 3F; note similarity of distribution with decreasing concentration



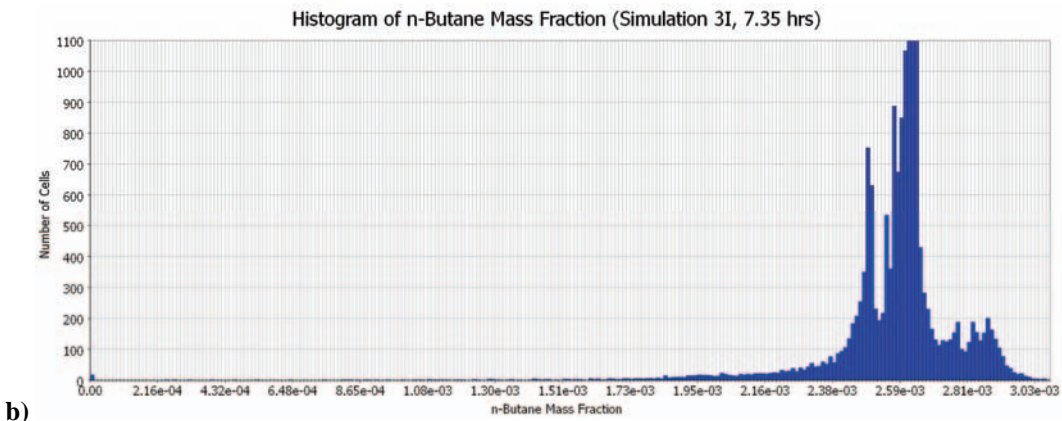


b)

Figure 5.47 - Histograms plots of C_4H_{10} concentration at two different times from simulation 3H - fully mixed initial state; again, concentration distribution is similar



a)



b)

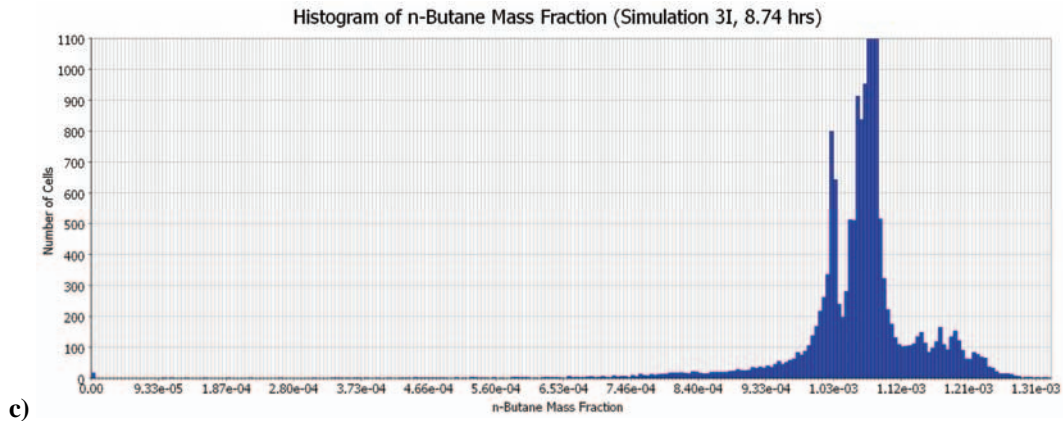


Figure 5.48 - Histograms of C_4H_{10} mass fraction from simulation 3I (blocked); after removal of layer, distribution over time also becomes similar

Like with simulation 3F, simulation 3I also attains a state of similar distribution once the stratified layer has been removed, with slowly reducing concentrations (Figure 5.48b and c); however, the time taken to reach this state is much longer due to the time required to properly gas-free all of the floor web-spaces.

Oxygen and CO_2 Distribution

Whilst the majority of the gas-freeing operation is about removing explosive vapours, re-oxygenation of the atmosphere is also required in the case of tank inspections or maintenance work on the tank interior.

When examining the effect of blockages in simulation 3I, it was shown that blockages in the contaminated zone greatly increased the residence time of butane gas. Although oxygen is not negatively buoyant like butane, the effects of blockages will still play a part due to the concentration distribution dependence on the velocity field; upper structural frames exist on all geometries in order to support the deck. Figure 5.49 shows contour plots of oxygen concentrations over three time steps; it can be seen that although the majority of the tank is slowly entraining oxygen from the supply, the upper frames are slow to re-oxygenate, in a similar trend to the upper frames taking longer to “fill up” with transported butane. Pockets of C_4H_{10}/CO_2 still reside in the upper frame web-spaces, and as was seen previously for butane removal in simulation 3I, the blockages make ventilation slow, relying on secondary vortices in the web-spaces to transfer contaminants back into the primary vortex and into the exhaust.

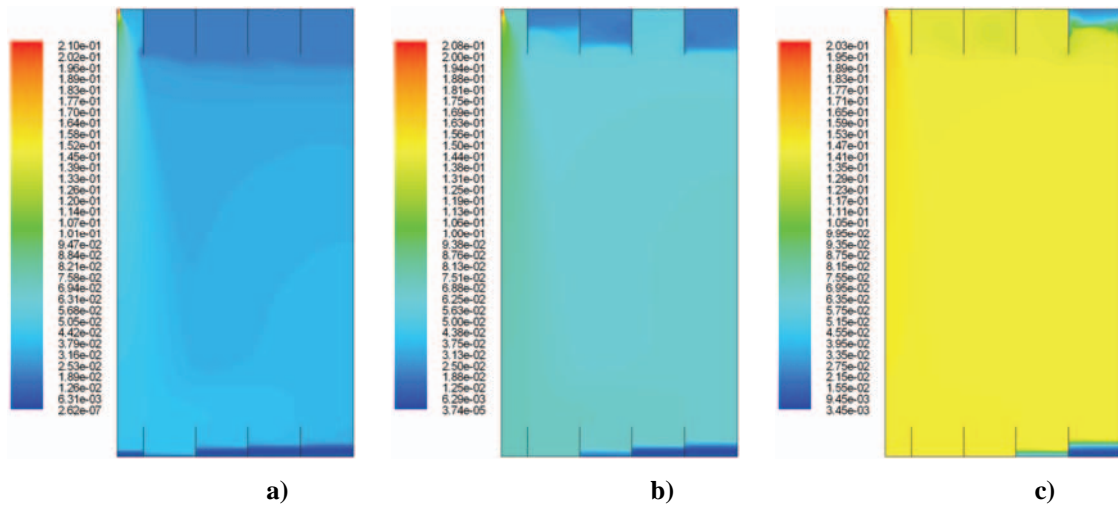


Figure 5.49 - Time-history contour plots of O₂ mass fractions; a) 440s; b) 0.41 hrs; c) 1.52 hrs

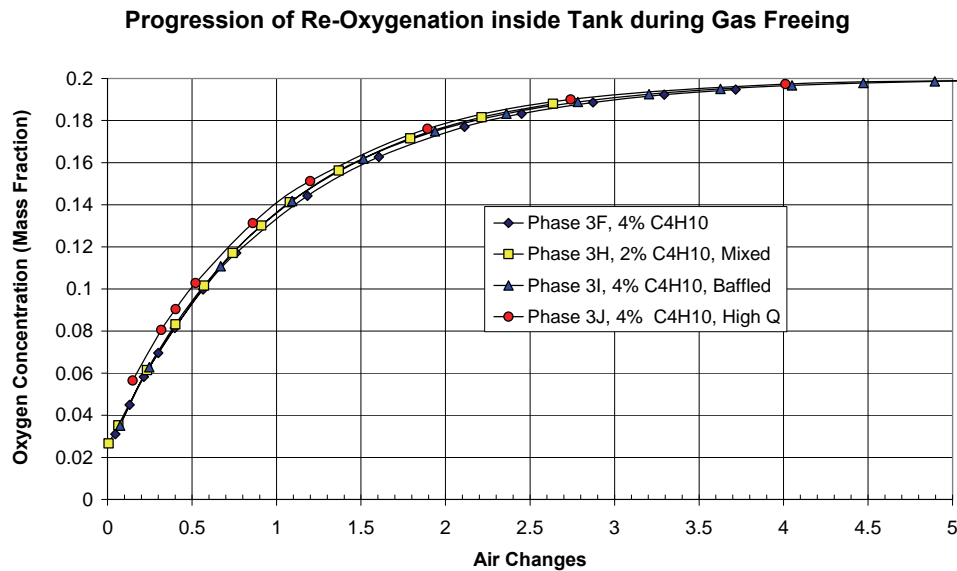


Figure 5.50 - Rate of change of global area-averaged oxygen concentration per air change

Similar to the prediction of exponential decay of butane, the average oxygen concentration at different points in time resembles an exponential function. However, the average does not highlight areas of poor ventilation. Figure 5.51 is a plot of *minimum* oxygen concentration in the tank; from this plot, it can be seen that the fully mixed simulation 3H follows a similar curve to those established in Figure 5.50 but with a time lag. The other simulations show very different trends which are indicative of the effects of structural blocking.

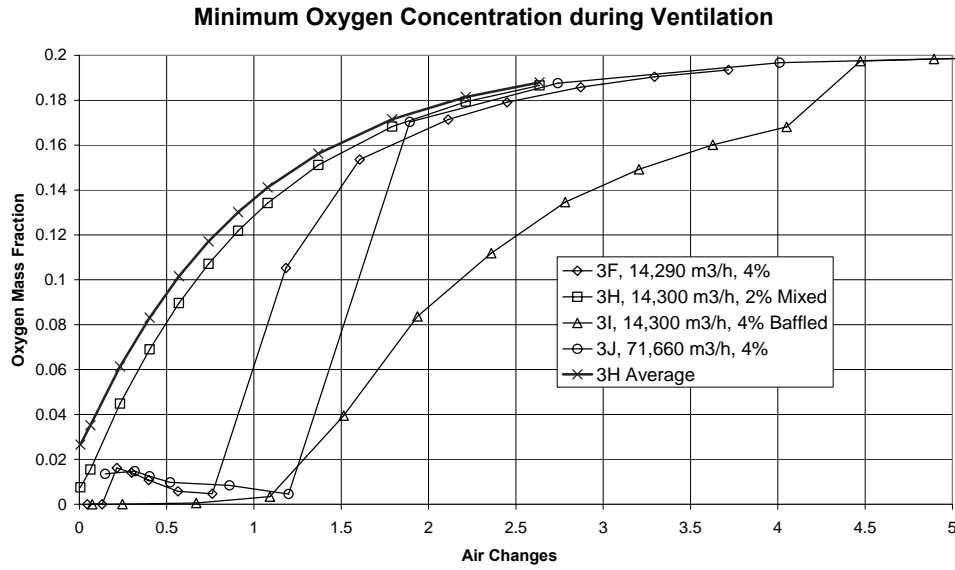


Figure 5.51 - Plots of minimum O₂ concentration during gas-freeing operation

As expected, simulation 3I requires more air changes to fully increase oxygen concentration to levels able to support life, mainly due to the time taken to gas-free and thus re-oxygenate the lower outboard web-space; oxygen cannot be supplied until all of the butane has been exhausted. In general, more than 4 air changes are required to re-oxygenate the tank.

Average carbon-dioxide levels follow an inverse trend to that of the oxygen concentrations shown previously, since both gases are neutrally buoyant in comparison to butane and so are easier to entrain and transport; this is shown in Figure 5.52.

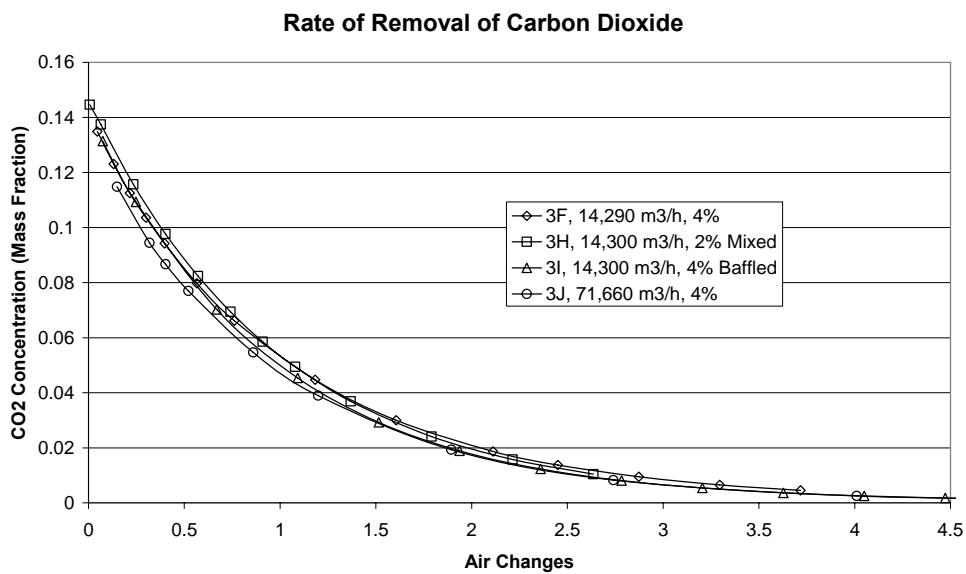


Figure 5.52 - Decay of field-average CO₂ mass fraction during gas-freeing operation

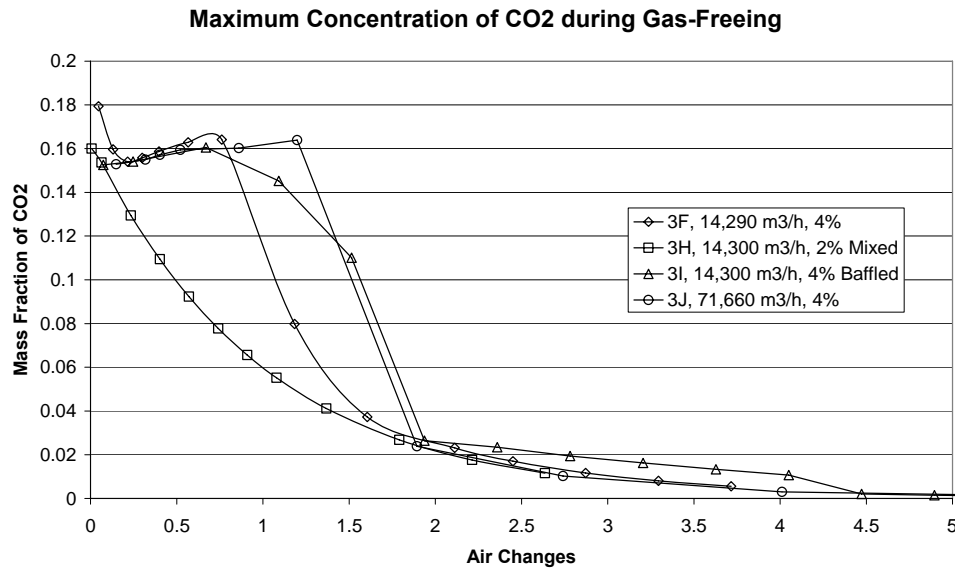


Figure 5.53 - Plot of field-maximum concentration of CO₂ during gas-freeing operation

Figure 5.53 shows the maximum domain concentrations (mass fractions) of CO₂ during the progression of the gas-freeing process. Again, simulation 3H follows a roughly regular decay of concentration due to its initially mixed state. Simulations 3I and 3J require more air-changes to remove areas of high concentration; in the case of 3I, it's due to the combination of blocking; simulation 3J follows a similar curve to that of 3F (i.e. blocking in the upper zone causes longer residence times) but has a much higher flow-rate, so although more air-changes are required, the *time* to remove the CO₂ is actually less. The increase in number of air-changes required (as opposed to only being a function of air-changes, resulting in the same curve as simulation 3F) is likely due to reliance on secondary vortices in the upper zone to entrain and transport fluid, rather than the primary vortex or impingement. Similar to re-oxygenation, CO₂ levels decrease beyond 1% in all cases after 4.5 air changes.

6.0 Discussion

6.1	Chapter Overview	145
6.2	Discussion on Aspects of the Numerical Models	145
6.2.1	Effect of Dissipation-Equation Buoyancy Extensions	145
6.2.2	Turbulence Modelling	149
6.2.3	Convergence.....	150
6.2.4	Thermal Effects.....	152
6.2.5	Impingement Zone Behaviour.....	153
6.3	Examination of Gas Freeing.....	154
6.3.1	Prediction of Gas Freeing Operations	154
6.3.2	The Initial Region	155
6.3.3	Initial Region Dynamics	157
	Effect of Obstructions.....	159
6.3.4	Determination of Initial Region Time.....	161
6.3.5	Exponential Decay Region.....	163
6.3.6	Discussion of 3-Dimensional Effects.....	165
6.3.7	Determination of Total Gas Freeing Times.....	168
6.3.8	Applicability of Regulations	171

6.1 Chapter Overview

This chapter presents the analysis of the data presented in Chapter 5. The results from the simulations using a particular turbulence model were compared with a simulation using a higher-fidelity closure scheme in order to determine the inaccuracies involved. Other aspects, such as thermal effects, convergence and impingement behaviour were also analysed. Following this appraisal of the numerical methodology and secondary effects, the gas freeing procedure was examined. The fluid behaviour during the progression of gas-freeing was demarcated into two regions. Each region of the gas-freeing progression was examined, and an analytical expression was derived to allow the approximate prediction of gas-freeing times given a set of initial conditions.

6.2 Discussion on Aspects of the Numerical Models

6.2.1 Effect of Dissipation-Equation Buoyancy Extensions

Anisotropy of turbulence in stratified environments is a well known phenomenon (Yamazaki & Osborn 1990, Garg *et al.* 2000, Werne & Fritts 2004 and Turner 1979), so when modelling such phenomena using a model where isotropic turbulence is assumed, it is expected that there will be inaccuracies. While it is well known (Sarkar 2003, Nishno 1996) that one direct influence of stratification is to reduce turbulence *production* to the point of the net P_k being negative in stronger stratification, the effect on turbulent dissipation is less clear, and some research has been conducted on ascertaining an appropriate value or function for the $C_{3\epsilon}$ variable. Although most authors have agreed that the $C_{3\epsilon}$ variable should be positive and of the order of $C_{1\epsilon}$, there is no major consensus on what the value or function should be.

Analysis of the effects here is difficult due to the combination of flows; most researchers use a single academic flow, such as sheared homogeneous turbulence, where certain properties of the flow can be used as a foundation for further calibrations (Launder & Spalding 1974, Launder *et al.* 1975); also, it is very common to use a standard K-Epsilon model as the basis of comparison. Here, the flow is far from simple, and a modified form of the K-Epsilon model (Shih *et al.*, 1994, p25) is used, whereby the C_μ parameter is variable (Equations (2.60) and (2.61)). Although a thorough investigation of turbulence model constants is outside the scope of this thesis, some comparative work has been performed in order to determine which setting gives a more accurate prediction.

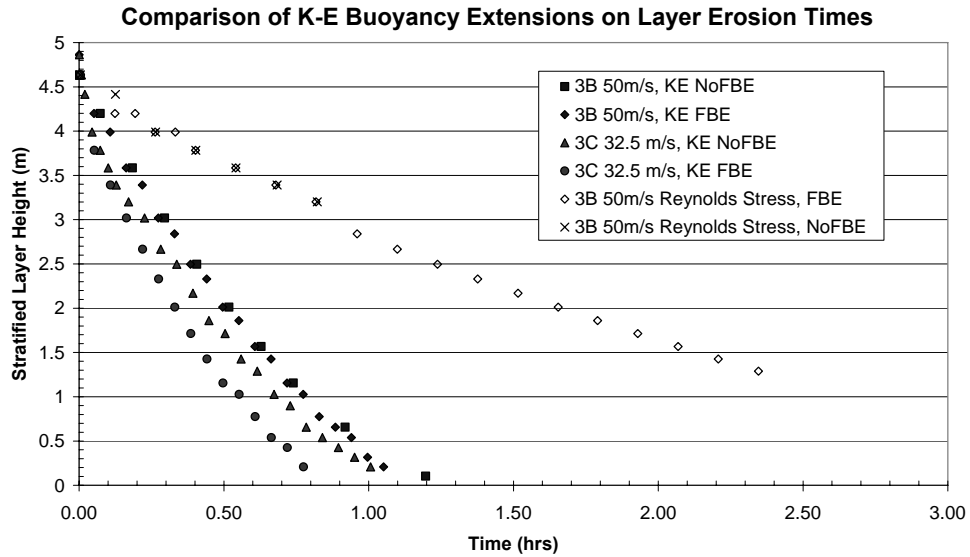


Figure 6.1 - Comparison of layer erosion rates between different turbulence models and buoyancy effects

Comparisons of layer erosion from the K-E and RSM model have been shown in Figure 6.1 - Comparison of layer erosion rates between different turbulence models and buoyancy effects. Two plots exist for each turbulence model - one using full buoyancy extensions (FBE, Equation (2.62)) in the epsilon equation, and one without.

The most evident disparity is the difference between K-E and RSM prediction in layer erosion times. Whilst all of the K-Epsilon predictions of layer erosion are in the vicinity of one hour, the Reynolds stress model predicts a much longer time which is over twice as long. The next outcome that can be seen is the relative indifference of both K-Epsilon models to the addition of the Epsilon-equation buoyancy extensions. In the Reynolds stress models, the two models coincide within the limit of resolution for this method, which is determined by the discretisation; the same is also true for the K-Epsilon case 3B simulation. Simulation 3C shows a larger change than 3B due to the closer proximity of the jet to the interface, thus higher turbulence levels are present. As the buoyancy extension decreases the dissipation, a greater amount of TKE exists, leading to faster layer erosion. Due to the naturally incorrect production of k in K-Epsilon models, the reduction in dissipation exacerbates the situation, making it qualitatively incorrect.

A similar trend can be seen in a comparison of the gas freeing ventilation curves, which are shown in Figure 6.2. Again, the addition of buoyancy extensions in the epsilon equation shows virtually no difference to the original model, and the same also follows for the K-Epsilon equation. Similar to the layer erosion times, the actual *rate* of ventilation for the Reynolds stress simulations is appreciably less in comparison to the K-Epsilon simulations, resulting the process taking just under *twice* as long as those predicted by the K-Epsilon model. Although the Reynolds stress

curves are incomplete, they appear to be following the trend of the K-Epsilon models, especially so in the initial region, but at a slower rate.

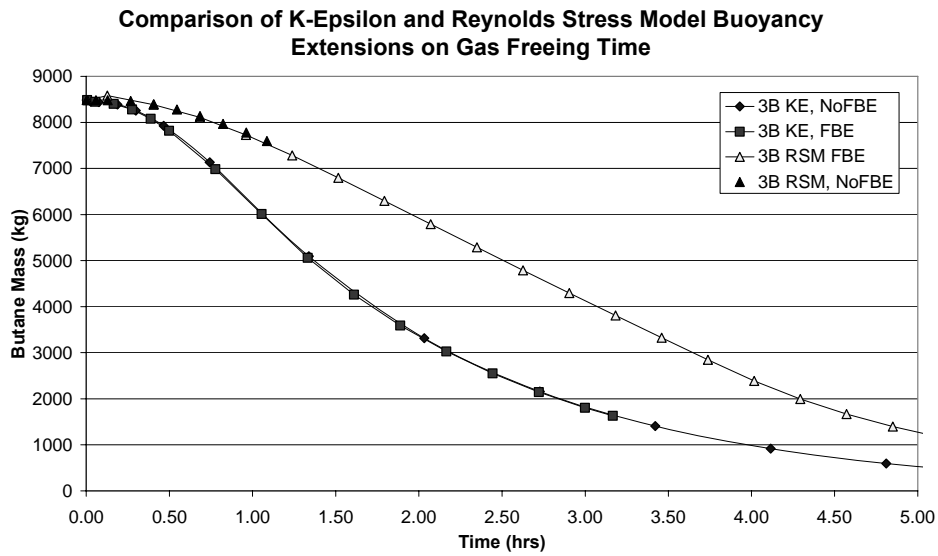


Figure 6.2 - Comparison of gas freeing ventilation curves for K-Epsilon and Reynolds stress models, with and without buoyancy extensions

Overall, the results for the simulation of case 3B suggests that the setting of $C_{3\epsilon}$ as a function of alignment of local velocity with the direction of gravity (Equation (2.62), p26) makes a negligible effect on the decay rate of C_4H_{10} vapour. The insignificant effect of the $C_{3\epsilon}$ variable on the macroscopic scale of species and heat transfer is similar to that found by Pikos (2006), who found that the addition of buoyancy extensions in the dissipation equation showed little effect on the flow-field.

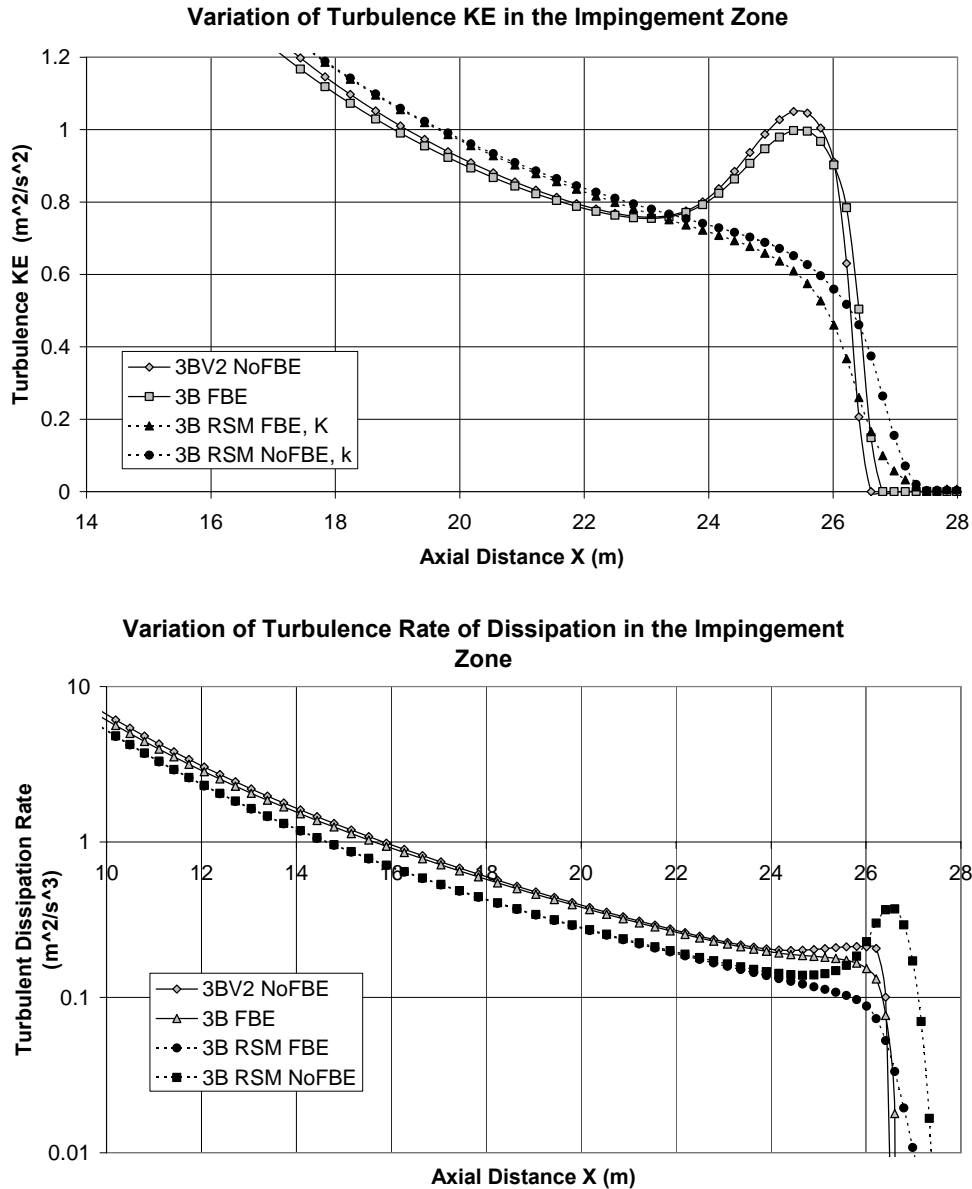


Figure 6.3 - Comparison of K (Top) and Epsilon (Bottom) in K-E and RSM models

In the approach to the stratified layer zone, the majority of the Epsilon plot (Figure 6.3, Right) are similar over the examined range, but at the stratification layer, there is a slight increase of the dissipation rate plots when buoyancy extensions are not included. The effect of the negative buoyancy source can be seen, as the transition across the layer is less sudden than compared to the simulation without the extension. Setting aside the over-prediction of k (to be discussed consequently), predictions of turbulent kinetic energy are approximately similar in the stratified zone irrespective of buoyancy extension, which reflects that with this formulation of the K-epsilon equation, buoyancy is accounted for by default.

In the Reynolds stress model, the prediction of, and the addition of the buoyancy extension, makes a small but visible difference in the rate of dissipation. The RSM simulation without

buoyancy extensions (3B RSM NoFBE) exhibits a fairly large jump in the prediction of the dissipation rate (larger than that found with the K-Epsilon equation) in the vicinity of the stratified layer, but the addition of the buoyancy extension removes this sudden increase, similar to that of the K-Epsilon prediction.

It can be seen that the $C_{3\varepsilon}$ does have some effect on the turbulence quantities in the flow but due to the incoming levels of turbulence (especially in the K-Epsilon equation) and the small scale of the $C_{3\varepsilon}$ equation on the rate-of-dissipation equation, it makes little difference to the flow and level of macroscopic mixing. It is far more likely that the effects of the buoyancy extension are more important when lower levels of turbulence are present, or in the case of unstably stratified layers when turbulence production can be driven by the unstable buoyant forces.

6.2.2 Turbulence Modelling

A comparison of the Realizable K-Epsilon model to the RSM LRR-IP (Launder, Recce & Rodi, Isotropization of Production) model was conducted previously (Figure 6.1 and Figure 6.2) where it was seen that the Reynolds stress model predicted a much slower rate of stratified layer erosion, as well as general ventilation in the exponential decay region.

Principally, both models use the Reynolds analogy in heat and mass transfer; as such, the main mechanisms in species transport are mass diffusivity and turbulent viscosity. Similar to fluid turbulence, the difference between the (laminar) mass diffusivities and turbulent (or eddy) diffusivities in fluids is several orders of magnitude, so turbulent viscosity becomes the primary numerical driver in transporting fluid species around the tank. Due to the large size of the tank, this entrainment and transport is provided by two different mechanisms - impingement transfer, and shear entrainment across the layer.

An examination of the turbulence quantities, k and ε , in Figure 6.3, showed that in comparison to the RSM model, the K-Epsilon model over-predicts the level of TKE in the impingement zone. While the addition of realizability constraints in the model of Shih (1994) ensures that the predictions maintain physicality, the tendency of the production term in the k equation to over-estimate is still a cause for concern (Figure 6.4). Here, the over-prediction is due to a known issue with the modelling of turbulence production in high strains. In the K-Epsilon model of turbulent production, the production of k is dependent on the gradients of stress gradients, whereas in the RSM the production is determined by the difference in normal stresses:

$$P_{RSM} = -(\overline{u_i^2} - \overline{u_j^2}) \frac{\partial U_i}{\partial x_i}; \quad P_{EV} = \mu_t \left(\frac{\partial U_i}{\partial x_i} \right)^2 \quad (6.1)$$

Generally, the K-Epsilon model instantly predicts a high level of production when the strain rate is high; the production in RSM is dependent on the variation of the normal strains themselves, and the difference changes slowly at a finite rate (Launder & Spalding 1972, Wilcox

1994) due to the small time required to transit the stagnation point (Laurence 2002, Hanjalic 2004). Although the Realizable model is sensitive to shear, it doesn't totally remove this unwanted behaviour, but may limit it to the upper bound determined by realizability (i.e. $2C_{\mu} \frac{k}{\varepsilon} \left| \frac{\partial U_i}{\partial x_i} \right| > 1$). As the resulting turbulent viscosities drive mass transfer, this over-prediction affects the transport and transfer of different species by artificially speeding up species transfer.

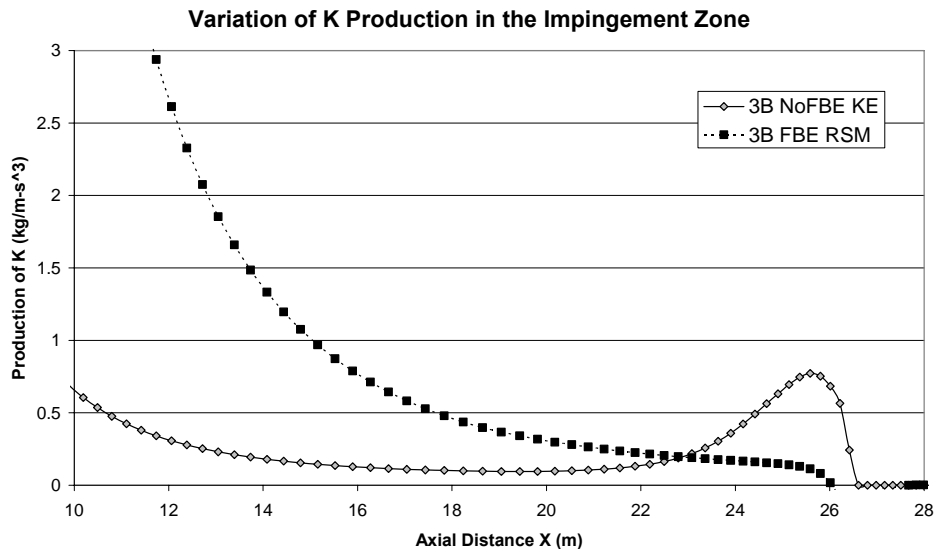


Figure 6.4 - Comparison of K Production between K-Epsilon and Reynolds Stress models

6.2.3 Convergence

The effect of convergence upon the final state of simulations and the required number of iterations required to reach the steady state varies significantly depending on the type of flow. With (thermal) buoyancy-dominated regimes such as the room ventilation case (Section 4.0), the tight coupling of numeric buoyant sources and the much longer buoyancy time scales ($(h/g')^{1/2}$, Linden 1999) and longer convective time scales due to the lower velocities involved, means that iterative convergence is typically slow, requiring a very large number of iterations in the order of 10^4 before a steady state is reached. During this period, traditional *numerical* residual reduction requirements (for example, below 1×10^{-3} or 1×10^{-6}) can usually be met without the flow being properly converged (Pikos 2006) - whilst the convective field may be converged, the thermal field driven by buoyancy changes may not be. As such, monitoring the change in temperature is generally a better method of establishing when a steady state is reached in this class of flows.

The behaviour of the flow solver for the tanker cases with the jet supplied (Section 5.0) varied depending on the physical models used. The 3-dimensional K-Epsilon model converged

fairly well for cases when convection and heat transfer were modelled. However, the introduction of a gas species modelling into the simulation negatively affected the convergence behaviour, whereby more severe relaxation was required, especially in the initial evolution of the jet, and in order to prevent divergence an appropriately small time step (in the order of 0.01s) was used.

The behaviour of the 2-dimensional cases was tamer in comparison, with the robustness of the K-Epsilon model allowing time-steps as large as 0.5s to be used after the flow field was well established; in comparison, due to the higher numerical coupling in RSMs, the limit of Δt possible was only 0.05s, a tenth of that possible in the K-Epsilon simulation.

Due to the long run times and large numbers of time-steps required to simulate the gas-freeing process (See Table 6.1), the convergence and effect on physical quantities across individual time-steps is of concern. Convergence of momentum equations, once a steady flow field is established, occurs fairly quickly due to the small changes that occur between time-steps. However, the equations which determine the change in concentration are more difficult to gauge, as the change between time-steps is quite substantial after jet impingement and the initial residual estimation was quite low. By default, the residual criterion was 1×10^{-6} , whereas in practice the species concentration residuals were typically 1×10^{-8} or smaller.

Table 6.1 - List of simulations, simulated time, final time-step and number of iterations

Simulation	Simulated Time (s)	Final Time step	Total Iterations
3B (KE)	29,783.8	69,933	1,204,979
3B (RSM)	19,537	391,628	4,662,335
3C	60,782	174,775	915,590
3D	26,304	99,416	1,782,298
3F	22,004.5	70,000	1,288,244
3H	15,595.5	55,000	782,910
3I	36,465	80,010	1,468,881
3J	6,535	20,600	483,264

After an examination of the convergence methodology, it was found that running each time-step for at least 15 iterations was sufficient to reduce the residuals, ensuring that a properly converged state was carried over to the next time-step. As the number of time steps is large, a series of poorly converged states can greatly affect the rate of change of species concentrations far more than the effects of turbulence buoyancy modifications - Figure 6.5 shows a comparison between two runs of simulation 3B conditions; the fully converged simulation adheres to the exponential decay plot, whereas the un-converged simulation lags behind substantially.

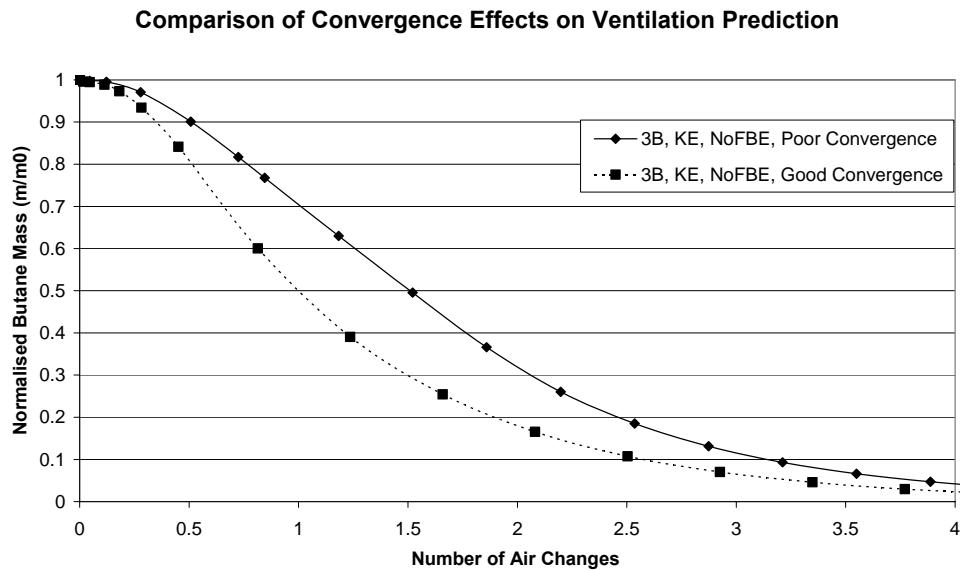


Figure 6.5 - Comparison of effect of poor species convergence on rates of ventilation

This behaviour is somewhat similar to the trend found in room ventilation scenarios, whereby residuals are not the best method in determining solution progression; instead, monitoring of physical quantities (temperature or species concentration) is a better metric.

6.2.4 Thermal Effects

It was shown in Section 4.0 that when the buoyant forces are on the order of those produced by thermal gradients, the correct prescription of thermal boundary conditions such as wall temperatures and heat losses are very important to obtaining an accurate representation of the flow field. In the prediction of room ventilation without thermal wall boundary conditions, the resulting internal scalar field was influenced greatly by the momentum sources in the room. When additional models and radiation were accounted for, the numerical model was able to produce a far more accurate profile of temperature, with the exception of a temperature defect which was due to unknown additional heat loads. Given the success of other authors using similar numerical methods (Howell & Potts 2002, Bournet *et al.* 2007), the temperature deficit suggests a failure of boundary condition prescription such as heat loads rather than a fault with the numerical accuracy. The effect of heat loading is to increase upper zone temperature, which by radiation, causes redistribution to the lower zone (Li *et al.* 1993).

Unlike the room ventilation case, the conditions inside a COT are vastly different, especially due to the designs of modern hulled tankers. Compared to the previous generation of singled hulled tankers, the thermal insulation afforded by a double hull and around 2m of void air space between them reduces the average heat transfer coefficient by almost two orders of magnitude, based on the calculations in Section 5.4.4 compared to the experimental results of

Saunders (1965). This has a very large effect on the thermal profile inside the tank; while the room ventilation study (Section 4.0) had a thermal difference spanning over 15 degrees from top to bottom, the COT had a thermal difference of only around 8-12 degrees, two thirds of which were confined to the upper zone. From a radiative aspect, the path length inside a COT is higher due to the geometric scale of the tank. The primary radiative path would likely be from the deck to the floor, so the path length aL is expected to be in the order of unity, as opposed to room ventilation cases where the path length is $aL \approx 0.1$. Also, as given in Section 5.4.5, the wall emissivity is likely to be high due to the accretion of organic compounds (oil film or oil sludge, and treated metal surfaces), further increasing the radiative transfer from surfaces. Given the high optical thickness and high wall emissivities, the role of radiation is quite strong, and with reference to the effects seen in the room ventilation case, it can be seen that the radiation will act to homogenise the internal temperature field.

The small thermal difference in modern double-hulled tankers is known anecdotally (Intertanko 2002, Rauta 2004) as well as from a more practical point of view in terms of the resulting consequences of a hotter tank, such as increased corrosion in tanks. From a physical standpoint, the small thermal gradients result in smaller buoyancy forces from density differences on the order of 0.01 kg/m^3 . Given that the density differences from the butane and atmospheric gases was an order of magnitude higher during the exponential decay region (and two orders higher during in initial region), and that the convective strength driven by the jet is sufficient to transport vapour against densimetric buoyancy (even in the lower flow-rate case), suggests that thermal buoyancy is small. Generally, flows with strong thermally-induced buoyancy can be characterised by the ratio of Gr/Re^2 greater than unity. Given that the smallest inlet Reynolds number examined (simulation 3C), based on diameter and mean flow velocity, is $\sim 6 \times 10^5$, it can be seen that the negation of thermal modelling seems justified.

6.2.5 Impingement Zone Behaviour

In comparison to previous data from Lin & Linden (2005), and Shy (1995) (Figure 5.42, p135), it can be seen that the penetration depths are higher in comparison to their experiments. Generally, the majority of the results exaggerate the impingement depths for the same Richardson number due to a combination of turbulence modelling (over-prediction of TKE in the K-Epsilon models), and possibly also due to a coarseness of discretisation at the interface. Compared to the other models with a large initial butane content, the 2D model (KE, Thin Layer) with a thin layer is an outlier from the trend marked by the other thick-layer K-Epsilon results (the 3D and other 2D results all have thicker initial butane layers, $\sim 4.5\text{m}$) suggests that end-effects of the tank cause a reduction in penetrative ability.

Although the coarseness of the data in the impingement zone precludes the examination of entrainment rates, approximate qualitative agreement is shown with the entrainment law (Equation

(2.85), p54) originally demonstrated by Turner (1979) and examined by others (Tanny et al. 1995, Cardoso & Woods 1993, for example).

6.3 Examination of Gas Freeing

6.3.1 Prediction of Gas Freeing Operations

The progression of the gas freeing operation from different simulations (Table 5.8) are shown in Figure 6.6 below. Immediately, it can be seen that a characteristic gas free curve can be divided into two regions - an *initial region* whereby the rate of decrease of gas is relatively low, and a second, much longer region, whereby the butane decreases at an exponential rate (depicted schematically in Figure 6.7).

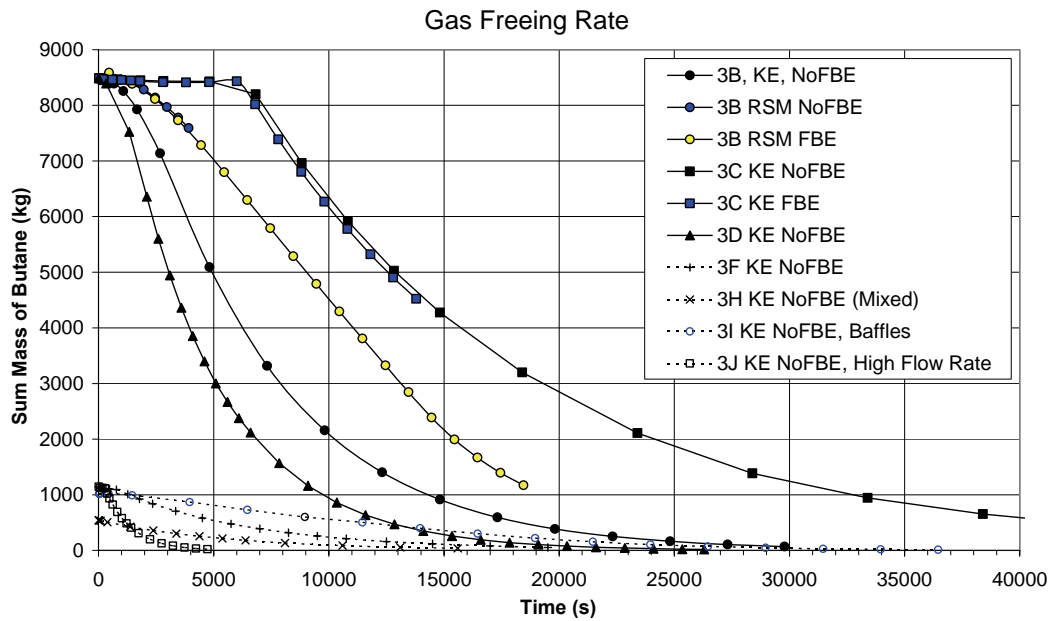


Figure 6.6 - Overlay of various gas freeing plots of mass sum of butane in tank versus time

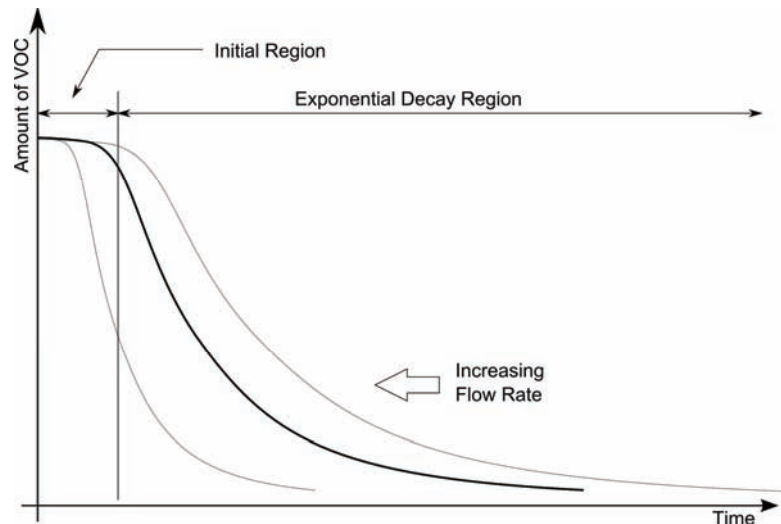


Figure 6.7 - Schematic of gas-freeing progression and separation of regions

The **initial region** is determined by the entrainment of VOC and the strength of the primary vortex inside the tank, generated by entrainment and shear from the jet. Vapours are not exhausted until they reach the vent, and when tank contents are in a fully stratified arrangement, vapours must first be entrained, *then* transported to the vent. Although the rate that vapour is removed from the stratified layer depends on the shear entrainment from the impingement, the time taken to transport gas to the exhaust vent is largely dependent on the strength of the vortex driven by the jet.

The **exponential decay region** takes place once vapour transport to the vent has occurred. Although the stratified layer appears to have been largely eroded by the time the process begins the exponential decay period, stratified layer decay and the *beginning* of the exponential decay period are do not appear to be correlated - the beginning of the exponential decay is dependent on the transport of vapour to the vent, *not* on the ability of the jet to erode the layer (however, the *progression* of the exponential decay region can be limited by layer erosion).

6.3.2 The Initial Region

The independence of the length of the initial region to the layer erosion time can be shown by comparison of simulations 3B and 3C, as depicted below in Figure 6.9. Although in comparison to 3B, the stratified layer in simulation 3C erodes quicker, the initial region in 3C lasts for a much *longer* period of time than 3B. This is quite evident in a time-series of contour plots (Figure 6.8) of the flow-field during the initial region period of ventilation - because of the lower flow rate, simulation 3C is less able to convect the contaminants to the exhaust vent, and a stratified “front” forms as the butane is slowly transported higher.

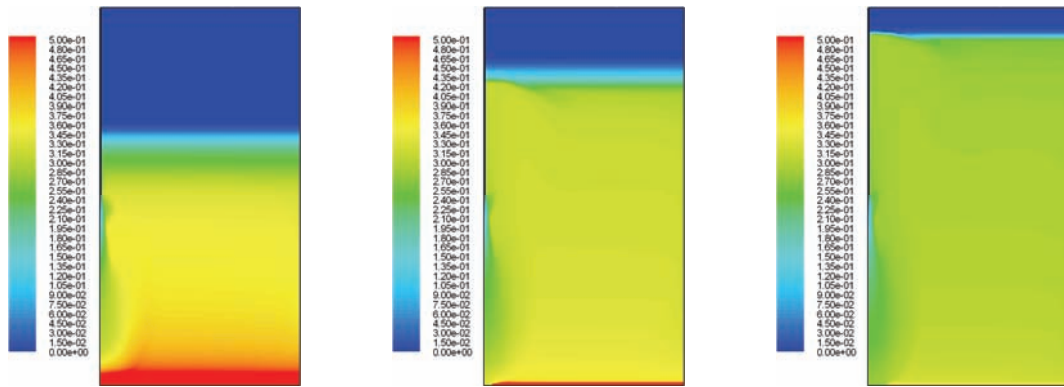


Figure 6.8 - C₄H₁₀ concentration contour plots showing movement of re-stratified butane at the top of the tank during gas-freeing. Left: 0.78 hrs; Centre: 1.34 hrs; Right: 1.62 hrs

On the other hand, simulation 3B is slightly slower to erode the layer, but the exponential decay curve is reached much quicker due to the higher flow rate, which results in a primary vortex that is much stronger, and therefore more able to transport vapour to the vent much quicker. Simulation 3D, with an even higher mean velocity of 75m/s completes all aspects even faster.

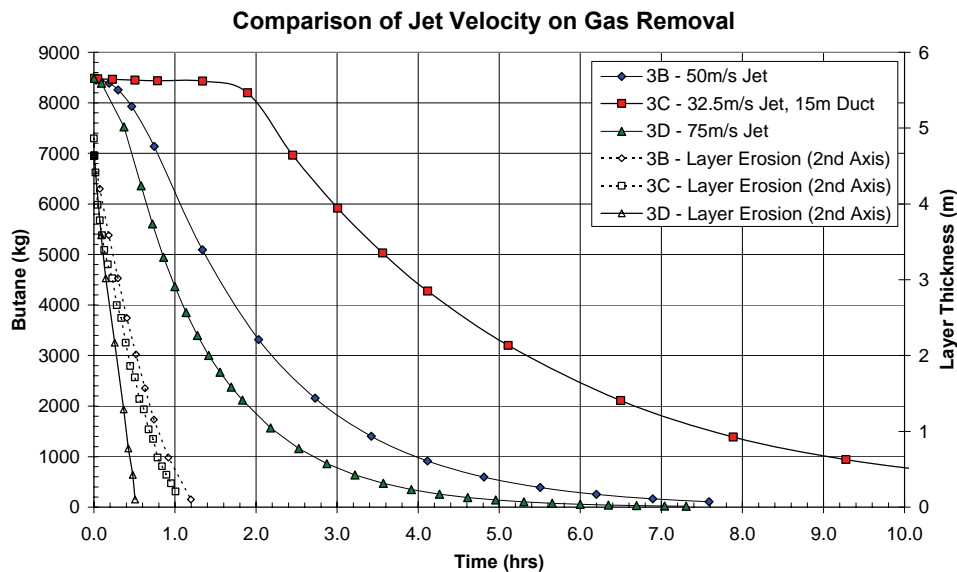


Figure 6.9 - Comparative plots of butane remaining in tank between 3B (50m/s) and 3C (32.54m/s, 15m ducting) and 3D (75m/s), showing differences in initial region and time to layer erosion

If contents are initially fully mixed, it can be expected that the initial region will be far shorter, as the gas will begin to be exhausted almost immediately; therefore in a fully mixed state, the initial region will be determined by the time taken to establish a steady flow field; this can be seen in Figure 6.10 below, which compares the initial regions of two stratified simulations (3F and 3J) with a fully mixed simulation (3H);

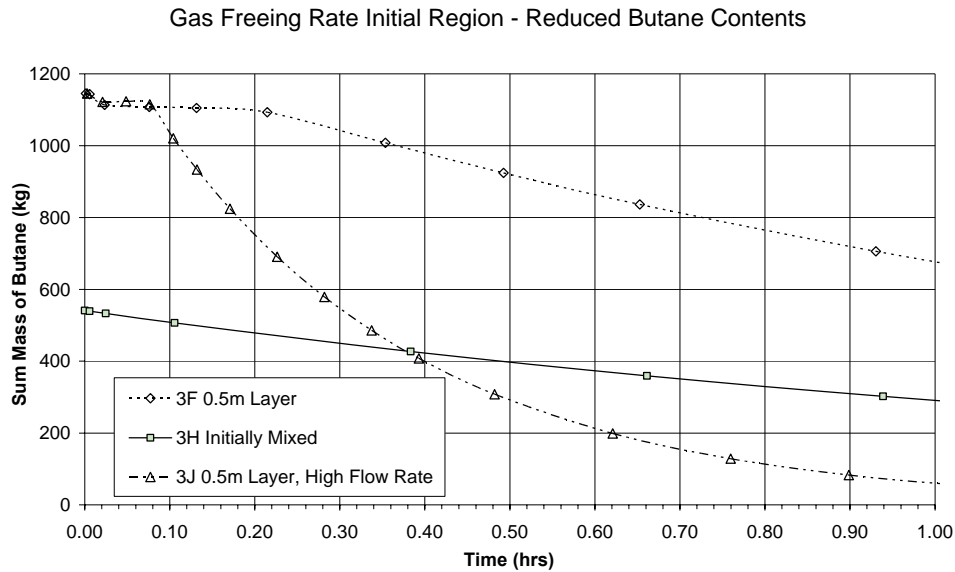


Figure 6.10 - Comparison of Initial Region in stratified and fully mixed simulations

Here, both layered simulations (3F and 3J) have a noticeable initial region, whereas simulation 3H ventilates almost immediately. Simulation 3J has a shorter initial region due to its higher flow rate ($71,660\text{m}^3/\text{h}$, as opposed to $14,290\text{m}^3/\text{h}$ for 3F).

6.3.3 Initial Region Dynamics

In the geometrically clean simulations, the length of the initial region appears to be a function of a number of variables, including the flow rate, structural blockage, and a function of the state of the initial mixture (initially fully mixed, or initially stratified). The primary vortex (Figure 5.39) was highlighted previously as being a flow structure which can characterise species transport in the flow-field. Because the primary vortex is defined by the flow rate, a qualitative understanding of the effect that different configurations of flow rate and jet vent ducting have on the overall gas freeing process can be gained by examining the stream function of the flow:

$$\rho u_i = \frac{\partial \psi}{\partial x_j} - \frac{\partial \psi}{\partial x_i} \quad (6.2)$$

Contour plots of the stream function show both the location and strength of the primary vortex which is driven by the jet, and are shown in Figure 6.11 and Figure 6.12:

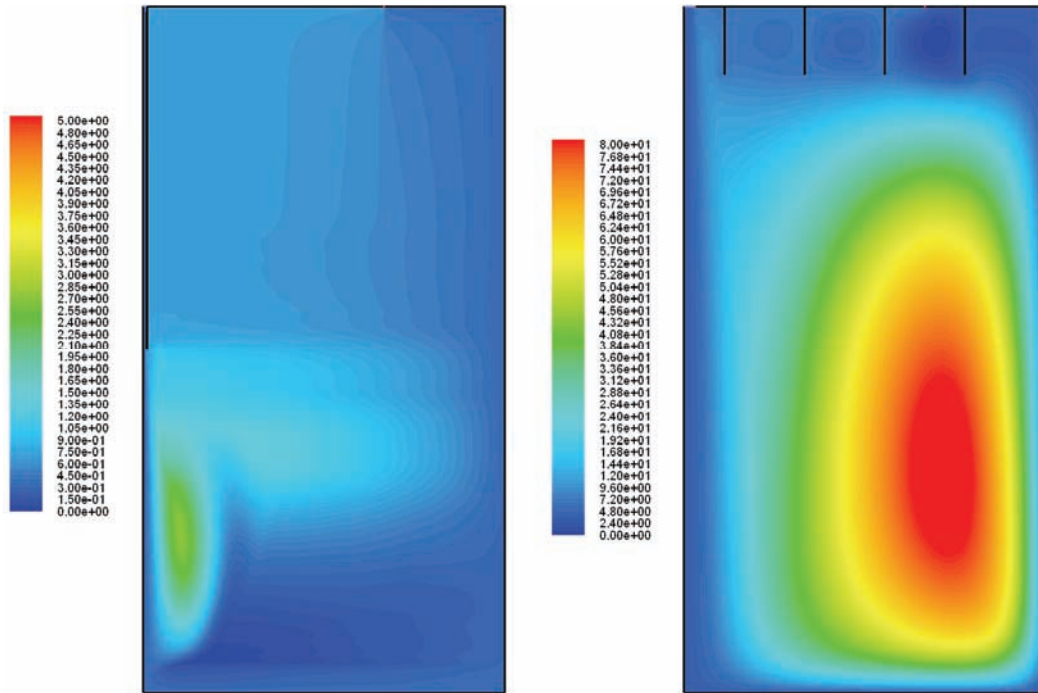


Figure 6.11 - Comparison of stream functions; Phase 3C (Left) with 15m duct and 7,110m³/hr flow rate; Phase 3D (Right) with 21,440 m³/hr flow rate; Note different contour ranges

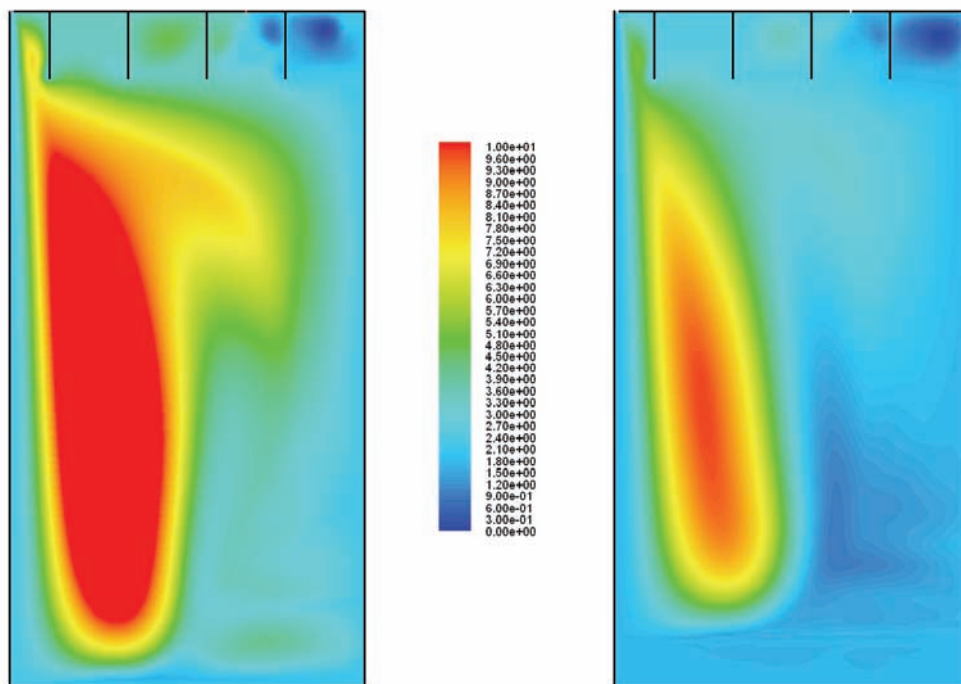


Figure 6.12 - Comparison of stream functions; Phase 3D (Left) with 21,440 m³/hr; Phase 3B (Right) with 14,290 m³/hr flow rate

It can be seen that the strength of the primary vortex is proportional to the flow rate. In particular, the ducted simulation (Phase 3C) has a much smaller primary vortex both in size and

strength, and is restricted to the region near the duct, compared to the other vortices which have a much larger vertical scale due to the jet positioning and higher flow rate. The lack of strength and ‘throw’ (or vertical extent) of the primary vortex can be related back to the long initial region in the ventilation curve (Figure 6.9) - as the vortex is fairly weak, it is unable to rapidly transport the VOC gas to the exhaust vent.

Effect of Obstructions

It can be seen that obstructions restrict the formation of the primary vortex, so that no large scale vortices can exist in the upper zone due to the presence of upper structural frames; instead, secondary shear-driven vortices are responsible for transport in these areas. This can be seen more clearly in Simulation 3I which has obstructions on both the top and bottom of the tank, as depicted in Figure 6.13.

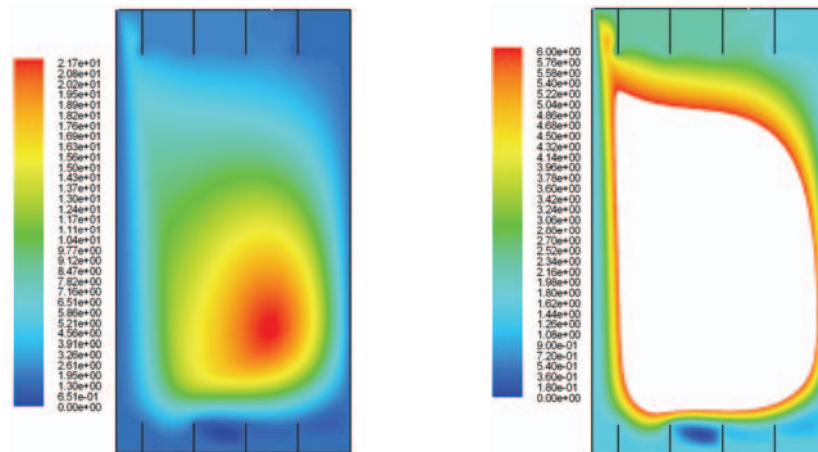


Figure 6.13 - Contour plots of stream-function for Simulation 3I. Left: Max = 21.7kg/s;
Right: Max = 6.0 kg/s

The addition of lower frames restricts the formation of flows through the floor area, so that the primary vortex forms in the clear zone above the structure. This forces the local ventilation in between frames to be driven by the weaker secondary vortices, leading to much longer ventilation times. From Figure 5.41, it can be seen that the web frame furthest from jet takes the longest time to ventilate, and also shows a very non-linear decay curve; this can be attributed to a number of physical reasons. From the impingement zone, the flow spreads out and flows horizontally, skimming over the web frames and inducing secondary motions inside them. As already discussed, these secondary vortices transfer butane vapours into the sideways-running flow, increasing their local concentration, which then continues outboard until meeting the outboard wall and being transported vertically. As the rate of entrainment depends on the concentration of the gas already inside the local fluid packet, i.e. $J = -D \frac{\partial \phi}{\partial x_j}$, the ventilation of the upstream frames increases the

local concentration of butane, reducing the concentration gradient; this is also supported by the total decay of the previous web-space - the change in ventilation curve of Web Space 5 coincides with the total decay in the upstream web-space; likewise, the behaviour of the ventilation curve of Web Space 4 in the first-quarter air-change is affected by the reduction of the upstream web frames also. Based on this, it is expected that obstructions of this kind will have an effect on gas freeing time. Figure 6.15 below shows the layer erosion with the overall gas-freeing curve overlaid with the curve from another unblocked simulation, where it can be seen that in comparison to simulation 3F, a greater number of air changes are required. This is the result of compartmentalisation of the contaminated region. Because the velocity field and turbulence levels downstream of the impingement zone reduce in magnitude, the entrainment of gas from each of the compartments is similarly non-uniform. As such, some web-spaces are evacuated far quicker than others.

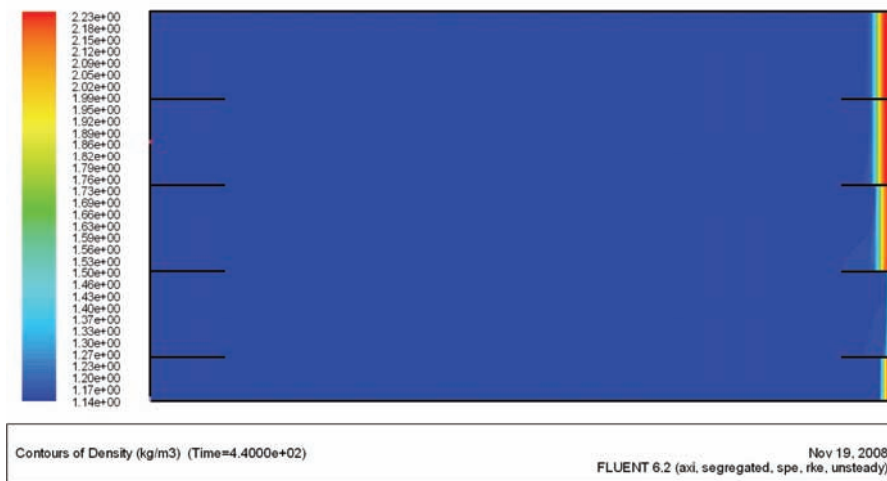


Figure 6.14 - Contour plot of density showing different rate of layer-erosion caused by obstruction

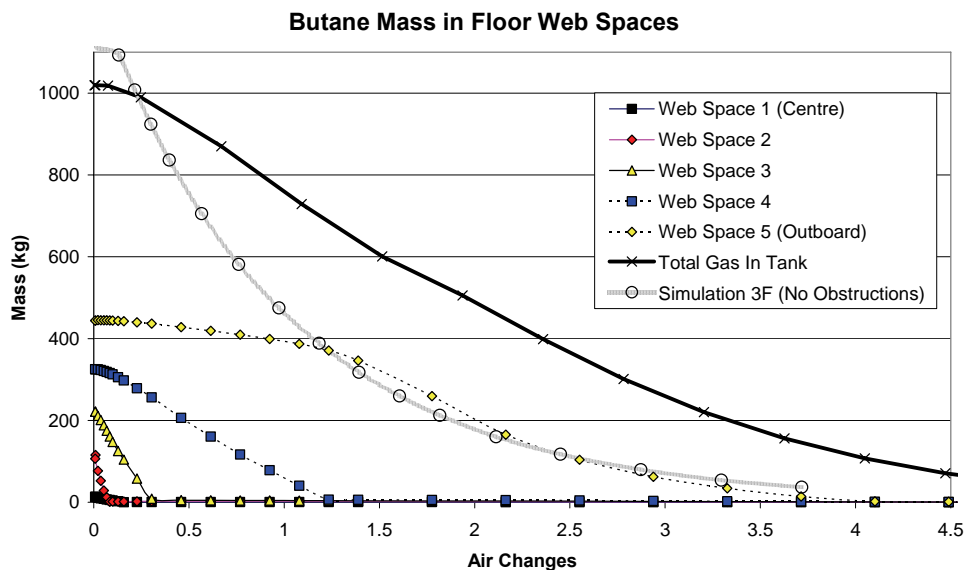


Figure 6.15 - Comparison of ventilation rates in each floor web-space compared to overall rate

This is reflected in a comparison of contour plots of the effective viscosity whereby the effective viscosity ($\mu + \mu_t$) is lower for the outboard webspace, shown in Figure 6.16, which in the K-Epsilon model is responsible for entrainment.

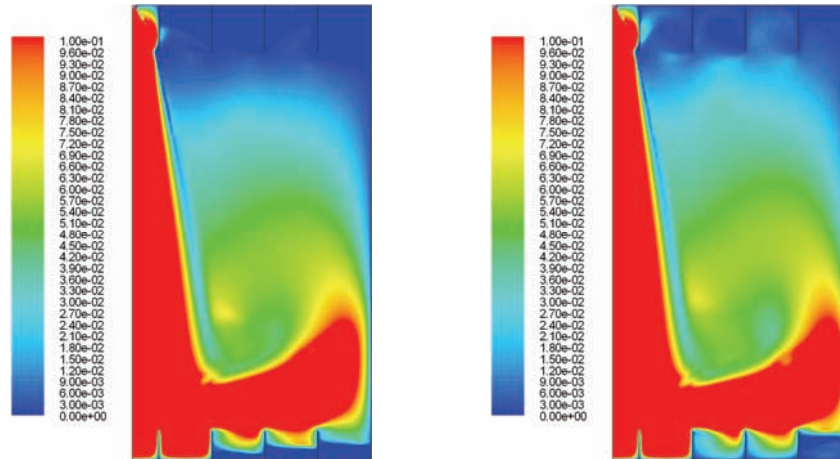


Figure 6.16 - Simulation 3I effective viscosity contour plots in obstructed geometry; Left: 0.41 hrs; Right: 3.18 hrs

It can be seen that the impingement zone has a much higher turbulent viscosity; it can also be seen that the level of turbulent viscosity also decreases towards the outboard frames.

6.3.4 Determination of Initial Region Time

Calculation of the time period inside the initial region is extremely difficult, since several distinct physical mechanisms inside the tank contribute towards this:

- Overall tank geometry;
- Internal blockage (especially in the stratified zone);
- Initial gas state (Stratified, or well mixed?)
- Air change rate;
- Entrainment of VOC gas.

In the absence of stratification, simulations showed that $t_{ir} \rightarrow 0$, indicating that the existence of a stratified layer was important to this time period. Therefore, internally blocking geometry in the stratified zone has a particularly large effect in altering the ventilation curve, removing the distinct change in concentration removal and blurring the demarcation between the exponential decay and initial regions, which makes a prediction of the initial region in this case difficult. However, given the cleaner internal design of modern double-hulled tankers, it is possible to neglect (for the purposes of this derivation) such obstructive internal structures.

Therefore, the initial region length t_{ir} can be determined by the stratification layer strength and the air change rate, which is also a measure of the strength of the supplied jet:

$$t_{ir} = \frac{V}{Q} \times Ri_i; \quad (6.3)$$

Where Ri_i is the interface Richardson number defined by:

$$Ri_i = g' \delta / u_j^2; \quad (6.4)$$

Here, g' is the relative gravity (Equation (2.9), p9) of the bulk fluid and the stratified layer; δ is the stratified layer thickness and u_j is the jet velocity at the layer height, i.e. the impingement velocity. This can be determined by measurement, from manufacturer information on the gas-freeing fan jet throw, or by the self-similar jet velocity extrapolated from the initial supplied jet velocity given in Equation(2.77)(p45), where U is the mean air supply velocity, d is the diameter of the supplied jet, and x is the downstream distance to the stratified layer. Rearrangement of Equation (2.77) gives the jet velocity at some distance downstream, $u(x)$, which is then used as u_j in Equation (6.4) to find the interface Richardson number. A formulation of the interface Richardson number (in Equation(6.4)) was also used by Shy (1995, p53) in order to calculate normalised penetration depths; however in a departure to his method, the extrapolated jet visual diameter is replaced with the stratified layer thickness, δ , as the jet at this point has such a large spread, the jet diameter is an inappropriate length scale, resulting in unusually high Richardson numbers. The inclusion of the Richardson number accounts for the fact that the jet must also entrain the stratified gas, where the entrainment law is known to be proportional to a function of the Richardson number (Turner 1979, Tanny *et al.* 1995, Fernando 1991):

$$E \propto Ri^{-n}; \quad (6.5)$$

Where n is a constant on the order of unity, though its precise definition is still subject to current research. Either way, this formulation reflects that stronger stratification leads to more difficult entrainment, leading to longer initial periods. Predicted initial region times are compared to raw data (presented in Figure 6.6), in Table 6.2.

Table 6.2 - Comparison of predicted and actual initial region times

Simulation	V/Q (s)	Ri	Predicted (s)	Actual (s)
3B	5918	0.48	2943	2672
3C	11895	0.41	4905	6000
3D	3945	0.507	1993	1332
3F	5919	0.63	3649	773

The prediction gives approximate results in the three simulations with a deep stratified layer ($> 4\text{m}$), but in Simulation 3F (where the layer is $\sim 0.5\text{m}$), the prediction is vastly over-estimated. As simulations 3B and 3F have the same inlet conditions, the rate of shear erosion is similar; however, due to the much thinner layer of stratified fluid in run 3F, the layer is eroded much quicker, so that the butane content of the tank is mixed into the air. Although the rate of entrainment by shear for both cases is the same, the thinner layer in simulation 3F allows the jet to ‘bore through’ far quicker. Once the jet reaches the floor, it is able to spread out sideways along the wall, intruding sideways directly into the stratified layer, swiftly dispersing the layer.

The prediction for Simulation 3C is less satisfactory. The simulation predicts a very long initial region due to the lack of convective transport to convey entrained VOC gas towards the exhaust (for example Figure 6.8), and the solid modelling of the duct wall ensures that there will be no entrainment until the jet, exaggerating the effect; in reality, there will be some entrainment as the ducting used in practice are generally non-rigid and at high enough pressures the interlocking rings can allow leakage.

6.3.5 Exponential Decay Region

The results show that in the majority of the geometries examined here, the rate of removal of VOC gas is exponential in decay. Figure 6.17 shows a compilation of plots of different gas-freeing scenarios inside the exponential decay region, where the plots have been normalised based on a ratio of remaining gas to initial gas mass, and ratio of time to residence time;

$$x(t) = t \frac{V}{Q}, \text{ and } y(t) = \frac{m_0}{m(t)} \quad (6.6)$$

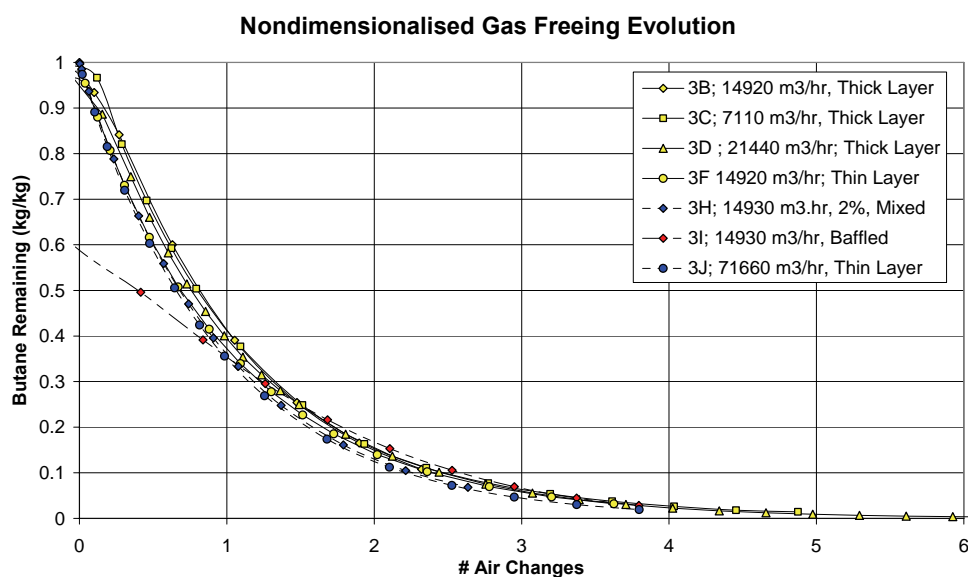


Figure 6.17 - Normalised exponential decay curves of butane gas

From Figure 6.17, it can be seen that for all flow rates examined, all of the ventilation plots follow a very similar trend irrespective of volumetric flow rate; ducting the jet (simulation 3C) does not appear to make a large difference, except around the beginning of the exponential decay region. Simulation 3I has a much more linear decay over the majority of the ventilation curve before entering into a more exponential curve towards the end. This is the result of 2m high floor-level obstructions reducing entrainment of C_4H_{10} , requiring a higher number of air changes for adequate ventilation.

The decay curves in the exponential region is as a result of the lack of geometrical disturbances in the flow field, so essentially the concentration decay is Fickian, whereby the diffusivity is accelerated by the supply of turbulence from the jet. Although it's common in existing literature to examine instantaneous concentration histories at set points (i.e. local) in the flow, the approximately exponential decay of global mass-averaged concentrations is seen in other works (Dakhel & Rahimi 2004, Fossett & Prosser 1948, Perona 1998, Yang *et al.* 2004, for example).

In terms of the bulk average fluid state in the tank, the change of species mass relative to its initial state (i.e. normalised decay) is the same as the decay rate of the concentration of that fluid species. In that sense, $m_0 / m(t) \approx C(t)$. Based on this relation, it can be seen that the two-dimensional simulations without blockages all follow a set curve (Figure 6.17):

$$\frac{m_0}{m(t)} \approx C(t) = e^{-t\lambda} \tag{6.7}$$

Where λ is the air-changes per hour, Q / V .

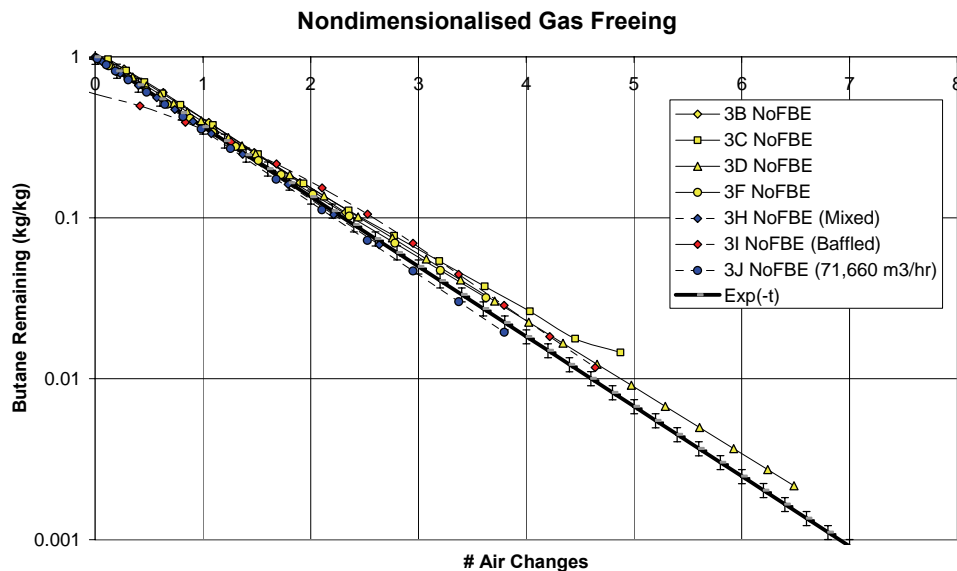


Figure 6.18 - Graph of non-dimensionalised ventilation progression simulations against exponential decay curve

The tight correlation with all of the unblocked 2D simulations to the curve is similar to a simple linear response system analysis used in chemical engineering, when subject to a constant tracer input, where the total mean concentration at a particular time is determined by the function $C(t) = e^{-\lambda t}$, which is described as piston-flow (Liao & Liang 2003), and as uniform mixing decay by Dickson (1985) which represents an ideal mixing exhaust scenario. Given that the concentration histograms (Figure 5.46, Figure 5.47 and Figure 5.48) show that the air concentration of butane is tightly banded into narrow groups *after* the erosion of the stratified layer, i.e. there are no regions of stagnant velocity resulting in areas where gas-freeing is impossible, this behaviour shows that the air jet is able to adequately ventilate the entire tank, even in areas of significant flow stratification.

Given the analysis of the layer erosion when subject to blocking, it can be seen that the decay region is distorted substantially when blocking is present, leading to much longer gas-freeing times. This curve can be approximated by using an additional efficiency parameter η , in line with that of Jennings & Armstrong (1971, in Liao & Liang 2003);

$$\frac{m_0}{m(t)} \approx C(t) = e^{-t\lambda\eta} \quad (6.8)$$

Where:

$$\eta = \begin{cases} 1 & \text{for perfect (piston - flow) mixing} \\ 0 & \text{Incomplete mixing} \end{cases} \quad (6.9)$$

By reducing the efficiency setting, the rate of decay of concentration can be reduced, resulting in a more moderate curve.

6.3.6 Discussion of 3-Dimensional Effects

Through the use of geometric scaling (Section 5.3), general flow similarity can be achieved with regards to turbulence (Reynolds number similarity), stratification (Richardson number similarity) and ventilation characteristics (air change rates). This ensures that the general behaviour of the ventilation inside the domain is correct from a similarity point of view.

As noted in Section 5.5.1, there is some deflection of the jet from the vertical due to the Coanda effect from the proximity of nearby walls; although this may result in stretching of the jet cross-section, unless the deflection is high, the major effect of this is the reduction of entrainment of vapours in the tank due to confinement.

The biggest aspect of an axisymmetric model is in the representation of geometry, and the inability to model partially-blocking features, making the axisymmetric model an ideal case:

- The domain is cylindrical and not rectangular - there is less scope for secondary, weaker eddies to exist in corners, which could entail reduced mixing;

- The jet is located centrally in the tank - this results in the creation of a primary toroidal vortex around the tank, such that the distribution of momentum and turbulence is more uniform; in a real-life scenario (for example, the models in Section 5.3.1), the jet could be offset to one side, which will result in one area of the tank being more remote to the jet;
- Typical floor-based structures were either full length or neglected, as the axisymmetric assumption doesn't allow partial blockage of the domain.

These assumptions allow the jet to move more freely, distribute momentum and turbulence more uniformly and with less obstruction to flow in critical areas; the results of the simulations represent a form of *best-case* scenario. Although it is difficult to examine how three-dimensionality will affect the flow without resorting to a full 3D model, simulation 3I gives some insight to the effect of floor-structure on ventilation ability when gas-freeing heavy gases, which may be similar to the effects of half-width frames on the floor of the tank.

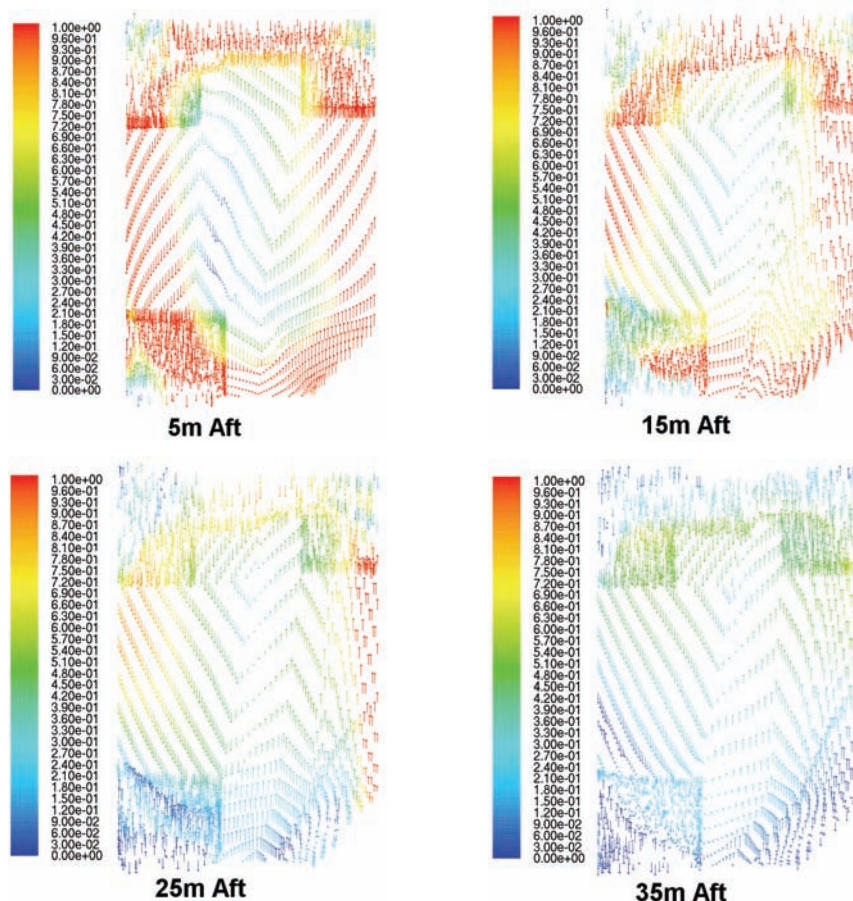


**Figure 6.19 - Vector plots of slices through 3-dimensional domain showing principle air movements;
Fore-aft planes (top left); Inboard-outboard plane through the jet axis (bottom right)**

Although it is possible to model total blocking, this is only typically present in the roof frames which run the full span of the ceiling in order to support the deck above. As such, the

inclusion of full-span lower frames in Simulation 3I was geometrically conservative for the two-dimensional simulations, as this is not a feature on the tank interior in modern ships. However, in comparison to a fully 3D case where the jet is offset to one side and supplied to an obstructed area of the floor such as those examined in Section 5.5, the interference from even half-span frames may be high, and may have a negative effect on the velocity and turbulence fields, though the distribution of concentration (Figure 5.38) shows that it is unlikely that the butane will stagnate.

Previously with the 2-dimensional simulations, it was seen that one of the principle flow features were the primary vortices driven by entrainment from the jet and shear from the impingement zone, which drive down and flow outboard after impinging, before rolling back up the outboard wall. In the 3D model, this feature is still present, seen in Figure 6.19 (top left), and the vortex “roll” generated by the jet appears to persist through the length of the domain. Further examination of the surface velocity vectors shows that due to the jet impingement zone confinement, a low velocity region of recirculating fluid is generated in the aft inboard side of the tank (Figure 6.20).

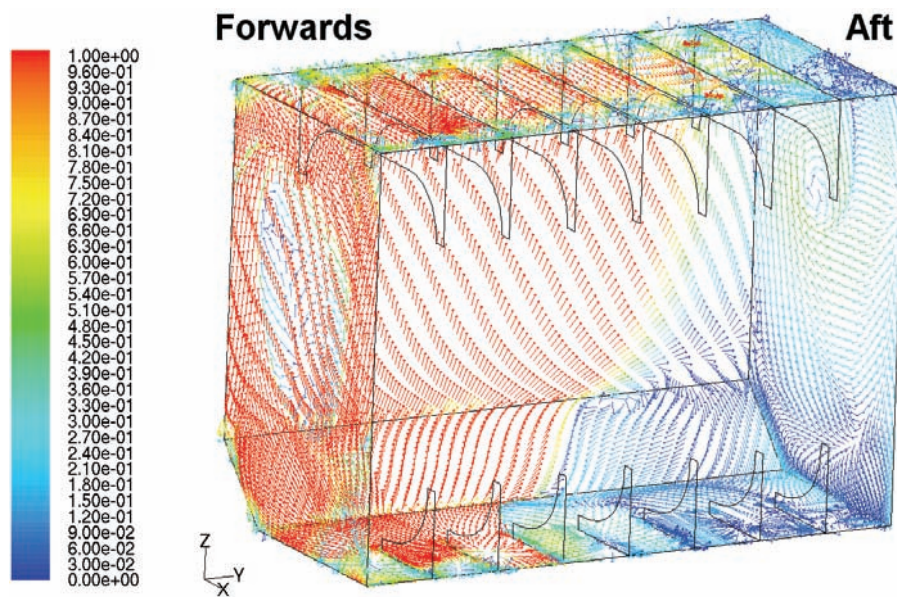


Figure 6.20 - Surface velocity vectors showing direction and magnitude of flows near the wall

As the two-dimensional simulation only models the plane normal to the forwards/aft walls, this lower velocity region is not captured by the model. As such, this region of air is expected to have a higher concentration due to its poor ventilation. This is confirmed by a steady-state simulation of the same tank with an initial 4m thick uniform layer of butane, Figure 6.21, which shows that, again, the areas remote to the jet are subject to much poorer ventilation. However, the maximum concentration is not between the half-span web frames on the floor, but in the outboard far corner next to the angled floor.

Since the rate of gas decay is exponential, steady state simulations slowly converge on a totally ventilated state as $t \rightarrow \infty$; As such, although the time history of the instance represented in Figure 6.21 is lost, the concentration profile is still a valid qualitative representation of what is likely to be encountered during a transient simulation of the same conditions, comparable to the 2D transient simulations.



Figure 6.21 - Butane mass fraction on a vertical normal plane 0.1m above the floor; note the higher concentration in the outboard corner, top right

6.3.7 Determination of Total Gas Freeing Times

Knowledge of the exponential decay curve given in Figure 6.18 allows the determination of gas freeing time only if the initial saturated butane mass or concentration (in terms of gas or LFL) is known. Procedure (OCIMF *et al.* 1996) states that the concentration of VOC gas prior to gas-freeing should be 2%, so this can be used as a means of determining the initial state.

From Section 2.6.4;

- Gas freeing for the reception of cargo requires VOC concentration to be <40% of the LFL;
- Gas freeing for tank entry and cold work requires VOC concentrations to be <1% of the LFL.

Based on the fully-mixed concentration decay time in an ideal mixing scenario (i.e. efficiency $\eta = 1$; Equation (6.7), p164), an absolute lower bound can easily be found based on the reduction of 2%/vol to both 40% and 1% of the LFL (which for butane, is 1.8%/Vol);

$$t = \frac{-\ln|C(t)|}{\lambda} \quad (6.10)$$

Sample calculations are displayed in Table 6.3 for the gas-freeing time required to gas-free a particular tank to the required criterion.

Although this analysis is quite straightforward, it can already be seen that the time required to gas-free for 1% of the LFL requires a much larger gas-freeing time. It should also be noted that this analysis is optimistic, as the initial region is assumed negligible (i.e. the gas is fully mixed and low transit times of gas to exhaust vent) and perfect mixing is assumed. Although the previous K-Epsilon simulations imply that the level of mixing is perfect, this is largely due to the higher turbulent viscosities.

Table 6.3 - Example calculations of gas-freeing time based on perfect, ideal mixing with no initial region

m_o	$m(t)$	$C(t)$	ACH (1/h)	t (hrs)
2%/vol	0.72%/vol (40% LFL)	0.36	0.608	1.68
2%/vol	0.018%/vol (1% LFL)	0.009	0.608	7.74
4.758%/v	0.2%/vol	0.042	4.2	0.75 ^a

^a Gas freeing on the S.T.S Zaphon (Logan & Drinkwater 1961) with these initial conditions took 90 minutes, but with a 30-minute initial region unaccounted for in this simple analysis

With the addition of the predictions of initial regions given earlier in Section 6.3.2, a more accurate description of the gas-freeing curve is given, as shown in Figure 6.22.

In these geometrically clean configurations, the analytical model over-predicts the gas-freeing time compared to the numerical simulations, though it must still be noted that the simulation models are optimistic. The analytical model describes the rate of gas-freeing generally well. In less clear geometry, and in comparison to the Reynolds stress model, the analytical model doesn't represent the more gradual initial region and more linear trend of the decay region (Figure 6.23) as well.

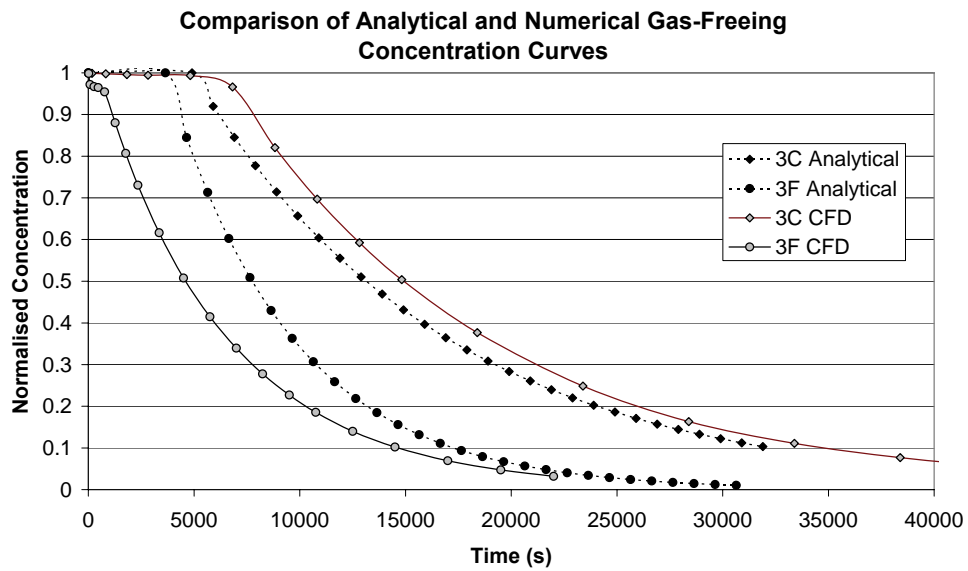
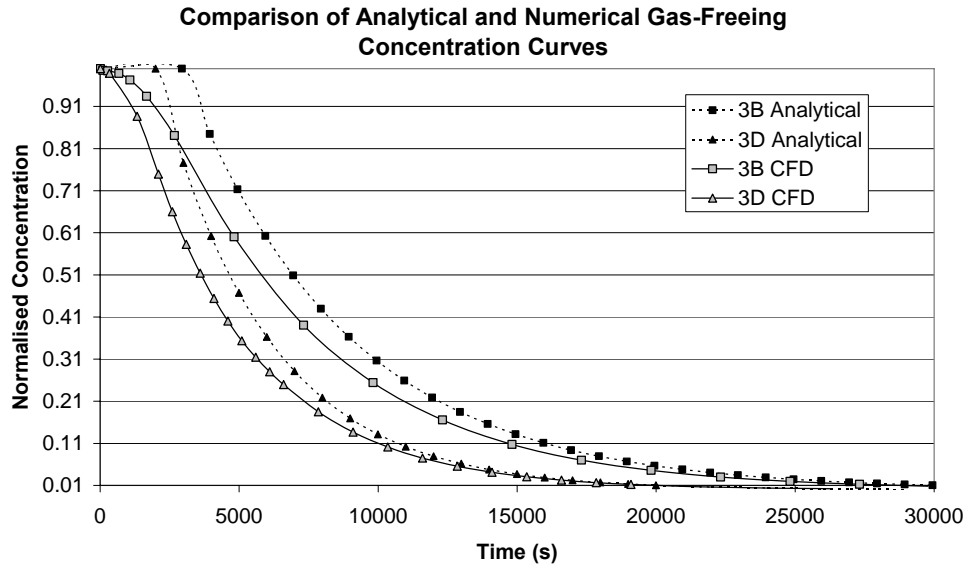


Figure 6.22 - Comparison of analytical model to numerical results; $\eta=1$ in all four cases

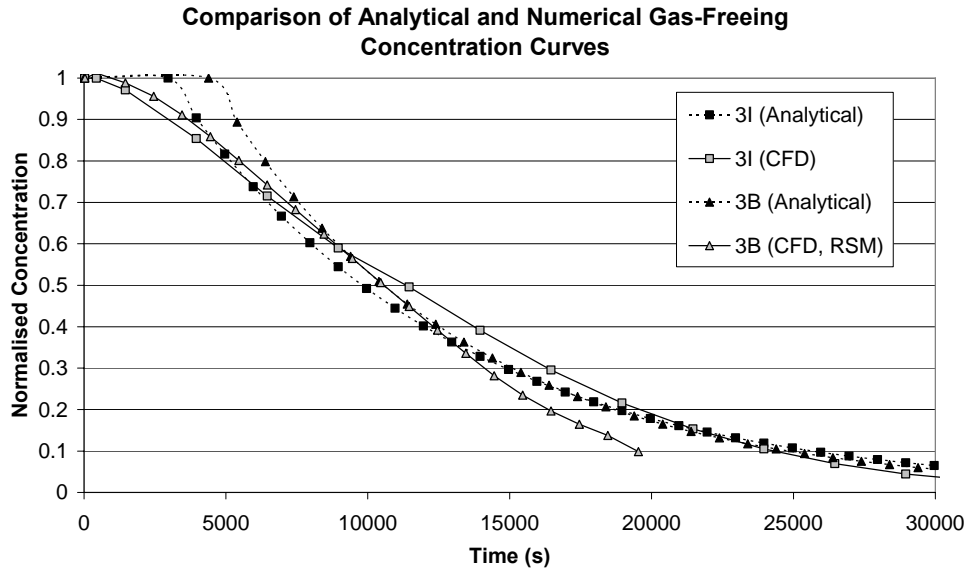


Figure 6.23 - Comparison of analytical to numerical simulations; $\eta = 2/3$ for simulation 3B(RSM), and 0.6 for simulation 3I.

The RSM simulation is modelling the same ‘clean’ geometry as run 3B, but Figure 6.23 suggests that an efficiency of $\eta = 2/3$ is more accurate than a perfect mixing efficiency, which given the behaviour of the K-Epsilon turbulence model, is most likely to be more optimistic and non-conservative.

6.3.8 Applicability of Regulations

From Table 6.3, reducing a 2% fully mixed butane-filled tank with no geometric obstructions in the stratified zone takes just over 1.5 hours to gas free to 40% of the LFL. However, this is under the assumption of perfect mixing; as seen, the likely efficiency is closer to $\eta = 2/3$. Adjusted for this change in efficiency, the gas-freeing rates from Table 6.3 are given below in Table 6.4.

Given the time-history concentrations shown previously in Figure 5.44 for the given scenario, there will not be any areas of concentration peaks (see Figure 5.47) inside the domain even after only 2.6 hours of gas-freeing, or 1.5 air changes. However, this is entirely dependent on the state of the tank before-hand - if there is any chance of initial stratification, then the gas-freeing time will become longer due to the time taken for gas to be eroded from the layer and transported (i.e. time in the initial region of gas-freeing); this initial region will add just over an hour to the required gas-freeing time in order to ensure that the tank is gas-free to 40% of the LFL.

Table 6.4 - Gas freeing times adjusted for 2/3 efficiency

State	m_o	$m(t)$	$C(t)$	ACH (1/h)	t (hrs)
Fully Mixed	2%/vol	0.72%/vol (40% LFL)	0.36	0.608	2.52
Fully Mixed	2%/vol	0.018%/vol (1% LFL)	0.009	0.608	11.61
Initially Stratified	4%/vol	0.72%/vol (40% LFL)	0.18	0.608	5.24 ^a
Assumed Fully Mixed	4.758%	0.2%	0.042	4.2	1.13 ^b

^a Total gas freeing time includes initial region time prediction for 3F, Table 6.2

^b Initial data based on data from Logan & Drinkwater (1961)

To this extent, the application of the regulations concerning the required LFL for cargo reception and tank entry are acceptable in themselves, as they will ensure the safety of the cargo and crew, but only if they are strictly adhered to. However, due to the uncertainty of the initial state of the tank, *a priori* calculation of gas-freeing time is more awkward, but the analytical relations formed here and the evolution of vapour content during gas freeing can be used to help define minimum ventilation times.

7.0 Conclusions

Numerical simulations concerning the physical mechanisms behind gas freeing, and the actual process itself, have been conducted. The numerical method, radiation and turbulence modelling aspects have been verified by comparison to experimental work in a related ventilation case to the results of Iial-Awad (2006). The work carried out in a comparison study also verified the importance of radiation in the prediction of temperature fields in room ventilation, similar to the findings by previous authors (Kondo et al. 2000, Glicksman & Chen 1998, Howell & Potts 2002).

Preliminary investigations into initial conditions in the interior of the COT examined the difference between single and double hulled tankers in terms of thermal insulation and temperature profile. It was found that the addition of double hulls sandwiching the void/ballast space between them resulted in a much higher level of insulation compared to the experimental work on single-hulled tankers performed by Saunders (1965); this higher level of insulation results in a temperature profile which is closer to being isothermal, whereby the variation in vertical temperature between the cold floor and the hot ceiling was only three degrees; this is in line with anecdotal evidence from various tanker organisations (OCIMF 1997, Intertanko 2002, Rauta 2004) whereby operators have experienced elevated tank temperatures which also exacerbates tank corrosion.

Examination of gas-freeing using transient numerical simulations has shown that once any stratified layer is removed, the total gas content of the tank decreases exponentially with time, and that the large scale blockages only have an effect if extant in the stratified layer. The result of these blockages is to reinforce the stratified layers by way of reducing the shear across the interface, due to obstruction of the local velocity field.

Numerical simulations used both K-Epsilon (Shih *et al.* 1994) and Reynolds stress model of Launder *et al.* (1975), finding that the K-Epsilon model, despite modifications to the baseline model of Launder & Spalding (1974) still over-predicts the production of turbulence. Comparisons to the RSM simulations allowed calibration of mixing efficiency during the formation of gas-freeing relations which were compared to data from Logan & Drinkwater (1961).

In summary:

1. Thermal radiation is an important part of heat transfer and affects the temperature gradient by redistributing thermal energy from hot to cold, acting to homogenise the thermal field;
2. Effect of radiation modelling on the prediction of the thermal profile is greater than the effect of turbulence modelling in room displacement-ventilation cases;

3. Inclusion of radiative modelling, using an appropriate radiation model for a given optical thickness, can result in far more accurate prediction of temperature profiles, surpassing scaled experimental methods such as salt baths;
4. In modern tankers, the addition of double hulls sandwiching a void space results in a far higher level of thermal insulation compared to older, single-hulled tankers;
5. Modelling of conjugate heat transfer including thermal radiation vastly reduces the vertical temperature gradient; combined with the increased insulation, it can be assumed that the COT is isothermal, and that conditions are adiabatic;
6. The K-Epsilon turbulence model provides optimistic results of impinging flows due to the over-prediction of TKE in the impingement zone; even though adjustments have been made to ensure realizability, it is insufficient to accommodate the errors inherent in the production of K;
7. The Reynolds stress model is a more suitable turbulence model to use in this process, but stronger numerical coupling forces the use of a small time-step, leading to much longer run-times to simulate a period of time in comparison a K-Epsilon model;
8. Jet gas freeing by mixing ventilation is still a viable method for tank gas-freeing despite the geometrical configuration;
9. It was found that once any stratified layers are removed, the rate of decay of vapour inside the tank is exponential;
10. Due to the scales involved, the time required to gas free a tank is in the order of hours; gas freeing to 1% of the LFL can take as much as half a day;
11. Separate analytical models have been formed to account for both the initial region and the exponential decay region of the gas freeing curve to predict the time taken to gas-free a tank.

7.1 Recommendations for Further Research

Due to the large number of potential structural configurations of tank design, and locations of vents, fans, number of fans used and fan capability, there is a clear scope for further work from an operational efficiency perspective. Numerically, there are a number of aspects that merit further examination, such as model validation with a different turbulence model (for example, further work with Reynolds stress models) and an examination of the gas freeing process with more gas species inside the tank.

In summary, the following avenues of study merit further research:

- Further examination of blockages on gas freeing time and distribution of VOC vapours;
- Examination of effect of different jet configurations on gas freeing and the time to gas free;
- Investigation of distribution of gases during gas freeing with more modelled gas species inside the tank;
- Exploration of different turbulence models on the prediction of gas-freeing.

References

- Abib, A., Jaluria, Y. (1995) 'Penetrative convection in a stably stratified enclosure.' *International Journal of Heat and Mass Transfer* 38(13), 2489-2500
- Abramovich, G. N. (1963) *The Theory of Turbulent Jets*. Cambridge, MA: MIT Press
- AEA Technology (2000). *CFX-TASCflow Computational Fluid Dynamics Software, Theory Documentation*. Ontario: AEA Technology
- Agrawal, A., Prasad, A. K. (2003) 'Integral Solution for the Mean Flow Profiles of Turbulent Jets, Plumes and Wakes.' *Journal of Fluids Engineering* 125(5), 813-822
- American Bureau of Shipping (2004). *Guide For Inert Gas System for Ballast Tanks*. Houston, TX: American Bureau of Shipping. Available from <
<https://eagle.onlineinventorystem.com/Clients/ABS/ELF1-5.nsf/catalog?open&category=Design%20&%20Analysis#>> [5 September 2004]
- Anderson, J. D. (1995). *Computational Fluid Dynamics; The Basics with Applications*. Singapore: McGraw Hill
- ASHRAE (2001) *Fundamentals: 2001 ASHRAE Handbook*. Atlanta, GA: American Society of Heating, Ventilation and Air-Conditioning Engineers
- Auban, O., Lemoine, F., Vallette, P., Fontaine, J. R. (2001) 'Simulation by solutal convection of a thermal plume in a confined stratified environment: application to displacement ventilation.' *International Journal of Heat and Mass Transfer* 44(24), 4679-4691.
- Baines, W. D., Turner, J. S. (1969) 'Turbulent buoyant convection from a source in a confined region.' *Journal of Fluid Mechanics* 37(1), 51-80
- Baker, A. J., Wong, K. L., Winowich, N. S. (2002) 'Design and Assessment of a Very Large-Scale CFD Industrial Ventilation Flowfield Simulation.' *ASHRAE Transactions* 108(1), 999-1004
- Bardina, J. E., Huang, P. G., Coakley, T. J. (1997). 'Turbulence Modelling Validation, Testing and Development', NASA TM-110446
- Beaubert, F., Viazzo, S. (2003) 'Large eddy simulations of plane turbulent impinging jets at moderate Reynolds numbers.' *International Journal of Heat and Fluid Flow* 24(4), 512-519
- Bejan, A., Kraus, A. D. (2003). *Heat Transfer Handbook*. Hoboken, NJ: John Wiley & Sons.
- Bettis, R. J., Allen, J. T. (1997), 'Improved validation of source term models: results of experimental study.' Health and Safety Laboratory Report IR/L/FR/97/6

- Bournet, P. E., Ould Khaoua, S. A., Boulard, T. (2007). 'Numerical prediction of the effect of vent arrangements on the ventilation and energy transfer in a multi-span glasshouse using a bi-band radiation model.' *Biosystems Engineering* 98, 224-234.
- Boussinesq, J. (1877) 'Théorie de l'Écoulement Tourbillant.' *Mem. Présentés par Divers Savants Acad. Sci. Inst. Fr.* 23, 46-50
- Brown, A. L., Dabberdt W. F. (2003) 'Modelling Ventilation and Dispersion for Covered Roadways.' *Journal of Wind Engineering and Industrial Aerodynamics* 91(5), 593-608
- Calay, R. K., Borrensen, B. A., Holdo, A.E. (2000). 'Selective Ventilation in Large Enclosures.' *Energy and Buildings* 32(3): 281-289
- Cardoso, S. S. S., Woods, A. W. (1993) 'Mixing by a turbulent plume in a confined stratified region.' *Journal of Fluid Mechanics* 250, 277-305
- Chen, Q. (1995). 'Comparison of Different K-E Models for Indoor Air Flow Computations.' *Numerical Heat Transfer, Part B* 28(3), 353-369
- Chow, K. (2005) *Improved Gas Freeing Fan Design*. Unpublished Report: University of Hertfordshire
- Chow, K., Holdø, A. E., Croft, R. J. (2005), 'Analysis of Gas Freeing of Oil Tankers Using CFD.' Paper no. PVP2005-71739. 2005 ASME Pressure Vessels and Piping Division Conference July 2005, Denver, Colorado USA. American Society of Mechanical Engineers
- Chung, Y. M., Luo, K. H., Sandham, N. (2002) 'Numerical study of momentum and heat transfer in unsteady impinging jets.' *International Journal of Heat and Fluid Flow* 23(5), 592-600
- Colomer, G., Costa, M., Consul, R., Oliva, A. (2004) 'Three-dimensional numerical simulation of convection and radiation in a differentially heated cavity using the discrete ordinates method.' *International Journal of Heat and Mass Transfer* 47(2): 257-269
- Corrsin, S. (1959). 'Outline of some topics in homogeneous turbulent flow.' *Journal of Geophysical Research* 64(12), 2134-2150
- Corrsin, S. (1964) 'The isotropic turbulent mixer: part II. Arbitrary Schmidt number.' *American Institute of Chemical Engineering Journal* 10(6), 870-877
- Cotel, A. J., (1995) *Entrainment and detrainment of a jet impinging on a stratified interface*. Ph.D Thesis, University of Washington
- Cotel, A. J., Breidenthal, R. E. (1997) 'Jet detrainment at a stratified interface.' *Journal of Geophysical Research* 102(D20), 23813-23818
- Cotel, A. J., Gjestvang, J. A., Ramkhelawan, N. N., Breidenthal, R. E. (1997) 'Laboratory experiments of a jet impinging on a stratified interface.' *Experiments in Fluids* 23(2), 155-160

Craft, T. J., Graham, L. J. W., Launder, B. E. (1993) 'Impinging jet studies for turbulence model assessment - II. An examination of the performance of four turbulence models.' *International Journal of Heat and Mass Transfer* 36(10), 2685-2697

COWI A/S (2004) *Oil Tanker Phase Out and the Ship Scrapping Industry - A study on the implications of the accelerated phase out scheme of single hull tankers proposed by the EU for the world ship scrapping and recycling industry*. Brussels: European Commission Directorate-General Energy and Transport

Dakhel, A. A., Rahimi, M. (2004) 'CFD Simulation of Homogenisation in Large Scale Crude Oil Storage Tanks.' *Journal of Petroleum Science and Engineering* 43(3-4), 151-161

Daly, B.J., Harlow, F.H. (1970) 'Transport Equations in Turbulence.' *Physics of Fluids* 13, 2634–2649.

Davidson, P. A. (2004) *Turbulence - An Introduction for Scientists and Engineers*. Oxford: Oxford University Press.

Department for Transport (2005), FOIA Request available from <<http://www.dft.gov.uk/foi/responses/2005/aug/chemicaltankers/dentreportaboutseamenwor2117.pdf>> [2 August 2005]

Devanney, J. (2006) *The Tankship Tragedy - The Impending Disasters in Tankers*. Tavernia, FL: The CTX Press

Dickson, D. J. (1985) 'Ventilation efficiency measurements in occupied mechanically ventilated buildings.' In *Ventilation Strategies and Measurement Techniques, 6th AIC Conference*. Held on September 16-19 1985. Het Meerdal Park, Netherlands.

Dimotakis, P. E. (2000). 'The mixing transition in turbulent flows.' *Journal of Fluid Mechanics* 409, 69-98

Dimotakis, P. E. (2005). 'Turbulent Mixing.' *Annual Review Fluid Mechanics* 37, 329-356.

Drikakis, D. (2003). 'Advances in turbulent flow computations using high-resolution methods.' *Progress in Aerospace Sciences* 39(6-7), 404-424.

Durbin, P. A. (1995) 'On the K-E Stagnation Point Anomaly.' *International Journal of Heat and Fluid Flow* 17(1), 89-90

Eckhart, C. (1948). 'An analysis of the stirring and mixing processes in incompressible fluids.' *Journal of Marine Research* 7, 265-275

Energy Institute (2004) 2nd edn, 'HM40 Guidelines for the Crude Oil Washing of Ships' Tanks and the Heating of Crude Oil Being Transported by Sea.' London: Energy Institute

- Eren, H., Celik, N., Yesilata, B. (2006) 'Nonlinear flow and heat transfer dynamics of a slot jet impinging on a slightly curved concave surface.' *International Communications of Heat and Mass Transfer* 33(3), 364-371
- Fernando, H. J. S., Long, R. R. (1985) 'The growth of a shear-free mixed-layer in a linearly stratified fluid.' *Physics of Fluids* 28(10), 2999-3003
- Fernando, H. J. S. (1991) 'Turbulent Mixing in Stratified Fluids.' *Annual Review Fluid Mechanics* 23, 455-493
- Ferziger, J. H., Peric, M. (2002) 3rd edn. 'Computational Methods for Fluid Dynamics.' London: Springer
- Fingas, M. (1994). 'A Literature Review of the Physics and Predictive Modelling of Oil Spill Evaporation.' *Journal of Hazardous Materials* 42(2), 157-175
- Fingas, M. (1997). 'Studies on the Evaporation of Crude Oil and Petroleum Products: The Relationship between Evaporation Rate and Time.' *Journal of Hazardous Materials* 56(3), 227-236
- Fluent Inc., (2005). *Fluent 6.2 User's Guide*, Lebanon, NH: Fluent Inc.
- Fossett, H., Prosser L. E. (1948) 'The Application of Free jets to the Mixing of Fluids in Bulk.' *Journal of the Institute of Mechanical Engineers* 160, 224-232
- Fox, E. A., Gex, V. E. (1956) 'Single Phase Blending of Fluids.' *American Institute of Chemical Engineering Journal* 2, 539-546
- Garg, R. P., Ferziger, J. H., Monismith, S. G., Koseff, J. R. (2000). 'Stably stratified turbulent channel flows. I. Stratification regimes and turbulence suppression mechanism.' *Physics of Fluids* 12(10), 2569-2594
- Germano, M., Piomelli, U., Moin, P., Cabot, W. H. (1991) 'A dynamic subgrid-scale eddy viscosity model.' *Physics of Fluids* 3(7), 1760-1765.
- Gilham, S., Deaves, D. M., Woodburn, P. (2000) 'Mitigation of dense gas releases within buildings: validation of CFD modelling.' *Journal of Hazardous materials* 71(1-3), 193-218
- Glicksman, L. R., Chen, Q. (1998) 'Interaction of Radiation Absorbed by Moisture in Air with other forms of Heat Transfer in an Enclosure.' In Roomvent 98, '6th International Conference on Air Distribution in Rooms.' Held June 14-17 1998 in Stockholm, Sweden, 111-118
- Grenville, R. K., Tilton, J. N. (1996) 'A New Theory Improves the Correlation of Blend Time Data from Turbulent Jet Mixed Vessels.' *Transactions of the Institute of Chemical Engineers* 74(3), 390-396
- Gurevich, M. I. (1965) *Theory of Jets in Ideal Fluids*. New York: Academic Press

- Gutmark, E., Wygnanski, I. (1976) 'The planar turbulent jet.' *Journal of Fluid Mechanics* 73(3), 465-495
- Haroutunian, V. (1995) 'Progress in Simulating Industrial Flows Using Two-Equation Models: Can More Be Achieved With Further Research?' in *Industry-Wide Workshop on Computational Turbulence Modeling*, NASA CP-10165, Held October 6-7 1994 at Lewis Research Center, Cleveland, OH. Washington D.C.: National Aeronautics and Space Administration
- Hanjalic, J. (1970) *Two-Dimensional asymmetric turbulent flow in ducts*, Ph.D thesis, University of London
- Hanjalic, K. (2004). 'Closure Models for Incompressible Turbulent Flows'. In van Beeck, J. P. A. J., Benocci, C. (eds), *Introduction to Turbulent Modeling*, Held on March 22-26 at Von Karman Institute for Fluid Dynamics. Rhode St. Genese: Von Karman Institute for Fluid Dynamics.
- Hinze, J. O. (1975) *Turbulence*. New York: McGraw Hill
- Holford, J. M., Hunt, G. R. (2003). 'Fundamental Atrium Design for Natural Ventilation.' *Journal of Building and Environment* 38(1), 409-426.
- Hottel, H. C., Sarofim, A. F. (1967). *Radiative Transfer*. New York: McGraw Hill
- Howell, S. A., Potts I. (2002). 'On the natural displacement flow through a full-scale enclosure, and the importance of the radiative participation of the water vapour content of the ambient air.' *Building and Environment* 37(8): 817-823.
- Hunt, G. R., Linden, P. F. (1999). 'The Fluid Mechanics of Natural Ventilation - Displacement Ventilation by Buoyancy-Driven Flows Assisted by Wind.' *Building and Environment* 34(6), 707-720
- Hunt, G. R., Cooper, P., Linden, P. F. (2001). 'Thermal Stratification Produced by Plumes and Jets in Enclosed Spaces.' *Building and Environment* 36(7), 871-882.
- Husain, M., Hunter, M., Altshuller, D., Shtepani, E., Luckhardt, S. (2003) 'Crude Oil Under Negative Pressures and Hydrocarbons Emission Containment.' *Transactions - Society of Naval Architects and Marine Engineers* 111, 584-607
- Iial-Awad, A. S. (2006) *Stratified Flow in the Built Environment*. Ph.D Thesis, University of Hertfordshire
- International Maritime Organisation (1990). *Inert Gas Systems*. London: International Maritime Organisation
- International Maritime Organisation (1998). *Focus on IMO*, September 1998. London: International Maritime Organisation

- International Maritime Organisation (2004). *SOLAS, Consolidated Edition, 2004: Consolidated Text of the International Convention for the Safety of Life at Sea, 1974, and its Protocol of 1988: Articles, Annexes and Certificates*. London: International Maritime Organisation
- International Maritime Organisation (2006). *MARPOL: Consolidated Edition, 2006 : Articles, Protocols, Annexes, Unified Interpretations of the International Convention for the Prevention of Pollution from Ships*. London: International Maritime Organisation
- Intertanko (2001) 'Types of modern oil tanker.' *The Tanker Newsletter* 5, May
- Intertanko (2002) 'Crude Oil Tanker Cargo Tank Corrosion Update.' In *UK Corrosion 2002*. Held on 22-24 October 2002 at Cardiff, Wales. London: Intertanko
- Jayanti, S. (2001) 'Hydrodynamics of Jet Mixing in Vessels.' *Journal of Chemical Engineering Science* **56**(1), 193-210
- Jennings, B. H., Armstrong, J. A. (1971) 'Ventilation theory & practice.' *ASHRAE Transactions* **77**(1), 50-60
- Ji, Y., Cook, M. J., Hanby, V. (2007) 'CFD modelling of natural displacement ventilation in an enclosure connected to an atrium.' *Building and Environment* **42**(3), 1158-1172.
- Jiang, X., Zhao, H., Luo, K. H. (2006) 'Direct computation of perturbed impinging hot jets.' *Computers and Fluids* **36**(2), 259-272
- Jiang, Y., Chen, Q. (2001) 'Study of Natural Ventilation in Buildings by Large Eddy Simulation.' *Journal of Wind Engineering and Industrial Aerodynamics* **89**(13), 1155-1178.
- Jiang, Y., Chen, Q. (2003) 'Buoyancy Driven Single Sided Natural Ventilation in Buildings with Large Openings.' *Journal of Heat and Mass Transfer* **46**(6), 973-988
- Jouvray, A., Tucker, P. G., Liu, Y. (2006) 'On nonlinear RANS models when predicting more complex geometry room air flows.' *International Journal of Heat and Fluid Flow* **28**(2), 275-288.
- Kim, C. N., Choi, W. H., Choung, S.J., Park, C-H., Kim, D. S. (2002) 'Efficient ventilation of VOC spread in a small-scale painting process.' *Building and Environment* **37**(12), 1321-1328.
- Kolmogorov, A. N. (1941). 'The Local Structure of turbulence in incompressible viscous fluid for very large Reynolds numbers.' *C. R. Acad. Sci., URSS* **30**, 301-305
- Kondo, Y., Ogasawara, T., Fujimura, J. (2000). 'Interactive Simulation of Room Air Temperature and Absorption/Emission of Radiative Heat with Room Moisture.' In *Proceedings of Roomvent 2000*, '7th International Conference of Ventilation for Health and Sustainable Environment.' Held at University of Reading, UK.

- Kuznik, F., Rusaouen, G., Brau, J. (2006) 'Experimental and numerical study of a full scale ventilated enclosure: Comparison of four two equations closure models.' *Building and Environment* 42(3), 1043-1053
- Lam, S. H. (1992) 'On the RNG Theory of Turbulence.' *Physics of Fluids A* 4, 1007-1017
- Landau, L. D., Lifshitz, E. M. (1987), 2nd edn. *Fluid Mechanics*. Oxford: Pergamon Press
- Launder, B. E., Spalding, D. B. (1972) '*Lectures in Mathematical Models of Turbulence.*' London: Academic Press.
- Launder, B. E., & Spalding, B. D. (1974). 'The Numerical Computation of Turbulent Flows.' *Computer Methods in Applied Mechanics and Engineering* 3(2), 269-289
- Launder, B. E., Reece, G. J., Rodi, W. (1975) 'Progress in the development of a Reynolds-stress turbulence closure.' *Journal of Fluid Mechanics* 68, 537-566
- Laurence, D. (2002) 'Applications of Reynolds Averaged Navier Stokes Equations to Industrial Flows.' In van Beeck, J. P. A. J., Benocci, C. (eds), *Introduction to Turbulence Modelling*, Held March 18-22 2002 at Von Karman Institute for Fluid Dynamics. Rhode St.Genese, Belgium: Von Karman Institute for Fluid Dynamics
- Lawson, N. J., Davidson, M. R. (2000) 'Self-Sustained Oscillation of a Submerged Jet in a Thin Rectangular Cavity.' *Journal of Fluids and Structures* 15(1), 59-81
- Leckner, B. (1972). 'Spectral and Total Emissivity of Water Vapor and Carbon Dioxide.' *Combustion and Flame* 19, 33-48
- Lee, C. H., Awbi, H. B. (2004a) 'Effect of Internal Partitioning on Indoor Air Quality of Rooms with Mixing Ventilation - Basic Study.' *Journal of Building and Environment* 39(2), 127-141
- Lee, H., Awbi, H. B. (2004b) 'Effect of Internal Partitioning on Room Air Quality with Mixing Ventilation - Statistical Analysis.' *Renewable Energy* 29(10), 1721-1732.
- van Leer, B. (1978). 'Towards the Ultimate Conservative Difference Scheme. V. A Second-Order Sequel to Godunov's Method.' *Journal of Computational Physics* 32, (1): 229-248.
- Leonard, B. P., Leschziner, M.A., McGuirk, J. (1978) 'Third-Order Finite-Difference Method for Steady Two Dimension Convection.' In *Numerical methods in laminar and turbulent flow*, '1st Conference on Numerical Methods in Laminar and Turbulent Flow.' Held July 17-21 at Swansea, Wales. London: Pentach Press
- Li, Y., Sandberg, M., Fuchs, L. (1993) 'Effects of thermal radiation on airflow with displacement ventilation: an experimental investigation.' *Energy and Buildings* 19(4), 263-274.

- Lienhard IV, J. H., Lienhard V, J. H. (2006) *A Heat Transfer Textbook* 3rd edn. Cambridge, MA: Phlogiston Press
- Lilly, D. K. (1991) 'A proposed modification of the Germano subgrid-scale closure method.' *Physics of Fluids* 4(1), 633-635.
- Lin, Y. J. P., Linden, P. F. (2005) 'The entrainment due to a turbulent fountain at a density interface.' *Journal of Fluid Mechanics* 542, 25-52.
- Linden, P. F., Lane-Serff, G. F., Smeed, D. A. (1990). 'Emptying filling boxes: the fluid mechanics of natural ventilation.' *Journal of Fluid Mechanics* 212, 309-33.
- Linden, P. F. (1999). 'The Fluid Mechanics of Natural Ventilation.' *Annual Review Fluid Mechanics* 31, 201-238
- Liao, C.-M., Liang, H.-M. (2003) 'A Linear Model of the Effects of Residence Time Distribution on Mixing Pattern in a Ventilated Airspace.' *Building and Environment* 38(1), 11-21
- List, E. J. (1982) 'Turbulent Jets and Plumes.' *Annual Review Fluid Mechanics* 14, 189-212.
- Lloyd's Register of Shipping, (2003). *World Fleet Statistics: Statistical Summary of the Current World Fleet of Propelled Sea-going Merchant Ships of Not Less Than 100 GT as at the End of the Year, and of Those Ships Completed During the Year 2003*. London: Lloyd's Register of Shipping
- Logan, A., Drinkwater, J. W. (1961) 'Gas Concentrations in the Cargo Tank of Crude Oil Carriers.' In *Annual Report and Transactions of the Royal Institute of Naval Architects, 1961*. London: The Royal Institute of Naval Architects
- Miles, J. W. (1961). 'On the stability of heterogeneous shear flows.' *Journal of Fluid Mechanics* 10, 496-508
- Minton, A. S. (1950) 'Marine Gassing and Fire and Explosion Hazards', *Institute of Marine Engineers Transactions* 62(10), 307-326
- Modest, M. F. (2003), 2nd edn, *Radiative Heat Transfer*. London: Academic Press
- Morton, B. R., Taylor, G., Turner, J. S. (1956). 'Turbulent gravitational convection from maintained and instantaneous sources.' *Proceedings of the Royal Society* 234A, 1
- Mundt, E., Klobut, K., Seppanen, O. (1994). 'Contamination Distribution in Displacement Ventilation - Influence of Disturbances.' *Journal of Building and Environment* 29(3), 311-317
- Mundt, E. (1995). 'Displacement Ventilation Systems - Convection Flows and Temperature Gradients.' *Building and Environment* 30(1), 129-133.
- Naot, D., Shavit, A., Wolfshtein, M. (1970). 'Interactions between components of the turbulent velocity correlation tensor due to pressure fluctuations.' *Israel Journal of Technology* 8, 259-269

- Nguyen, A. V., Evans, G. M. (2006) 'Computational fluid dynamics modelling of gas jets impinging onto liquid pools.' *Applied Mathematical Modelling* 30(11), 1472-1484
- Nishino, K., Samada, M., Kasuya, K., Torii, K. (1996) 'Turbulence statistics in the stagnation region of an axisymmetric impinging jet flow.' *International Journal of Heat and Fluid Flow* 17(3), 193-201
- Nordkvist, M., Grotkjaer, T., Hummer, J. S., Villadsen, J. (2003) 'Applying Rotary Jet Heads for Mixing and mass Transfer in a Forced Recirculation Tank Reactor System.' *Journal of Chemical Engineering Science* 58(17), 3877-3890
- OCIMF, ICS, IAPH, (1996). *International Safety Guide for Oil Tankers and Terminals*, 4th Ed. London: Witherby & Company
- OCIMF (1997) 'Factors Influencing Accelerated Corrosion of Cargo Oil Tanks, September 1997.' London: Oil Companies International Maritime Forum
- Oldervik, O., Neeraas, B. O., Strom, T., Martens, O. M., Meek-Hansen, B. (2000). *VOC Emission Control Systems for Shuttle Tankers and Floating Storage Systems (VOCON) - Final Report, MT23 F00-137*. Trondheim: Norwegian Marine Technology Institute
- Papageorgakis, G. C., Assanis, D. N. (1994). 'Comparison of Linear and Nonlinear RNG-Based K-E Models for Incompressible Turbulent Flows.' *Numerical Heat Transfer, Part B* 35, 1-22.
- Patankar, S. V. (1980). *Numerical Heat Transfer and Fluid Flow*. Washington: Taylor & Francis
- Patwardhan, A. W. (2002) 'CFD Modelling of Jet Mixed Tanks.' *Chemical Engineering Science* 57(8), 11
- Perona, J. J., Hylton, T. D., Youngblood, E. L., Cummins, R. L. (1998) 'Jet Mixing of Liquids in Long Horizontal Cylindrical Tanks.' *Industrial and Engineering Chemical Research* 37(4), 1478-1482
- Pikos, K., (2006) *The Stability of Stratified Layers within Ventilated Enclosures*, Ph.D Thesis, University of Hertfordshire
- Piomelli, U. (1999) 'Large-eddy simulation: achievements and challenges.' *Progress in Aerospace Sciences* 35, 335-362.
- Pope, S. B. (2000). *Turbulent Flows*. Cambridge: Cambridge University Press
- Popiel, C. O., Boguslawski, L. (1979) 'Flow structure of the free round turbulent jet in the initial region.' *Journal of Fluid Mechanics* 90(3), 531-539.
- Popiel, C. O., Trass, O. (1991) 'Visualization of a Free and Impinging Round Jet.' *Experimental Thermal and Fluid Science* 4, 253-264

- Quinn, W. R. (1992) 'Turbulent free jet flows issuing from sharp-edged rectangular slots : the influence of slot aspect ratio.' *Experimental Thermal and Fluid Science* 5(2), 203-215.
- Raithby, G. D. (1999). 'Discussion of the Finite-Volume Method for Radiation, and its Application using 3D Unstructured Meshes.' *Numerical Heat Transfer, Part B* 35: 389-405
- Ranade, V. V. (1996) 'Towards Better Mixing Protocols by Designing Spatially Periodic Flows: The Case of a Jet Mixer.' *Journal of Chemical Engineering Science* 51(11), 2637-2642
- Rauta, D. (2004) 'Double Hull and Corrosion.' Paper DHT04/3 in *Proceedings of the Royal Institute of Naval Architects*, 'Design & Operation of Double Hull Tankers'. Held February 25-26 2004 in London. London: RINA
- Riley, J. J., Lelong, M. P. (2000) 'Fluid Motions in the Presence of Strong Stable Stratification.' *Annual Review Fluid Mechanics* 32, 613-657
- Roe, P. L., (1986) 'Characteristic-based schemes for the Euler equations.' *Annual. Review Fluid Mechanics* 18, 337-365
- Rotta, J. C. (1951) 'Statistische Theorie nichthomogener Turbulenz.' *Zeitschrift für Physik A Hadrons and Nuclei* 131(1), 51-77
- Sagaut, P. (1998). 'Large Eddy Simulation for Incompressible Flows.' Berlin: Springer.
- Sarkar, S. (2003) 'The Effect of Stable Stratification on Turbulence Anisotropy in Uniformly Sheared Flow.' *Computers and Mathematics with Applications* 46(4), 639-646
- Saunders, R. J. (1965). *Heat Losses from Oil-Tanker Cargoes*, B.S.R.A Report NS.90, Marine Engineering Report No. 60. London, The British Ship Research Association.
- Savage, K. M. (1976) 'Marine Gas Hazards Control: Cleaning and Gas-Freeing Shipboard Tanks.' *Environmental Research* 11(2), 213-219.
- Shah, L. J., Furbo, S. (2003) 'Entrance Effects in Solar Storage Tanks.' *Solar Energy* 75(4), 337-348.
- Sherman, F. S., Imberger, J., Corcos, G. M. (1978) 'Turbulence and Mixing in Stably Stratified Waters.' *Annual Review Fluid Mechanics* 10, 267-288
- Shih, T. H., Liou, W. W., Shabbir, A., Yang, Z., Zhu, J. (1994) 'A New K-E Eddy Viscosity Model for high Reynolds Number Turbulent Flows.' *Computers and Fluids* 24(3), 227-238.
- Shy, S. S. (1995) 'Mixing Dynamics of Jet Interaction with a Sharp Density Interface.' *Experimental Thermal and Fluid Science* 10(3), 355-369.
- Siegel, R., Howell, J. (2002), 6th edn. *Thermal Radiation Heat Transfer*. London: Taylor & Francis.

Singh, G., Sundararajan, T., Bhaskaran, K. A. (2003) 'Mixing and Entrainment Characteristics of Circular and Non-Circular Confined Jets.' *Journal of Fluids Engineering* 125(5), 835-843

Skistad, H. (1998). 'Utilizing Selective Withdrawal In The Ventilation Of Large Rooms: "Select Vent"'. In *Roomvent 1998*, 'The 6th International Conference on Air Distribution in Rooms,' Held June 14-17 1998 in Stockholm, Sweden, 17-23.

Smagorinsky, J. (1963) 'General Circulation experiments with the primitive equations I. The basic experiment.' *Monthly Weather Review* 91(3), 99-164

Smyth, W. D., Moum, J. N. (2001) '3D Turbulence'. In Encyclopedia of Ocean Sciences. ed John, H. S. New York: Academic Press: 2947-2955

Stymne, H., Sandberg, M., Mattsson, M. (1991). 'Dispersion pattern of contaminants in a displacement ventilated room - implications for demand control.' In *12th AIVC Conference - 'Air Movement & Ventilation Control Within Buildings'*, Held September 24-27 1991, Ottawa, Canada. 173-190

Tanker Structure Co-operative Forum (1995) *Guidelines for the Inspection and Maintenance of Double Hull Tanker Structures*. London: Witherby

Tennekes, H., Lumley, J. L. (1974). *A First Course in Turbulence*. Cambridge, MA: The MIT Press.

Tanny, J., Chai, A., Kit, E. (1995) 'On the law of turbulent entrainment across a density interface.' *Fluid Dynamics Research* 15(1), 69-74

Tien, C. L. (1968). 'Thermal Radiation Properties of Gases.' *Advances in Heat Transfer* 5, 253-324

Travnicek, Z., Peszynski, K., Hosek, J., Wawrzyniak, S. (2002) 'Aerodynamic and Mass Transfer Characteristics of an annular bi-stable impinging jet with a Fluidic Flip-Flop Control.' *International Journal of Heat and Mass Transfer* 46(7), 1265-1278

Tsubokura, M., Kobayashi, T., Taniguchi, N., Jones, W. P. (2003) 'A numerical study on the eddy structures of impinging jets excited at the inlet.' *International Journal of Heat and Fluid Flow* 24(4), 500-511

Turner, J. S. (1979). *Buoyancy Effects in Fluids*. Cambridge: Cambridge University Press

USCG (2005) *Explosion and sinking of the Chemical Tanker BOW MARINER in the atlantic ocean on Februaru 28, 2004 with loss of life and pollution*. Washington: United States Coast Guard

Vandoormaal, J. P., Raithby, G. D. (1984) 'Enhancements of the SIMPLE Method for Predicting Incompressible Fluid Flows.' *Numerical Heat Transfer* 7, 147-163

Wallis, R. A. (1983) *Axial Flow Fans and Ducts*. New York: John Wiley & Sons, Inc.

- Weiss, J. M., Smith, W. A. (1995) 'Preconditioning Applied to Variable and Constant Density Flows.' *AIAA Journal* 33, (11) 2020-2057
- Werne, J., Fritts, D. C. (2004) 'Anisotropy in a Stratified Shear Layer.' *Physics and Chemistry of the Earth, Part B* 26(4), 263-268
- Wilcox, D. C. (1994) *Turbulence Modelling for CFD*. La Canada, CA: DCW Industries, Inc.
- Xing, H., Awbi, H. B. (2002). 'Measurement and Calculation of the Neutral Height in a room with Displacement Ventilation.' *Journal of Building and Environment* 37(2), 961-967.
- Yakhot, S., Orszag, S. A. (1986a). 'Renormalisation Group Analysis of Turbulence.' *Applied and Computational Mathematics* 57(14), 1722-1724
- Yakhot, S., Orszag, S. A. (1986b). 'Renormalization Group Analysis of Turbulence. I. Basic Theory.' *Journal of Scientific Computing* 1(1), 3-51.
- Yamazaki, H., Osborn, T. (1990) 'Dissipation Estimates for Stratified Turbulence.' *Journal of Geophysical Research* 95(C6), 9739-9744
- Yang, X., Srebric, J., Li, X., He, G. (2004) 'Performance of Three Air Distribution Systems in VOC Removal from an Area Source.' *Building and Environment* 39(11), 1289-1299
- Zughbi, H. D., Rakib M. A. (2004) 'Mixing in a Fluid Jet Agitated Tank: Effects of Jet Angle and Elevation and Number of Jets.' *Journal of Chemical Engineering Science* 59(4), 829-84

Appendices (JOURNAL ARTICLES REMOVED)

-

—

—

2
Height (m)
1
0

Fig. 8. Contours of turbulent intensity; (a) Adiabatic, no conduction or radiation; (b) Non-adiabatic with radiation modelling.

Temperature (C)

Height (m)

